

**Effects of elevated temperature exposure on the microstructural  
evolution of Ni(Cr)-Cr<sub>3</sub>C<sub>2</sub> coated 304 stainless steel**

Yi Ding

Thesis submitted for the degree of Doctor of Philosophy at the  
University of Nottingham

June 2009

**Abstract**

Agglomerated and sintered 25Ni(Cr)-75Cr<sub>3</sub>C<sub>2</sub> powder was deposited onto 304 stainless steel substrates by HVOF thermal spraying. Post spraying thermal treatments were carried out on as-sprayed samples at different temperatures (700°C and 800°C) in air (oxidising). Samples were heat treated from 1 hour up to 16 days and furnace cooled. The powder, coatings and substrate were characterised by a variety of techniques including optical microscopy, X-ray diffraction (XRD), scanning electron microscopy (SEM), microhardness testing and thermogravimetric analysis (TGA).

The results of agglomerated and sintered powder coating microstructural characterisation show that the as-sprayed coating comprised the carbide phase Cr<sub>3</sub>C<sub>2</sub>, a small amount of amorphous phase and a metallic phase which was Ni-rich. The spray process also led to the formation a small amount of Cr<sub>2</sub>O<sub>3</sub> in the coatings. In the heat treated coatings, the carbides Cr<sub>7</sub>C<sub>3</sub> and Cr<sub>23</sub>C<sub>6</sub> were found at the coating substrate interface, the amorphous structure phase was eliminated. With heat treatment, matrix phase supersaturation was reduced, while widespread carbide nucleation and growth generated an expansive carbide skeletal network especially near the coating/substrate interface. An initial softening of the coatings occurred but subsequently the hardness increased again after 2 days was a function of carbide development.

The oxidation kinetics of the 25Ni(Cr)-75Cr<sub>3</sub>C<sub>2</sub> powder and coatings during elevated temperature oxidation in air at 650°C to 1000°C have also been studied. The oxidation behaviour was found to be governed by a parabolic rate law up to 800°C. The activation energy of the coating oxidation reaction, *Q*, was found to be 164 kJ/mol. The mechanism of high temperature oxidation of 25Ni(Cr)-75Cr<sub>3</sub>C<sub>2</sub> coating on top surface has been discussed.

Inter-diffusion between the coating and the 304 stainless steel substrate has been investigated. A distribution of the precipitate phase  $\text{Cr}_{23}\text{C}_6$  within the 304 steel was found from etched substrate samples. The decrease of the microhardness measured with distance away from the interface also revealed that diffusion occurred between coating and substrate during the annealing period. Carbon diffusion distances at different annealing conditions in this work have been measured according to the appearance of the  $\text{Cr}_{23}\text{C}_6$  precipitates and variation in microhardness away from the interface. A simple mathematical model has been used to calculate the theoretical carbon diffusion distance in substrate.

## **Acknowledgements**

Doing a PhD is fulfilling my dream. When the dream comes true, there are many people who I am indebted.

I would like to thank my supervisors Prof. Graham McCartney and Prof. Philip Shipway for their continued support and guidance. I am especially grateful to Prof. Graham McCartney for his outstanding support, encouragement and guidance throughout my PhD studies. I also would like to thank the technicians and administrative staff in the School of Mechanical, Materials and Manufacturing Engineering of Nottingham University. They are Mr. Keith Dinsdale, Mr. Graham Malkinson, Mr. Tom Buss, Mr. Martin Roe and Dr. Nigel Neate. Also Dr Deen Zhang and Mr Rory Sreaton for help with thermal spraying.

I would also like express my thanks to the friends who have been supporting and helping me during last three years. They are: Yan Zhang, Yining Zhang, Tian Feng Tao, Min Chen, Xin Yu Ma, and Zhe Kai Zhu.

Most importantly, the thesis would not have been possible without the encouragement and financial support of my parents, to whom I am eternally indebted. The PhD honour is not just for me, it is a great expectation from my parents. Without their support and love, I can never reach where I am. Here I just want to express my deepest gratitude to them.

## **Abbreviations**

b.c.c	body centre cubic
BSE	backs scattered electrons
C	carbon
C <sub>12</sub> H <sub>26</sub>	kerosene
Cr	chromium
DJ	diamond jet
EDX	electron dispersive x-ray
f.c.c	face centre cubic
Fe	iron
HV	vickers hardness
HVOF	high velocity oxy-fuel
JCPDS	Joint Committee on Powder Diffraction Standard
LALLS	Low Angle Laser Light Scattering
Ni	nickel
O	oxygen
OM	optical microscopy
Q	activation energy
SE	secondary electrons
SEM	scanning electron microscopy
TGA	thermogravimetric analysis
W	tungsten
wt%	weight percent
XRD	X-ray diffraction

---

<b>Abstract</b>	i
<b>Acknowledgements</b>	iii
<b>Abbreviations</b>	iv
<b>Contents</b>	v
<b>Chapter 1 Introduction</b>	1
<b>Chapter 2 Literature review</b>	4
2.1 Thermal spraying	4
2.1.1 Thermal spraying techniques	4
2.1.2 High velocity oxy-fuel spraying (HVOF)	6
2.2 Metallurgy of Ni(Cr)-Cr <sub>3</sub> C <sub>2</sub>	9
2.2.1 CrC-NiCr	9
2.2.1.1 Chromium-Carbon system	9
2.2.1.2 Nickel-Chromium system	10
2.2.1.3 Nickel-Carbon system	11
2.2.1.4 Chromium-Nickel-Carbon system	11
2.2.2 Characterisations of Ni(Cr)-Cr <sub>3</sub> C <sub>2</sub> coatings	12
2.2.2.1 Characterisations of the as-sprayed Ni(Cr)-Cr <sub>3</sub> C <sub>2</sub> coatings	12
2.2.2.2 Characterisation of Ni(Cr)-Cr <sub>3</sub> C <sub>2</sub> coatings and the effect of elevated temperature exposure	18
2.2.2.3 Summary	22
2.3 Microstructural features of austenitic stainless steel	23
2.3.1 The Iron-Chromium-Nickel system	23
2.3.2 Structure and morphology of precipitates	24
2.3.3 Transformation of metastable austenite	25
2.3.4 Summary	26
2.4 Atomic mechanisms of diffusion	28
2.4.1 Carbon activity	28
2.4.2 Mechanism of carbon diffusion in austenite stainless steel	29

---

2.4.3 Summary	31
2.5 Oxidation of metal and metal carbide	32
2.5.1 Oxidation of Metals	32
2.5.1.1 Thermodynamic considerations	32
2.5.1.2 Kinetics of oxidation	34
2.5.1.3 Oxidation of Ni, Cr and Ni-Cr alloys	36
2.5.2 Oxidation of carbides	38
2.5.3 Oxidation of metal-chromium carbide composite systems	39
<b>Chapter 3 Experimental procedures</b>	<b>63</b>
3.1 Introduction	63
3.2 Materials	64
3.2.1 Ni(Cr)-Cr <sub>3</sub> C <sub>2</sub> powders	64
3.2.2 Substrates	64
3.3 Thermal spray procedures	65
3.3.1 Sample preparation and HVOF system	65
3.3.2 Deposition procedure	66
3.4 Heat treatment of Ni(Cr)-Cr <sub>3</sub> C <sub>2</sub> coatings	68
3.5 Powder and coating characterisation	69
3.5.1 Size analysis of powder sample	69
3.5.2 Optical Microscopy (OM)	69
3.5.3 X-ray Diffraction (XRD)	69
3.5.4 Scanning Electron Microscopy (SEM) and EDX Analysis	71
3.5.5 Thermogravimetric Analysis (TGA)	72
3.5.6 Hardness tests	72
3.5.7 Porosity analysis	73

<b>Chapter 4: Microstructure formation in as-sprayed NiCr-Cr<sub>3</sub>C<sub>2</sub> coatings:</b>	<b>76</b>
<b>Results and Discussion</b>	
4.1 Results	76
4.1.1 Introduction	76
4.1.2 Feedstock powder characterisation	77
4.1.2.1 Morphology and size range	77
4.1.2.2 Phase Analysis	77
4.1.3 Influence of spray conditions on coating deposition efficiency	79
4.1.4 Coating from Metallisation powder	81
4.1.4.1 Optical microscopy	81
4.1.4.2 X-ray diffraction	81
4.1.4.3 Scanning Electron Microscopy	81
4.1.4.4 Thickness and hardness	82
4.1.5 Coating from Praxair powder	83
4.1.5.1 Optical microscopy	83
4.1.5.2 X-ray diffraction	83
4.1.5.3 Scanning Electron Microscopy	83
4.1.5.4 Thickness and hardness	84
4.2 Discussion	85
4.2.1 Comparison of the coating from Metallisation and Praxair powder suppliers	85
4.2.2 Comparison with previous work	86
4.2.3 Mechanism of microstructure formation	89
4.2.3.1 Melting and dissolution	89
4.2.3.2 Oxidation during spraying	89
4.2.3.3 Solidification	90
<b>Chapter 5: Effect of elevated temperature exposure on Ni(Cr)-Cr<sub>3</sub>C<sub>2</sub> coated stainless steel: Results and Discussion</b>	<b>109</b>
5.1 Results	109

---

5.1.1	Introduction	109
5.1.2	Characterisation of as-received and heat treated 304 stainless steel	111
5.1.2.1	Characterisation of 304 stainless steel material	111
5.1.2.2	Heat treated stainless steel substrate	112
5.1.3	Characterisation of Ni(Cr)-Cr <sub>3</sub> C <sub>2</sub> coating following high temperature exposure	114
5.1.3.1	Introduction	114
5.1.3.2	Exposure at 700°C in air	114
5.1.3.3	Exposure at 800°C in air	117
5.1.3.4	Summary	120
5.1.4	Characterisation of Ni(Cr)-Cr <sub>3</sub> C <sub>2</sub> coated stainless steel substrate following high temperature exposure	121
5.1.4.1	Introduction	121
5.1.4.2	Scanning Electron Microscopy	121
5.1.4.3	X-ray Diffraction	123
5.1.4.4	Microhardness measure	124
5.1.4.5	Summary	124
5.2	Discussion	126
5.2.1	Influence of heat treatment on the structure of Ni(Cr)-Cr <sub>3</sub> C <sub>2</sub> coatings	126
5.2.1.1	Microstructures of Ni(Cr)-Cr <sub>3</sub> C <sub>2</sub> coatings after heat treatment	126
5.2.1.2	Microhardness of Ni(Cr)-Cr <sub>3</sub> C <sub>2</sub> coatings after heat treatment	128
5.2.2	Diffusion between the coating and the substrate at elevated temperature	130
5.2.2.1	Activity calculations for elements diffusion between coating and substrate	130
5.2.2.2	Modelling of carbon diffusion in as-coated stainless steel 304	131
5.2.3	Summary	135
<b>Chapter 6 Effect of elevated temperature oxidation on Ni(Cr)-Cr<sub>3</sub>C<sub>2</sub> coating: Results and Discussion</b>		<b>172</b>
6.1	Results	172
6.1.1	Introduction	172

---

6.1.2 Thermogravimetric analysis and oxidation kinetics	173
6.1.2.1 Oxidation of Praxair Ni(Cr)-Cr <sub>3</sub> C <sub>2</sub> powder	173
6.1.2.2 Oxidation of Praxair Ni(Cr)-Cr <sub>3</sub> C <sub>2</sub> powder coatings	173
6.1.2.3 Calculation of Ni(Cr)-Cr <sub>3</sub> C <sub>2</sub> coating oxidation kinetics	174
6.1.3 X-ray Diffraction and phase identification	177
6.1.3.1 Ni(Cr)-Cr <sub>3</sub> C <sub>2</sub> coating heated at 700°C in air	177
6.1.3.2 Ni(Cr)-Cr <sub>3</sub> C <sub>2</sub> coating heated at 800°C in air	177
6.1.4 Scanning electron microscopy and EDX analysis of the microstructure	178
6.1.4.1 Cross-sectional morphology of Ni(Cr)-Cr <sub>3</sub> C <sub>2</sub> coating heated at 700°C in air	178
6.1.4.2 Cross-sectional morphology of Ni(Cr)-Cr <sub>3</sub> C <sub>2</sub> coating heated at 800°C in air	178
6.1.5 Top surface oxide morphology of Ni(Cr)-Cr <sub>3</sub> C <sub>2</sub> coating	180
6.1.5.1 Top surface oxide morphology of as-sprayed Ni(Cr)-Cr <sub>3</sub> C <sub>2</sub> coating	180
6.1.5.2 Top surface oxide morphology of Ni(Cr)-Cr <sub>3</sub> C <sub>2</sub> coating heated at 700°C and 800°C in air	180
6.1.6 Summary	183
6.2 Discussion	184
6.2.1 Kinetics of the elevated temperature oxidation for Praxair Ni(Cr)-Cr <sub>3</sub> C <sub>2</sub> powder coating	184
6.2.2 Mechanism of the elevated temperature oxidation for Ni(Cr)-Cr <sub>3</sub> C <sub>2</sub> coating	187
6.2.2.1 Mechanism of the high temperature oxidation of Ni(Cr)	187
6.2.2.2 Mechanism of the high temperature oxidation of Cr <sub>3</sub> C <sub>2</sub> particles in coating	188
6.2.2.3 Mechanism of the high temperature oxidation of Ni(Cr)-Cr <sub>3</sub> C <sub>2</sub> coating	189
6.2.3 Summary	191
<b>Chapter 7 Conclusions</b>	<b>218</b>
<b>References</b>	<b>221</b>
<b>Appendix: X-ray diffraction standards and X-ray diffraction spectra</b>	<b>230</b>

## Chapter 1 Introduction

Thermal spraying is a coating process in the field of surface engineering which is used extensively for a wide range of industrial applications. The technique generally involves the spraying of molten or semi-molten powder or wire feedstock to form metallic and non-metallic coatings. There are many variations of thermal spraying technology, such as high velocity oxy-fuel spraying (HVOF), vacuum plasma spraying (VPS), flame spraying (FS) and arc spraying. In HVOF spraying an oxygen-fuel mixture is burned in a chamber at high pressure and flow rate. Powder particles are injected into the hot gas and heated, accelerated to give extremely high particle velocities and low temperatures compared with other thermal spray process such as air or vacuum plasma spraying (Smith, 1991). The coatings produced through HVOF spraying develop low porosity and high bond strengths with lower thermal input. Due to these characteristics, HVOF spraying is widely used in aero-engine components, engineering components of pumps, shafts or compressors, and many other applications which are all under the aggressive working conditions.

There is an extensive range of materials that can be thermally sprayed for a variety of applications in industrial machinery. Some of these materials include cermets such as WC-Co, Ni(Cr)-Cr<sub>3</sub>C<sub>2</sub>, ceramics such as Al<sub>2</sub>O<sub>3</sub>-TiO<sub>2</sub>, Cr<sub>2</sub>O<sub>3</sub> and metals such as Mo-based alloys, aluminium bronze, and nickel alloys. Among them the WC-Co, 25Ni(Cr)-75Cr<sub>3</sub>C<sub>2</sub> based cermets are the most commonly used for wear and corrosion resistant coatings at ambient and elevated temperatures respectively. These system provide high hardness, good wear resistance and good protection against aqueous corrosion. However, in air or other oxidising environments WC-Co coatings begin to degrade as the temperature is increased and service temperatures are limited to below about 350°C (Berger, 1996). On the other hand, Ni(Cr)-Cr<sub>3</sub>C<sub>2</sub> coatings can be used extensively to mitigate wear at higher temperatures where WC based cermets are not suitable. Ni(Cr)-Cr<sub>3</sub>C<sub>2</sub> coatings can operate in oxidising environments at service

temperature up to 900°C (He, 2000). At lower temperatures Ni(Cr)-Cr<sub>3</sub>C<sub>2</sub> system coatings still can be used to against wear and corrosion.

The complex metastable state of as-sprayed Ni(Cr)-Cr<sub>3</sub>C<sub>2</sub> coatings leads to complex microstructural and compositional transformations when they are exposed to elevated temperatures. The mechanical properties also change, in particular the microhardness which is commonly related to the performance of carbide coatings under wear conditions (Matthews, 2003). Recently, several groups have investigated the microstructural characterisation and microhardness variation in relation to carbide development and other microstructural changes in heat treated NiCr/CrC thermal spray coatings. (Guilemany 2002; Matthews, 2003; He, 2001) However, knowledge about this area especially the effect of heat treatment is still limited. Also the microstructural development will depend on the initial as-sprayed coating structure. This will in turn depend on the feedstock powder and the HVOF spray system used. Also during high temperature operation there is the potential for interdiffusion between the NiCr-Cr<sub>3</sub>C<sub>2</sub> coating and the substrate material. This could lead to changes in the properties of both the coating and the substrate. This aspect has received little attention in the literature.

A future aspect of considerable importance is the oxidation behaviour of NiCr-Cr<sub>3</sub>C<sub>2</sub> coatings in air at temperatures as high as 800°C. Such high temperature oxidation of nickel-based chromium carbide coatings has been studied by only a few investigators (Matthews, 2009; Ye, 2008). However, the knowledge about this area especially with the mechanism of the oxidation of chromium carbide is still very limited.

The overall aim of this work was to investigate the effects of elevated temperature exposure on the microstructural evolution of the NiCr-Cr<sub>3</sub>C<sub>2</sub> coated 304 stainless steel system. Specific objectives were as follows:

(i) To investigate as-sprayed microstructures produced by the Met Jet HVOF system and changes in as-sprayed microstructures as a result of long term exposure to

elevated temperatures and oxidising environments. Also to better understand the relationship between the observed changes in microstructure and hardness.

(ii) To investigate and explain the changes of microstructures occurring within both the coating and the substrate as a result of high temperature inter-diffusion.

(iii) To investigate and explain NiCr-Cr<sub>3</sub>C<sub>2</sub> coating oxidation in air at the coating surface at elevated temperatures from 650°C to 1000°C.

## Chapter 2: Literature review

### 2.1. Thermal spraying

Thermal spraying is a well-established technology which is extensively used for a wide range of industrial applications for applying wear and corrosion resistant coatings in many main industrial sectors, including aerospace, automotive, power generation and offshore. In this technique, typically powder or wire are melted or partially melted by a heat combustion source, accelerated by the hot gas and impacted onto a properly prepared substrate. Solidification occurs very quickly with cooling rates of splats around  $10^6$  K/s. Thus, the as-sprayed deposit can be ultra-fine grained. In the following sections the main spraying techniques and some post-spray treatments will be introduced.

#### 2.1.1. Thermal spraying techniques

There are many variations of thermal spraying technology which are widely used in the thermal spray industry. Apart from high velocity oxy-fuel spraying (HVOF), some other common thermal spraying processes are plasma spraying (PS), flame spraying (FS) and arc spraying (AS).

Plasma spraying (PS):

In the arc plasma process a plasma is created by an electric arc between a nozzle shaped copper anode and a tungsten cathode. A gas, usually argon, flows around the cathode and through the anode. A high voltage discharge between the electrodes ionizes the gas and forms a plasma exiting the gun via the nozzle, resulting in very high temperatures, up to  $16000^{\circ}\text{C}$ , being generated. The powder is injected radially into the plasma, melted or partially melted, accelerated up to  $\sim 200\text{ ms}^{-1}$  and deposited onto the surface forming a coating.

Plasma spraying involves three principal techniques: air plasma spraying (APS), argon-shrouded plasma spraying (ASPS) and vacuum plasma spraying (VPS). Typical bond strengths of alloy coatings by VPS are higher than 80 MPa with porosity typically less than 5%. The thickness range is about 150-500  $\mu\text{m}$ . VPS installations are usually developed to deposit coatings for hot corrosion resistance with materials such as Ni-based alloys which are widely used for gas turbine and aircraft engine components (ASM, 1987).

Flame spraying (FS):

Flame spraying sometimes called combustion flame spraying. Powder, wire or rod can be used as the coating materials in this technique. For the powder flame spraying process, powder is fed directly into the flame by a stream of compressed air or inert gas (argon or nitrogen). The melted particles accelerate in the direction of the workpiece with a speed of about 30-120  $\text{ms}^{-1}$  and coated on the surface. For the wire flame spraying process, the wire feed rate and flame settings must be balanced to produce continuous melting of the wire to give a fine particulate spray. The flame melts the end of the wire/rod, which is atomized by compressed air and accelerates towards the substrate. The highest melting point of material which can be deposited is 2800°C. Typical values of the bond strength are in the range of 15 MPa for ceramics coatings to 30 MPa for other materials. The range of porosity is usually about 10-20%. The thickness range is about 100-2500  $\mu\text{m}$  (ASM, 1987).

Arc (AS) spraying:

Arc spraying is a thermal spray process in which a pair of electrically conductive wires is melted by means of an electric arc. The molten material is atomized by jets of compressed air or gas and sprayed on to the substrate surface with a velocity about 240  $\text{ms}^{-1}$  and rapidly solidified to form a coating. The typical temperature in the gun is about 5500°C, and the bond strength is in the range of 10-30 MPa. The range of porosity in the coating is usually about 7-8%. Thickness range of the coating is approximate 100-1500  $\mu\text{m}$  (ASM, 1987).

### 2.1.2. High velocity oxy-fuel spraying (HVOF)

The HVOF (high velocity oxy-fuel) thermal spray process is now one of the most widely used thermal spraying techniques. The HVOF torch was invented at the end of the 1970s and beginning of the 1980s. Nowadays, there are a number of different designs of HVOF guns which use different methods to achieve high velocity spraying (Wirojanupatump, 1999).

In the HVOF process, the fuel is burnt with oxygen at a high pressure (up to 12 bar) with the temperature of the gas up to 3000°C and accelerated to very high velocities up to 1000 ms<sup>-1</sup>. The powder is injected into the hot gas jet as a suspension in a carrier gas. Typical liquid fuel is normally kerosene with H<sub>2</sub> and C<sub>3</sub>H<sub>6</sub> as gas fuels. The combustion chamber and the nozzle are water-cooled. Schematic designs of different high velocity oxy-fuel spraying guns are shown in Fig 2.1. The bond strength of HVOF coatings can be as high as 90 MPa. The range of porosity can be as low as 0.5%. Thickness range is typically about 100-300 µm (Sturgeon, 1992).

According to the different types of fuel, the HVOF spray gun system can be classified into two groups. One of them is gaseous fuel guns which include Diamond Jet, HV2000, Top Gun and Jet-Kote. The other is liquid fuel guns such as the JP5000 and Met-Jet guns. They are all based on the same fundamental principles, but each one has differences in design. Firstly, the powder feed position of the HV2000 and Top Gun is different from that of the Jet-Kote and Diamond Jet systems. In the HV2000 and Top Gun systems, powder is fed axially into the back of the combustion chamber whereas for the Jet-Kote and Diamond Jet systems the powder is fed into the exhaust barrel at a different distance from the chamber in each case (Wirojanupatump, 1999).

Kamnis (2008) has studied the numerical simulation of Inconel 718 particles during thermal spraying by Met-Jet HVOF system. He found that the location of powder injection in the gun is very important to generate consistent coating products. The

particle velocity and particle surface temperature profiles from different injection positions as well as the gas flow velocity and temperature profiles are compared and shown in Fig 2.2. It is clear to see that the gas flow at the combustion chamber exit reaches highest temperature of 3000K and the temperature at the powder injection location drops to 2200K. Additionally, Kamnis also examined the effect of different particle sizes on particle behaviour during thermal spraying. The velocity and temperature profiles of particles of different sizes range from 5 to 40  $\mu\text{m}$  are shown in Fig 2.3. It is clear to see that the smaller particles have higher velocity during thermal spraying. It is also apparent that large particles (30 or 40  $\mu\text{m}$ ) have low temperature profiles (less than 1300 K) during the flight while small particles (5  $\mu\text{m}$ ) reach the maximum temperature of 2000 K.

Characteristics of thermal spray processes and as-sprayed coatings introduced by different thermal spraying techniques are compared in Table 2.1. In this table the HVOF sprayed coating gives the highest bond strength and lowest porosity compared with other sprayed coatings. Hence, it is expected to give better environmental protection and other properties. Compared to similar plasma air spraying, HVOF has lower thermal energy-combustion temperature than plasma; but higher kinetic energy-gas velocity at the nozzle exit which is supersonic, compared to subsonic gas velocity of plasma (Berger, 1996). Investigations by Dulin (1990) and Ohliger (1990) on a Ni-Cr base alloy, using HVOF and plasma system. Their results showed that HVOF thermally sprayed coating gave better coating structures than that by plasma spraying.

In this research, the Ni(Cr)-Cr<sub>3</sub>C<sub>2</sub> cermet system was investigated for the production of sprayed coatings which can potentially be used in high temperature-wear resistance and oxidation resistant applications in aerospace and engineering industries. The Ni(Cr)-Cr<sub>3</sub>C<sub>2</sub> coatings can have good performance in environments at service temperatures up to 800°C. As mentioned above, the high velocity oxy-fuel (HVOF) thermal spraying process has been shown to be one of the best methods for depositing

conventional Ni(Cr)-CrC feedstock powders, because the hypersonic velocity of the flame shortens the time of interaction between the powder and the flame (Matthews, 2009). The microstructures of 25Ni(Cr)-75Cr<sub>3</sub>C<sub>2</sub> coatings sprayed by three different thermal spraying systems (HVOF DJ, Plasma arc and APS) have been compared by Berger (1996). He showed that the HVOF process could lead to thicker and better coatings than these produced by other methods.

## 2.2. Metallurgy of Ni(Cr)-Cr<sub>3</sub>C<sub>2</sub>

### 2.2.1 CrC-NiCr

Nickel-chromium-chromium carbide contains chromium carbide which has good performance of high temperature wear resistance. Ni-Cr alloy as the metallic binder phase has moderate strength and oxidation resistance at elevated temperatures. Ni(Cr)-Cr<sub>3</sub>C<sub>2</sub> cermets coating are used for a wide variety of applications such as aircraft gas turbines, steam turbine power plants and nuclear power systems. The following section covers the results of investigations into the chromium-carbon, nickel-chromium and nickel-carbon systems.

#### 2.2.1.1. Chromium-Carbon system

The binary phase diagram recommended by Venkatraman and Neumann (1990) is shown in Fig 2.4. According to the diagram, three well-characterised carbides of chromium can be listed as Cr<sub>23</sub>C<sub>6</sub>, Cr<sub>7</sub>C<sub>3</sub> and Cr<sub>3</sub>C<sub>2</sub> in Table 2.2 (Louis, 1971).

At 1534±10 °C the first eutectic reaction  $L = (Cr) + Cr_{23}C_6$  happens and the solubility of C in the Cr-C solid solution phase extends to 0.07 wt% C. A peritectic reaction of  $L + Cr_7C_3 = Cr_{23}C_6$  takes place at 1576±10 °C. Moreover, at 1727±7 °C there is another eutectic reaction  $L = Cr_7C_3 + Cr_3C_2$  and a melting temperature of 1756±10 °C for Cr<sub>7</sub>C<sub>3</sub>. The second peritectic reaction forming Cr<sub>3</sub>C<sub>2</sub> happens at 1811±10 °C due to the reaction  $L + C = Cr_3C_2$ .

#### Crystal structures

In the Cr-C system, three kinds of crystal structures are formed of the intermediate phases named as Cr<sub>23</sub>C<sub>6</sub>, Cr<sub>7</sub>C<sub>3</sub> and Cr<sub>3</sub>C<sub>2</sub> (Louis, 1971). Cr<sub>23</sub>C<sub>6</sub> has the lowest carbon content and is reported to be a complex fcc crystal with the cube edge 1.0655 nm with 116 atoms/unit cell (Xie, 2006). Cr<sub>7</sub>C<sub>3</sub> is reported as an orthorhombic structure with a rather elongated c-axis ( $c/a=2.683$ ) and its unit cell contains 80 atoms (Music, 2004, Esteve, 2005). Xie's (2005) report indicated that in Cr<sub>7</sub>C<sub>3</sub> there are many Cr atoms at

a distance of about 0.25 nm from C atoms and the Cr atom reacts strongly with the C atom at these distances. The structure of  $\text{Cr}_3\text{C}_2$  is orthorhombic with lattice parameter dimensions of  $a=0.1147$ ,  $b=0.5545$ ,  $c=0.2830$  (the vertical axis). In each individual type of structure carbon atoms are situated at the centre of a trigonal prism and the corner of the prisms are occupied by chromium atoms. Every vertical cell contains a C atom, but only alternate horizontal cells do so. Cottrell (1995) indicated in his study of the crystal structures of transition metal carbides that the structure of  $\text{Cr}_3\text{C}_2$  can be regarded as units stacked in vertical columns, each unit consisting of two vertical and four horizontal cells.

### **Mechanical properties**

In the carbide series ( $\text{Cr}_{23}\text{C}_6$ ,  $\text{Cr}_7\text{C}_3$  and  $\text{Cr}_3\text{C}_2$ ),  $\text{Cr}_3\text{C}_2$  has the best mechanical properties and coatings with greater content of this carbide will have better wear resistance. The Vickers hardness of  $\text{Cr}_3\text{C}_2$  is  $1600 \text{ kgf/mm}^2$ .  $\text{Cr}_7\text{C}_3$  chromium carbide has a typical nominal hardness of  $1300 \text{ kgf/mm}^2$ , and  $\text{Cr}_{23}\text{C}_6$  has the lowest value of hardness  $1000 \text{ kgf/mm}^2$  in the carbide series. (Storms, 1967)

#### **2.2.1.2. Nickel-Chromium system**

From the chromium-nickel binary phase diagram in Fig 2.5 (Venkatraman, 1990), the melting points of nickel and chromium are  $1455^\circ\text{C}$  and  $1907^\circ\text{C}$ , respectively. A eutectic reaction happens at  $1345^\circ\text{C}$  extending from 47 to 65 wt. % and the eutectic point is at 53 wt. % Cr. Two solid solutions, face-centered cubic (FCC) nickel and body-centered cubic (BCC) chromium, are formed during the eutectic reaction as  $L = \text{Cr} + \text{Ni}$ . Solubility of Cr in Ni in the solid state is restricted at  $500^\circ\text{C}$  to 21 wt% Cr, but there is a nickel-rich single phase region  $\text{Ni}_2\text{Cr}$  with an orthorhombic structure extending from 22 to 37 wt% Cr which intervenes below  $580^\circ\text{C}$ .

The nickel-chromium series of alloys led the way to higher strength and wear resistance at elevated temperatures (Chawla, 1993). The nickel-chromium alloys are used for a wide variety of applications such as aircraft gas turbines, nuclear power

systems and chemical and petrochemical industries for corrosion resistance and heat resistance.

### 2.2.1.3. Nickel-Carbon system

The nickel-carbon phase diagram is shown in Figure 2.6 (Venkatraman, 1990) which includes a simple eutectic reaction  $L = Ni + C$  which takes place at  $1326.5^{\circ}\text{C}$  with the solubility of carbon in nickel in the solid state is 0.6 wt% C.

### 2.2.1.4. Chromium-Nickel-Carbon system

The phase equilibria of the chromium-nickel-carbon system which gives valuable information at the service temperature were studied by Kajihara (1990) and Velikanova (1998). They calculated isothermal sections at 1200, 1100, 1000 and  $800^{\circ}\text{C}$  of the ternary Cr-Ni-C system which are shown in Fig 2.7. There are three carbides:  $\text{Cr}_{23}\text{C}_6$ ,  $\text{Cr}_7\text{C}_3$  and  $\text{Cr}_3\text{C}_2$ . Kajihara (1990) investigated the solubility of nickel in  $\text{Cr}_3\text{C}_2$  which is about 1 at.% at  $1100^{\circ}\text{C}$ . He also indicated that carbon can be dissolved in the nickel-rich fcc phase only to a with very limited extent and is also severely restricted in the chromium-rich bcc phase. With the increasing temperature, the carbon solubility in the fcc phase increases. Velikanova (1998) also gave vertical sections of the Cr-Ni-C phase diagram in Fig 2.8 which are through the tie lines between Ni and different carbides.

## **2.2.2. Characterisation of HVOF sprayed Ni(Cr)-Cr<sub>3</sub>C<sub>2</sub> coatings**

### **2.2.2.1. Characterisations of the as-sprayed Ni(Cr)-Cr<sub>3</sub>C<sub>2</sub> coatings**

25Ni(Cr)-75Cr<sub>3</sub>C<sub>2</sub> coatings produced by thermal spraying generally exhibit good wear and corrosion or oxidation resistance at elevated temperatures. However, these wear and corrosion resistant behaviours are significantly affected by the microstructure of the coatings. Therefore, it is important to understand and control microstructure formation.

#### **Microstructures**

Generally, in HVOF spraying of cermet powder, particles are heated so that the metallic phase becomes molten or partially molten allowing the carbide phase to begin to dissolve into it. Also the particles are exposed to an atmosphere which contains oxygen and has the potential to oxidise the phases present. On impact with the substrate the molten phase re-solidifies at high cooling rates. Therefore, coating microstructure formation is complex and will depend very much on precise process conditions and powder type. In previous investigations (Table 2.3), four types of Ni(Cr)-chromium carbide powder based on different manufacturing techniques, namely: agglomerated and sintered; sintered and crushed; blended; and composite, were employed for thermal spraying researches. Also coatings were deposited using different HVOF thermal spray systems.

#### **Agglomerated and sintered**

Agglomeration (spray-drying) is the most versatile technique to agglomerate the metals and carbides or cermets together. In this process, a slurry which contains finely dispersed material, organic binder and water is fed into a centrifugal atomizer or nozzle atomizer by pump. The slurry is dried with hot air in a drying chamber and the moisture in the droplets evaporates during flight in the chamber. Powder is discharged continuously from the drying chamber. In the sintering process, the powder produced from spray-drying will be heated at low temperature to burn off the

organic binder and sintered at high temperature to fuse the particles together. This technique is an ideal process where the end-product must comply with precise quality standards regarding particle size distribution, residual moisture content, bulk density, and particle shape. (Pawlowski, 1995)

There are a number of published works on microstructure formation and phase transformations in thermally sprayed agglomerated 25Ni(Cr)-75Cr<sub>3</sub>C<sub>2</sub> powder coatings. For example, Zimmermann (1996) has reported the phase analysis of the agglomerated and sintered 25Ni(Cr)-75Cr<sub>3</sub>C<sub>2</sub> powder coatings by using the Diamond Jet system. The phases existing in the as-received powder were clearly identified by XRD as Cr<sub>3</sub>C<sub>2</sub> and Ni(Cr) and the coatings showed only Cr<sub>3</sub>C<sub>2</sub>. He (2000) and Manish (2006) also reported Cr<sub>3</sub>C<sub>2</sub> was the only carbide phase present in as-sprayed agglomerated 25Ni(Cr)-75Cr<sub>3</sub>C<sub>2</sub> powder coatings. Additionally, Matthews (2009) also found significant Cr<sub>3</sub>C<sub>2</sub> phase peaks indicated by XRD after spraying the agglomerated and sintered 25Ni(Cr)-75Cr<sub>3</sub>C<sub>2</sub> powders using a HVOF Microjet system. He mentioned, however, that the concentration of Cr<sub>7</sub>C<sub>3</sub>, which might be formed in flight, was too low to be distinguished definitively from the background in the XRD pattern. Similar work has been done by Suegama (2006), he used XRD to analyse the agglomerated 25Ni(Cr)-75Cr<sub>3</sub>C<sub>2</sub> powder and coatings sprayed by the DJ HVOF system. It is reported that powders comprised Cr<sub>3</sub>C<sub>2</sub>, Cr<sub>7</sub>C<sub>3</sub> and Ni matrix. The coating also showed clearly these same two carbides. Moreover, Guliemany (1996) reported three carbide phases Cr<sub>3</sub>C<sub>2</sub>, Cr<sub>7</sub>C<sub>3</sub> and Cr<sub>23</sub>C<sub>6</sub> were present in both the agglomerated and densified 25Cr<sub>3</sub>C<sub>2</sub>-75Ni(Cr) powder and its as-sprayed coating. These three carbides Cr<sub>3</sub>C<sub>2</sub>, Cr<sub>7</sub>C<sub>3</sub>, Cr<sub>23</sub>C<sub>6</sub> were also found in Monhanty's (1996) investigation of the sliding wear behavior of thermally sprayed agglomerated 75/25 Cr<sub>3</sub>C<sub>2</sub>/Ni(Cr) powder coatings produced by the Jet Kote II HVOF system. Some of the investigators above (Matthews, Guilemany and He) also found an amorphous matrix phase based on Ni(Cr, C) in the as-sprayed coating due to the dissolution of carbides during the spraying.

Sasaki et al. (1992) using a DJ (Diamond Jet) HVOF system reported that X-ray diffraction showed that the only chromium carbide phase present in a coating using sintered, crushed 75Ni(Cr)-25Cr<sub>3</sub>C<sub>2</sub> powder was Cr<sub>3</sub>C<sub>2</sub>. However, Edris (1997) has characterized the sintered and crushed 25Cr<sub>3</sub>C<sub>2</sub>-75Ni(Cr) powder and the coating sprayed by the Top Gun-HVOF spray system. The powder only contained Cr<sub>3</sub>C<sub>2</sub> and Ni(Cr). The as-sprayed coating appeared to have the new carbide phase Cr<sub>7</sub>C<sub>3</sub>, retained Cr<sub>3</sub>C<sub>2</sub> and the Ni(Cr) matrix. Edris explained that high cooling rate during deposition process most probably lead to the formation of fine scale Cr<sub>7</sub>C<sub>3</sub> and amorphous regions in the coating. Wirojanupatump (2001) using XRD analysis also found Cr<sub>3</sub>C<sub>2</sub> and some Cr<sub>7</sub>C<sub>3</sub> in the sintered and crushed 25Cr<sub>3</sub>C<sub>2</sub>-75Ni(Cr) powder coating by Top Gun HVOF spraying. In addition, the existence of Cr<sub>3</sub>C<sub>2</sub>, Cr<sub>7</sub>C<sub>3</sub> and Cr<sub>23</sub>C<sub>6</sub> was confirmed in Ji's (2006) report. In his experiment, the sintered and crushed Cr<sub>3</sub>C<sub>2</sub>-25wt%Ni(Cr) powder was used for a CH-2000 HVOF spray system introduced in Li's (1999) report. The results showed that the Cr<sub>3</sub>C<sub>2</sub> particle size was significantly reduced after the spraying and Cr<sub>7</sub>C<sub>3</sub> carbide was mainly present around the primary Cr<sub>3</sub>C<sub>2</sub> carbide, and the small Cr<sub>23</sub>C<sub>6</sub> carbide dispersed in the Ni(Cr) alloy matrix with a nano-crystalline structure.

### **Blended**

Wirojanupatump (2001) has also reported the phase analysis of blended 75Ni(Cr)-25Cr<sub>3</sub>C<sub>2</sub> powder and HVOF-sprayed coatings by Top Gun system. The phases existing in the as-received powder were clearly identified by XRD as Cr<sub>3</sub>C<sub>2</sub> and Ni(Cr) phases whilst the coatings showed only Cr<sub>3</sub>C<sub>2</sub> as the carbide phase. Shaw (1994) claimed that Cr<sub>3</sub>C<sub>2</sub> decarburizes as a result of HVOF spraying using a Jet Kote gun forming predominately Cr<sub>2</sub>C and Cr<sub>23</sub>C<sub>6</sub> phases. This agreed with the results of phase identification of the blended 75Ni(Cr)-25Cr<sub>3</sub>C<sub>2</sub> powder coating sprayed by a Jet Kote HVOF system (Hwang, 1993). The phases identified were Cr<sub>3</sub>C<sub>2</sub>, Cr<sub>2</sub>C and Cr<sub>23</sub>C<sub>6</sub>. In addition, Crawmer (1992) reported that X-ray diffraction scans showed the presence of Cr<sub>7</sub>C<sub>3</sub> and Cr<sub>23</sub>C<sub>6</sub> phases in coatings.

### Composite

Composite 30NiCr-70CrC powder coating has been studied by Wirojanupatump (2001) using a Top Gun HVOF spray system. In his XRD results,  $\text{Cr}_{23}\text{C}_6$  was identified as the only carbide in both powder and its as-sprayed coating. Ye (2008) reported the XRD patterns of the Diamond Jet-sprayed Cr-(39 wt%)Ni-(7 wt%)C coatings showed  $\text{Cr}_3\text{C}_2$  as the only detectable carbide phase in coating. He also mentioned small amounts of  $\text{Cr}_7\text{C}_3$  might have formed through decarburization of  $\text{Cr}_3\text{C}_2$ , but its concentration was too low to be distinguished from other overlapping peaks.

As mentioned above, most of the investigators indicated the as-sprayed coating matrix contained the carbides appearing in different grey levels of contrast in the SEM, and was formed as a result of the partial dissolution of chromium carbide and the formation of an amorphous matrix phase with Ni(Cr, C). On the other hand, some of the investigators indicated that  $\text{Cr}_3\text{C}_2$  was the only carbide in the as-sprayed coatings whilst some other investigators found  $\text{Cr}_7\text{C}_3$  or  $\text{Cr}_{23}\text{C}_6$  in their coatings. So the formation of other carbides during thermal spraying has not been fully understood by the previous researchers.

Coating performance is strongly dependent on the coating microstructure, which in turn is dependent on the characteristics of the starting powder from which the coating is formed and the spray system employed. Wirojanupatump (2001) has compared the microstructural characterisation of NiCr-CrC coatings sprayed by different types of powders based on different manufacturing techniques including sintered and crushed, blended and composite. But in his studies the agglomerated and sintered powder was not investigated. Although, several researchers have also attempted to compare the microstructures of 25Ni(Cr)-75 $\text{Cr}_3\text{C}_2$  coatings sprayed by different HVOF spraying systems including Diamond Jet, Top Gun, JP5000 and Jet Kote (Zimmermanne, 1996; Beger, 1996). Little has been reported about the coating sprayed with Met Jet system.

### Oxidation during coating deposition

The oxidation behavior of 25Ni(Cr)-75Cr<sub>3</sub>C<sub>2</sub> powder during thermal spraying has been studied. An investigation by Sasaki (1992) reported that in the sintered, crushed and clad 25Ni(Cr)-75Cr<sub>3</sub>C<sub>2</sub> coatings using a METCO DJ (Diamond Jet) system there were some oxides (mainly Cr<sub>2</sub>O<sub>3</sub>) formed on the coating surface with a depth of 20µm and very little oxidation within the body of the coating. Sobolev (1995) indicated in his report that the coating structures formed by Top Gun HVOF spraying of the composite and agglomerated 25Ni(Cr)-75Cr<sub>3</sub>C<sub>2</sub> powders have Cr<sub>2</sub>O<sub>3</sub> near the particle surface. Guilemany (2002) claimed that during thermal spraying there were structural and compositional modifications of the phases present in the initial powders and oxidation of the particles took place during spraying leading to the formation Cr<sub>2</sub>O<sub>3</sub>. Zimmermann (1996) showed that the 25Ni(Cr)-75Cr<sub>3</sub>C<sub>2</sub> coatings applied with Diamond Jet and the JP-5000 systems all contain Cr<sub>2</sub>O<sub>3</sub> as the only chromium oxide during spraying. He also mentioned Cr<sub>7</sub>C<sub>3</sub> and Cr<sub>23</sub>C<sub>6</sub> appeared as oxidation products in the coatings. However, these phases were difficult to detect due to the high number of coincident diffraction lines.

In Wirojanupatump's (2001) work, there were two different oxides identified in the XRD spectra of the sintered and crushed 25Ni(Cr)-75Cr<sub>3</sub>C<sub>2</sub> powder coating, they were Cr<sub>2</sub>O<sub>3</sub> and CrO. While in as-sprayed composite 25Ni(Cr)-75Cr<sub>3</sub>C<sub>2</sub> powder coating, several different peaks of chromium oxides were found in the XRD spectra namely Cr<sub>2</sub>O<sub>3</sub>, CrO and Cr<sub>3</sub>O<sub>4</sub>. The mechanism of phase formation was explained in his thesis Wirojanupatump (1999). It was explained that the liquid may precipitate either solely through eutectic solidification as



or through monotectic and follow by eutectic solidification as



and then



Matthews (2009) has studied the oxide scales formed on agglomerated and sintered Ni(Cr)-Cr<sub>2</sub>C<sub>3</sub> coatings during thermal spraying. He indicated that the Ni(Cr) and Cr<sub>3</sub>C<sub>2</sub> phases oxidised independently. The carbide forms a thin adherent Cr<sub>2</sub>O<sub>3</sub> scale, the Ni(Cr) splats form large bulbous NiO scales on small sections which are exposed to the surface, whilst on larger matrix regions the NiO scale is consumed by a solid state reaction with Cr<sub>2</sub>O<sub>3</sub> to form NiCr<sub>2</sub>O<sub>4</sub>. Edris (1997) found the presence of phases with the Cr<sub>2</sub>O<sub>3</sub> and NiCr<sub>2</sub>O<sub>4</sub> (spinel) crystal structures from his XRD spectra of the as-sprayed coating. As mentioned above, a summary of oxide phases in as-sprayed Ni(Cr)-Cr<sub>2</sub>C<sub>3</sub> coatings by different investigators are listed in Table 2.4.

### **Microhardness**

Microhardness of 25Ni(Cr)-75Cr<sub>3</sub>C<sub>2</sub> as-sprayed coatings produced by different spraying systems has been investigated in previous studies. Wirojanupatump, (2001) reported the influence of three different 25Ni(Cr)-75Cr<sub>3</sub>C<sub>2</sub> powders on the coating characteristics by using Top gun HVOF spray system. The sintered and crushed powder coating shows the highest microhardness value 910 HV<sub>300</sub>, the microhardness of the blended powder coating is 650 HV<sub>300</sub>, and the value of the composited powder coating was 820 HV<sub>300</sub>. Furthermore, Matthews (2003) used agglomerated and sintered powder by GMA Microjet HVOF system, and formed the microhardness 1155 HV<sub>300</sub>. Moreover, the microhardness of agglomerated and densified 25Ni(Cr)-75Cr<sub>3</sub>C<sub>2</sub> powder sprayed by DJ2700 HVOF gun was 743 HV<sub>300</sub> (Guilemany, 2002). He also claimed that higher coating microhardness values will be achieved when samples are oxidised and forming hard Cr<sub>2</sub>O<sub>3</sub> phase in the coating during thermal spraying. These microhardness values are listed in Table 2.5.

### 2.2.2.2 Characterisation of Ni(Cr)-Cr<sub>3</sub>C<sub>2</sub> coatings and the effect of elevated temperature exposure

HVOF chromium carbide coatings are widely used for high-temperature wear-resistant applications in aerospace, automotive and other industries. During deposition compositional degradation occurs through dissolution of the carbide phase into the matrix. High temperature exposure leads to transformations in the microstructure, which also influence the mechanical properties such as coating microhardness. Few previous researchers have studied 25Ni(Cr)-75Cr<sub>3</sub>C<sub>2</sub> coatings after annealing at elevated temperatures within different exposure times. An overview of all types of work is listed in Table 2.6.

#### Microstructure

Previous work on both short term and long term heat treatments of 25Ni(Cr)-75Cr<sub>3</sub>C<sub>2</sub> thermal spray coatings shows the rapid transformation of the metastable as-sprayed coating composition upon exposure at elevated temperature (Matthews, 2003).

For the short term (<24h) annealing conditions, Guilemany (2002) has studied the 25Ni(Cr)-75Cr<sub>3</sub>C<sub>2</sub> coatings after 1 hour annealing in air at 450, 760 and 880°C. The XRD patterns show a dramatic microstructural development in the coating after heat treatment. After 760°C the amorphous peak from the as-sprayed coating disappeared, with narrow, intense Ni(Cr) peaks dominating the matrix phase spectra. Cr<sub>3</sub>C<sub>2</sub> was the only carbide phase detected throughout the period of heat treatment. He also mentioned that all the samples treated above 450°C show an increase in the intensity of the Cr<sub>3</sub>C<sub>2</sub> peaks. Cr<sub>2</sub>O<sub>3</sub> was detected in these XRD spectra with low intensity, noisy peaks indicating that this phase was present in very low concentrations after 1 hour exposure. With continued exposure, the intensity of the Cr<sub>2</sub>O<sub>3</sub> peaks increased in XRD spectra. The SEM cross sectional images of his short term heat treated coatings also show a greater amount of black layers (Cr<sub>2</sub>O<sub>3</sub>) than that in the as-sprayed coating. The results published by He (2001) also showed that Cr<sub>2</sub>O<sub>3</sub> was the only chromium

oxide detected by XRD from the 25Ni(Cr)-75Cr<sub>3</sub>C<sub>2</sub> coating after 8hours annealing in air at 800°C.

For the long term (>24h) annealing conditions, Edris (1997) has studied the HVOF sintered and crushed 25Ni(Cr)-75Cr<sub>3</sub>C<sub>2</sub> powder coatings heat-treated at 900°C for 50 and 100 hours. The XRD patterns of these coatings after the top 50 µm had been removed show clear evidence for the presence of Cr<sub>7</sub>C<sub>3</sub>. He explained the carbide change during the heat treatment from Cr<sub>3</sub>C<sub>2</sub> to Cr<sub>7</sub>C<sub>3</sub> on the basis of thermodynamic equilibrium. In the ternary phase diagram for Cr, Ni and C the average composition of the starting powder gives a thermodynamic driving force for the formation of the M<sub>7</sub>C<sub>3</sub> and M<sub>3</sub>C<sub>2</sub> phase in heat treatment process. Moreover, Edris did not see a noticeably different Cr<sub>2</sub>O<sub>3</sub> content after 100hours 900°C annealing compared to the original coating (having removed the surface layer).

Matthews (2003 & 2009) has investigated the microstructure of agglomerated and sintered 25Ni(Cr)-75Cr<sub>3</sub>C<sub>2</sub> powder HVOF coatings after long term exposure from 2 to 60 days at 900°C. Fig 2.9 shows the SEM (BSE) images of his coating samples. After 2 days heat treatment, marked precipitation of fine carbide particles occurred in the matrix. Such phase development happens due to rapid recovery and re-crystallisation of the matrix phase and the nucleation of carbide grains from the supersaturated matrix as it tends towards an equilibrium composition. After 20 days heat treatment, a significant structural modification took place which involved the loss of the faceted or rounded structure of the initial carbides and the development of a sponge-like three dimensional structure generating a widespread skeletal network. XRD analysis indicated that the NiCr phase underwent recrystallisation and a reduction in Cr content as the carbide phase developed. Cr<sub>3</sub>C<sub>2</sub> was the only carbide phase detected in the coating throughout the period of heat treatment (Matthews, 2009). These fine precipitates in the matrix have been verified as Cr<sub>3</sub>C<sub>2</sub> by He (2001) in TEM examination of the sample annealed at 800°C. According to the microstructures of these annealed coating samples a schematic illustration of the three

generalised regions of carbide development within a splat during heat treatment of the HVOF coating was given by Matthews (2003) in Fig 2.10. Region 1 occurs in the middle of the largest splats in pools of material largely unaffected by the deposition process. Carbide dissolution is minimal and the matrix phase in this region becomes softened but not melted during spraying. Region 2 occurs midway between the splat core and periphery in large splats, or in the center of smaller splats. Great amount of carbide dissolution occurs and sponge-like agglomerates formed via coalescence of large number of nucleated carbides in this region. Region 3 is at the splat boundary, where the carbides formed long thin stringers with three dimensions and forming plate like morphologies.

### **Microhardness**

High temperature exposure of these coatings influences the mechanical properties significantly such as coating microhardness. In a coating, microhardness mainly depends on the microstructure, such as precipitation which depends on size, distribution and behaviours of the precipitates formed, usually causes hardening (Mott, 1940). A high density of fine, hard and dispersed precipitates in the matrix significantly increases microhardness (Ardell, 1985). The size, distribution and density of precipitates result from the combined effect of nucleation and growth of the precipitates, which are determined by heat treatment processing, mainly the heat treatment temperature and time. This has been studied by many investigators (Han, 1982) (Sundararaman, 1988) (He, 1995) For most types of precipitates, the relationship between the nucleation of precipitates and heat treatment temperature can be represented by a C-shaped curve (Haasen, 1996). Haasen also showed that a typical hardness vs ageing time curve in precipitation hardening alloys shows three stages, under-aged, aged and overaged stages. The hardness of the alloy increases sharply in the under-aged stage and reaches its maximum value in the aged stage, then decreases with increasing ageing time in the over-aged stage because of coarsening of precipitates. According to the previous researches on the coating

hardness at different annealing conditions, the results can be separated into two groups as short-term and long term exposure.

The short-term investigation of microhardness variation has been studied by Guilemany (2002). In his work heat treatments were carried out on samples following different annealing temperatures (450, 760 and 880°C) in air for 1hour. The microhardness of the coatings is listed in Table 2.7. Samples treated at 760°C show the highest microhardness because finely distributed carbide precipitation in Ni matrix was produced and hard Cr<sub>2</sub>O<sub>3</sub> phase was formed as well. With higher temperature heat treatment at 880°C, a growth of the carbides was produced, which decreased the coating hardness. Similarly, Zimmermann (1996) also found that peak hardness was achieved in the range 600 °C ~ 800 °C after 1hour heat treatment, with the coatings softening at higher temperature. He indicated this response was attributed to the precipitation of chromium carbides with heat treatment, with the peak hardness achieved when the carbide nuclei reached the optimum size to strengthen the structure. Softening at high temperature was due to the coarsening of the carbide structure. In He's (2001) work, the microhardness of the 25Ni(Cr)-75Cr<sub>3</sub>C<sub>2</sub> coatings all increased with increased exposure to all temperature ranges from 200 to 800°C. He indicated that the increase in microhardness is attributed to the precipitation of a high density of nano-sized oxide particles which lead to significant increase in the microhardness. Internal oxidation process is thought to be responsible for the precipitation of the dispersed Cr<sub>2</sub>O<sub>3</sub> particles during heat treatment. Furthermore, other investigators Murthy (2007) and Kim (2001) also reported the microhardness changes in short-term exposure, they found an increase in hardness in the HVOF sprayed 25Ni(Cr)-75Cr<sub>3</sub>C<sub>2</sub> coatings after short-term heat treatment below 800 °C and a decrease in hardness with higher temperature.

The long-term investigation of microhardness variation has been done by Matthews (2003). In his work, the microhardness of HVOF 25Ni(Cr)-75Cr<sub>3</sub>C<sub>2</sub> coatings was assessed following treatment at 900°C for up to 60 days in air and argon. In Fig 2.11

initially all the samples showed a drop in hardness. This was attributed to the reduction on strengthening mechanisms of the matrix phase with heat treatment. After 30 days hardness recovered and achieved stable values, this was due to the precipitation and development of the carbide phase. He also mentioned that the air treated coatings were consistently harder than those treated in argon as a result of internal oxidation. Suegama (2006) also found an increase in hardness in the HVOF-sprayed 75%Cr<sub>3</sub>C<sub>2</sub>-25%Ni(Cr) coating after heat treatment in air at 760°C and 880°C for 2 days, which resulted from the formation of chromium oxides and precipitation of chromium carbide. Further, the microhardness variation of the coatings was studied by Tao (2009) as a function of microstructural development following heat treatment at 650°C for periods of up to 200h in air. He indicated the carbide precipitation and content increased, resulting from phase transformation (Cr<sub>3</sub>C<sub>2</sub> → Cr<sub>7</sub>C<sub>3</sub> → Cr<sub>23</sub>C<sub>6</sub>) compensated the hardness decrease by grain coarsening, and further led to the increase in the overall coating hardness.

### 2.2.2.3 Summary

As above, the previous work on both short term and long term heat treatments of 25Ni(Cr)-75Cr<sub>3</sub>C<sub>2</sub> thermal spray coatings shows the rapid transformation of the as-sprayed coating composition and microstructure at elevated temperatures. The amorphous matrix phase from the as-sprayed coating disappears after short term trials and carbide starts to grow and form new carbides such as Cr<sub>7</sub>C<sub>3</sub> or Cr<sub>23</sub>C<sub>6</sub> with continued exposure. The microhardness of these coatings shows a drop initially. It recovers and achieves a stable hardness value after long term exposure due to the precipitation and development of the carbide phase. These experiments above have only been investigated with the coatings which were removed from the substrate before heat treatment. As a result, the characterisations in each coating after exposure are homogeneous. However, no research has been considered on annealing the coating with substrate together.

## 2.3 Microstructural features of austenitic stainless steel

Stainless steel 304 is the most popular grade in the series of austenitic stainless steel based on 18 wt% Cr and 9 wt% Ni and is used in a wide variety of applications which require a good combination of corrosion resistance and formability. Normally, austenitic stainless steels are given a high-temperature heat-treatment which gives a fully austenitic solid solution. However the exposure of austenitic stainless steel to elevated temperatures for long periods of time can result in the formation of chromium-rich carbides precipitates (Sedriks, 1996). Phase transformation and formation of such precipitates will be described in the following sections.

### 2.3.1 The Iron-Chromium-Nickel system

Austenitic stainless steel is mainly based on the Fe-Cr-Ni systems due to the high alloying contents of Cr and Ni. Chromium is the principal alloying element in stainless steel. The binary iron-chromium equilibrium diagram (Fig 2.12) shows that chromium restricts the occurrence of the  $\gamma$ -loop to the extent that above 13wt% Cr the binary alloys are bcc ferrite ( $\alpha$ ) over the whole temperature range, while there is a narrow ( $\alpha$ - $\gamma$ ) range between 12 and 13 wt% Cr (Llewellyn, 1996). Whereas chromium restricts the formation of austenite, nickel has the opposite effect and, as illustrated in Fig 2.13, the iron-nickel equilibrium diagram displays an expanded austenite phase ( $\gamma$ ) field. In the context of stainless steels, chromium is therefore termed a ferrite ( $\alpha$ ) former and nickel an austenite ( $\gamma$ ) former.

A ternary diagram for the Fe-Cr-Ni system just below the solidus temperature (about 1400 to 1450°C) is shown in Fig 2.14 (ASTM, 2004). Compositions approximating to the stainless steel 304 (18% Cr-9% Ni-70% Fe) would be predicted to fall within the  $\alpha$ + $\gamma$  field. In order to better understand the phase relationships the vertical section through the ternary diagram were introduced by (ASTM, 2004) Fig 2.15 shows sections for constant iron contents of 50, 60, 70, 80, and 90%. In these equilibrium diagrams the dashed lines are used to separate the phase fields at lower temperatures

which means the transformations are not observed under practical conditions. Instead an alloy cooled from the  $\gamma$  field across dashed lines will remain austenitic. Stainless steel 304 (18% Cr-9% Ni) in the 70% Fe phase diagram shows that it will cross  $\alpha+\gamma$  dashed line and remain  $\alpha$  and  $\gamma$  phase when it was cooled from higher temperature. The existence of fcc austenite phase ( $\gamma$ ) and bcc ferrite phase ( $\alpha$ ) in XRD spectra of as-received stainless steel 304 has been proved by many investigators. (Karimi, 2008; Burstein, 2000)

### 2.3.2 Structure and morphology of precipitates

Simple austenitic steels usually contain between 0.03 and 0.1 wt% carbon apart from chromium and nickel. The solubility limit of carbon is about 0.05 wt% at 800°C up to 0.5 wt% at 1100°C. Therefore, solution treatment between 1050°C and 1150°C will give a supersaturated austenite solid solution at room temperature by rapid cooling. However, slow cooling or reheating within the range 550-800°C will lead to the rejection of carbon from solution, usually as chromium-rich carbide,  $M_{23}C_6$ , even if the carbon content of the steel is lower than 0.05 wt% (Bhadeshia, 2006). To better understand the microstructure of these precipitates, a pseudo-binary phase diagram for Fe-18% Cr-8% Ni alloy with varying carbon content is illustrated in Fig 2.16 (Colombier, 1967). This figure shows that in stainless steel 304 containing less than 0.1% carbon, the equilibrium structure at room temperature should contain  $\gamma$  austenite,  $\alpha$  ferrite, and carbide ( $M_{23}C_6$ ). It also shows that carbide phase  $M_{23}C_6$  exists below about 900°C, and it goes into solution when the steel is heated to 1100-1150°C and on quenching a precipitate-free austenite is obtained. When the supersaturated austenite is reheated to elevated temperatures within the  $\gamma+M_{23}C_6$  field, further precipitation of the chromium-rich  $M_{23}C_6$  will take place at austenite grain boundaries. Hong (2001) also found  $M_{23}C_6$  precipitates on the grain boundaries of stainless steel 304 after certain heat treatment. Hiroyuki also indicated that the frequency of intergranular carbide precipitation increases with the holding time at every temperature (Fig 2.17). Sourmail (2003) studied the chromium concentration profiles

in austenitic stainless steels and found the chromium–depleted zone on the grain boundaries and around carbides in austenitic stainless steels. Combinations will be sufficient to precipitate the chromium-rich  $M_{23}C_6$  in certain time-temperature, but insufficient to re-diffuse chromium back into the austenite near the carbide (Sedirks, 1996).

### 2.3.3 Transformation of metastable austenite

Many investigators have also studied the effect of plastic deformation on austenitic stainless steels (Burstein, 2000; Tavares, 2006; Mangonon, 1970; etc). The formation of deformation induced martensitic in metastable austenitic stainless steel 304 have been extensively reported. Pecker (1977) reported that stainless steel 304 transformed into  $\alpha'$  (bcc) martensite from  $\gamma$  (fcc) austenitic during plastic deformation below the  $M_s$  temperature and in hydrogen gradients. Reed (1962) also reported that most of the 300 series stainless steels can undergo martensitic transformations and form  $\epsilon$  (hcp) martensite and  $\alpha'$  (bcc) martensite as a result of cold working, particularly below room temperature. Mangonon and Thomas (1970) studied the transformation during tensile testing of a stainless steel 304 and found that  $\epsilon$  martensite is formed at the beginning of deformation and reaches a peak value at about 5% of tensile strain during the tensile test. After this the  $\epsilon$  phase decreased to almost zero at 20% of plastic strain. They also indicated the martensite  $\alpha'$  increased continuously with strain and at high plastic deformations this was the only martensitic phase present in the steel. Furthermore, an increase of the  $\alpha'$  martensite volume fraction in metastable austenitic steel due to heat treatment at 400°C after deformation was also reported by Gauzzi (1999) and Guy (1983). A phase distribution in the surface layers of stainless steel 304 after hydrogen charging and during age at room temperature is given in Fig 2.18 by Rozenak (2006). The amount of  $\epsilon$ -phase increased to 56% and the  $\alpha'$ -phase increased to about 4% on the surface. These amounts of  $\epsilon$  and  $\alpha'$  phases decreased rapidly from the surface to zero at a depth of approximately 3.7  $\mu\text{m}$ .

As mentioned above austenitic stainless steel can be heavily plastically deformed by grinding or rolling. A martensitic phase transformation occurs which causes significant changes in the bulk and surface mechanical properties such as microhardness or strains (Peterson, 1997) of the alloy. In Burstein's (2000) work, he showed that martensitic structures in stainless steel 304 after cold-rolling or grinding can be removed by appropriate electrochemical treatment in aqueous solutions at very low temperature or by the conventional annealing treatments at several hundred degrees °C. Fig 2.19 shows the X-ray diffraction patterns of type 304L stainless steel surface with different treatments. Fig 2.19a is the original surface achieved by polishing to 0.25  $\mu\text{m}$  and it is clearly to see a small peak of  $\alpha'$  phase at  $2\theta=44.69^\circ$ . Fig 2.19b is the surface after electrochemical pulse treatment in 8 M sodium nitrite at a temperature of 80°C, and the martensite phase has been removed. Fig 2.19c is the original polished surface after a thermal annealing procedure at 750°C for 20 min, which shows the loss of the martensite phase. Fig 2.19d shows the steel after cold-rolling with the formation of a significant  $\alpha'$  martensite peak. Fig 2.19e shows the cold-rolled steel after the same electrochemical treatment as in b, and the peak due to martensite is substantially reduced. Additionally, microhardness of these surfaces was measured as well. As a result, the surface after annealing thermally at 750°C for 20min shows a decrease on hardness compared to that of the original surface. While the surface using electrochemical treatment at lower temperature still remains high hardness, despite the loss of martensite.

### 2.3.4 Summary

Microstructural features of austenitic stainless steel have been introduced above. To conclude, the austenitic stainless steels such as type 304 containing 18 wt% Cr and 8 wt% Ni are based on the Fe-Cr-Ni and Fe-Cr-Ni-C systems. In the phase diagrams, nickel balances the effect of chromium to stabilise the austenitic phase.  $\text{M}_{23}\text{C}_6$  chromium-rich carbides are the most commonly encountered precipitates in austenitic stainless steel, and these precipitates mainly occur on the grain boundaries. Moreover,

the transformation of metastable austenite  $\gamma$  (fcc) to martensite  $\alpha'$  (bcc) occurs when steel is cold-rolled or has mechanical surface grinding. However, the new  $\alpha'$  martensite can be removed by certain electrochemical or elevated temperature annealing treatments.

## 2.4 Atomic mechanisms of diffusion

Diffusion is a process where material is transported by atomic motion. There are two basic mechanisms for diffusion: substitutional diffusion and interstitial diffusion. The reason for the two types of diffusion stems from the relationship between their relative atomic sizes. Substitutional diffusion occurs mainly by a vacancy mechanism by a similar size or substitutional atoms; whereas interstitial diffusion occurs when diffusing atom is small enough to move between the larger atoms in the lattice. Interstitial diffusion requires no vacancy defects in order to operate.

### 2.4.1 Carbon activity

Carbon activity is very important information for diffusion process since the greater the difference in carbon activities, the greater the gradient of carbon activity on the diffusion interface. The carbon diffusion flow across this interface is proportional to this gradient. For instant, carbon always diffuses to a site of lower carbon activity value in steels. As Sopousek (2008) mentioned in his report that carbon concentration cannot be used instead of carbon activity in steels which may lead to erroneous conclusions.

The influence of alloying elements on the carbon activity in steel was reported by Sanbongi (1957). For determining the effect of Xi (alloy element) on the activity coefficient of C,  $\gamma_C$ , the interaction parameter  $\epsilon_C^X$  is defined by the equation  $\epsilon_C^X = \partial \ln \gamma_C / \partial N_X$  and was calculated and shown in Table 2.8. The relation between the atomic number of the elements and the values of interaction parameter is shown in Fig 2.20. According to the Table 2.8, the elements with positive values increase the activity of C in molten iron while those with negative values decrease it. Additionally, Sopousek (2008) calculated the carbon activity of steels with different chromium concentration in P91 using the CALPHAD method. According to the results he suggested that chromium can reduce carbon activity, and it is same as the results

given in Sanbongi's table where shows Cr has the negative value and will decrease the carbon activity.

The experimental measurement of the activity of carbon mentioned by (Nishizawa, 1977) and (Lee HM, 1974) are in principle and possible. But such experimental results are few since the measurement of activities is always connected with the necessity of long time equilibration. Nowadays the most effective method of obtaining the activities of elements is using thermodynamic calculations based on the CALPHAD method (Sopousek, 2008).

#### 2.4.2 Mechanism of carbon diffusion in austenite stainless steel

Carbon diffusion in austenite plays a critical role in phase transformation in steel. Studies of carburization of austenitic stainless steels have been done by many investigators (Michal, 2006) and (Stasiek, 2006). The aim of carburization in industrials is to increase the carbon concentration in the surface layers of a steel product by carbon diffusion in order to achieve a harder wear-resistant surface. During the carburization, the high concentration of carbon maintains at a stable constant value at the surface of the steel. At the same time carbon continually diffuses from the surface into the steel which gives a concentration profiles obtained after different times shown in Fig 2.21 (Porter, 1992). According to Fick's second law by using the boundary conditions:  $C_B(x=0) = C_s$  and  $C_B(\infty) = C_0$  where  $C_B$  stands for the carbon concentration at boundary condition. The equation of carbon diffusion in steel was given as

$$C = C_s - (C_s - C_0) \operatorname{erf} \left( \frac{x}{2\sqrt{(D_c t)}} \right) \quad (2.1)$$

where  $C_s$  stands for the carbon concentration at the surface of steel,  $C_0$  is the original carbon concentration of the steel,  $x$  is the carbon diffusion distance. The 'erf' stands for error function which can be shown graphically in Fig 2.22. Since  $\operatorname{erf}(0.5) \approx 0.5$  the depth at which the carbon concentration is midway between  $C_s$  and  $C_0$  is given by

$\left(\frac{x}{2\sqrt{(D_c t)}}\right) \approx 0.5$  that is  $x \approx \sqrt{D_c t}$  when  $\text{erf}\left(\frac{x}{2\sqrt{(D_c t)}}\right) = 1$  (Porter, 1992). Further,

$D_c$  is the carbon diffusion coefficient which is one of the most important parameters in the modelling of phase transformation in steel. The carbon diffusivity  $D_c$  also based on the substitutional atoms contained in the steel, such as chromium. This influence can be expressed in the form of (Foret, 2001)

$$D_c = D_{c(0)} \exp(\beta_C^{Cr} N_{Cr}) \quad (2-2)$$

where  $D_{c(0)}$  is the carbon diffusion coefficient in a nonalloyed steel, as expressed in (Million, 1995) by the equation

(1) Temperature from 1100°C to 800°C

$$D_{c(0)} = 2.25 \times 10^{-3} \exp\left(-\frac{92.7}{RT}\right) \quad [\text{cm}^2/\text{s}, \text{kJ/mol}] \quad (2-3)$$

(2) Temperature from 750°C to 500°C

$$D_{c(0)} = 1.91 \exp\left(-\frac{143.6}{RT}\right) \quad [\text{cm}^2/\text{s}, \text{kJ/mol}] \quad (2-4)$$

from the experimental data and  $\beta_C^{Cr}$  is the Cr-C diffusion interaction coefficient which is expressed in (Million, 1995) by the equation

(1) Temperature from 1100°C to 800°C

$$\beta_C^{Cr} = 94 - \left(\frac{133000}{T}\right) \quad [\text{at.fr.}^{-1}] \quad (2-5)$$

(2) Temperature from 750°C to 500°C

$$\beta_C^{Cr} = 99.7 - \left(\frac{121000}{T}\right) \quad [\text{at.fr.}^{-1}] \quad (2-6)$$

Million (1995) also gave a common equation of  $\beta_C^{Cr}$  which is

$$\beta_C^{Cr} = 73.8 - \left(\frac{108000}{T}\right) \quad [\text{at.fr.}^{-1}] \quad (2-7)$$

$N_{Cr}$  in equation 2-2 is the thermodynamic chromium equivalent in the atom fraction which is expressed from the equation,

$$N_{Cr} = \sum K_{Cr(C)}^j N_j \quad (2-8)$$

This equation relates to all substitutional elements in the steel.  $K_{Cr(C)}^j$  is the equivalence constant which is the ratio of the interaction coefficient of element  $j$  and chromium. The equivalence constant value of each element can be obtained by Table 2.9 and 2.10 (Pilous and Stransky, 1998). In Table 2.9 each element is related to a characteristic number  $v_c^j$  and according to this number the equivalence constant  $K_{Cr(C)}^j$  can be obtained from Table 2.10.

Nowadays, comparable numerical procedures have been developed and implemented in general purpose thermokinetic software such as DICTRA, Thermo-Calc or MatCalc which are based on the databases for calculations involving computational thermodynamics and diffusion controlled simulations using CALPHAD method. The CALPHAD method is based on the fact that a phase diagram is a representation of the thermodynamic properties of a system which are the sum of the properties of the individual phases. Thus the multi-component phase diagrams can be calculated by the given thermodynamic properties. Sopousek (2004 & 2008) and Kozeschnik (2002) have reported the simulation by using these computer based software in their work which shows good agreement by comparing with the experimental data and the results. Thus the computer based modelling of carbon diffusion is suggested to be used in future work.

### 2.4.3 Summary

In this section the previous work on carbon diffusion in steel has been introduced which includes carbon activity and carbon diffusion modelling methods. To conclude, diffusion is driven by an activity gradient from a higher value to the lower. The carbon activity is also influenced by alloying elements in an alloy. Furthermore, the mechanism of carbon diffusion in austenitic stainless steel can be simulated by modelling using the equation for calculation or computer based software. Computer simulation can be useful for modelling the element distribution in future work.

## 2.5 Oxidation of metal and metal carbide

### 2.5.1 Oxidation of metals

Oxidation of metals is a reaction between metals and oxygen with an oxide produced at the surface. The purpose of oxidation experiments is generally to assess reaction kinetics and mechanisms with studies on scales from structural and morphological viewpoints, transport properties in scales, phase-boundary reactions.

#### 2.5.1.1 Thermodynamic considerations

Thermodynamics is the study of heat in changing physical and chemical processes; it also allows prediction of the final equilibrium state for a reaction. The second law of thermodynamics is an expression of the universal law of increasing entropy, stating that the entropy of an isolated system which is not in equilibrium will tend to increase over time, approaching a maximum value at equilibrium. For phase changes, the second law is most conveniently written in terms of the Gibbs free energy ( $\Delta G$ ) which is a measure of the thermodynamic driving force that makes a reaction occur. The equation for Gibbs free energy is:

$$\Delta G = \Delta H - T\Delta S \quad (2-9)$$

where  $\Delta H$  is the enthalpy and  $\Delta S$  the entropy of the system. The enthalpy is a measure of the actual energy that is liberated when the reaction occurs. The entropy is a measure of the change in the possibilities for disorder in the products compared to reactants. Under these conditions the second law states: a negative value for  $\Delta G$  indicates that a reaction can proceed spontaneously without external inputs; a zero value means a reaction is at equilibrium; a positive value indicates that a reaction is a thermodynamically impossible process.

On the other hand, the process of oxidation of a metal is an electrochemical one, which may be represented, for divalent metal M, by the following reaction;



The above reaction includes two half-reactions: the oxidation half-reaction which is the formation of metal ions and occurs at the metal-scale interface as follows:



The other half-reaction is oxidation which produces oxygen ions and happens at the scale –gas interface as follows:



For the oxide scale formation, it is necessary that electrons be conducted to the scale-gas interface, at which point the reduction reaction occurs; in addition.  $M^{2+}$  ions must diffuse away from the metal-scale interface, and/or  $O^{2-}$  ions must diffuse toward this same interface. Furthermore, the scale may protect the metal from rapid oxidation by building a barrier to ionic diffusion and/or electrical conduction.

The standard free energy,  $\Delta G$ , available for the formation of an oxide is written as:

$$\Delta G = -RT \ln K \quad (2-13)$$

Here, R is the universal gas constant and T is the Kelvin temperature. K is called the equilibrium constant which is used to describe the equilibrium state of the reacting system. In the specific case of a reaction (2-10),

$$K = a_{MO} \cdot a_M^{-1} \cdot a_{O_2}^{-1/2} \quad (2-14)$$

Here  $a_{MO}$ ,  $a_M$  and  $a_{O_2}$  are activities of the components in the reaction.  $\Delta G$  is expressed as:

$$\Delta G = -RT \ln \left( \frac{a_{MO}}{a_M \cdot a_{O_2}^{1/2}} \right) \quad (2-15)$$

Plots of the standard free energy of reaction  $\Delta G$  as a function of temperature commonly called Ellingham diagram, is used to predict the stability of metals and their oxidized products at high temperature. Ellingham diagram in Fig 2.23 is a particular graphical form of the Second Law of Thermodynamics [ $\Delta G = \Delta H - T\Delta S$ ]. The values of the  $\Delta G$  on an Ellingham diagram are expressed as kJ per mole  $O_2$  to normalize the scale and are able to compare the stability of these oxides directly. In

the diagram, the noble metals which are difficult to oxidise occur at the top of the diagram, and the more reactive metals are at the bottom. In Fig 2.23 the standard free energy value of chromium is below that of nickel, which means chromium is easier to be oxidised than nickel at certain temperatures.

### 2.5.1.2 Kinetics of oxidation

The rate of reactions cannot be determined by thermodynamics. Therefore, kinetics is introduced to express the rate of oxidation process, which is dependent on the temperature, pressure of oxygen, surface area and reaction time. Three basic kinetic laws have been used to characterize the oxidation rates of pure metals, namely: parabolic rate law, linear rate law and logarithmic rate law.

The parabolic rate law assumes that the rate controlling step in the oxidation process is the diffusion of ions through a compact barrier of the oxide with chemical potential gradient as the driving force. The concentrations of diffusing species at the oxide-metal and oxide-gas interfaces are assumed to be constant. The diffusivity of the oxide layer is also assumed to be invariant. This parabolic rate law is usually associated with uniform, coherent oxides, such as the oxidation of Ni, Cr, Fe and Cu. The parabolic rate law follows an Arrhenius type relationship:

$$(\Delta m/a)^2 = K_1 t + C \quad (2-16)$$

where  $a$  is the area on which the reaction happens,  $\Delta m$  is mass gain,  $K_1$  is the diffusion rate constant which is directly proportional to diffusivity of ionic species,  $t$  is the reaction time and  $C$  is the time-independent constant. The diffusion rate constant  $K_1$  can be written:

$$K_1 = A \exp(-Q/RT) \quad (2-17)$$

where  $A$  is the constant of partial pressure of the reacting gas,  $Q$  is the activation energy of the reaction,  $R$  is the gas constant and  $T$  is Kelvin temperature. The  $\exp(-Q/RT)$  term in equation 2-17 shows that chemical reaction rates are

temperature-dependent. The parabolic oxidation law suggests that temperature is the most important factors affecting metal oxidation.

The linear rate law is applicable to the formation and build-up of a non-protective oxide layer, such as porous scales those which flake off the linear rate line is

$$\Delta m / a = K_2 t \quad (2-18)$$

where  $K_2$  is a constant. Under these conditions oxygen is always available for reaction with an unprotected metal surface as the oxide does not act as a reaction barrier.

The logarithmic rate law often obeys for relatively thin films at lower temperature and the oxidation rate is inversely proportional to time with the equation:

$$\Delta m / a = K_3 \log(K_4 t + K_5) \quad (2-19)$$

where  $K_3$   $K_4$   $K_5$  are constants.

### Pilling-Bedworth ratio

The Pilling-Bedworth ratio (P-B ratio) is defined as the ratio of the oxidation rate and the tendency of the film to protect the metal from further oxidation are related to the relative volumes of the metal oxide produced on a metal consumed:

$$\text{P - B ratio} = \frac{\text{oxide volume per metal atom}}{\text{metal volume per metal atom}} = \frac{(M_{\text{oxide}}) \cdot (\rho_{\text{metal}})}{n(M_{\text{metal}}) \cdot (\rho_{\text{oxide}})} \quad (2-20)$$

In equation (2-20)  $M_{\text{oxide}}$  and  $M_{\text{metal}}$  are the atomic or molecular mass of the metal and oxide,  $\rho_{\text{oxide}}$  and  $\rho_{\text{metal}}$  are the oxide and metal densities and  $n$  is the number of metal atoms in the oxide (Donald, 2006).

Pilling and Bedworth realized that, when R is less than one, a pure metal oxide tends to be porous and non-protective because it cannot cover the whole metal surface. If

the ratio is between one and two, an adherent, nonporous, protective film forms and the kinetics of film formation follow parabolic, linear, or logarithmic rate laws (William, 1997). For the ratio greater than two, a large volume of oxide forms and may crack and flake off from the surface, exposing fresh metal which continues to oxidize. Table 2.11 presents P-B ratios for metals that form protective coatings and for those that do not.

In addition to R, factors such as the relative coefficients of thermal expansion, the adherence between metal oxide and metal, a relatively high melting point and good high-temperature plasticity for the oxide should also be favorable in order to produce a protective oxide (William, 1997).

### 2.5.1.3 Oxidation of Ni, Cr and Ni-Cr alloys

The oxidation of nickel has been studied for many years. Under normal temperature and pressure conditions, single NiO scale forms which is controlled by outward cation ( $\text{Ni}^{2+}$ ) diffusion. A duplex NiO scale forms under high temperature conditions, which includes small equiaxed grains at the metal-oxide interface and large columnar grains in the external part. Birks (1983) showed that the large columnar grains in the outer layer grew by outward cation migration and the small equiaxed grains at the inner layer grew by inward migration of oxygen. Atkinson (1982) indicated that oxygen penetrated down to the metal-oxide interface and that short-circuit diffusion of oxygen contributed to the growth of the inner layer of the duplex scale.

Chevalier (2005) has studied the oxidation kinetics and morphology of Ni in air under atmospheric pressure over the temperature range 600-900°C. The plots of weight gain per unit area vs. time at high temperature indicated the oxidation of pure Ni showed a parabolic reaction with the activation energy of  $220 \pm 5 \text{ kJ.mol}^{-1}$ . Chevalier (2005) noted that the oxide grain size increased with temperature as well as the numbers of pores and a very few platelets are visible on some specimens. Peraldi (2002) also agreed about the morphology and microstructure of NiO scales grown at high

temperature on high purity nickel. Cross-sectional images of a nickel specimen oxidized at 800°C for 12 hours taken by Chevalier shows a duplex microstructure composed of small equiaxed oxide grains near metal-oxide interface and large columnar oxide grains on top of the oxides in Fig 2.24.

The oxidation of pure Cr forms a stable chromium oxide Cr<sub>2</sub>O<sub>3</sub> at temperatures up to 1000°C. The Cr<sub>2</sub>O<sub>3</sub> scales are normally formed as an oxidation protection layer for many engineering alloy, it increases the alloy's resistance to hot corrosion at high temperatures. Volatilization occurs of the Cr<sub>2</sub>O<sub>3</sub> layer occurs when the temperature is over 1000 °C. Birks (1983) stated that oxide scales of pure Cr started to be thinned by CrO<sub>3</sub> evaporation at 1000°C. Berthod (2005) has studied the volatilization of the external chromia layer formed by oxidation of a Ni-30Cr alloy and also indicated the vaporization of chromia into volatile CrO<sub>3</sub> occurred when the temperature was higher than 1000°C. The formation of CrO<sub>3</sub> follows the reaction



The mechanism of chromia volatilization is explained by Birks (1983). The volatile metal and oxide species formed at the metal-oxide interface are transported through the oxide lattice, mechanically forming cracks in the oxide layer. With continuing exposure, the volatile oxide gases form directly at the oxide-gas interface and oxygen diffuses through a barrier layer of the volatilized oxides.

Nickel chromium alloys have excellent resistance to high temperature oxidation and corrosion and good wear resistance. The oxidation behaviour of this alloy has been studied by several people (Ignatov, Berthod and Allam). Alloys in this system with low Cr (<20 wt%) contents show a mixture of nickel and chromium oxides scales within different temperatures. Ignatov (1965) showed that at 400°C the oxide of nickel (NiO) was formed originally on this alloy, at 500-700°C the oxide of chromium (Cr<sub>2</sub>O<sub>3</sub>) was formed with a matrix of almost pure Ni, with diffused oxygen

in alloy, at 800-1000°C an outer layer of NiO was formed with an inner layer of NiO containing NiCr<sub>2</sub>O<sub>4</sub> which was a spinel type structure. Birks (1983) indicated that the outer scale advanced into the metal and the Cr<sub>2</sub>O<sub>3</sub> internal oxide scales are surrounded by NiO and a solid state reaction happens to form NiCr<sub>2</sub>O<sub>4</sub>.



Since Ni ion diffusion is much slower through the NiCr<sub>2</sub>O<sub>4</sub> spinel than it is through NiO, NiCr<sub>2</sub>O<sub>4</sub> in the scale acts as diffusion blocks for migrating Ni ions. Thus as the Cr content of the alloy increases, the volume fraction of spinel increases which reduces the total Ni flux through the scale and the oxidation rate starts to fall. Finally as the Cr content is increased upto 10% at 1000°C, the mode of oxidation is changed to form a complete external scale of Cr<sub>2</sub>O<sub>3</sub> (Birks, 1983). A schematic diagram (Fig 2.25) of the initial oxidation of Ni-20Cr alloy was given by Allam (1978). It also shows the co-existing of NiO, Cr<sub>2</sub>O<sub>3</sub> and NiCr<sub>2</sub>O<sub>4</sub> on the top surface during the initial exposure time.

The volatilization of the external chromia layer formed by oxidation of NiCr70/30 alloy was studied at 1000, 1100, 1200 and 1300°C by Berthod (2005). The activation energy for oxidation of 70Ni30Cr alloy is 167 kJ·mol<sup>-1</sup> which was calculated from the mass gain curves obtained by thermogravimetry on the basis of the differential equation describing the oxidation kinetics.

### 2.5.2 Oxidation of carbides

High temperature oxidation of titanium carbide, tungsten carbide and chromium carbide were studied by some investigators (Voitovich and Berger) due to these compounds excellent performance as wear resisting materials.

High temperature oxidation of titanium carbide has been studied in the temperature range 600-1200°C by Voitovich (1997). He reported that a one-layer oxide scale was formed at 900°C and a two-layer scale was formed in the temperature range of

1000-1200°C. The inner layer had a multiphase structures and was composed of various titanium oxides (TiO, Ti<sub>2</sub>O<sub>3</sub>, TiO<sub>2</sub>). The outer layer was composed of TiO<sub>2-x</sub> only. It was assumed that an outer scale was formed over the inner scale via diffusion of titanium cations, whereas the inner layer was formed by the diffusion of oxygen. Voitovich (1997) also indicated that the oxidation of compact titanium carbide at high temperatures (1000-1200°C) had four stages. Oxidation kinetics followed the parabolic law in the first three stages; parabolic oxidation was displaced by linear behavior with time.

Berger (1998) compared the oxidation behaviour of WC, Cr<sub>3</sub>C<sub>2</sub>, and TiC from WC-Co, 25Ni(Cr)-75Cr<sub>3</sub>C<sub>2</sub> and TiC-Ni-based materials in his studies. He indicated Cr<sub>3</sub>C<sub>2</sub> had the best oxidation resistance behaviour because of the formation of dense oxide layers which was detected as Cr<sub>2</sub>O<sub>3</sub> only. On the other hand, WC showed the lowest oxidation resistance due to the linear dependence of mass gain on oxidation time in isothermal heat treatment with results in coatings without protective properties against further oxidation. The oxidation products of WC were detected as WO<sub>3</sub> which was characterized by a high volatility.

### 2.5.3 Oxidation of metal-chromium carbide composite systems

High temperature oxidation of nickel-based chromium carbide coatings has been studied by a few investigators (Kunioshi, Matthews and Ye etc). Kunioshi (2006) has studied the high temperature oxidation behavior of HVOF sprayed 75(Ni20Cr)-25Cr<sub>3</sub>C<sub>2</sub> coating compared with Ni-20Cr and WC-20Cr-7Ni coatings. These coating has been compared by weight gain after 5 hours oxidation at various temperatures. 75(Ni20Cr)-25Cr<sub>3</sub>C<sub>2</sub> and Ni-20Cr coatings show higher oxidation resistance than the that of WC-20Cr-7Ni coating, especially at temperature over 800°C. On the other hand, the surface morphology of the oxidized specimens in his report shows that the crystallite size of the chromium oxide significantly increases at higher temperature.

Matthews (2009) has studied the oxide scales formed on blended powder NiCr-Cr<sub>2</sub>C<sub>3</sub> coatings after 850°C heat treatment. He indicated that heat treatment led to carbide formation and a reduction in the Cr content of Ni(Cr) matrix. During the heat treatment, carbide elements are diffused into the NiCr splats which increase the Cr content of this phase. Cr<sub>2</sub>O<sub>3</sub> is therefore able to dominate the matrix phase scale from an early stage and prevented bulbous NiO formation. With extended oxidation, lateral Cr<sub>2</sub>O<sub>3</sub> growth from the matrix phase begins to encroach over the carbide splats and dominate the coating scale to topography shown in Fig 2.26.

Ye (2008) also indicated in his report about oxidation behavior of Cr<sub>39</sub>Ni<sub>7</sub>C cermet coatings at 800°C during 100h heat treatment. He found a black tarnish layer formed on the coatings surface after oxidation exposure and a large amount of Cr<sub>2</sub>O<sub>3</sub> in the XRD pattern after heat treatment. As a result, coating was covered by Cr<sub>2</sub>O<sub>3</sub>.

The high temperature oxidation behavior of the related nickel-based chromium carbide cermet system has been investigated by Berthod (2007). He indicated that the presence and the concentration of the interdendritic carbides network of cast nickel alloys can help chromium diffused towards the oxidation front. Chromium carbides have an effectively influence on easy chromium diffusion. The diffusion coefficients increase when the density increases. Since they contain a part of chromium in the carbides the grain boundaries act as rapid diffusion paths for chromium and this contribution is bassed to the volume diffusion of chromium. Berthod also found the depth of the carbide-free zone depends on the concentration of the initial carbides. Since the chromium carbides disappear from the oxidation front at a depth which increases with time and also with temperature during oxidation. Moreover, the oxidation kinetics increases when the carbides concentration in the alloy increases. The activation energy for oxidation of 70Ni30Cr alloy is 167 kJ·mol<sup>-1</sup> Ni-30Cr-0.8C alloy is 204 kJ·mol<sup>-1</sup> and Ni-30Cr-0.2C alloy is 201 kJ·mol<sup>-1</sup> which were calculated from the mass gain curves obtained by thermogravimetry on the basis of the differential equation describing the oxidation kinetics.

Table 2.1 Comparison of the coating properties with PS, FS, AS and HVOF (ASM, 1987; Sturgeon 1992; Thorpe, 1993)

Spraying system	Sprayed material	Typical particle velocity ( $\text{ms}^{-1}$ )	Typical temperature in gun ( $^{\circ}\text{C}$ )	Bond strength (Mpa)	Porosity (% by volume)	Thickness ( $\mu\text{m}$ )
Plasma spraying(PS)	Powder	120-900	5500-16000	80	<5%	150-500
Flame spraying(FS)	Powder ,wire or rod	30-120	2800	10-30	10-20%	100-2500
Arc spraying(AS)	Powder ,wire or rod	240	5500	10-30	7-8%	100-1500
High velocity oxy-fuel spraying(HVOF)	Powder	1000	2800	90	0.1-2%	100-300

Table 2.2 Characterisation of three carbides of chromium (Louis, 1971)

Phase	Crystal structure	Lattice parameter (nm)
$\text{Cr}_{23}\text{C}_6$	Complex fcc with 116 atoms per unit cell	a=1.0655
$\text{Cr}_7\text{C}_3$	Hexagonal with 80 atoms per unit cell	a=1.401, c=0.4525
$\text{Cr}_3\text{C}_2$	Orthorhombic with 20 atoms per unit cell	a=0.1147, b=0.5545, c=0.2830

Table 2.3 Summary of previous studies of carbide phases present in the as-sprayed  $\text{Cr}_x\text{C}_y\text{-Ni}(\text{Cr})$  powder coatings (\* means possibly existing phase)

Powder	HVOF System	Carbide Phases in coating	Reference
Agglomerated and sintered 25Ni(Cr)-75Cr <sub>3</sub> C <sub>2</sub>	DJ	Cr <sub>3</sub> C <sub>2</sub>	Zimmermann (1996)
Agglomerated 25Ni(Cr)-75Cr <sub>3</sub> C <sub>2</sub>	DJ	Cr <sub>3</sub> C <sub>2</sub>	He (2000)
Agglomerated and densified 25Ni(Cr)-75Cr <sub>3</sub> C <sub>2</sub>	DJ	Cr <sub>3</sub> C <sub>2</sub> , Cr <sub>7</sub> C <sub>3</sub>	Suegama (2006)
Agglomerated and densified 25Ni(Cr)-75Cr <sub>3</sub> C <sub>2</sub>	DJ	Cr <sub>3</sub> C <sub>2</sub> , Cr <sub>7</sub> C <sub>3</sub> , Cr <sub>23</sub> C <sub>6</sub>	Guilemany (1996)
Agglomerated and sintered 25Ni(Cr)-75Cr <sub>3</sub> C <sub>2</sub>	Microjet	Cr <sub>3</sub> C <sub>2</sub> (Cr <sub>7</sub> C <sub>3</sub> )*	Matthews (2009)
Agglomerated 25Ni(Cr)-75Cr <sub>3</sub> C <sub>2</sub>	Jet Kote	Cr <sub>3</sub> C <sub>2</sub> , Cr <sub>7</sub> C <sub>3</sub> , Cr <sub>23</sub> C <sub>6</sub>	Monhanty (1996)
Agglomerated and densified 25Ni(Cr)-75Cr <sub>3</sub> C <sub>2</sub>	JP5000	Cr <sub>3</sub> C <sub>2</sub>	Manish (2006)
Sintered and crushed 25Ni(Cr)-75Cr <sub>3</sub> C <sub>2</sub>	DJ	Cr <sub>3</sub> C <sub>2</sub>	Sasaki (1992)
Sintered and crushed 25Ni(Cr)-75Cr <sub>3</sub> C <sub>2</sub>	Top-Gun	Cr <sub>3</sub> C <sub>2</sub> , Cr <sub>7</sub> C <sub>3</sub>	Edris (1997)
Sintered and crushed 25Ni(Cr)-75Cr <sub>3</sub> C <sub>2</sub>	Top-Gun	Cr <sub>3</sub> C <sub>2</sub> , Cr <sub>7</sub> C <sub>3</sub>	Wirojanupatump (2001)
Sintered and crushed 25Ni(Cr)-75Cr <sub>3</sub> C <sub>2</sub>	CH-2000	Cr <sub>3</sub> C <sub>2</sub> , Cr <sub>7</sub> C <sub>3</sub> , Cr <sub>23</sub> C <sub>6</sub>	Ji (2006)
Blended 25Ni(Cr)-75Cr <sub>3</sub> C <sub>2</sub>	Top-Gun	Cr <sub>3</sub> C <sub>2</sub>	Wirojanupatump (2001)
Blended 25Ni(Cr)-75Cr <sub>3</sub> C <sub>2</sub>	Jet Kote	Cr <sub>3</sub> C <sub>2</sub> , Cr <sub>2</sub> C, Cr <sub>23</sub> C <sub>6</sub>	Shaw (1994)
Blended 25Ni(Cr)-75Cr <sub>3</sub> C <sub>2</sub>	Jet Kote	Cr <sub>3</sub> C <sub>2</sub> , Cr <sub>2</sub> C, Cr <sub>23</sub> C <sub>6</sub>	Hwang (1993)
Blended 25Ni(Cr)-75Cr <sub>3</sub> C <sub>2</sub>	Jet Kote	Cr <sub>3</sub> C <sub>2</sub> , Cr <sub>7</sub> C <sub>3</sub> , Cr <sub>23</sub> C <sub>6</sub>	Crawmer (1992)
Composite Cr-39Ni-7C	DJ	Cr <sub>3</sub> C <sub>2</sub> (Cr <sub>7</sub> C <sub>3</sub> )*	Ye (2008)
Composite 30Ni(Cr)-70CrC	Top-Gun	Cr <sub>23</sub> C <sub>6</sub>	Wirojanupatump (2001)

Table 2.4 Summary of previous studies of oxide phases present in the as-sprayed  $\text{Cr}_3\text{C}_2\text{-Ni}(\text{Cr})$  powder coatings

Powder	Oxide phases in coating	Reference
Sintered, crushed and clad 25Ni(Cr)-75Cr <sub>3</sub> C <sub>2</sub>	Cr <sub>2</sub> O <sub>3</sub>	Sasaki (1992)
Composited and Agglomerated 25Ni(Cr)-75Cr <sub>3</sub> C <sub>2</sub>	Cr <sub>2</sub> O <sub>3</sub>	Sobolev (1995)
Agglomerated and densified 25Ni(Cr)-75Cr <sub>3</sub> C <sub>2</sub>	Cr <sub>2</sub> O <sub>3</sub>	Guilemany (2002)
Sintered and crushed 25Ni(Cr)-75Cr <sub>3</sub> C <sub>2</sub>	Cr <sub>2</sub> O <sub>3</sub> , CrO	Wirojanupatump (2001)
Composite 30Ni(Cr)-70CrC	Cr <sub>2</sub> O <sub>3</sub> , CrO, Cr <sub>3</sub> O <sub>4</sub>	Wirojanupatump (2001)
Agglomerated and sintered 25Ni(Cr)-75Cr <sub>3</sub> C <sub>2</sub>	Cr <sub>2</sub> O <sub>3</sub> , NiO, NiCr <sub>2</sub> O <sub>4</sub>	Matthews (2008)
Sinter-crushed 25Ni(Cr)-75Cr <sub>3</sub> C <sub>2</sub>	Cr <sub>2</sub> O <sub>3</sub> , NiCr <sub>2</sub> O <sub>4</sub>	Edris (1997)

Table 2.5 Summary of previous studies on Microhardness from different Ni(Cr) –Cr<sub>3</sub>C<sub>2</sub> powder coatings with different HVOF spray systems

Powder	HVOF System	Microhardness	Reference
Blended 25Ni(Cr)-75Cr <sub>3</sub> C <sub>2</sub>	Top Gun	650 HV <sub>300</sub>	Wirojanupatump, 2001
Sintered and crushed 25Ni(Cr)-75Cr <sub>3</sub> C <sub>2</sub>	Top Gun	910 HV <sub>300</sub>	Wirojanupatump, 2001
Composite 30Ni(Cr)-70CrC	Top Gun	820 HV <sub>300</sub>	Wirojanupatump, 2001
Agglomerated and sintered 25Ni(Cr)-75Cr <sub>3</sub> C <sub>2</sub>	GMA Microjet	1155 HV <sub>300</sub>	Matthews, 2003
Agglomerated and densified 25Ni(Cr)-75Cr <sub>3</sub> C <sub>2</sub>	DJ 2700	743 HV <sub>300</sub>	Guilemany, 2002

Table 2.6 List of previous studies on HVOF Ni(Cr)-Cr<sub>3</sub>C<sub>2</sub> coatings under different types of annealing conditions

Powder	Gun system	Annealing conditions	References
Agglomerated and densified 25Ni(Cr)-75Cr <sub>3</sub> C <sub>2</sub>	DJ 2700	Air heat treatment 450°C 1hours, 760°C 1hour, 880°C 1 & 24hours	Guilemany, 2002
Agglomerated 25Ni(Cr)-75Cr <sub>3</sub> C <sub>2</sub>	DJ	Air heat treatment 200,400,600,800°C 8hours	He, 2001
Sinter-crushed 25Ni(Cr)-75Cr <sub>3</sub> C <sub>2</sub>	Top gun	Air heat treatment 900°C 50 & 100hours	Edris, 1997
Agglomerated and sintered 25Ni(Cr)-75Cr <sub>3</sub> C <sub>2</sub>	GMA Microjet	Air heat treatment 900°C 2,5,10,20,30,40 and 60 days	Matthews, 2003, 2009

Table 2.7 Microhardness of the agglomerated and densified 25Ni(Cr)-75Cr<sub>3</sub>C<sub>2</sub> coatings (load = 500g) ( Guilemany, 2002)

	As-sprayed	450°C 1hour	760°C 1hour	880°C 1hour
<b>Air annealing</b>	743 HV <sub>500</sub>	807 HV <sub>500</sub>	1015 HV <sub>500</sub>	900 HV <sub>500</sub>

Table 2.8 Interaction parameter (Pilous and Stransky, 1998)

X <sub>i</sub>	S	P	Si	Al	Cu	Ni	Co	Mn	Cr	V	Ti
$\epsilon_C^X$	5.54~4.78	5.24~4.02	4.23~3.4	2.7~2.4	1.2	0.48	0.2	-0.47	-1.4	-2.25	-3.34

Table 2.9 Characteristic numbers  $\nu_C^j$  for individual elements on the periodic system of elements (Pilous and Stransky, 1998)

Characteristic number $\nu_C^j$	Period						
	1	2	3	4	5	6	7
1				Sc	Y	La*)	Ac**
2				Ti	Zr	Hf	Ku
3				V	Nb	Ta	
4		(0)		Cr	Mo	W	
5		F	Cl	Mn Br	Tc J	Re At	
6	He	Ne	Ar	Fe Kr	Ru Xe	Os Ru	
7	H	(Li)	Na	K Co	Rb Rh	Cs Ir	Fr
8		(Be)	Mg	Ca Ni	Sr(Pd) Cd	Ba Pt	Ra
9		B	Al	Cu	Ag	Au	
10		C	Si	Zn	Cd	Hg	
11		N	P	Ga	In	Tl	
12		(O)	S	Ge	Sn	Pb	
13				As	Sb	Bi	
14				Se	Te	Po	

\*) Lanthanides, \*\*) actinides, () position of the elements in the brackets is not certain. Statistical processing of experimental data shows that  $\nu_C^j = \nu_i^j$ , where  $i = N, H, B$ .

Table 2.10 Dependence of the equivalence constants  $K_{Cr(C)}^j$  on characteristic numbers  $\nu_C^j$  elements in the periodic table of elements (Pilous and Stransky, 1998)

Characteristic number $\nu_C^j$	1	2	3	4	5	6	7	8	9	10	11	12	13	14
Equivalence constant $K_{Cr(C)}^j$	11.40	4.35	2.08	1.00	0.386	0	-0.259	-0.442	-0.574	-0.673	-0.749	-0.807	-0.852	-0.887

Table 2.11 Pilling-Bedworth Ratios for a Number of Metals

<b>Protective</b>		<b>Nonprotective</b>	
Ce	1.16	K	0.45
Al	1.28	Li	0.57
Pb	1.40	Na	0.57
Ni	1.52	Cd	1.21
Be	1.59	Ag	1.59
Pd	1.60	Ti	1.95
Cu	1.68	Ta	2.33
Fe	1.77	Sb	2.35
Mn	1.79	Nb	2.61
Co	1.99	U	3.05
Cr	1.99	Mo	3.40
Si	2.27	W	3.40

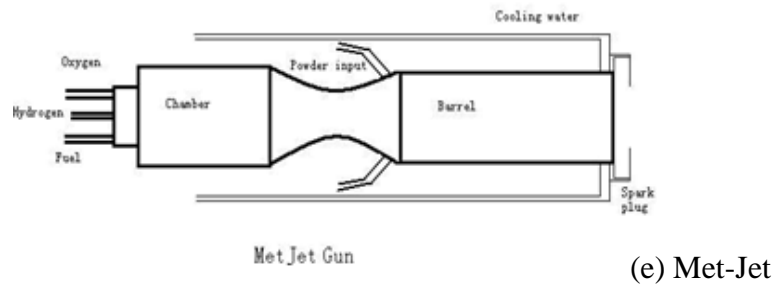
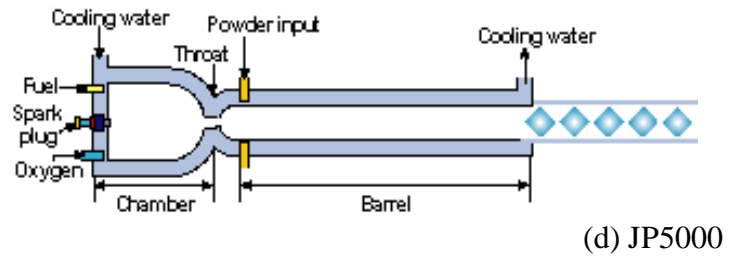
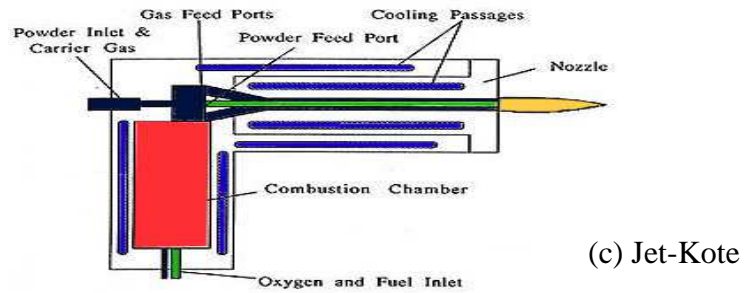
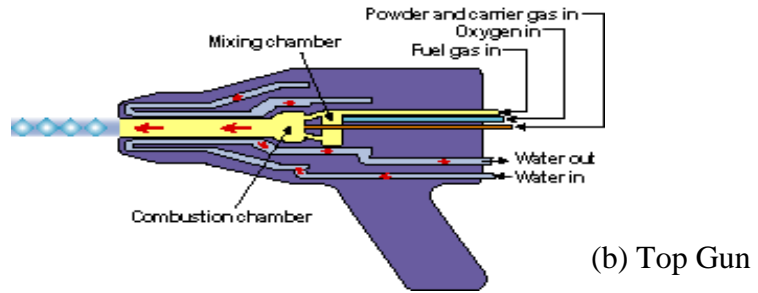
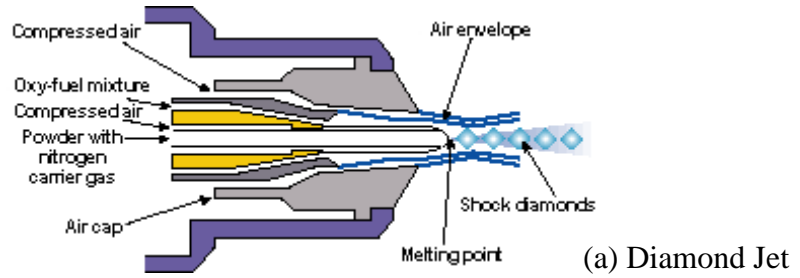


Fig. 2.1 Schematic diagrams of different types of HVOF thermal spray guns (Wirojanupatump, 1999)

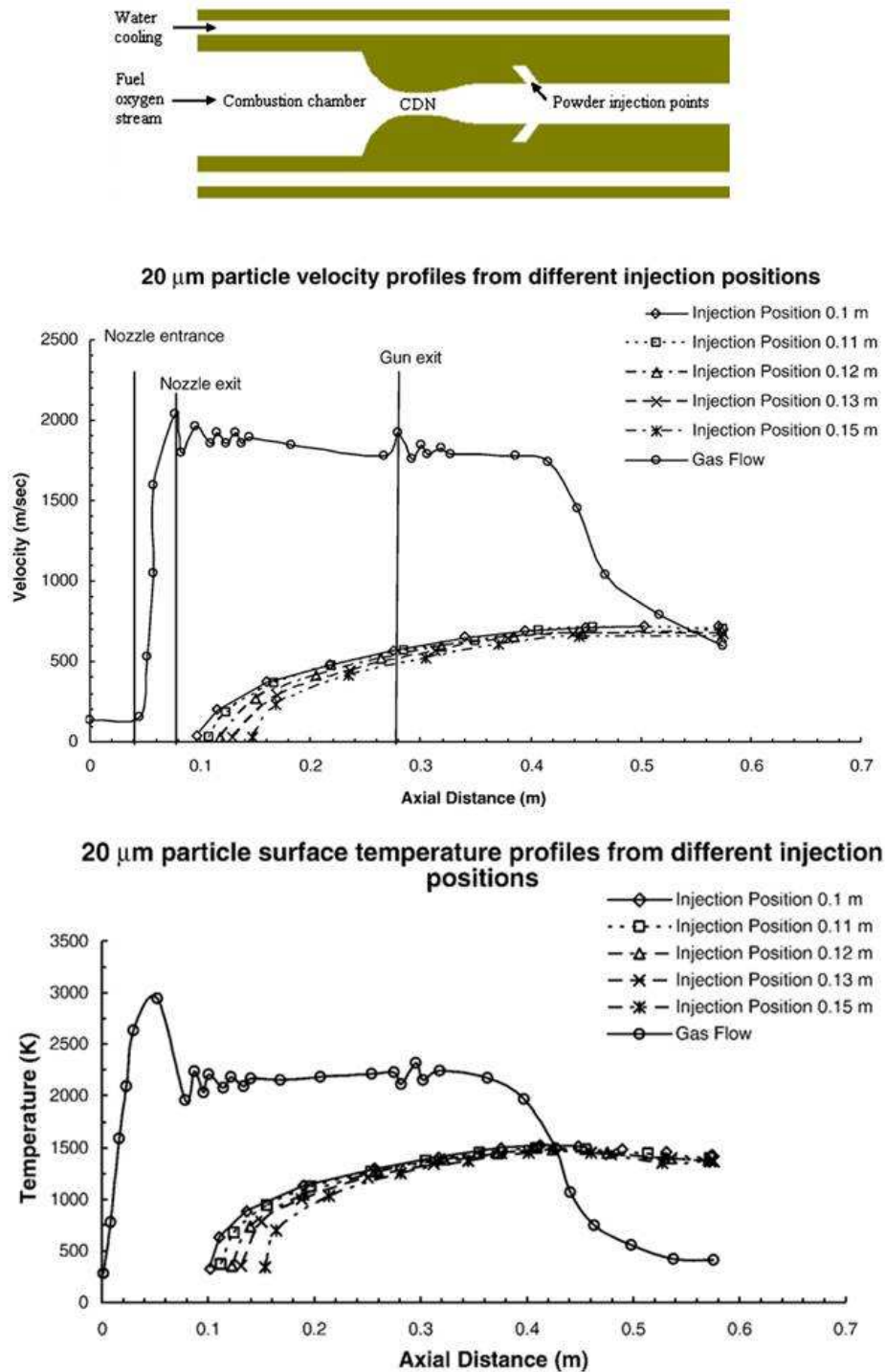


Fig 2.2 Particle velocity and particle surface temperature profiles from different injection positions in HVOF Met-Jet gun system (Kamnis, 2008)

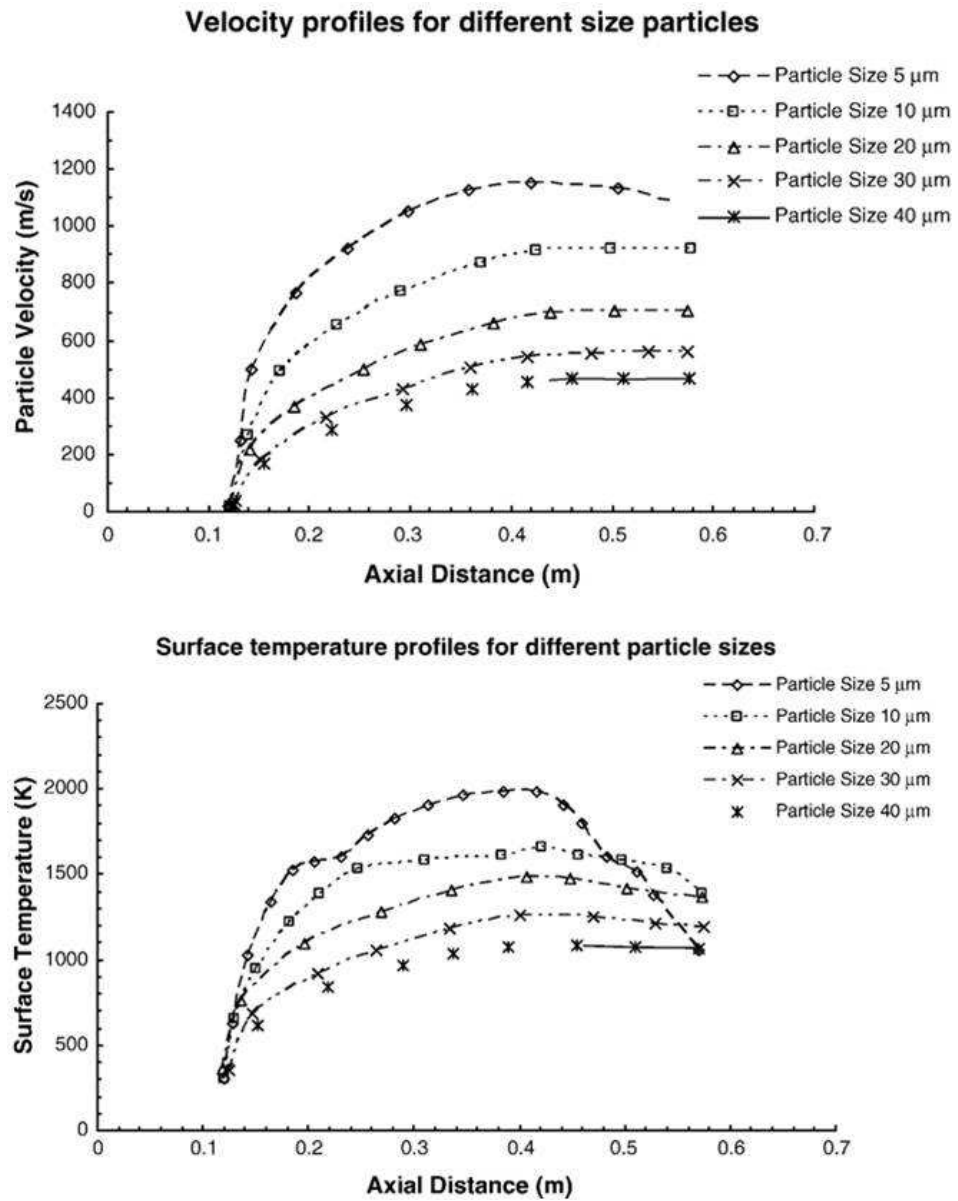


Fig 2.3 Particle velocity and particle surface temperature profiles for different size particles in HVOF Met-Jet gun system (Kamnis, 2008)



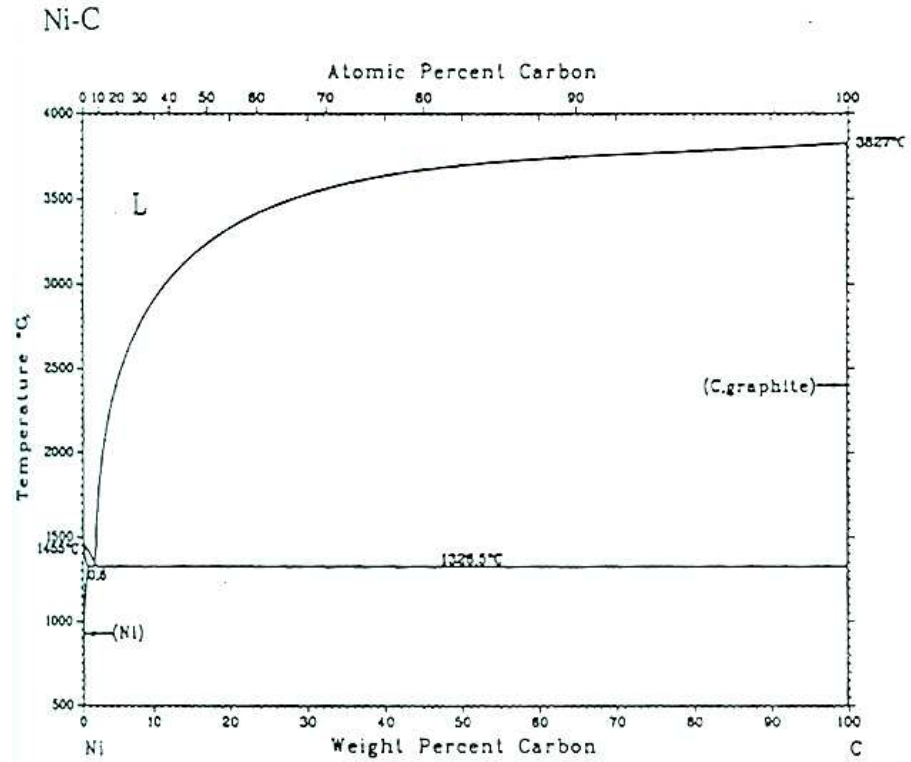


Fig 2.6 Equilibrium diagram of nickel-carbon (Venkatraman and Neumann, 1990)

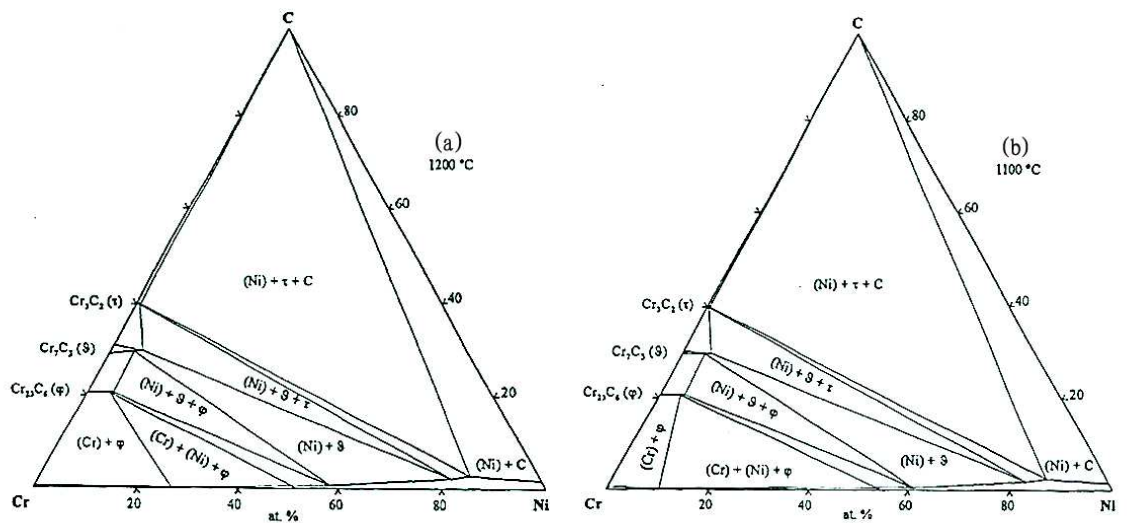


Fig 2.7 Isothermal section of the Cr-Ni-C phase diagram (Velikanova, 1998)

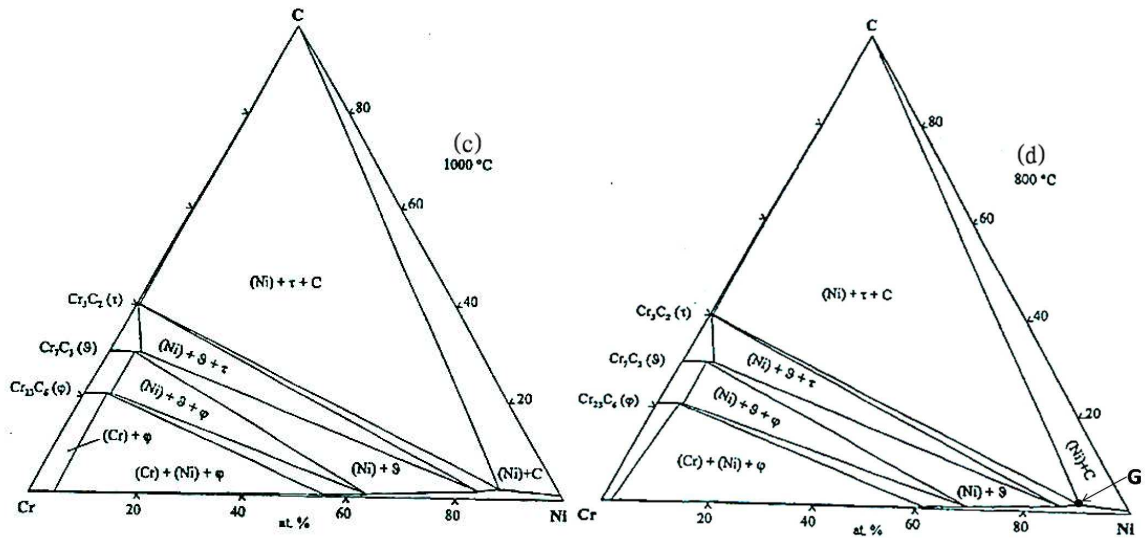


Fig 2.7 (continued) Isothermal section of the Cr-Ni-C phase diagram (Velikanova, 1998)

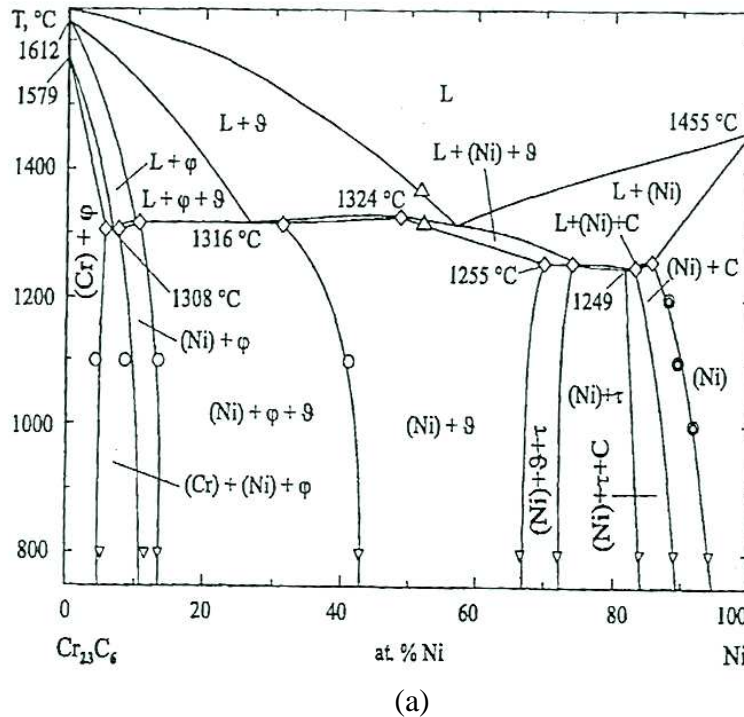
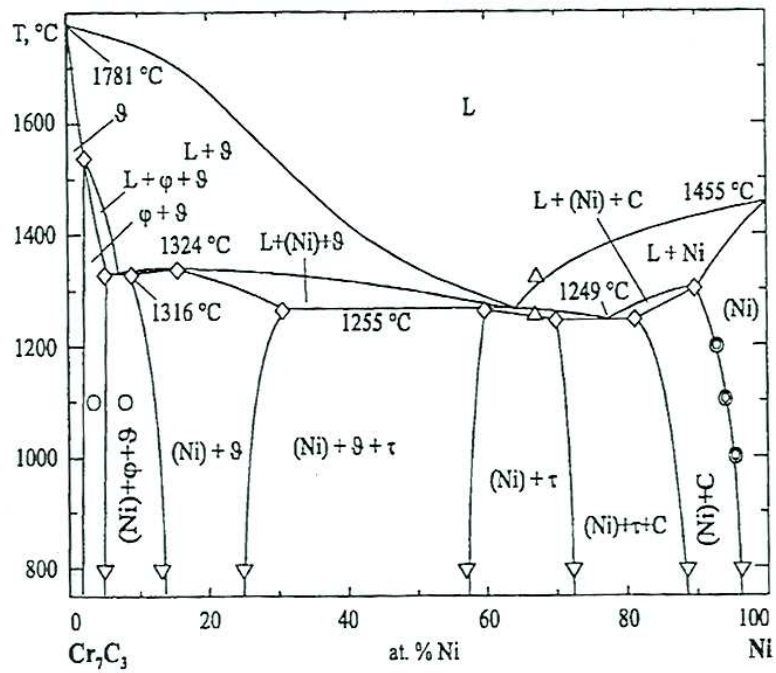
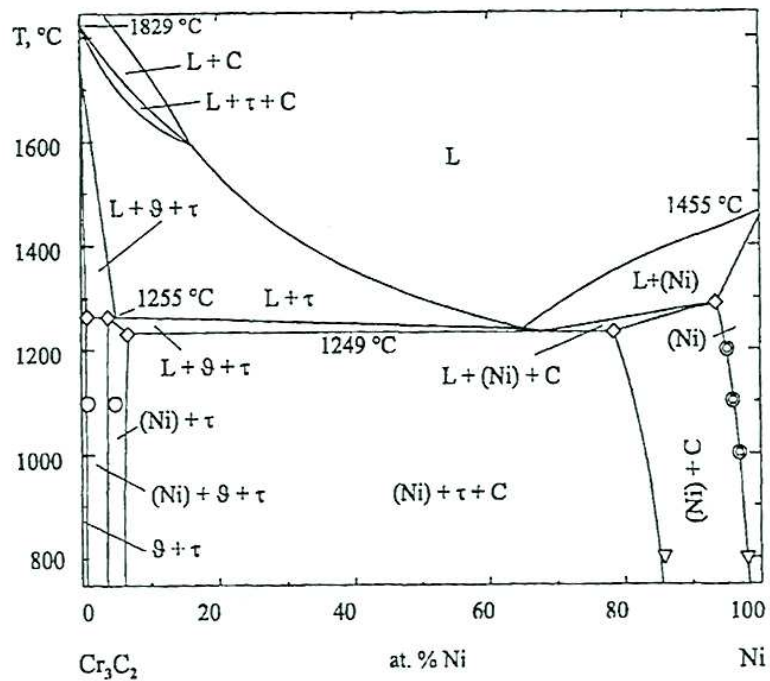


Fig 2.8 The vertical section of the Cr-Ni-C phase diagram: through the tie line with Ni and carbides (a)  $Cr_{23}C_6$  (Velikanova, 1998)



(b)



(c)

Fig 2.8 (continued) The vertical section of the Cr-Ni-C phase diagram: through the tie line with Ni and carbides (b)  $\text{Cr}_7\text{C}_3$  and (c)  $\text{Cr}_3\text{C}_2$  (Velikanova, 1998)

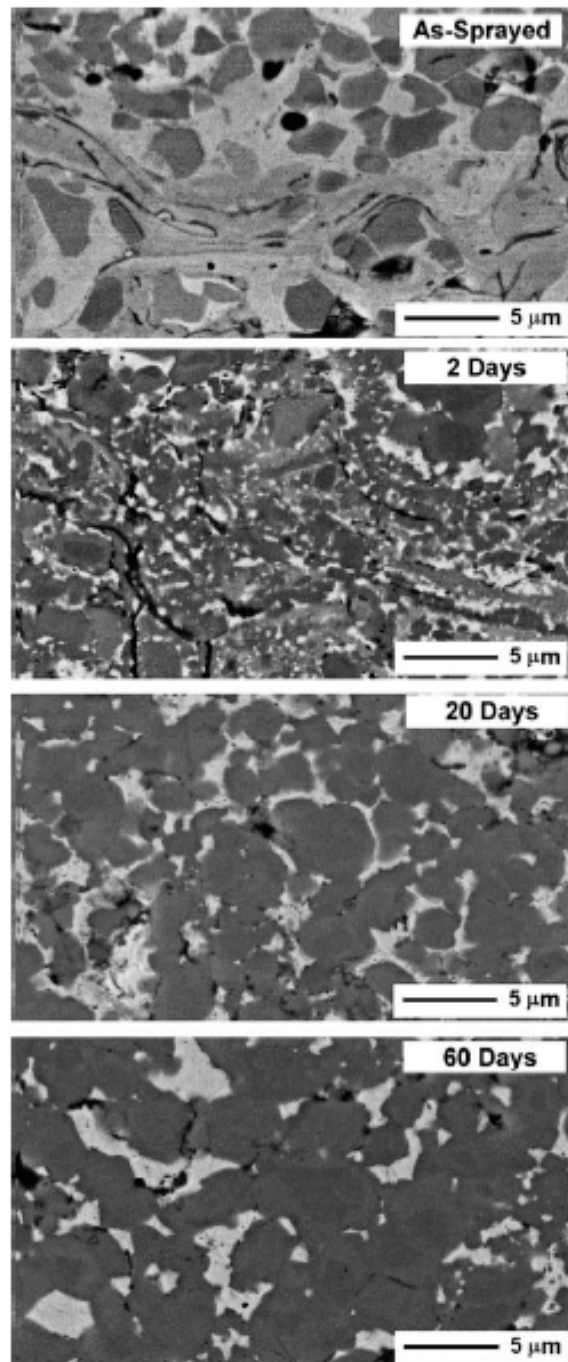


Fig 2.9 BSE images of the HVOF microstructure in the as-sprayed condition and after 2, 20 and 60 days of treatment at 900 °C (Matthews, 2003)

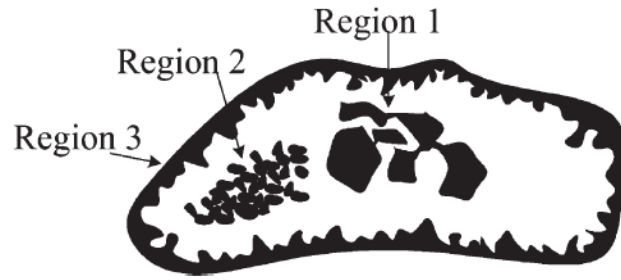


Fig 2.10 A schematic illustration of the three carbide developments in different regions within a splat during heat treatment of the HVOF coating (Matthews, 2003)

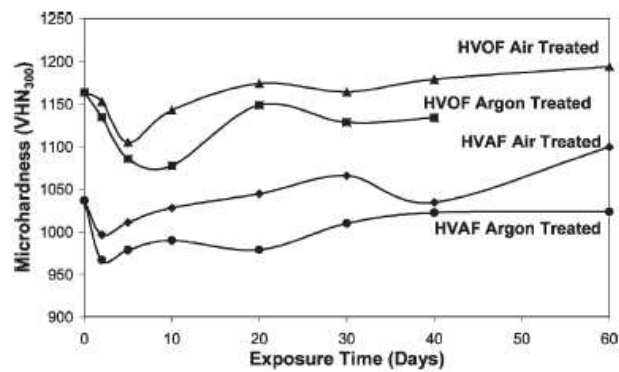


Fig 2.11 Vickers microhardness values of the HAVF and HVOF coatings treated in air and argon at 900 °C (Matthews, 2003)

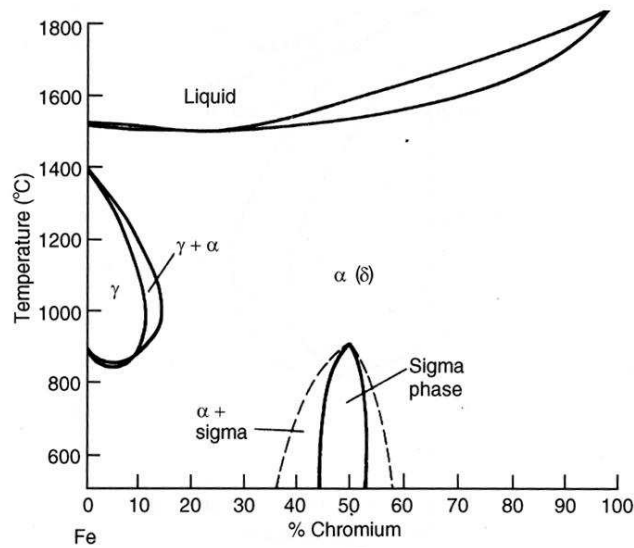


Fig 2.12 Iron-Chromium equilibrium diagram (Llewellyn, 1996)

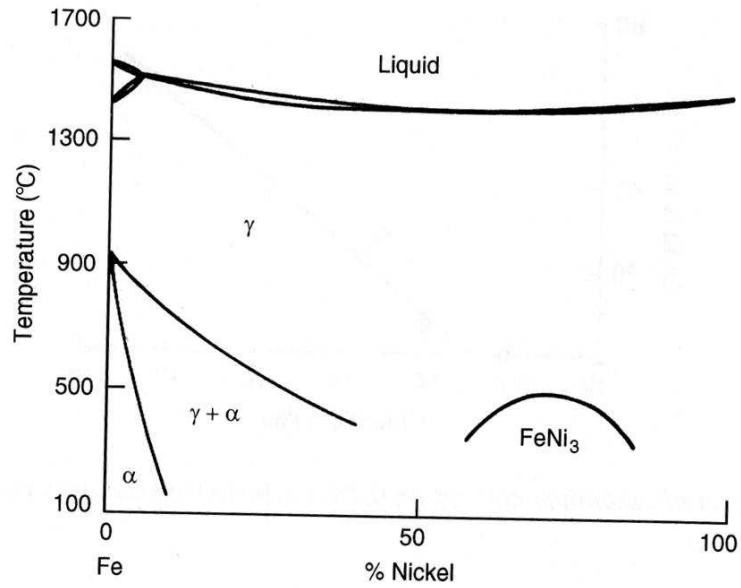


Fig 2.13 Iron-Nickel equilibrium diagram (Llewellyn, 1996)

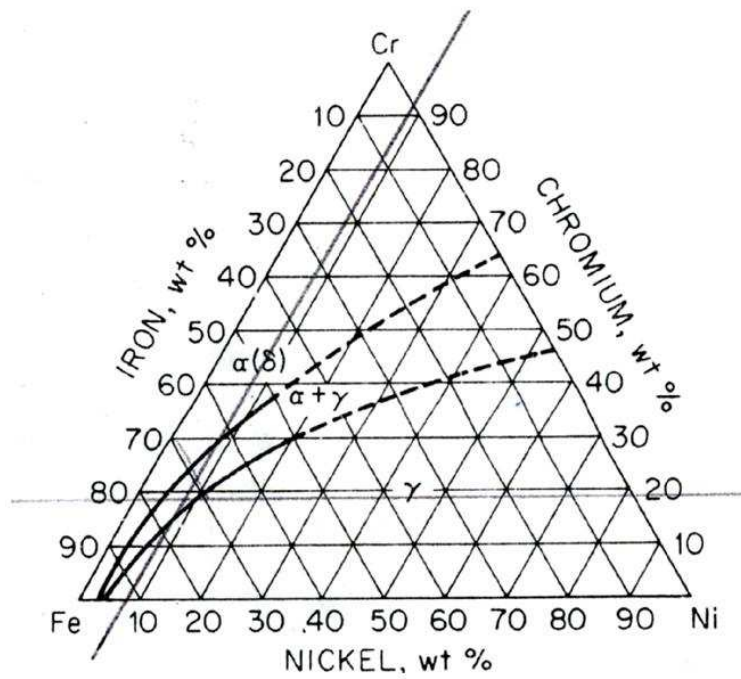


Fig 2.14 Fe-Cr-Ni system just below the solidus temperature (ASTM, 2004)

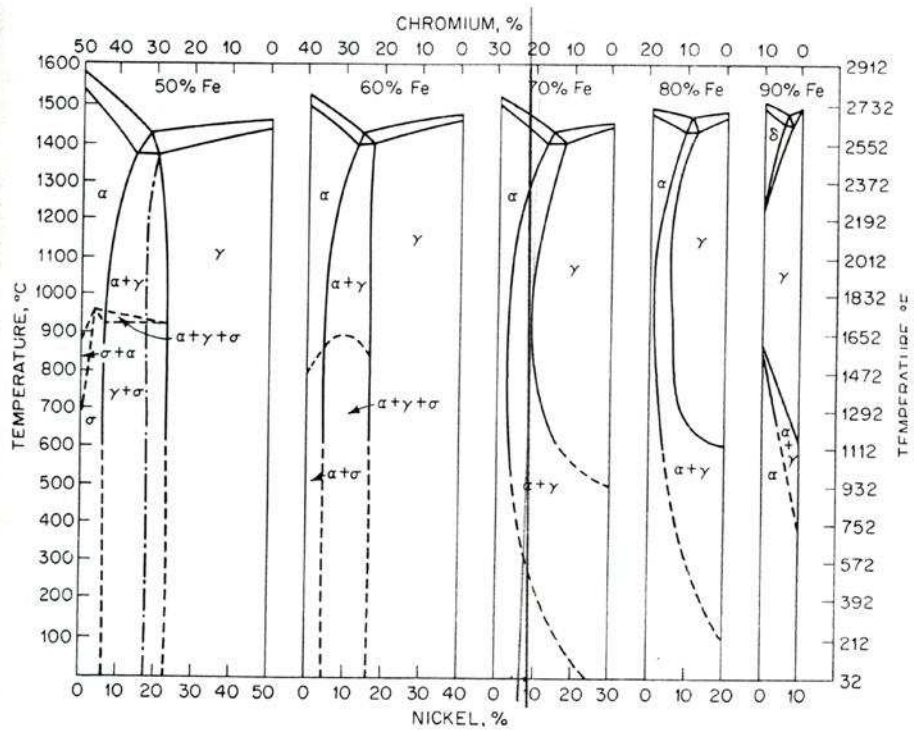


Fig 2.15 Cross sections of Fe-Cr-Ni ternary (ASTM, 2004)

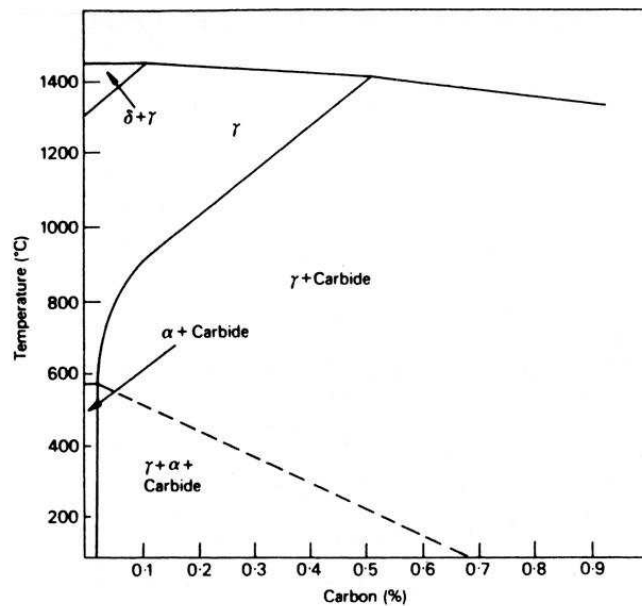


Fig 2.16 is the pseudo-binary phase diagram for Fe-18%Cr-8%Ni alloy with varying carbon content by (Colombier, 1967).

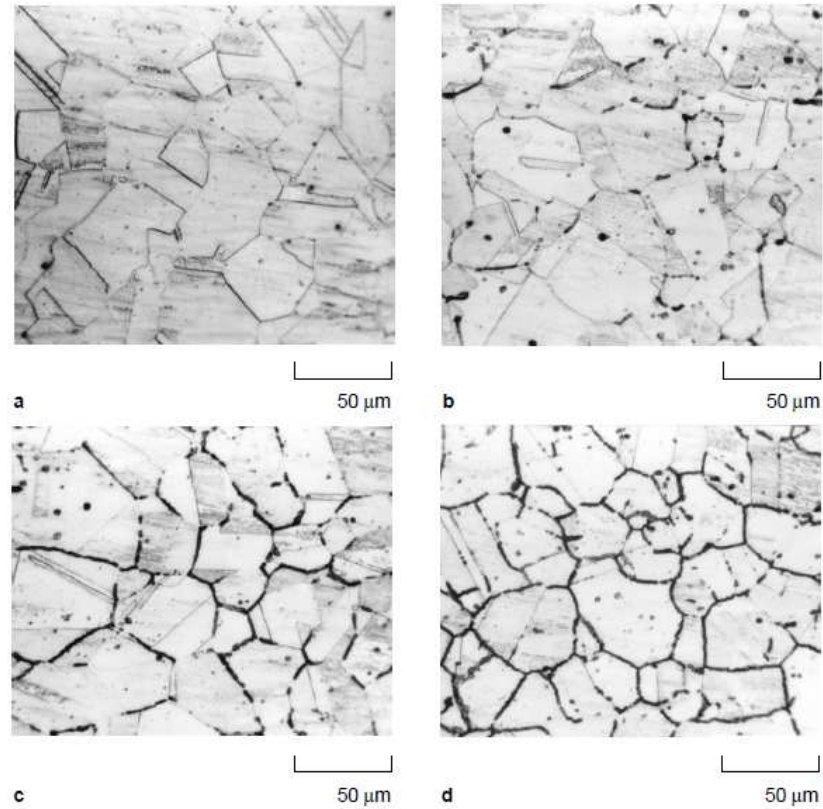


Fig 2.17 Optical microstructures of 304 stainless steel that were heat-treated at 1,000K for (a) 0s, (b) 100s, (c) 1,000s and (d) 10,000s (Hiroyuki, 2000)

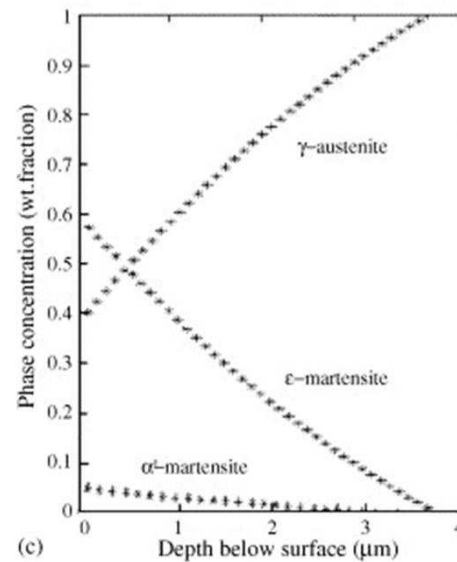


Fig 2.18 Phase distribution in the surface layers of stainless steels 304 after 24h of electrochemical charging and 10h of aging at room temperature (Rozenak, 2006)

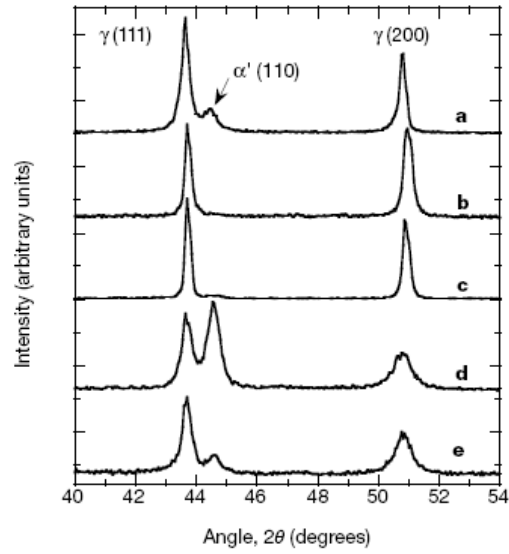


Fig 2.19 X-ray diffraction patterns of type 304L stainless-steel surfaces with Cu Ka radiation (Burstein, 2000)

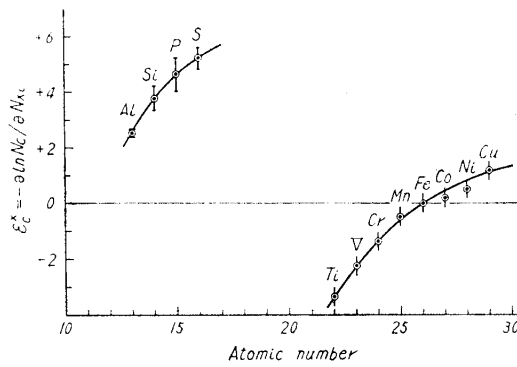


Fig 2.20 Relationship between atomic number of solute X and interaction parameter  $\epsilon_C^X$  (Sanbongi, 1957)

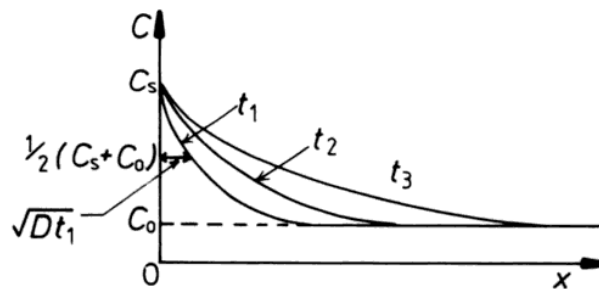


Fig 2.21 Concentration profiles at successive times ( $t_3 > t_2 > t_1$ ) for diffusion into a semi-infinite bar when the surface concentration  $C_s$  maintains constant (Porter, 1992)



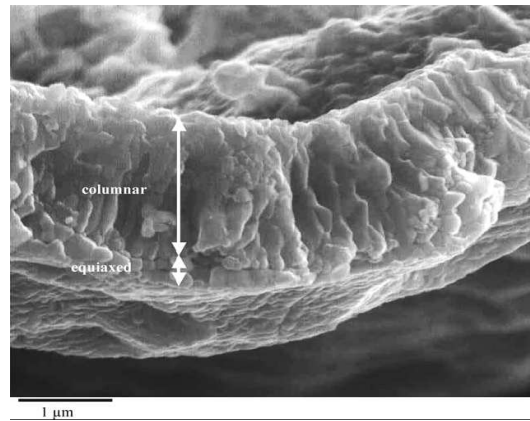


Fig 2.24 SEM observation of a fracture cross-section of NiO scale formed during 12 hours at 800 °C in air under atmospheric pressure (Peraldi, 2002)

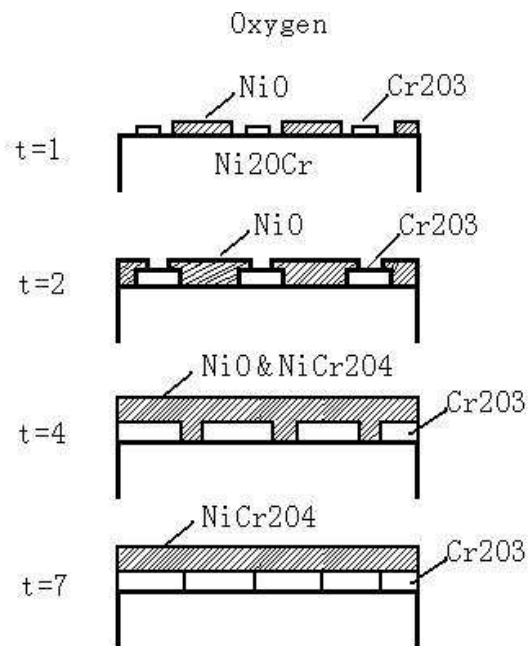


Fig 2.25 Schematic diagram illustrating the oxidation of Ni-20Cr in the initial exposure time (Allam, 1978)

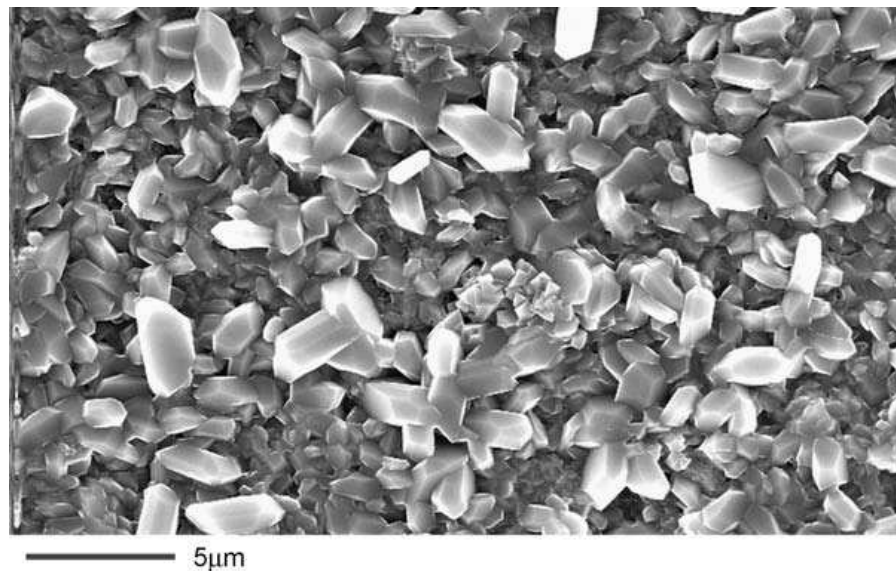


Fig 2.26 Surface of blended 75(Ni20Cr)-25Cr<sub>3</sub>C<sub>2</sub> coating oxidised for 48h at 850 °C  
(Matthews, 2009)

## **Chapter 3: Experimental procedures**

### **3.1 Introduction**

Thermal sprayed 25Ni(Cr)-75Cr<sub>3</sub>C<sub>2</sub> cermets have been used extensively to mitigate wear and high temperature oxidation resistance. In this work the main aim was to understand the effect of elevated temperature on the microstructures and microhardness of the coatings deposited by the HVOF process using a Met-Jet gun system. Two packs of powder with the same composition, agglomerated and sintered 75Cr<sub>3</sub>C<sub>2</sub>-25NiCr powder ordered from different companies, were selected. Both original powders and coatings were characterised using a variety of techniques. The details of materials used, spraying conditions and characterisation techniques are described in the following sections.

## 3.2 Materials

### 3.2.1 Ni(Cr)-Cr<sub>3</sub>C<sub>2</sub> powders

Two kinds of agglomerated and sintered 75Cr<sub>3</sub>C<sub>2</sub>-25NiCr powder were ordered from Metallisation and Praxair Company. Suppliers and broad specifications of the powders are listed in Table 3.1.

### 3.2.2 Substrates

The substrate used was stainless steel 304. The reason this was chosen as a substrate is because stainless steel has excellent behaviour of corrosion resistance and heat resistance and is widely used in a range of high temperature atmospheric environments and many corrosive media. Therefore, this project is to understand how as-sprayed microstructures change as a result of long term exposure to elevated temperatures and oxidising environments. Table 3.2 shows the composition of the steel provided by the supplier. The bulk stainless steel was cut into the dimensions of 58 x 25 x 2 mm. These sample dimensions were used for all coating deposition. Substrates were cleaned and roughened just prior to coating by grit blasting with brown alumina of ~250 um particle size.

### 3.3 Thermal spray procedures

#### 3.3.1 Sample preparation and HVOF system

##### Substrate preparation

Substrate (stainless steel 304) was cut into several pieces with the dimensions of 58 x 25 x 2 mm. SWI solution was used to clean the surface of the substrate, in order to get rid of the oil and water. The next step was to roughen the surface of the substrate by grit blasting with brown alumina of ~250 um particle size.

##### HVOF system preparation

The MET-JET II system was chosen for HVOF thermal spraying and includes 4 components:

##### Met-jet gun

The Met-Jet gun made by Metallisation is shown in Fig.3.1a, which has unique features to give the most consistent and reliable spray. The combustible mixture is fed into the combustion chamber through an array of ports giving a wider flame front and promoting complete burning within the chamber. The hydrogen pilot system is sequenced to burn both before and after the main flame to ensure a clean start and stop without fear of fuel being sprayed out onto the work piece. Powder injection is designed on both sides of nozzle and the pressures of which are very low preventing burnt gases running along the powder feed tube and a transducer is used to measure the chamber pressure avoiding inaccurate measurement due to leaking lines. Overall, the gun is robustly constructed to give a long service life.

##### Met jet mass flow meter controller

The Controller which is shown in Fig 3.1b brings together all elements of the system and provides the necessary controls and interlocks to ensure easy, consistent and safe operation. Only the most robust components are used so that it will continue to

provide trouble-free service. The controller contains a mass flow meter control system giving coating quality and reliability.

### **PFI powder feeder**

The PFI Powder Feeder shown in Fig 3.1c is a precision system using a positive displacement feed screw to accurately meter powder feed rate. The speed of the feed screw is controlled through a closed loop control system and thereby maintains an extremely accurate and consistent feed rate which is easily reproduced. The PFI integrates with the associated control systems to give warnings of low gas flows or blockages of the powder feed tube or spray nozzle. The unit can be mounted on a fixed ground or wall stand or fitted with castors for mobility.

### **Cooling system**

The cooling system shown in Fig 3.1d can be a recirculating cooler, a refrigerated chiller, or in some cases a water/water heat exchange system depending on the operational circumstances.

## **3.3.2 Deposition procedure**

Oxy-fuel (kerosene) mix is atomized after it passes through an orifice into the combustion chamber, thereby creating a stable, clean and uniform combustion process. Pressure in the combustion chamber is monitored to ensure the proper combustion mode and constant pressure which directly affects the powder particle velocity. The unique, converging/diverging exit nozzle of the combustion chamber is so designed to create a supersonic jet that maintains a low pressure area where the powder is radially injected through multiple ports. The powder then mixes with the hot combustion gases and is accelerated towards the substrate. This results in producing consistent coating quality with residual stresses in compression mode. The substrates will be mounted on a turntable which can hold 12 pieces/6 pieces of

substrate and rotated while the gun is traversed vertically. The schematic diagram of spray gun and sample holder are shown in Fig.3.2.

The spray parameters are very important to the properties of the coatings. The spray gun supplier provided some parameters for the different powders. In order to get the optimum coatings, these parameters have been modified. In the next chapter the effect of spray parameters such as the oxygen/fuel flow, gas flow and powder feed rate on the coating structures will be introduced and detailed.

### **3.4 Heat treatment of Ni(Cr)-Cr<sub>3</sub>C<sub>2</sub> coatings**

The specimens of as-coated substrates were heat treated at 700°C and 800°C in air for 1 hour, 2, 8 and 16 days. These samples were heated inside the furnace from room temperature to 700°C or 800°C and then maintained for the selected time and they were cooled inside the furnace to room temperature. However the response of substrate stainless steel 304 was also assessed after being annealed for various times at 700°C and 800°C in air. These results are used to provide a reference for comparison with annealed coated samples.

## **3.5 Powder and coating characterisation**

### **3.5.1 Size analysis of powder sample**

The powder size was measured by a Mastersizer 2000 particle analyser with the Low Angle Laser Light Scattering (LALLS) method. This analysis system allows accurate results over a large size range (0.02-2000µm typically). It was assumed that each particle of the agglomerated and sintered powders was similar in shape and their size distribution was thus measured by the light scattering size measurement. By using the laser diffraction measurement, particles are passed through a focused laser beam. These particles scatter light at an angle that is inversely proportional to their size. The angular intensity of the scattered light is then measured by a series of photosensitive detectors which have been optimized to achieve maximum resolution across a broad range of sizes. The map of scattering intensity versus angle is the primary source of information used to calculate the particle size distribution which can be predicted by the Mastersizer 2000 software.

### **3.5.2 Optical Microscopy (OM)**

The optical microscope (Nikon UFX-II with attached Nikon FX-35A camera) was mainly used to analyse the coating microstructures such as the thickness, porosity, oxide, deformation of the substrate, and distribution of phases. On the other hand, the transverse section provides information about the surface of the substrate and changes in the microstructure, which occurred during the coating deposition. (Pawlowski, 1995) Samples for optical microscopy were polished and etched before examination. To etch the NiCr-CrC coatings 10% oxalic acid in water with electrode potentials of 6V was recommended for use. (Edris, 1997)

### **3.5.3 X-ray Diffraction (XRD)**

X-ray diffraction is a routine technique used for phase analysis of powders and as-sprayed coatings. It was carried out using a Simens D500 equipped with

DACO-MP X-ray diffract meter and was operated at 40kV and 20mA to generate Cu  $K_{\alpha}$  radiation at wavelength of 1.540Å. Diffractograms were obtained using the Cu  $K_{\alpha}$  radiation with a step size of 0.02° and a 4 second counting time for a range of 2θ values (20°~100°) . The exposure area for coating samples was about 5x15mm.

Peak identification and phase determination were performed with the aid of the JCPDS powder diffraction files. A given substance always produces a characteristic diffraction pattern which is like a fingerprint of the substance to be identified. However, diffraction can show the presence of a compound whereas chemical analysis can only show the presence of separate elements. Substances are classified using the Powder Diffraction File. In this system any one powder is classified in terms of d spacing or 2θ positions and relative intensities.

In order to insure the X-rays were collected from the right region of the sample, the depth of X-ray penetration should also be considered. In this project two kinds of materials were used for X-ray diffraction, stainless steel 304 and 25Ni(Cr)-75Cr<sub>3</sub>C<sub>2</sub> coatings. The calculations of the depth of x-ray penetration in these two materials are as follow.

- Calculate the depth of x-ray penetration in stainless steel 304

2θ=20°~100°,  $G_x=90\%$ , Cu  $K_{\alpha}$ 1.542Å

Composition: 70.5%Fe+19.5% Cr+8.6%Ni+1.38%Mn

According to the table 'Mass Absorption coefficients  $\mu/\rho$  (cm<sup>2</sup>/gm) and Densities  $\rho$ ' (Cullity, 2001)

$$\begin{aligned}\mu_{Fe} &= 304.4 \times 7.87 = 2395.6 \text{ cm}^{-1} \quad \mu_{Cr} = 252.3 \times 7.19 = 1814.0 \text{ cm}^{-1} \\ \mu_{Ni} &= 48.83 \times 8.91 = 435.1 \text{ cm}^{-1} \quad \mu_{Mn} = 272.5 \times 7.47 = 2035.6 \text{ cm}^{-1} \\ \mu' &= 70.5\% \mu_{Fe} + 19.5\% \mu_{Cr} + 8.6\% \mu_{Ni} + 1.38\% \mu_{Mn} \\ &= 2108.1 \text{ cm}^{-1}\end{aligned}$$

$$G_x = (1 - e^{-\mu x / \sin \theta})$$

$$\rightarrow x = \frac{\ln\left(\frac{1}{1 - G_x}\right) \cdot \sin \theta}{2\mu}$$

$$\rightarrow x_{2\theta=20^\circ} = 0.95 \text{ um}$$

$$\rightarrow x_{2\theta=100^\circ} = 4.18 \text{ um}$$

⇒ Depth of X - ray penetration in stainless steel 304 is 0.95 ~ 4.18 um

- Calculate the depth of x-ray penetration in 25(80Ni20Cr)-75(Cr<sub>3</sub>C<sub>2</sub>) coatings

$$2\theta=20^\circ \sim 100^\circ, \quad G_x=90\%, \quad \text{Cu K}\alpha 1.542 \text{ \AA}$$

Composition: 70%Cr+20%Ni+10%C

$$\begin{aligned}\mu_{Cr} &= 252.3 \times 7.19 = 1814.0 \text{ cm}^{-1} \quad \mu_{Ni} = 48.83 \times 8.91 = 435.1 \text{ cm}^{-1} \\ \mu_C &= 4.219 \times 2.27 = 9.577 \text{ cm}^{-1} \\ \mu' &= 70\% \mu_{Cr} + 20\% \mu_{Ni} + 10\% \mu_C = 1357.8 \text{ cm}^{-1}\end{aligned}$$

$$G_x = (1 - e^{-\mu x / \sin \theta})$$

$$\rightarrow x = \frac{\ln\left(\frac{1}{1 - G_x}\right) \cdot \sin \theta}{2\mu}$$

$$\rightarrow x_{2\theta=20^\circ} = 1.47 \text{ um}$$

$$\rightarrow x_{2\theta=100^\circ} = 6.49 \text{ um}$$

⇒ Depth of X - ray penetration in 25NiCr - 75Cr3C2 coatings is 1.47 to 6.49 um

### 3.5.4 Scanning Electron Microscopy (SEM) and EDX analysis

The scanning electron microscope (SEM) is a type of electron microscope capable of producing high resolution images of a sample surface. A Philips XL30 SEM was used for analysis and characterisation of both powder and coatings with an accelerating voltage of 15kV in secondary and backscattered electron modes and for EDX analysis.

The spot size is about 4-4.5nm on the surface of the sample and the scanned areas are squares having sides of between 5um and 1 mm in length (Pawlowski, 1995).

X-rays, which are also produced by the interaction of electrons with the sample, may be detected in an SEM equipped for energy dispersive X-ray spectrometry (EDX). EDX is used for identifying the elemental composition of the specimen and quantifying light elements such as carbon and oxygen in a thin window mode. However, in order to ensure the accuracy of EDX analysis system when quantifying carbon in the NiCr-CrC coating, a 100% cobalt standard was calibrated before and after analysis of the samples.

### **3.5.5 Thermogravimetric Analysis (TGA)**

The oxidation behavior of NiCr-Cr<sub>3</sub>C<sub>2</sub> powder and coatings in thermal air was investigated using a TA instruments Q600 thermogravimetric analyzer. Oxidation tests of NiCr-CrC powder were carried out in commercial grade bottled air at 700°C and 800°C with a compressed air flow rate of 100 sccm and ramped heating rate of 50°C/min. It was held at the test temperature for more than 4 hours after the temperature was attained. Oxidation tests of NiCr-Cr<sub>3</sub>C<sub>2</sub> powder and coatings were carried out with the temperatures at 650°C, 700°C, 800°C, 900°C and 1000°C. In addition, for each coating sample a square of 3x3 mm test specimen was cut from the thin foil of a debonded coating layer for oxidation kinetic studies. These specimens were cleaned, dried and weighted. The total surface area for each specimen was also recorded. As a result, a continuous plot of change in mass versus time was recorded for each of the test temperatures. These curves were used for determining the oxidation kinetics of NiCr-Cr<sub>3</sub>C<sub>2</sub> coating debonded from a 304 stainless steel substrate.

### **3.5.6 Hardness tests**

The Vickers hardness test is the standard microhardness test employed for thermal

spray coatings and substrates. The indenter is a pyramidal diamond of normal dimensions that is charged with a load in the range 0.1N to 50N. The specimens for Vickers testing should be metallographically polished. Most of the measurements made on the longitudinal sections are used for optical microscopy observations. (Pawlowski, 1995). Microhardness testing of the NiCr-CrC coatings was performed using a 300g load on a Leco M-400 Hardness tester with a dwell time of 5s. An average microhardness measurement was calculated from ten random indents which were taken from close to the top surface, in the middle of the coating and close to the coating/substrate interface. Ten readings should provide adequate assurance that the hardness of a given specimen has been appropriately measured. Obvious coating defects and edges should be avoided during hardness readings.

The microhardness of the as-coated 304 stainless steel substrate was measured using a 100gm load with a dwell time of 5s and obtained from ten indents along a line parallel to the surface and in the middle of the bulk. The microhardness of these samples was also measured at approximately 5 $\mu$ m away from the grit blasted surface. Microhardness measurements were also taken from substrate/coating interface penetrates to the substrate edge to determine the possibility of a variation in microhardness through the depth of substrate.

### **3.5.7 Porosity analysis**

The porosity in coatings was estimated with ImageJ software which is a Java-based image processing program developed at the National Institute of Health. It can calculate area and pixel value statistics of user-defined selections and intensity thresholded objects. In the previous studies investigators (e.g. Venkataraman, 2007) have been using ImageJ software to analyse the microstructural features (pores) in plasma sprayed ceramic coatings and obtained good results.

Table 3.1 Nominal powder characteristics

<b>Powder type</b>	<b>Chemical formula</b>	<b>Size (um)</b>	<b>Trade name</b>	<b>Supplier</b>
Agglomerated and sintered	$75\text{Cr}_3\text{C}_2\text{-}25(\text{Ni}20\%\text{Cr})$	15-45	1375VM	Praxair US
Agglomerated and sintered	$75\text{Cr}_3\text{C}_2\text{-}25(\text{Ni}20\%\text{Cr})$	15-45	99785/32	Metallisation UK

Table 3.2 Compositions of the stainless steel 304 provided by supplier

<b>Composition</b>	<b>Wt. %</b>
C	Max 0.08
Cr	18-20
Fe	66.345-74
Mn	Max 2
Ni	8-10.5
P	Max 0.045
S	Max 0.03
Si	Max 1



Fig 3.1 HVOF thermal spray system (a) MET JET spray gun (b) controller (c) powder feeder (d) cooling system

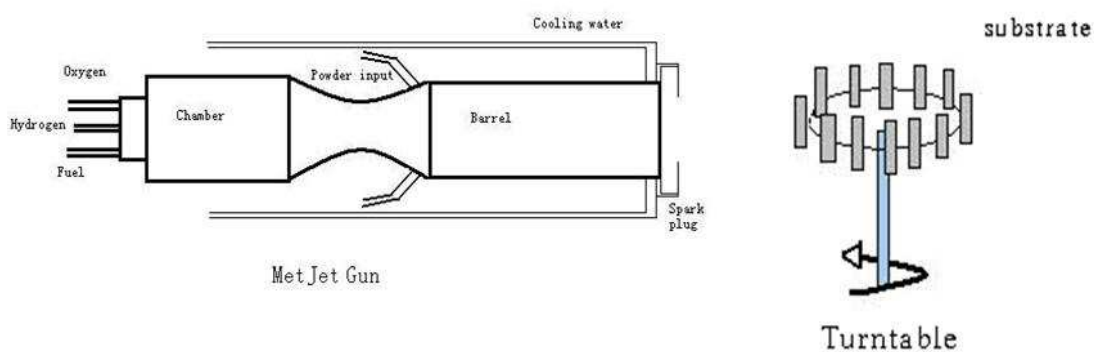


Fig.3.2 Schematic diagram of spray setup

## **Chapter 4: Microstructure formation in as-sprayed**

### **Ni(Cr)-Cr<sub>3</sub>C<sub>2</sub> coatings: Results and Discussion**

#### **4.1 Results**

##### **4.1.1 Introduction**

Two types of nickel chromium-chromium carbide (NiCr-Cr<sub>3</sub>C<sub>2</sub>) powders produced by different companies namely Metallisation and Praxair have been sprayed onto stainless steel substrates by HVOF thermal spraying. As-sprayed coating microstructures were found to depend on the spray process and powder characteristics. The investigation of the effect of HVOF thermal spray parameters, namely powder feed rate and carrier gas flow rate on coating microstructure were studied and reported in this chapter. As-sprayed coatings and the two powders were characterised by a variety of techniques including optical microscopy, X-ray diffraction, scanning electron microscopy (SEM), microhardness testing and porosity analysis.

## 4.1.2 Feedstock powder characterisation

### 4.1.2.1 Morphology and size range

The secondary electron images of the powder are shown in Figs 4.1 and 4.2, which reveal a largely spherical particle morphology. Powder particles from Metallisation appear denser and with a smoother surface than the powder from Praxair. In Fig 4.1 the particle size range is approximately 15-40  $\mu\text{m}$  which is quite close to the size distribution results given by the powder supplier in Table 3.1. Laser diffraction size analysis of the powder from Metallisation shows a broad size distribution ranging from about 15 to 85  $\mu\text{m}$  with the average size of 38  $\mu\text{m}$  (Fig 4.3). On the other hand, the Praxair powder size range was about 10-45  $\mu\text{m}$  from its SEM images in Fig 4.2. The particle size distribution of this powder as determined by laser diffraction analysis is shown in Fig 4.4 with the most size range 10 to 105  $\mu\text{m}$  with the average size of 43  $\mu\text{m}$ .

### 4.1.2.2 Phase Analysis

XRD identifies phases in the powder. Both of these powders give the same set of peaks in their XRD patterns shown in Figs 4.5 and 4.6. The first set of peaks represent a fcc lattice which belongs to Ni based alloy solid solution. The second set of peaks represents an orthorhombic Cr<sub>3</sub>C<sub>2</sub> crystal lattice.

SEM-BSE images of the as-polished sections of the 25NiCr-Cr<sub>3</sub>C<sub>2</sub> powder from Metallisation shows a uniform particle structures in Fig 4.7. The brighter regions could well be metallic phase (higher mean atomic number) whilst the darker regions represent carbide phase (lower mean atomic number). SEM-BSE images of the as-polished sections of the 25Ni(Cr)-75Cr<sub>3</sub>C<sub>2</sub> powder from Praxair shown in Fig 4.8 exhibit a very porous microstructure with clear contrast between the carbide and Ni(Cr) matrix phases. Phase composition revealed by EDX-SEM showed the bright areas (M) in Fig4.8 were identified as a Ni(Cr) alloy whereas the dark areas (C) contained principally chromium and carbon with a composition close to chromium

carbide Cr<sub>3</sub>C<sub>2</sub> as expected from XRD results. The chemical compositions in atomic percent (at %) of different phases in the powder determined by EDX analysis are summarised in Table 4.1. The carbide grains are evenly distributed, forming an interconnecting network within each powder particle.

### 4.1.3 Influence of spray conditions on coating deposition efficiency

Both Metallisation and Praxair powders were sprayed using the same oxygen and kerosene flow rates based on 'MET JET III SPRAY PARAMETERS' recommended by Metallisation. The powder feed rate and carrier gas flows were varied for the Praxair powder. Table 4.2 shows the parameters for each spray run. In order to get better flowability, powder was stored in an aluminium can and dried in air at 120°C for 18 hours immediately before being sprayed. The coating using Metallisation powder gave a thickness about  $200 \pm 5$   $\mu\text{m}$  and the thickness of the coating from Praxair powder was about  $400 \pm 4$   $\mu\text{m}$ . The estimated deposition efficiency of both spray runs is calculated below.

For the thermal spray using Metallisation powder, the total powder feeding time was 403s and the scan time was 354s. Total weight of powder used for spraying was 384.4 g. Powder feed rate of this spray run was about 59 g/min while the Metallisation recommended value is 70 g/min. Estimated deposition efficiency  $D_0$  is calculated below:

$D_0$ : deposition efficiency,  $h_1$ : coating thickness,  $h_2$ : theoretical coating thickness,  $t_1$ : scan time (time for the gun starting to have vertical movement until it stopped),  $t_2$ : total powder feed time (time for the powder starting to come out until the gun was shut down),  $m_1$ : powder deposited on the scanned area,  $m_2$ : total powder consumption,  $d$ : diameter of carousel,  $s$ : scan distance,  $\rho$ : density of 25Ni(Cr)-75Cr<sub>3</sub>C<sub>2</sub> coating (Metallisation product catalogue)

$$D_0 = \frac{h_1}{h_2} \times 100 \quad (1)$$

$$m_1 = d \cdot \pi \cdot s \cdot h_2 \cdot \rho$$

$$\Rightarrow h_2 = \frac{m_1}{d \cdot \pi \cdot s \cdot \rho} \quad (2)$$

$$\frac{m_1}{t_1} = \frac{m_2}{t_2}$$

$$\Rightarrow m_1 = \frac{t_1}{t_2} m_2 \quad (3)$$

From(1),(2)and(3)

$$\Rightarrow D_0 = \frac{d \cdot \pi \cdot s \cdot t_2 \cdot \rho}{t_1 \cdot m_2} h_1 \% \quad (4)$$

*Deposition efficiency Metallisation powder*

$$\begin{aligned} \therefore d &= 22.2\text{cm} & s &= 8.8\text{cm} & \rho &= 7125 \text{ kg/m}^3 & \pi &= 3.14 \\ t_1 &= 354\text{s} & t_2 &= 403\text{s} & m_2 &= 398.37\text{g} & h_1 &= 200\mu\text{m} \end{aligned}$$

$$\begin{aligned} \therefore \Rightarrow D_0 &= \frac{d \cdot \pi \cdot s \cdot t_2 \cdot \rho}{t_1 \cdot m_2} h_1 \% \\ &= \frac{22.2 \times 10^{-2} \text{m} \times 3.14 \times 8.8 \times 10^{-2} \text{m} \times 7125 \text{ kg/m}^3 \times 403\text{s} \times 200 \times 10^{-6} \text{m}}{354\text{s} \times 398.37 \times 10^{-3} \text{kg}} \% \\ &= 25\% \end{aligned}$$

For the thermal spray using Praxair powder,  $t_2$  for this spray run was 611s and  $t_1$  was 544s. Total weight of powder used for spraying was 525.94g. Powder feed rate of this spray run is about 51.56 g/min and the metallisation recommended value 70 g/min. Estimated deposition efficiency  $D_0$  is calculated below:

*Deposition efficiency Praxair powder*

$$\begin{aligned} \therefore d &= 22.2\text{cm} & s &= 8.8\text{cm} & \rho &= 7125 \text{ kg/m}^3 & \pi &= 3.14 \\ t_1 &= 544\text{s} & t_2 &= 611\text{s} & m_2 &= 525.94\text{g} & h_1 &= 400\mu\text{m} \\ \therefore \Rightarrow D_0 &= \frac{d \cdot \pi \cdot s \cdot t_2 \cdot \rho}{t_1 \cdot m_2} h_1 \% \\ &= \frac{22.2 \times 10^{-2} \text{m} \times 3.14 \times 8.8 \times 10^{-2} \text{m} \times 7125 \text{ kg/m}^3 \times 611\text{s} \times 400 \times 10^{-6} \text{m}}{544\text{s} \times 525.94 \times 10^{-3} \text{kg}} \% = 37.3\% \end{aligned}$$

According to the calculation above powder, from Praxair had a better deposition efficiency than Metallisation powder. The characterisation of both coatings will be introduced and compared in the following sections.

#### 4.1.4 Coating from Metallisation powder

##### 4.1.4.1 Optical microscopy

Optical micrographs of as-polished, cross-sectioned NiCr-Cr<sub>3</sub>C<sub>2</sub> Metallisation powder coatings are shown in Fig 4.9. Features present in the middle of the coating include bright regions (M) corresponding to alloy matrix, grey layers (O) corresponding to oxide and some dark regions (P) corresponding to porosity. Coating porosity was measured by computer based software 'Image J' and gives the value  $1.8 \pm 0.8\%$ .

##### 4.1.4.2 X-ray diffraction

The results of X-ray diffraction analysis for the Metallisation powder coating is shown in Fig 4.10. All the information was obtained from the coating after about 100  $\mu\text{m}$  being ground away from the top surface. The main peaks can be identified as: Cr<sub>3</sub>C<sub>2</sub> and Ni(Cr). In addition, some weak peaks at the  $2\theta$  values of  $33.6^\circ$  and  $54.8^\circ$  are identified as arising from Cr<sub>2</sub>O<sub>3</sub>. A significant broad diffraction halo between  $40^\circ$  and  $45^\circ$  is seen in the XRD pattern from the coating when it is compared with the original powder pattern in Fig 4.11. (XRD pattern is provided in Appendix)

##### 4.1.4.3 Scanning Electron Microscopy

The microstructure of the as-sprayed Metallisation powder coating was revealed by backscattered electron (BSE) imaging of coating cross-sections shown in Fig 4.12. The coating had a generally dense structure with a random distribution of micron sized incompletely melted carbide particles (dark and light grey), dark regions (P) representing pores and bright contrast regions (M).

Phase compositions, analysed by EDX-SEM are shown in Table 4.3. According to this table it is possible to identify the phase compositions from backscattered electron image in the SEM. In Fig. 4.12 the dark angular particles which are marked within **C** are identified as Cr<sub>3</sub>C<sub>2</sub> and the brightest phase marked within **M** corresponds to the Ni(Cr) solid solution matrix. The grey regions (**G**) are seen to contain Ni as well as

Cr and C. The average composition of the coating shows higher carbon content ~ 37at% than that in the original powder ~30at% but this is probably not significant because it is difficult to measure carbon content by EDX analysis.

#### **4.1.4.4 Thickness and hardness**

The average thickness of this coating was  $200 \pm 3$   $\mu\text{m}$ . Microhardness tests were performed along a line parallel to the interface in the middle of cross-sectioned coatings using a 300 gm load with a Vickers indenter. The average microhardness from ten measurements of the coating is  $829 \pm 48$   $\text{HV}_{300}$ .

### 4.1.5 Coating from Praxair powder

#### 4.1.5.1 Optical microscopy

Optical micrographs of as-polished, cross-sectioned 25Ni(Cr)-75Cr<sub>3</sub>C<sub>2</sub> Praxair powder coatings are revealed in Fig.4.13 which shows the coating microstructure near the top surface, in the middle and at the coating/substrate interface respectively. Some layered structures (O), which are probably bands of oxide are present as arrowed in the middle of the coating. The coating appears to be reasonably well bonded to the substrate with limited porosity in the coating and at the interface. Some black regions (P) which are considered as pores are indicated in Fig.4.13. Coating porosity measured by 'Image J' gave the value  $3.2 \pm 1.1\%$ .

#### 4.1.5.2 X-ray diffraction

The X-ray diffraction pattern for the Praxair powder coating is shown in Fig.4.14 from which the presence of the primary phases Cr<sub>3</sub>C<sub>2</sub> and Ni(Cr) is identified. In addition, Cr<sub>2</sub>O<sub>3</sub> peaks, presumably arising from Cr<sub>2</sub>O<sub>3</sub> which formed during the spraying process, also exist at 2-Theta values of 24.5°, 33.6°, 41.8°, 54.8°, 63.5° and 65.1°. All the information was obtained from the coating after about 100 μm had been ground away from top surface. Comparing the trace from as-sprayed coating to the trace from the original powder, Fig.4.15 also shows a distinct decrease of Ni(Cr) peak at 44.3° with a large broad diffracting halo between 40° and 45° in the coating trace which has the similar peaks shown in Fig 4.11. (XRD pattern is provided in Appendix)

#### 4.1.5.3 Scanning Electron Microscopy

The typical surface topography of the NiCr-Cr<sub>3</sub>C<sub>2</sub> coating from Praxair powder is shown in the SEM micrograph of Fig.4.16. Large splats ~ 10 μm along with much finer spherical particles which are probably a result of droplet disintegration at impact during spraying process are found in Fig.4.16a. On the other hand a number of apparently unmelted particles (U) are observed as shown in Fig.4.16b and are

typically 3~4 μm in diameter.

The as-sprayed coating from Praxair powder exhibited a dense coherent structure with various phases present which are revealed in the cross-sectional backscattered electron image as shown in Fig.4.17. As shown in Table 4.4 phase compositions of different regions were analysed by EDX-SEM spot analysis. In Fig.4.17 the dark angular particles which are marked with **C** are identified as Cr<sub>3</sub>C<sub>2</sub> and the brightest phase marked within **M** corresponds to the Ni(Cr) solid solution matrix. The light grey carbides (**G1**) are possibly from Cr<sub>3</sub>C<sub>2</sub> that partially dissolved forming Cr(Ni)<sub>3</sub>C<sub>2</sub> carbides on solidification of the splat. The grey area (**G2**) are the Ni(Cr) matrix with carbide that has possibly re-precipitated during splat solidification. The dark layer (**O**) in the matrix could possibly be the oxide phase given the high oxygen levels in EDX spectrum. The oxide phase could be Cr<sub>2</sub>O<sub>3</sub> which was identified by XRD. From the EDX result, region **G** is Cr-rich phase and also contains significant amounts of carbon. The average composition in the coating shows higher carbon content ~ 35at% than that in the original powder ~30 at%.

#### 4.1.5.4 Thickness and hardness

The average thickness of this coating was 400±4 μm. The average microhardness and standard deviation value of the coating is 1067±44 HV<sub>300</sub>.

## 4.2 Discussion

### 4.2.1 Comparison of the coating from Metallisation and Praxair powder suppliers

As mentioned before, two kinds of agglomerated and sintered 25Ni(Cr)-75Cr<sub>3</sub>C<sub>2</sub> powder from different suppliers were used in HVOF thermal spraying. Characterisations of these two powder coatings introduced in previous sections will be compared as follows.

First, the Metallisation powder coating shows a lower porosity which is possibly due to the microstructure of the original powder. In their SEM cross-section images Metallisation powder shows a denser and more uniform structure than the Praxair powder. Second, Praxair powder coating exhibits higher deposition efficiency and a thicker coating after a certain number of passes. Third, Praxair powder coating also has a higher microhardness than the Metallisation powder coating. In the SEM cross-sectioned images of the Metallisation powder coating, more un-melted carbide particles are visible than in the Praxair powder coating. More significant in-flight carbide dissolution occurred in the HVOF Praxair powder coating, the Ni(Cr) matrix become supersaturated with Cr and C, as highlighted by the grey area (G2) in Fig 4.17. These grey areas contain more carbon than the bright matrix area (M), which will cause the increase of matrix hardness. On the other hand, the Praxair powder coating shows higher oxide (Cr<sub>2</sub>O<sub>3</sub>) peaks in its X-ray diffraction pattern than the Metallisation powder coating. Higher microhardness values will be achieved in the Praxair powder coating due to the formation of the hard Cr<sub>2</sub>O<sub>3</sub> phase and also the increased matrix supersaturation.

Characterisation of the coatings sprayed from two kinds of powder is summarised in table 4.5 which includes porosity, thickness, deposition efficiency and microhardness. Praxair powder coatings have been used for all the further experiments, because its better coating deposition efficiency and higher microhardness.

### 4.2.2 Comparison with previous work

In this section some comparisons between the as-sprayed Praxair powder coating and previous work on HVOF thermal sprayed NiCr-Cr<sub>3</sub>C<sub>2</sub> coatings will be discussed. As the thermally sprayed coatings contain an enormous variety of features, it will be useful to compare them by the principal phases and constituents observed from this work and previous researches.

#### Carbide phases

SEM observation revealed the rounded carbides with various size distributed in the Praxair powder coating after thermal spraying. The EDX analysis of these phases shows a composition close to Cr<sub>3</sub>C<sub>2</sub>. Some light grey carbides (**G1**) in Fig.4.17 are considered as Cr(Ni)<sub>3</sub>C<sub>2</sub> carbides from the EDX spectrum. This is because of the solidification of partially dissolved Cr<sub>3</sub>C<sub>2</sub> carbides. The XRD data indicated the presence of Cr<sub>3</sub>C<sub>2</sub> as the only carbide phase in as-sprayed NiCr-Cr<sub>3</sub>C<sub>2</sub> Praxair powder coating. Several investigators (Matthews, 2009; Guilemany, 2002; Wirojanupatump, 2001; etc) working on NiCr-Cr<sub>3</sub>C<sub>2</sub> coatings using HVOF systems, reported the presence of carbide phases in coatings listed in Table 2.3. In the main these were identified only by XRD. Some of the investigators as Matthews (2009) and Ye (2008) reported the presence of Cr<sub>3</sub>C<sub>2</sub> as the only carbide in coating, but they also mentioned that the amount of Cr<sub>7</sub>C<sub>3</sub> which might be formed in flight might be too low to be distinguished definitively from the background noise by XRD. Other investigators such as Guilemany (1996) and Wirojanupatump (2001), they reported the presence of Cr<sub>3</sub>C<sub>2</sub>, Cr<sub>7</sub>C<sub>3</sub>, Cr<sub>23</sub>C<sub>6</sub> in their thermally sprayed coatings. This might be caused by several reasons. (a) Different powder type with different carbide phases or constituents in the original powder gives different results. Guilemany (1996) found the appearance of Cr<sub>3</sub>C<sub>2</sub>, Cr<sub>7</sub>C<sub>3</sub> and Cr<sub>23</sub>C<sub>6</sub> carbide phases in his 25Ni(Cr)-75Cr<sub>3</sub>C<sub>2</sub> cermet powder by XRD which might give different carbide phases in the as-sprayed coating. (b) Different HVOF systems (spray guns) or thermal spray parameters might also give

different results. In different spraying conditions, the gas temperatures might affect the decarburization of Cr<sub>3</sub>C<sub>2</sub> and lead to the formation of Cr<sub>7</sub>C<sub>3</sub> and Cr<sub>23</sub>C<sub>6</sub> (Ji, 2006).

### Ni(Cr) rich matrix

It is possible to distinguish the alloy matrix phase in the SEM as a light contrast area (**M**) shown in Fig 4.17. The EDX analysis shows the chemical composition of this phase as Ni and Cr rich metallic regions with a composition close to 80 wt%Ni, 20 wt%Cr. However, there is still a small amount of C detected in this area which possibly can be due to (a) the signal picked from the carbides phase nearby or (b) the dissolution of carbide precipitates in matrix. On the other hand, some light grey area (**G2**) are also found in matrix in Fig 4.17 which reveal a significant amount of carbon. These regions can be considered as Ni(Cr) alloy matrix containing carbide having re-precipitated during splat solidification. This super-saturation of Ni(Cr) binder phase with Cr and C due to the inflight dissolution of some chromium carbide particles during the spraying process is found to produce peak broadening in the X-ray diffraction pattern forming a significant amorphous phase structure giving a background seen between  $2\theta=40^\circ$  and  $50^\circ$ . Several investigators reported the presence of the broadening of peaks in their XRD results. Guilemany (2002) indicated that in the solidification process a part of the NiCr matrix solidifies with an amorphous or nanocrystalline structure because of the high cooling rate. Matthews (2003) also found similar peaks in his studies and he explained that the dissolution of carbide into the matrix and the consequent solidification of the super saturated matrix with gave rise to an amorphous background in the XRD spectrum.

### Oxide phases

In the SEM, around 1 $\mu$ m thick oxygen rich stringers (**O**) were identified in Fig 4.17. The XRD data showed the presence of Cr<sub>2</sub>O<sub>3</sub> in the as-sprayed coating as the only oxide phase. As mentioned in the literature (Kamnis, 2008), in the Met-Jet system the gas temperature can reach up to 3000K and the surface temperature of some fine particles with the size around 5  $\mu$ m can be heated up to 2000K. At this temperature

these small particles can easily form chromium oxide by oxidation of Cr present in the Ni(Cr) matrix.

In comparison several investigators (Table 2.4) reported the presence of Cr<sub>2</sub>O<sub>3</sub> as the only chromium oxide during spraying. Some of the researchers also proposed other oxide such as Cr<sub>3</sub>O<sub>4</sub> by Wirojanupatump (2001) and the NiCr<sub>2</sub>O<sub>4</sub> with spinel crystal structure reported by Edris (1997) and Matthews (2008). These oxide phases were not observed in this study.

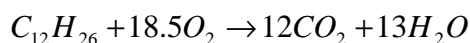
### 4.2.3 Mechanism of microstructure formation

#### 4.2.3.1 Melting and dissolution

In HVOF thermal spraying, the flame temperature is altered by the fuel quality and the oxygen to fuel ratio (O/F ratio). As mentioned before, in Kamnis' (2008) Met-Jet system model the gas temperature can reach up to 2750°C and the particles surface temperature can be from 1000°C to 1750°C depending on the particle size. In this work, during the whole deposition process sintered and agglomerated NiCr-Cr<sub>3</sub>C<sub>2</sub> powder was injected into the gun then heated, accelerated and deposited on the substrate forming a coating. Some particles such as the NiCr alloy can be fully molten due to the melting point at 1440°C. Whereas the carbide phase is likely to remain solid due to its higher melting point around 1820°C compared to that of the metal phase. Some Cr<sub>3</sub>C<sub>2</sub> particles (< 5 μm) will experience relatively higher temperature, albeit for shorter times, than larger ones. They will dissolve into the molten metallic (NiCr) phase forming a variety of contrasts (**G2** region) in the solidified coating. Fig 4.17 shows rounder edges of carbide particles (**G1**) indicating their partial dissolution which is schematically depicted in Fig 4.18. The thermodynamics of dissolution are governed by ternary phase diagram, where liquidus surface projection is shown in Fig 4.19. It is clear to observe that Cr<sub>3</sub>C<sub>2</sub> dissolves in the liquid metal to form liquid phases with the temperature from 1742 °C to 1829 °C.

#### 4.2.3.2 Oxidation during spraying

The formation of oxides of NiCr and carbide are expected in HVOF spraying because of the high temperature gaseous environment both during combustion and the free jet exhaust gas stream emerging from the nozzle. Fig 4.20 shows the relationship between oxygen flow and fuel flow (kerosene) ratio followed by the stoichiometric reaction for kerosene:



In this graph the oxygen/fuel stoichiometric line employed in this work (107% stoichiometric) was plotted which would lead to excess oxygen in the spray gun (7% excess O<sub>2</sub>) available to oxidise of the powder particles. Furthermore air would have been turbulently mixed into the exhaust gas jet as it left the gun which contributes to in-flight oxidation. The Ellingham diagram in Fig 2.23 which gives the data on standard free energies of formation of oxides shows that chromium is more likely to be oxidized than Ni and C below 1200 °C. However, because of the negative free energy slope in the C/CO reaction with temperatures, the stability of this reaction at temperature higher than 1200°C is greater than Cr and Ni oxide formation. Carbon can be oxidised to CO and escape from the alloy powder. It is hard to measure accurately and compare the C concentration before and after spraying by EDX but some investigators (Matthews, 2003) (Li, 2002) found carbon loss of in-flight particle and 25Ni(Cr)-75Cr<sub>3</sub>C<sub>2</sub> coating during HVOF spraying, as a result of CO or CO<sub>2</sub> formation.

#### **4.2.3.3 Solidification**

The microstructure of the HVOF thermal sprayed coating mainly depends on the powder particle solidification. A splat is formed from a molten droplet which strikes the substrate, flattens out and solidifies. The schematic diagram of splat formation is shown in Fig 4.21. The final shape of a splat is determined by droplet spreading and rate of solidification and the splat morphology also affects coating properties such as porosity. The rate of solidification during droplet deposition is unknown due to difficulties in in-situ measurements. But the solidification is influenced by droplet overheating, substrate temperature, thermal contact resistance, and thermo-physical properties of all relevant materials (Javad, 2002). Also in the present system the splat will be a two phase mixture of carbide and molten Ni(Cr) alloy.

During the deposition process shown schematically in Fig 4.22, because of the high cooling rate about 10<sup>7</sup> K.s<sup>-1</sup> (Moreau, 1992) after hot particles have arrived at the substrate, the solidification process of each splat leads to strong non-equilibrium

solidification of the liquid (Ni, Cr, C) phase. The possible phases present following impact and solidification include: chromium carbides (mainly Cr<sub>3</sub>C<sub>2</sub>), chromium oxide (Cr<sub>2</sub>O<sub>3</sub>), metal rich crystalline (NiCr) and amorphous phases (Ni Cr C) as shown schematically in Fig 4.23. As described above, a schematic depiction of NiCr-Cr<sub>3</sub>C<sub>2</sub> powder coating build-up process in HVOF thermal spray is shown in Fig 4.24.

**Table 4.1** EDX analysis results for average compositions (4 measurements) of different phases of polished Cr<sub>3</sub>C<sub>2</sub>-25NiCr agglomerated and sintered powder from Praxair

Region	Phase composition (at%)		
	Cr	Ni	C
<b>C</b> (dark area)	59.8±2.7	--	40.2±4.1
<b>M</b> (bright area)	16.0±1.8	84.0±2.1	--

**Table 4.2** Spray parameters of each HVOF thermal spray experiments.

Parameters	Metallisation	Praxair
Oxygen flow (L/min)	900	900
Fuel flow (mL/min)	435	435
Chamber pressure (Bar)	7.4	7.4
Nozzle length (mm)	100	100
Spray distance (mm)	355	355
Powder port	Twin	Twin
Gas flow (Ltr/Min)	4	6
Powder feed (R.P.M)	253	300
Vibrator amplitude	50	50
Numbers of passes	26	30

**Table 4.3** EDX (Cobalt standard) results for average compositions (4 measurements ) of 25Ni(Cr)-75Cr<sub>3</sub>C<sub>2</sub> agglomerated and sintered Metallisation powder coating

Region	Phase composition (at%)		
	Cr	Ni	C
Whole area 20x20 μm	45±1.8	18±2.1	37±4.8
C (dark area)	56±2.3	1±0.2	43±5.0
M (bright area)	23±1.9	74±3.9	3±1.0
G (grey area)	41±3.1	29±2.8	30±3.1

**Table 4.4** EDX (Cobalt standard) results for average compositions (4 measurements) of the 25Ni(Cr)-75Cr<sub>3</sub>C<sub>2</sub> agglomerated and sintered Praxair powder coating

Region	Phase composition (at%)			
	Cr	Ni	C	O
Whole area 20x20 μm	43±2.9	21±1.1	36±2.3	---
C (dark area)	55±2.8	1±0.2	44±4.9	---
M (bright area)	20±1.2	76±3.5	4±1.2	---
G1 (grey area)	53±2.4	9±1.3	38±3.2	
G2 (grey area)	48±3.1	30±1.8	22±3.6	---
O (Dark layer)	30±2.3	5±0.8	---	65±3.1

**Table 4.5** Summary of the characterisations of the coatings sprayed from Metallisation and Praxair powder

	Metallisation powder coating	Praxair powder coating
Thickness (μm)	200±3	400±4
Porosity (%)	1.8±0.8	3.2±1.1
Microhardness (HV <sub>300</sub> )	829±48	1067±44
Deposition efficiency (%)	25	37.3
Phases in coating	Ni(Cr), Cr <sub>3</sub> C <sub>2</sub> , Cr <sub>2</sub> O <sub>3</sub>	Ni(Cr), Cr <sub>3</sub> C <sub>2</sub> , Cr <sub>2</sub> O <sub>3</sub>

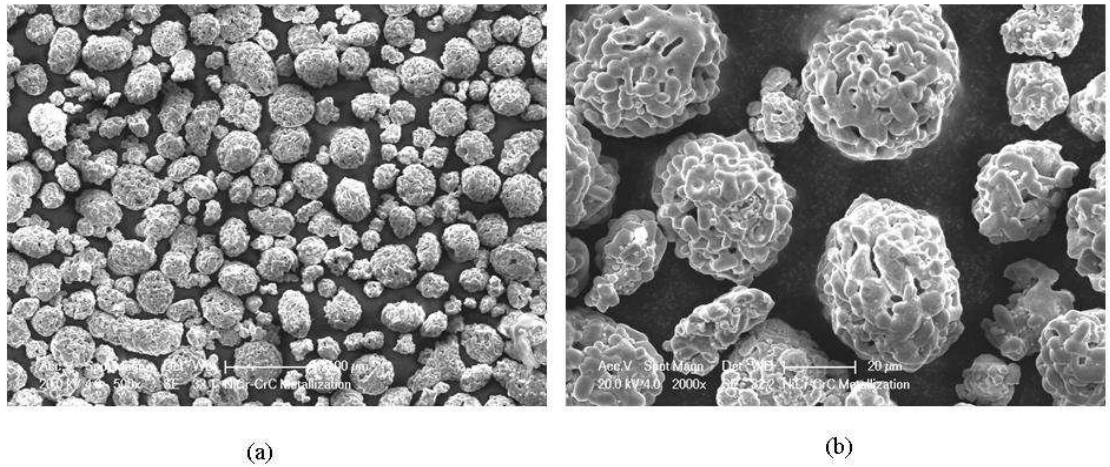


**Fig.4.1** Morphology of 25NiCr-Cr<sub>3</sub>C<sub>2</sub> agglomerated and sintered powder from Metallisation by SEM

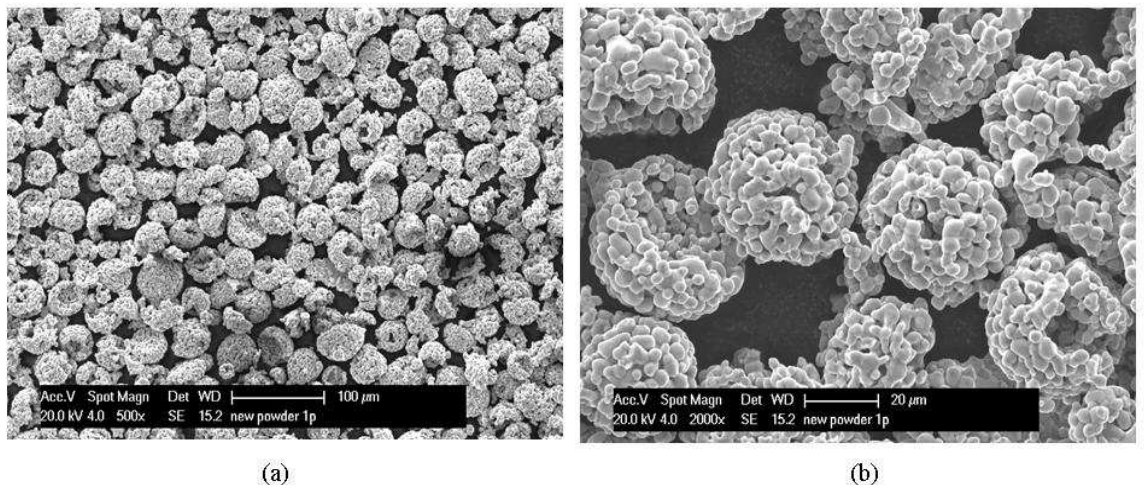


**Fig.4.2** Morphology of 25NiCr-Cr<sub>3</sub>C<sub>2</sub> agglomerated and sintered powder from Praxair by SEM

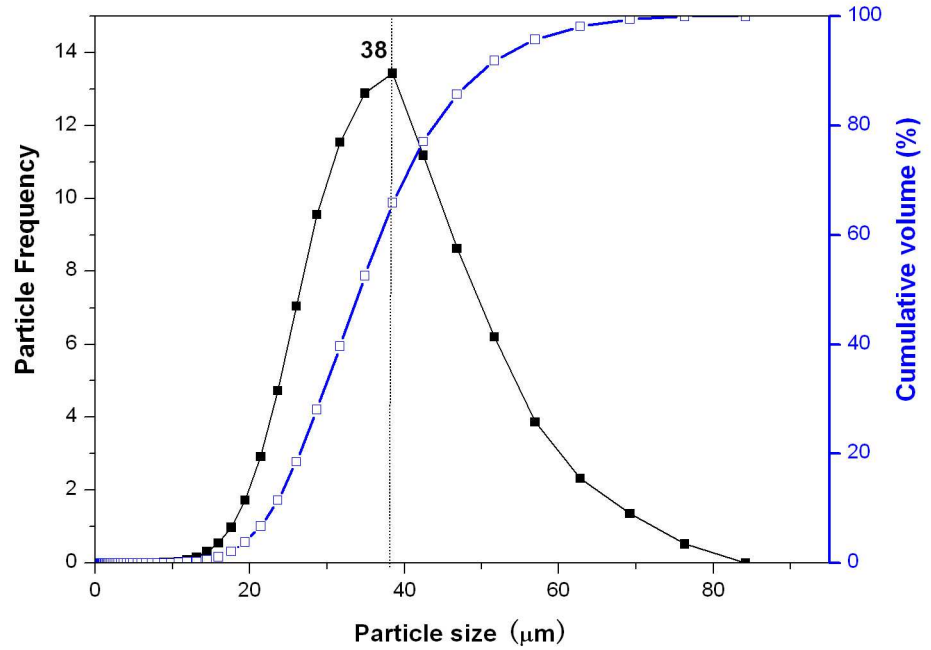


**Fig.4.3** Particle size distribution of 25NiCr-Cr<sub>3</sub>C<sub>2</sub> agglomerated and sintered powder from Metallisation by laser diffraction analysis

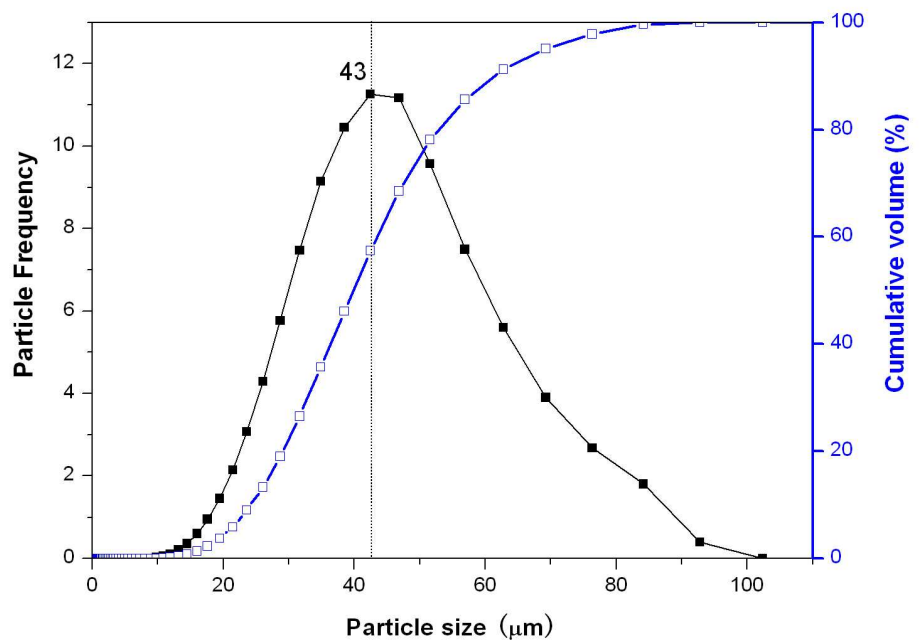


**Fig.4.4** Particle size distribution of 25NiCr-Cr<sub>3</sub>C<sub>2</sub> agglomerated and sintered powder from Praxair by laser diffraction analysis

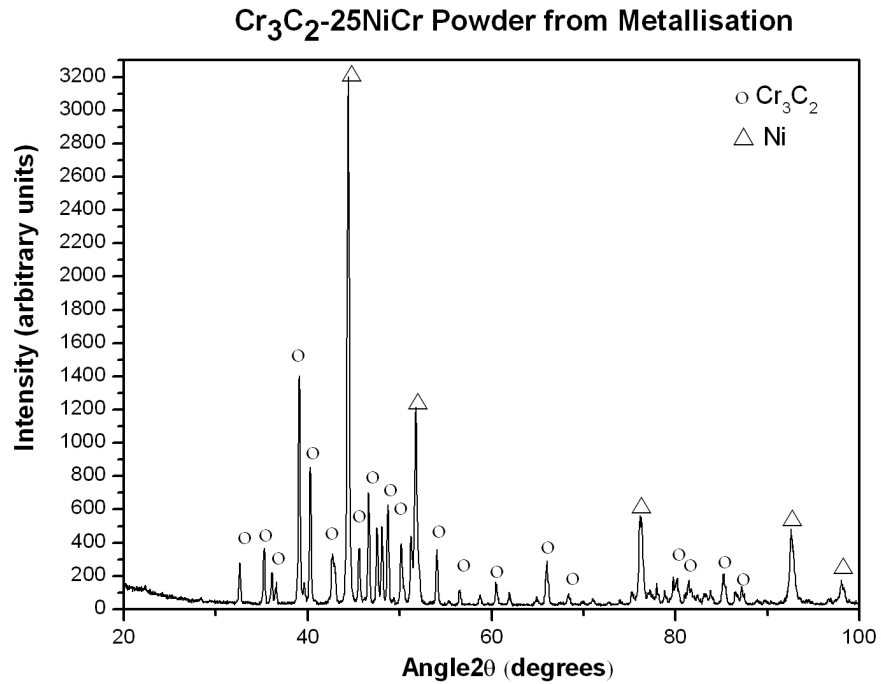


**Fig.4.5** X-ray diffraction diagram of 25NiCr-Cr<sub>3</sub>C<sub>2</sub> agglomerated and sintered powder from Metallisation (20° to 100°) (Provided in appendix)

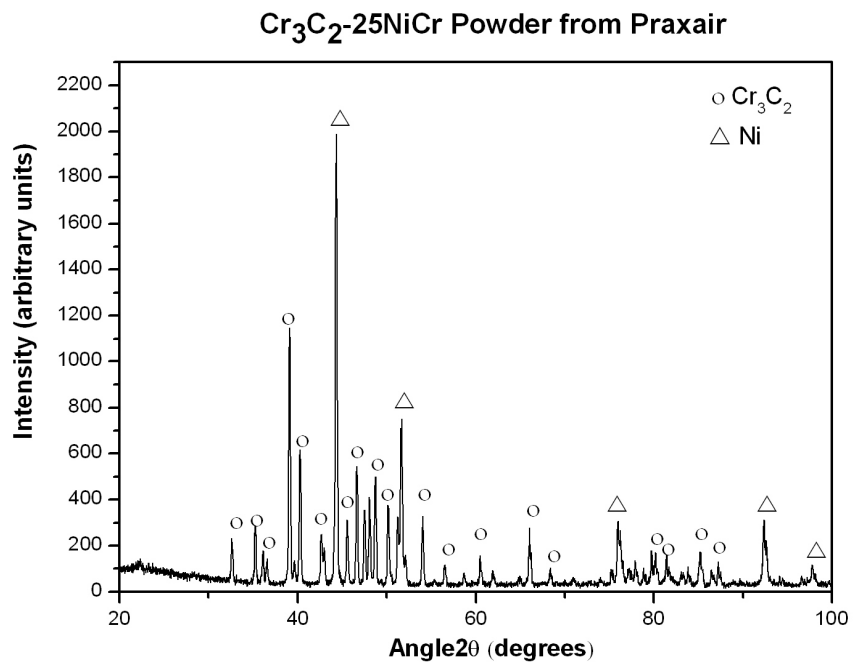


**Fig.4.6** X-ray diffraction diagram of 25NiCr-Cr<sub>3</sub>C<sub>2</sub> agglomerated and sintered powder from Praxair (20° to 100°) (Provided in appendix)

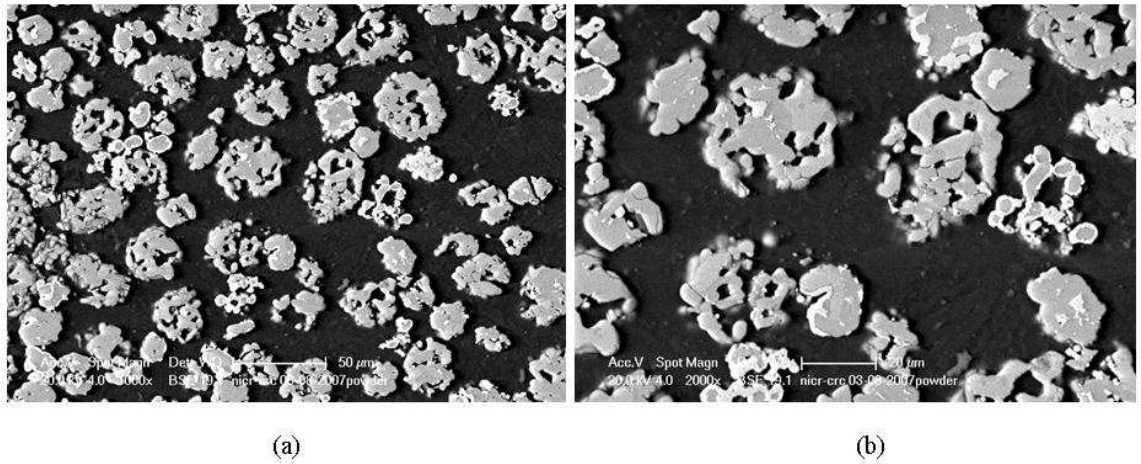


**Fig.4.7** Morphology of 25NiCr-Cr<sub>3</sub>C<sub>2</sub> agglomerated and sintered powder from Metallisation by backscattered electron image-SEM

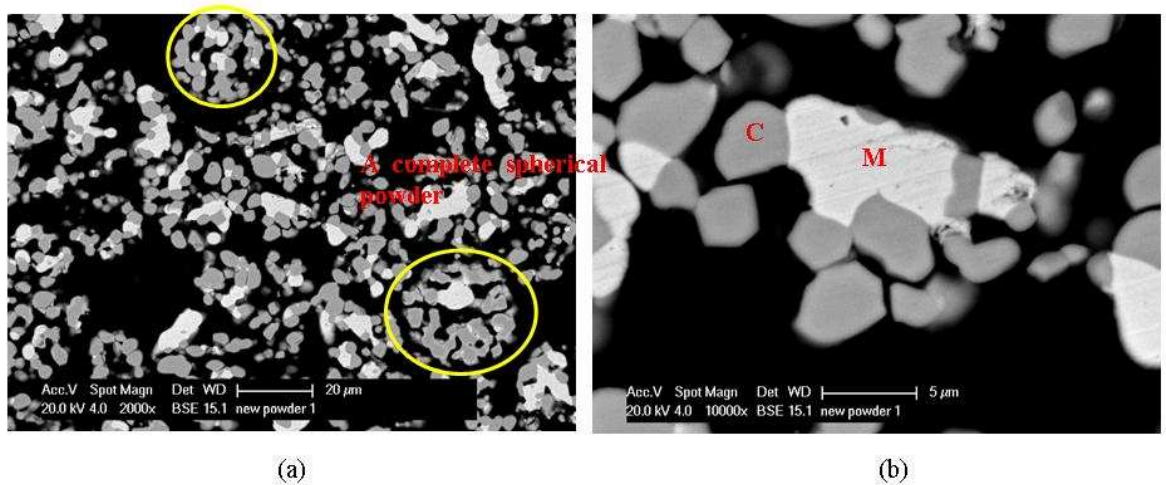


**Fig.4.8** Morphology of 25NiCr-Cr<sub>3</sub>C<sub>2</sub> agglomerated and sintered powder from Praxair by backscattered electron image-SEM

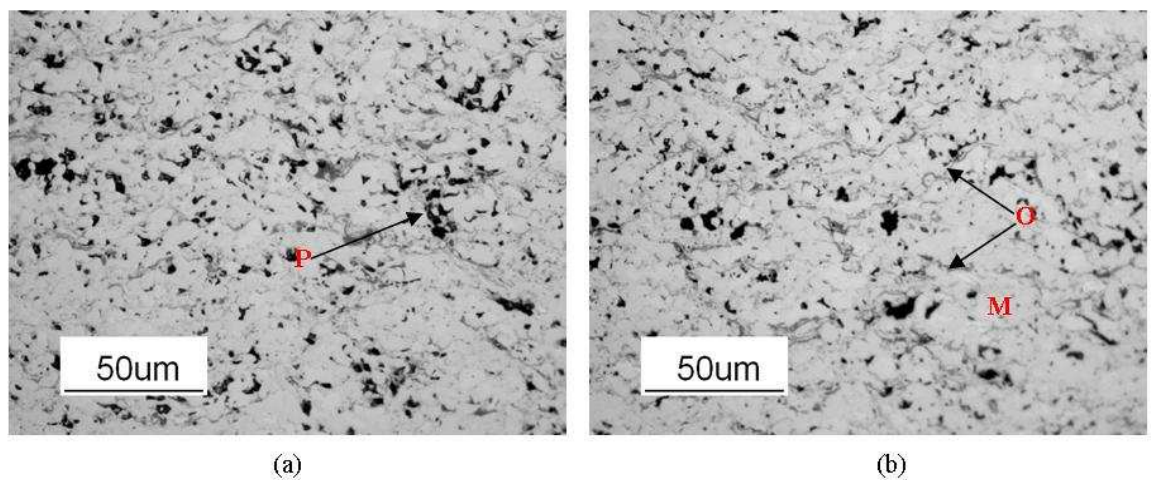


**Fig 4.9** Optical micrograph of the polished, cross-sectioned as-sprayed 25NiCr-Cr<sub>3</sub>C<sub>2</sub> coating from Metallisation powder

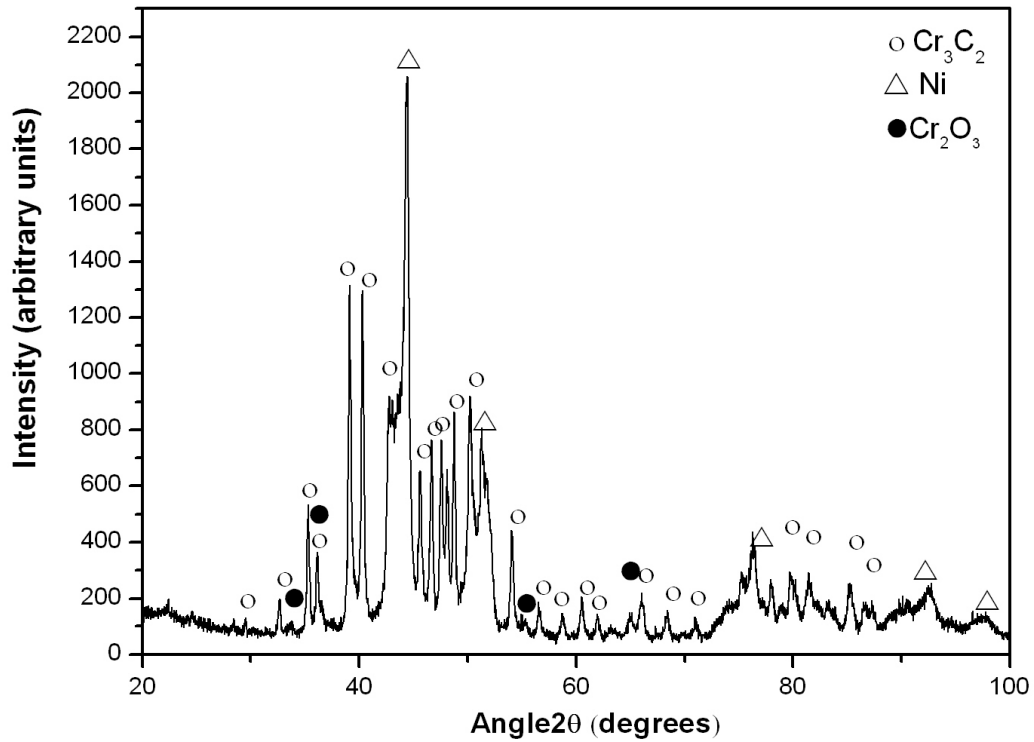
As-sprayed Cr<sub>3</sub>C<sub>2</sub>-25NiCr Metallisation powder coating

Fig 4.10 X-ray diffraction pattern of agglomerated and sintered powder as-sprayed coating from Metallisation (20° to 100°)

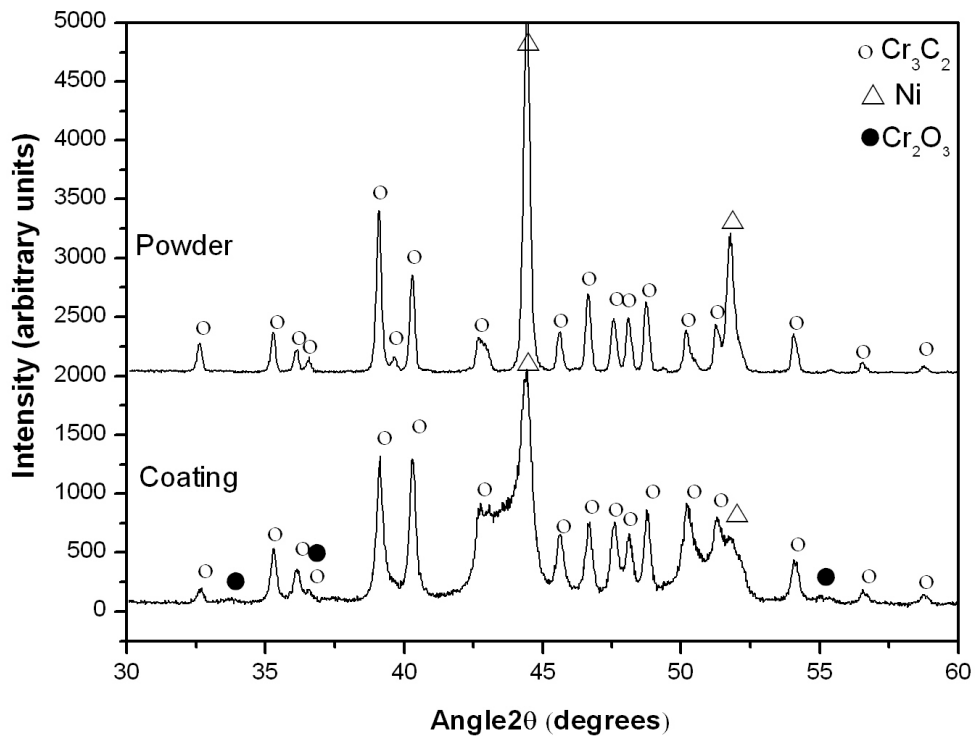
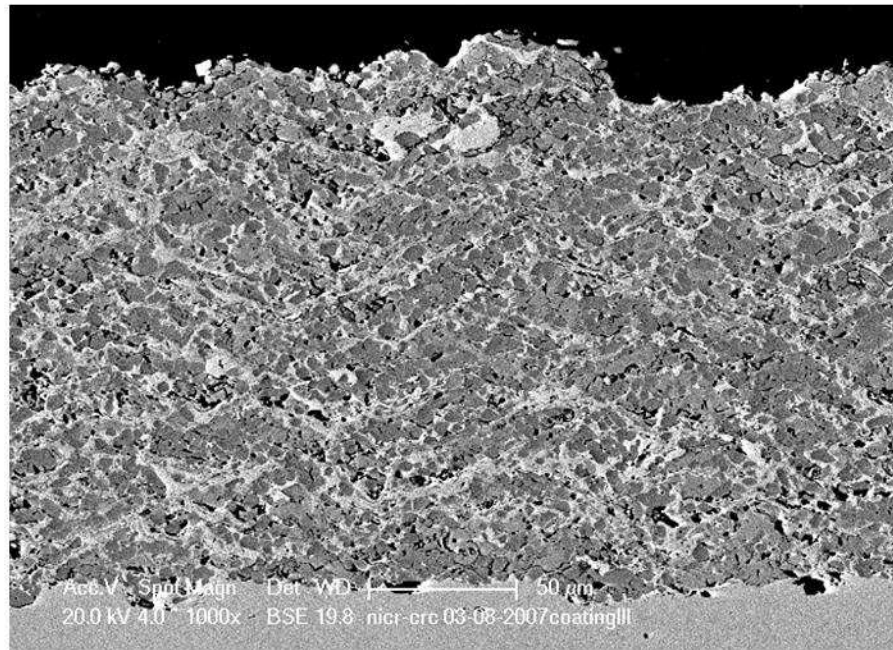
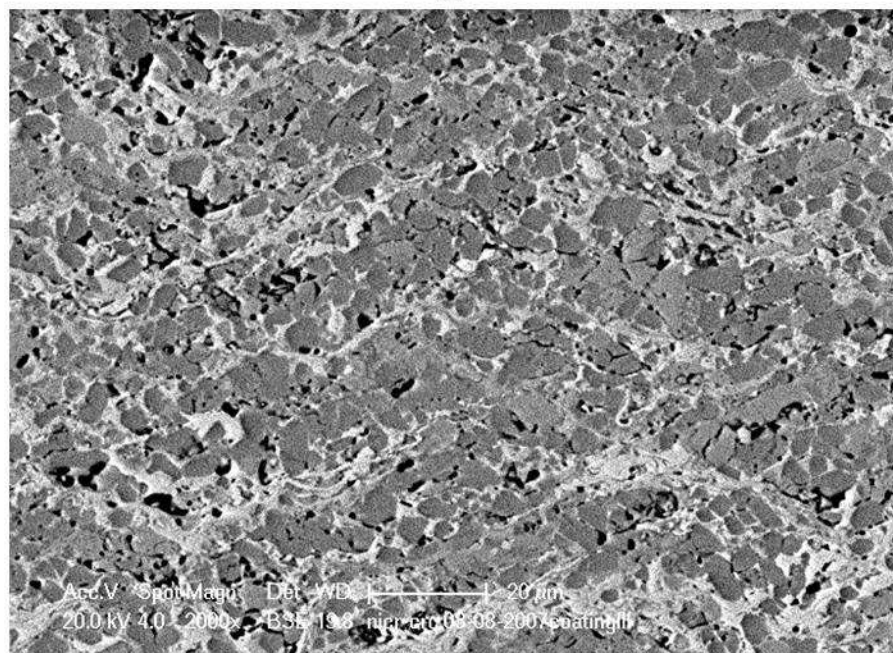


Fig 4.11 X-ray diffraction pattern of NiCr-Cr<sub>3</sub>C<sub>2</sub> agglomerated and sintered powder from Metallisation compared with its as-sprayed coating (30° to 60°)

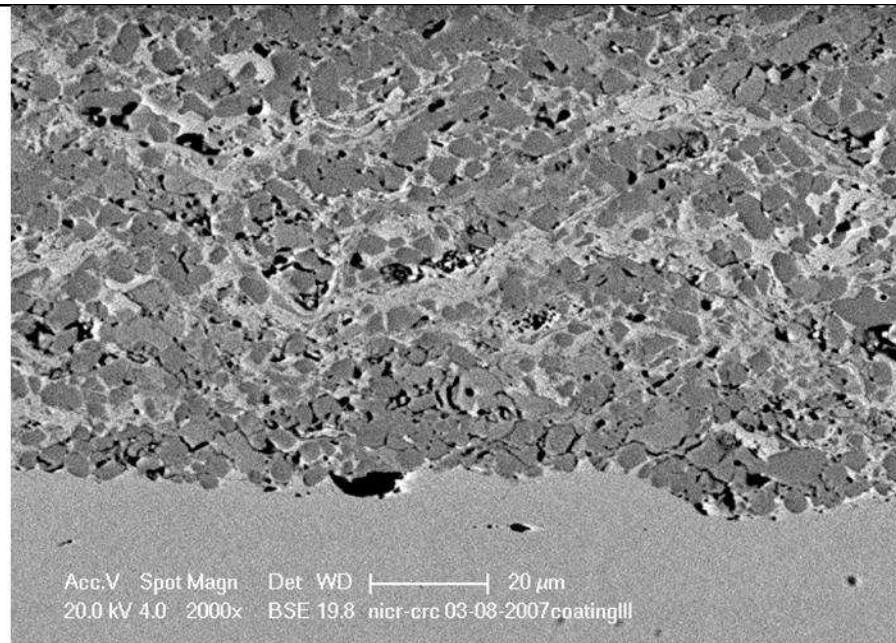


(a)

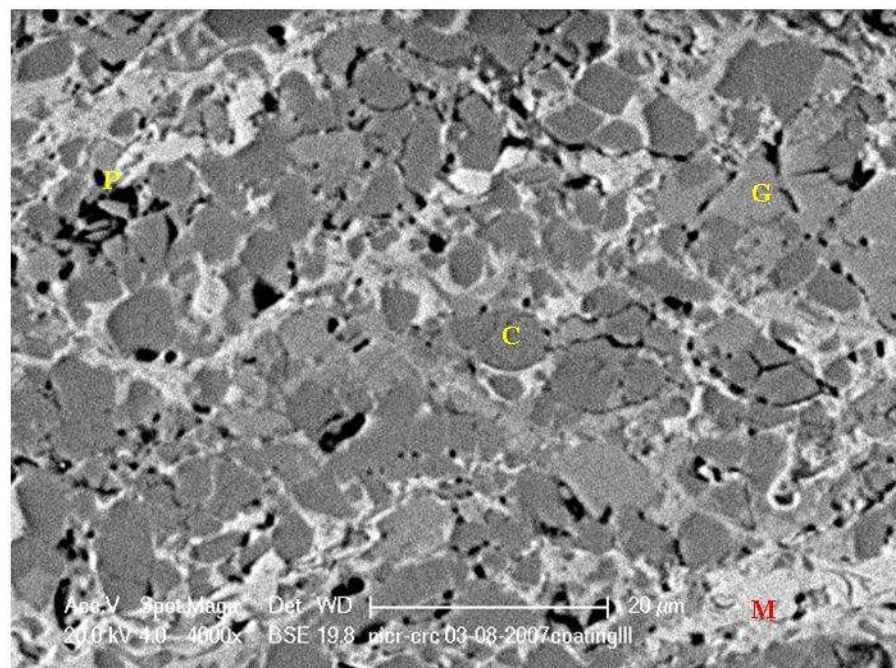


(b)

**Fig 4.12** Backscattered electron image-SEM show cross-section of 25Ni(Cr)-75Cr<sub>3</sub>C<sub>2</sub>  
(Metallisation) powder coating at different magnifications



(c)



(d)

**Fig 4.12** (continued) Backscattered electron image-SEM show cross-section of 25Ni(Cr)-75Cr<sub>3</sub>C<sub>2</sub> (Metallisation) powder coating at different magnifications

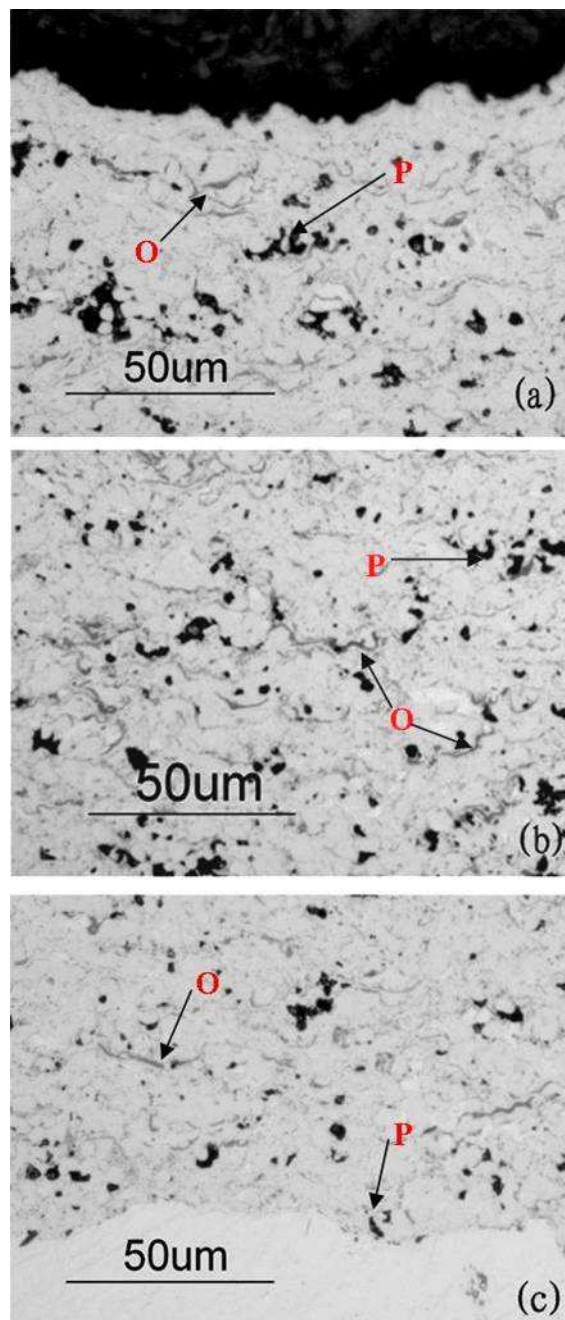


**Fig.4.13** Optical micrograph of the polished, cross-sectioned as-sprayed NiCr-Cr<sub>3</sub>C<sub>2</sub> coating from Praxair powder (a) top surface (b) middle and (c) coating/substrate interface

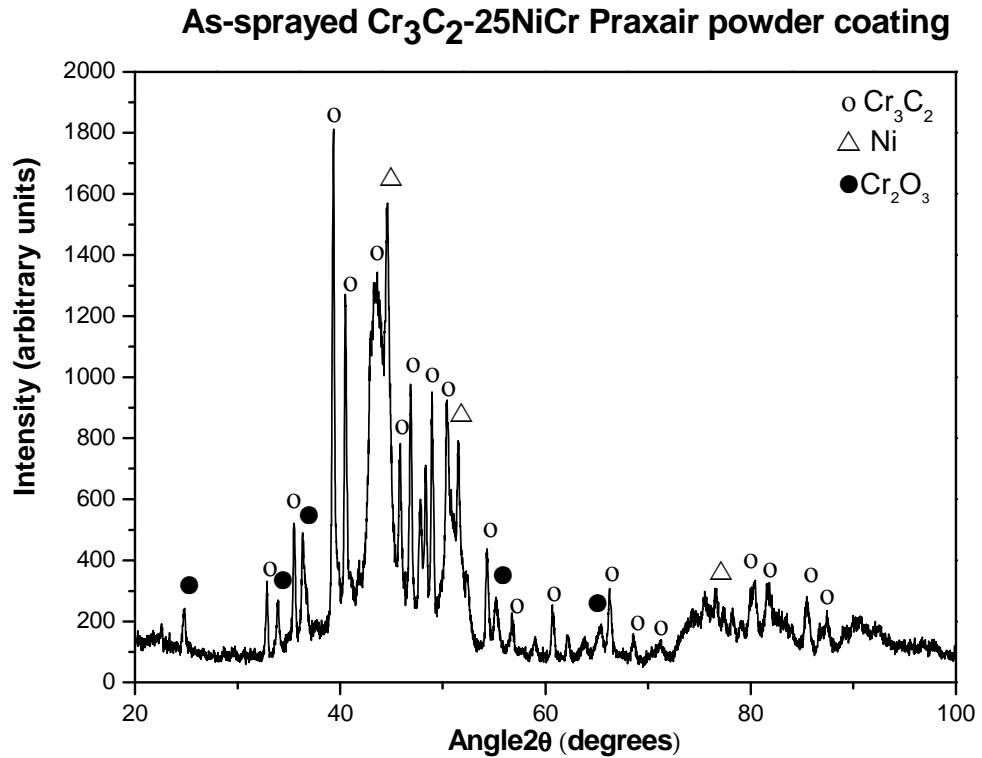


**Fig.4.14** X-ray diffraction pattern of agglomerated and sintered powder as-sprayed coating from Praxair (20° to 100°)

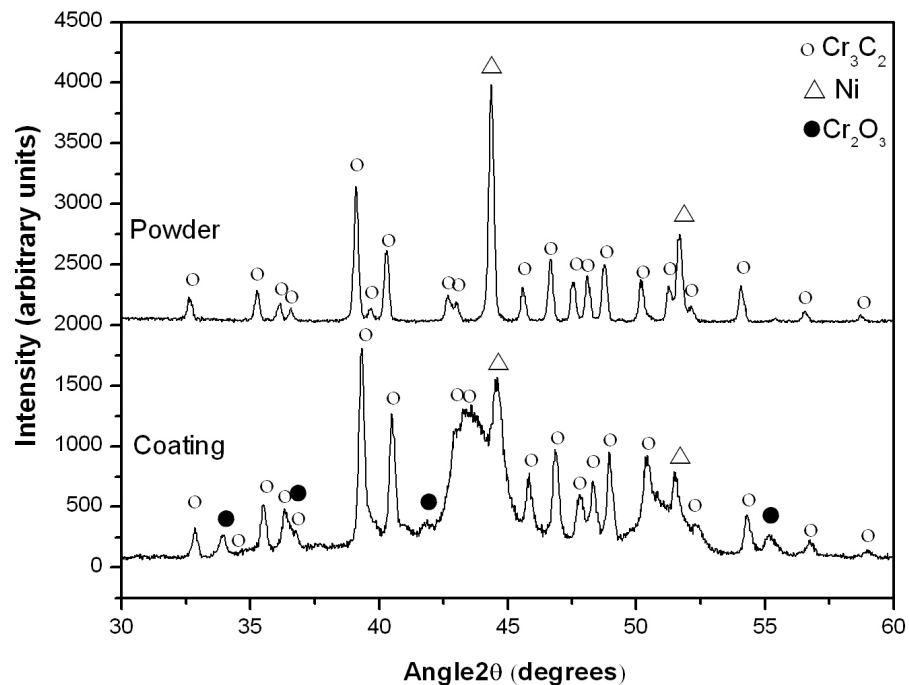
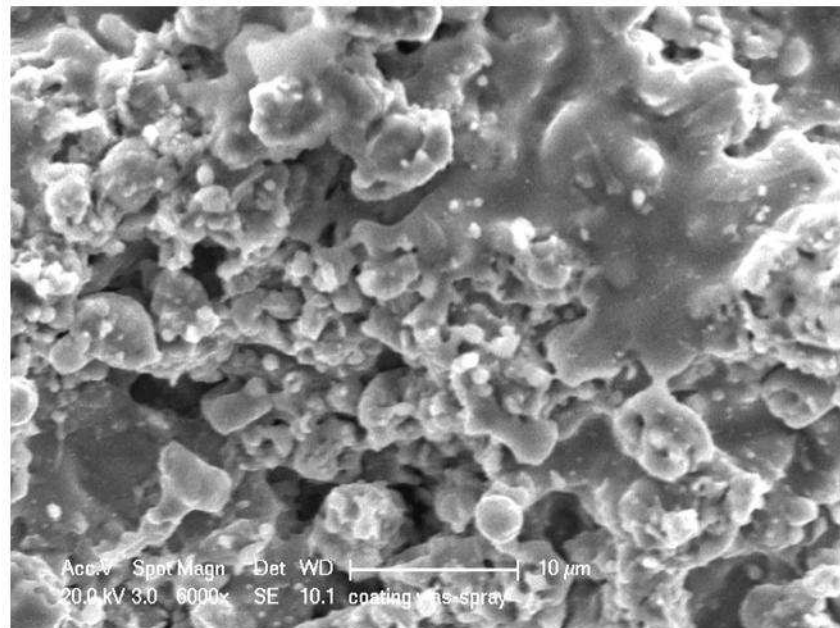
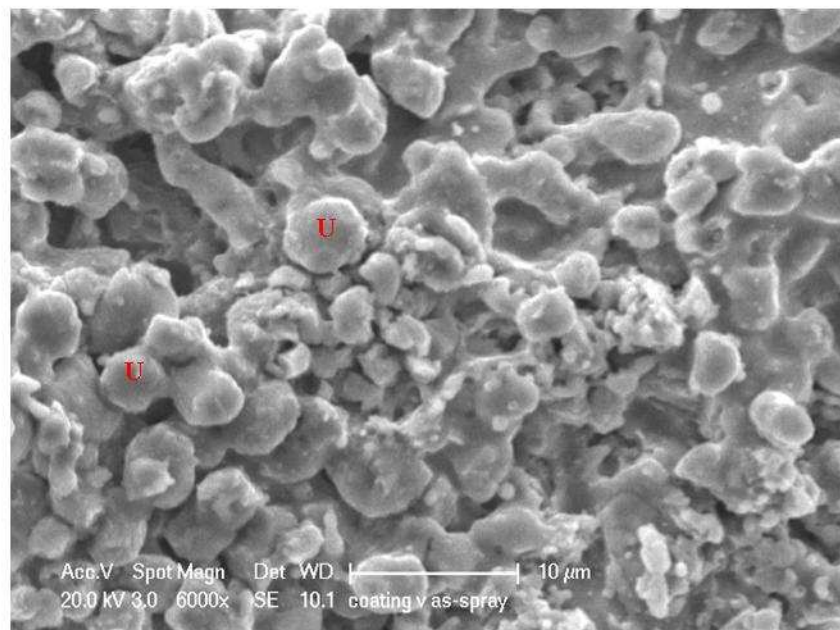


**Fig.4.15** X-ray diffraction pattern of NiCr-Cr<sub>3</sub>C<sub>2</sub> agglomerated and sintered powder from Praxair compared with its as-sprayed coating (30° to 60°)

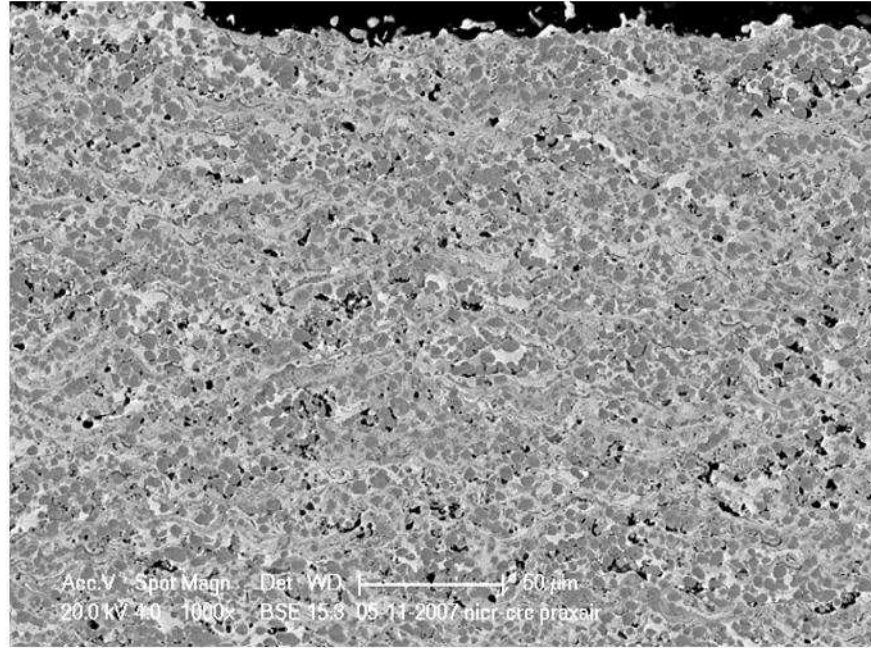


(a)

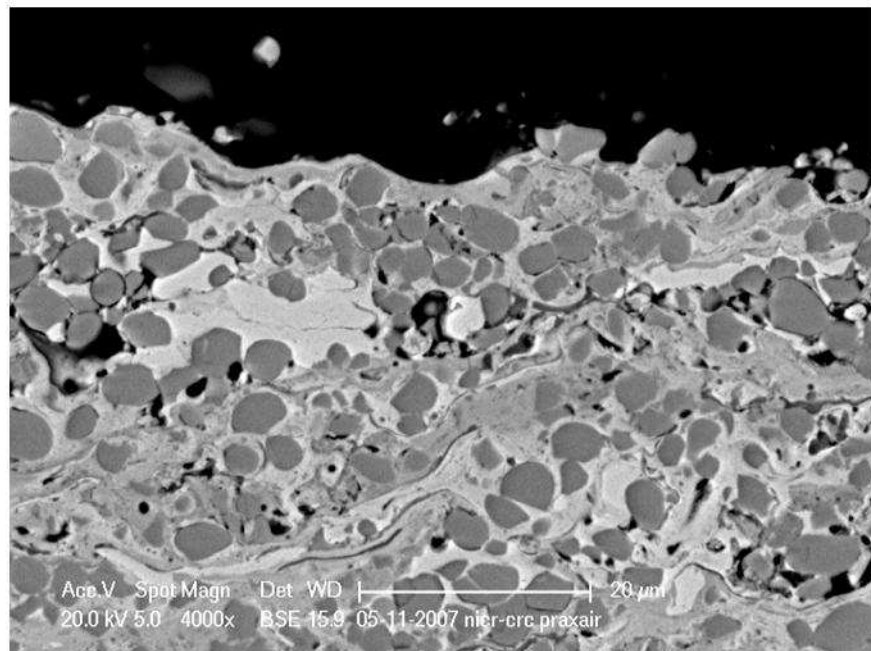


(b)

**Fig.4.16** SEM micrographs show surface topography of Praxair NiCr-Cr<sub>3</sub>C<sub>2</sub> agglomerated and sintered powder coating

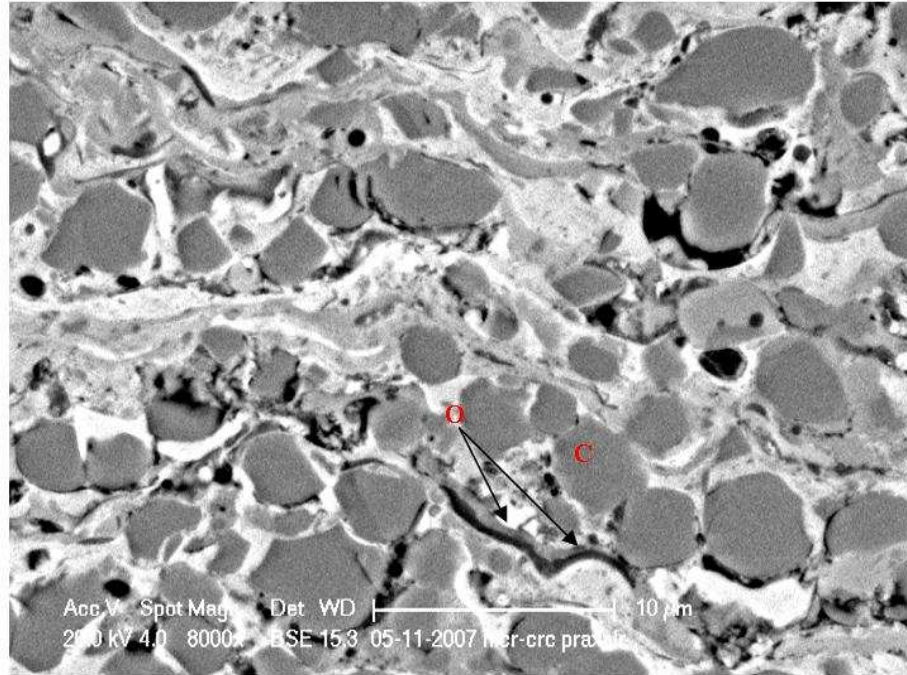


(a)

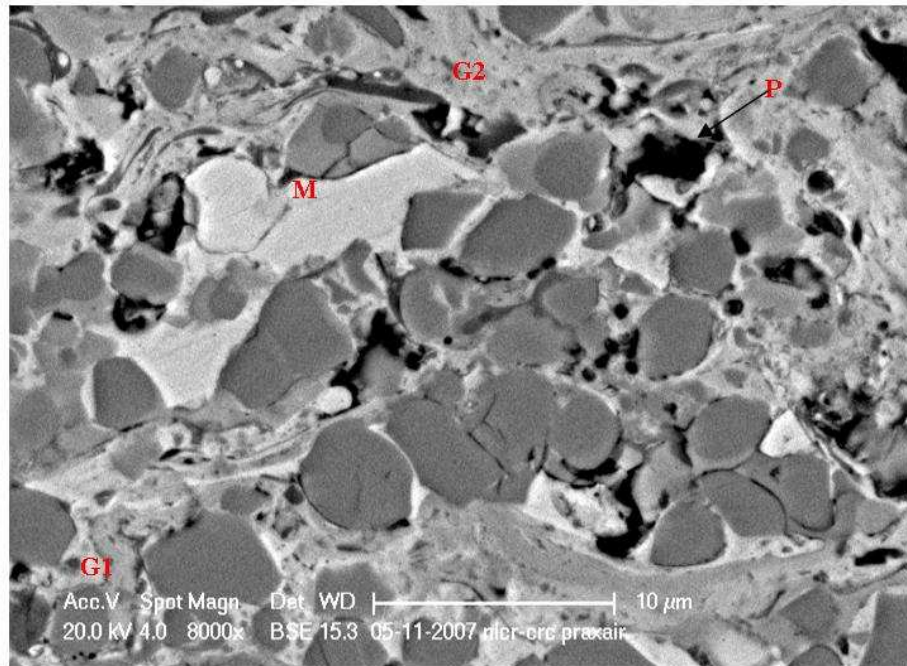


(b)

**Fig.4.17** Backscattered electron image-SEM show cross-section of NiCr-Cr<sub>3</sub>C<sub>2</sub> agglomerated and sintered (Praxair) powder coating



(c)



(d)

**Fig.4.17** (continued) Backscattered electron image-SEM show cross-section of NiCr-Cr<sub>3</sub>C<sub>2</sub> agglomerated and sintered (Praxair) powder

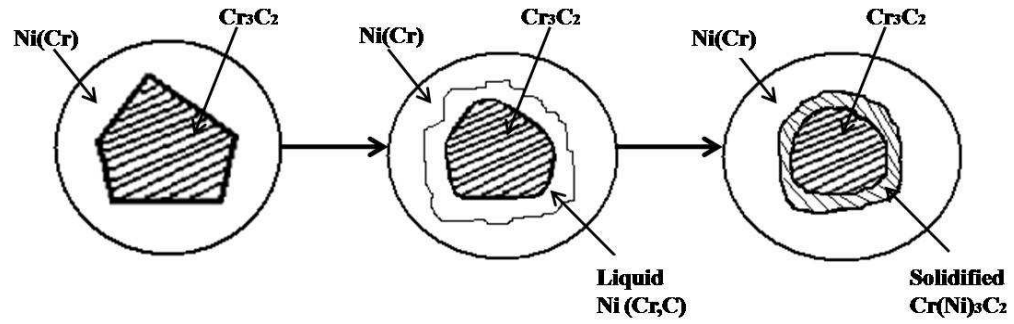


Fig 4.18 Schematic diagram of the dissolution of chromium carbide (Cr<sub>3</sub>C<sub>2</sub>)

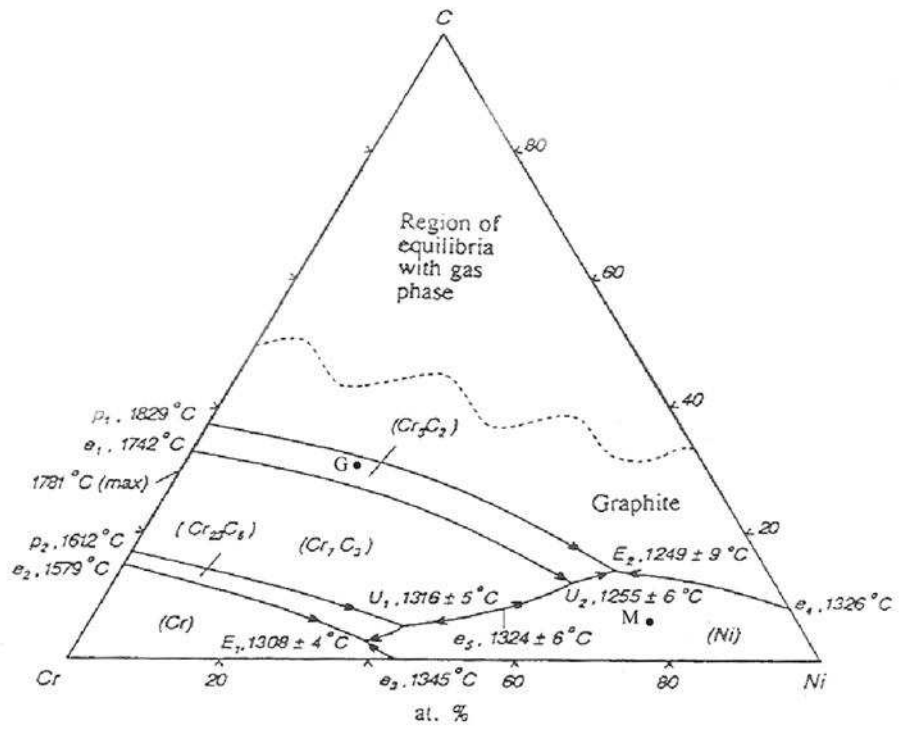


Fig 4.19 Projection of the liquidus surface of the Cr-Ni-C system

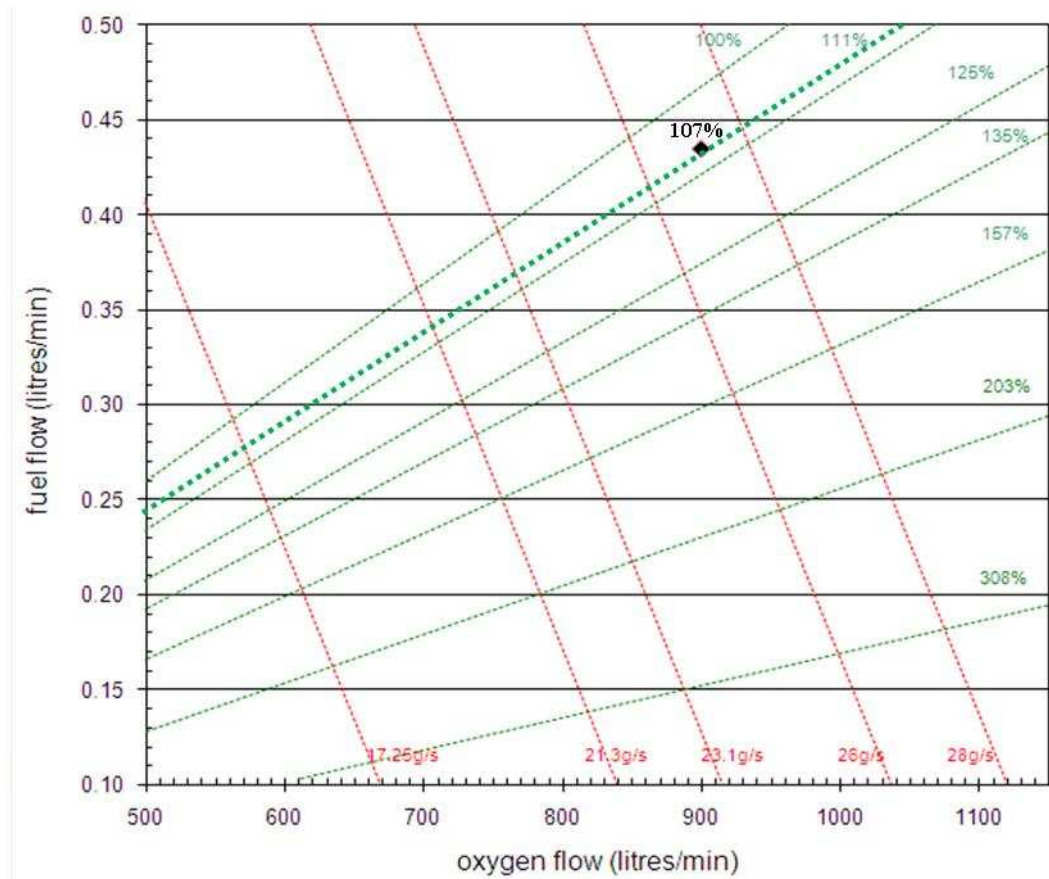


Fig 4.20 Oxygen and Kerosene ratio graph in HVOF Met-Jet thermal spray system (Red dash lines are total weight input lines; Green dash lines are stoichiometric lines)

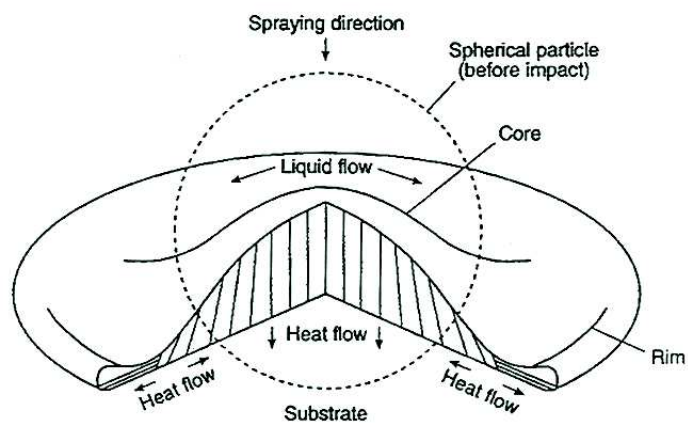


Fig 4.21 Schematic diagram of the solidification and microstructure development of a single splat (Herman & Sampath, 1996)

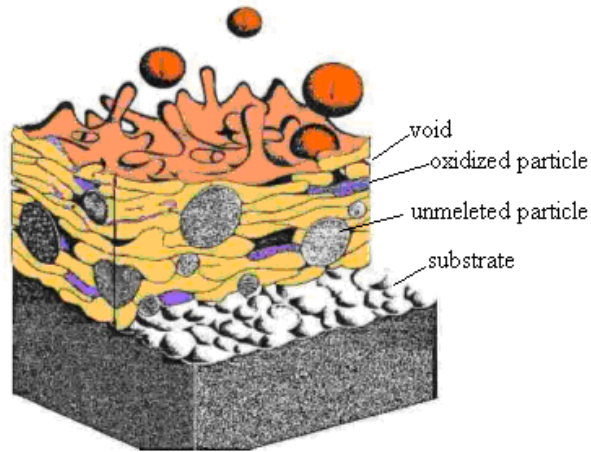


Fig 4.22 Schematic diagram of HVOF metal coating deposition process (Herman, 1988)

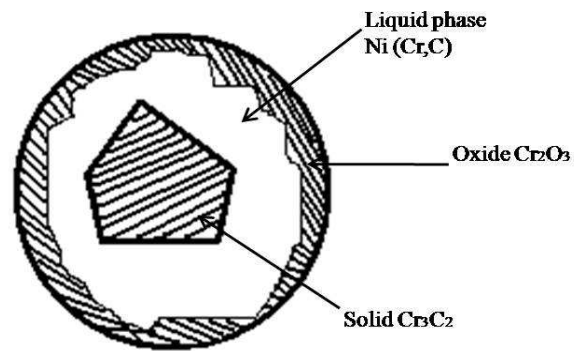


Fig 4.23 Schematic diagram of powder particle before arriving at the substrate.

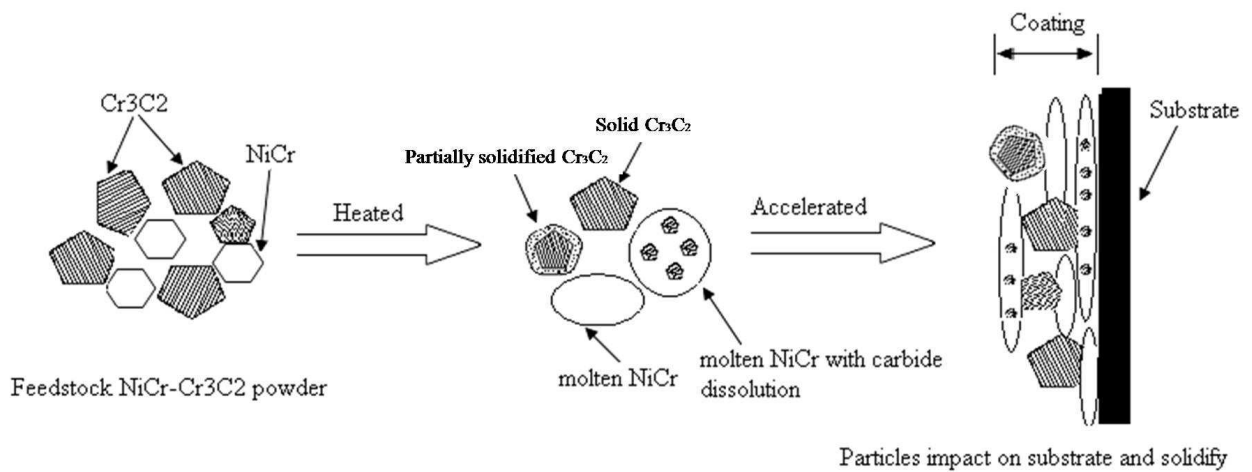


Fig 4.24 A schematic depiction of NiCr-Cr<sub>3</sub>C<sub>2</sub> coating build-up process in HVOF thermal spray.

## **Chapter 5: Effect of elevated temperature exposure on Ni(Cr)-Cr<sub>3</sub>C<sub>2</sub> coated stainless steel: Results and Discussion**

### **5.1 Results**

#### **5.1.1 Introduction**

NiCr-Cr<sub>3</sub>C<sub>2</sub> thermal spray coatings are extensively used for a wide range of industrial applications due to their properties such as high hardness and good wear resistance at high temperatures or in aggressive environments. Hence, the purpose of the work reported in this chapter was to investigate the thermal stability of NiCr-Cr<sub>3</sub>C<sub>2</sub> coated stainless steel.

The characterisation of the as-received and heat treated 304 stainless steel, used as the substrate for coating deposition, will be introduced first in this chapter. The aim of this work was to analyse the effect of elevated temperature exposure on the bulk 304 stainless steel and to better understand the relationship between the observed changes in microstructure and microhardness. The response of the 304 stainless steel was assessed following heating for various times at 700°C and 800°C in air. These results are used to provide a reference for comparison with annealed coated stainless steel substrates which were heated in air to 700 + 800°C for various times.

The characterisation of heat treated NiCr-Cr<sub>3</sub>C<sub>2</sub> coated samples will be described in a following section with the variation in coating and substrate microstructures characterised and correlated with the variation in microhardness. The main purpose of this work was to investigate how the as-sprayed microstructures change as a result of exposure to elevated temperatures and to better understand the relationship between the observed changes in microstructure and hardness. The changes were assessed after exposure at 700°C and 800°C for periods from 1 hour up to 16 days in air.

This chapter also describes changes which occurred in the stainless steel substrate as a result of high temperature inter-diffusion between the coating and the substrate. The characteristics of these microstructural changes were studied by SEM-EDX, XRD analysis and microhardness variation. Specifically, the changes which occurred with distance from the interface from the coating were investigated.

## **5.1.2 Characterisation of as-received and heat treated 304 stainless steel**

### **5.1.2.1 Characterisation of 304 stainless steel material**

The material used as substrate for spray deposition was 304 stainless steel in the form of sheet 2 mm thick. Apart from the near surface, the 304 alloy was two phase ( $\gamma + \alpha$ ) with a composition, analysed by EDX-SEM, as shown in Table 5.1. The compositions of the as-received 304 stainless steel provided by the supplier are shown in Table 3.2. The stainless steel had an equiaxed grain structure and a microhardness of  $229.5 \pm 1.2 H_{v100}$ . However, the samples which were used for spray deposition were prepared by grit blasting. The effect of this was to modify the microhardness near the surface as shown in Fig 5.1a. This figure shows three rows of the microhardness indents at the top grit blasted surface, the mid-plane and the bottom as-received surface. Clearly, grit blasting significantly increased the surface hardness.

XRD of the as-received 304 stainless steel surface revealed that the structure comprised the face centred cubic  $\gamma$  phase and the body centred cubic  $\alpha$  phase as shown by the peaks at  $2\theta = 43.65^\circ$  and  $2\theta = 44.69^\circ$  in Fig 5.2a. XRD of the grit blasted surface shows a large peak due to reflection from  $\alpha'$  martensite phase with the expected strong austenite phases ( $\gamma$ ) peaks in Fig 5.2b. This two phase structure, in nominally austenitic steel, has been observed previously (Burstein, 2000) and is a well known effect of surface deformation. The X-ray diffraction pattern for the grit blasted surface after annealing at  $750^\circ\text{C}$  for 20 minutes followed by oil quenching shows the loss of the peak due to the  $\alpha'$  martensite phase at  $2\theta = 44.69^\circ$  in Fig 5.2c. The XRD pattern of the annealed surface at  $750^\circ\text{C}$  for 20 minutes with air cooling shows a decrease of the peak from the  $\alpha'$  martensite phase at  $2\theta = 44.69^\circ$ , and an increase of the peak from  $\gamma$  austenite phase in Fig 5.2d which is similar to the XRD pattern of as-received 304 stainless steel shown in Fig 5.2a. This martensitic phase

generated by grit blasting can be reduced by a thermal annealing procedure at 750°C for 20 minutes.

### **5.1.2.2 Heat treated stainless steel substrate**

Substrate samples were annealed for various times at 700°C and 800°C in order to provide a reference for comparison with coated samples which were annealed. These annealing treatments had a number of effects as set out below:

#### **Surface $\gamma/\alpha$ phases and oxide**

The XRD traces from the top surfaces of samples after heat treatment at 700°C and 800°C for 2 days followed by air cooling are shown in Fig 5.3 along with the XRD trace taken from grit blasted stainless steel 304 in Fig 5.3a. The XRD traces from the top surface of the heat treated samples Fig 5.3 b and c show several strong Cr<sub>2</sub>O<sub>3</sub> peaks at  $2\theta=33.59^\circ$  and  $2\theta=36.19^\circ$ . On the other hand,  $\alpha'$  martensitic phase from Fig 5.3a shows a gently decreasing intensity while the  $\gamma$  phase grows relatively in intensity with increasing time and temperature. The XRD traces indicate that the longer the exposure time and higher temperature the greater chromium oxide thickness on the top surface. Additionally, some weak peaks which might be chromium-rich carbides M<sub>23</sub>C<sub>6</sub> are found from the XRD trace of the 800°C annealed sample. These M<sub>23</sub>C<sub>6</sub> peaks are highlighted in Fig 5.3.

#### **Microstructures**

Fig 5.4 shows the grain structure of as-received 304 and 304 following 2 days annealing at 800°C followed by air cooling. There are optical micrographs of the specimens polished and etched using 12ml nitric acid and 35ml hydrochloric acid solution in 53ml H<sub>2</sub>O. Many of the grains in the as-received stainless steel 304 contain twins. In heat treated specimens, there was no effect on grain size but the frequency of carbide precipitates increased along the grain boundaries with increasing exposure temperature at 800°C.

**Microhardness measurements**

The microhardness of as-received and heat treated samples was measured using a 100 g load with a Vickers indenter and obtained from ten indents along a line parallel to the surface and in the middle of the sheet. The microhardness of these samples was also measured at approximately 5µm away from the grit blasted surface in an identical manner. The values obtained are given in Fig 5.6. The hardness measured near the grit blasted surface (Fig 5.6a) shows a higher value than the hardness measured in the middle of the bulk (Fig 5.6b) which is due to the mechanical deformation by grit blasting. The microhardness measured near the grit blasted surface shows a rapid reduction in the first hour of heat treatment. With continued exposure the hardness decreases gradually. The microhardness measured in the middle of the bulk decreased in the initial period of the heat treatment and slowly increased after 2 days treatment. Thermal treatment at 700°C generated consistently harder 304 than at 800°C. The time temperature and transformation diagram in Fig 5.5 shows that the austenite stainless steel 304 (with max 0.08% C) forms M<sub>23</sub>C<sub>6</sub> precipitates at both 700 and 800°C after one hour annealing followed by furnace cooling. Coarsening of these carbide precipitates is produced during annealing which has been considered as the most notable effects of hardness loss. As the diffusivity of carbon atoms in the iron based matrix is higher at higher temperatures, a sample heat treated at 800°C will give a faster coarsening process and form a larger size but lower amount of carbide precipitates in matrix and boundary than the sample heat treated at 700°C. Hence the samples heat treated at 700°C containing a larger amount of finer precipitates in matrix shows higher hardness values than at 800°C.

### **5.1.3 Characterisation of Ni(Cr)-Cr<sub>3</sub>C<sub>2</sub> coating following high temperature exposure**

#### **5.1.3.1 Introduction**

The purpose of this section of work was to look at the long-term evolution of NiCr-Cr<sub>3</sub>C<sub>2</sub> coatings in terms of microhardness and microstructure and to better understand the response of these coatings to elevated temperature exposure. In this work, coatings were heat treated at 700°C and 800°C in air, for times of 1 hour, 2 days 8 days and 16 days. The variation in microstructures and the correlation with the variation in microhardness and interfacial integrity will be described.

#### **5.1.3.2 Exposure at 700°C in air**

##### **Optical Microscopy**

Specimens of as-polished, cross-sectioned NiCr-Cr<sub>3</sub>C<sub>2</sub> coatings were examined by optical microscopy. Fig 5.7 shows the microstructures observed in the middle of the coatings which were annealed at 700°C for times ranging from 1 hour up to 16 days. In Fig 5.7 some pores (P) and layered structures (O) which are probably bands of oxide present are arrowed. Comparing these four images taken from different heating times, it is difficult to see an obvious change in oxide layers. However, the porosity showed a rapid growth in the middle of the coating with continued exposure. In addition, the formation of oxides and microstructural features at the interface of cross-sectioned coatings are shown in Figs 5.8 and 5.9. The microstructures of the original as-sprayed NiCr-Cr<sub>3</sub>C<sub>2</sub> coating are also provided as a reference for comparison with these annealed coating samples. It is hard to identify any oxide layer on the coating surface before heat treatment. In Fig 5.8, there is a very thin oxide layer formed on the top of the coating at 700°C in a short term 1hour air heat treatment. However, the oxide layer appears to thicken with a longer period of exposure. For the coating sample which was exposed for 16 days at 700°C, a thicker oxide layer can be found on the surface of the coating. More details about oxide formation on the coating after annealing will be introduced in next chapter. In Fig

5.9(c) a very thin oxide layer started to build-up along the interface within 2 days of heat treatment and thickened with continued exposure. In Fig 5.9(e) a more porous coating-substrate interface is formed with larger oxide layers and higher porosity between the coating and substrate.

### **X-ray Diffraction**

The XRD patterns from the as-sprayed coating and the coatings annealed at 700°C for times of 1 hour to 16 days are shown in Fig 5.10. The top layers of these annealed coatings (approximately 20 μm thick) were ground and removed before XRD examination. From the as-sprayed coating, the principal phases were identified as Cr<sub>3</sub>C<sub>2</sub> with an amorphous halo believe to result from rapid solidification of a Ni-Cr-C liquid. After 1 hour heat treatment, this amorphous halo disappeared, while with increasing exposure time the crystalline matrix peaks became more defined and increased in intensity relative to the carbide peaks. The carbide peaks also became more defined. No significant new carbide phases were detected from the ground coating surface after heat treatment. The only carbide phase which dominates the carbide spectra is Cr<sub>3</sub>C<sub>2</sub>. No definitive peaks of Cr<sub>23</sub>C<sub>6</sub> or Cr<sub>7</sub>C<sub>3</sub> are found. Peaks corresponding to Cr<sub>2</sub>O<sub>3</sub> also occurred indicating the formation of some oxide layers within the coating. The intensity of Cr<sub>2</sub>O<sub>3</sub> peaks does not show any significant increase with increase in annealing time.

The coatings after 2 days and 16 days annealing at 700°C were removed by a mechanical method from the substrate and on XRD spectrum obtained from the surface of the coating that was in contact with the substrate. These are given in Fig 5.11. It is apparent that spectra from the coating bottom layer show a significant difference from the as-sprayed coating and also from the top surface of the same heat treated samples. The dominant Cr<sub>3</sub>C<sub>2</sub> peaks at 2θ from 46 to 49° in the as-sprayed coating show a rapid decrease after 2 days annealing and nearly disappear after 8 days time. Instead of Cr<sub>3</sub>C<sub>2</sub> peaks, peaks corresponding to Cr<sub>23</sub>C<sub>6</sub> and Cr<sub>7</sub>C<sub>3</sub> appear and increase in intensity in the XRD spectra after heat treatment.

**Scanning Electron Microscopy**

The phase changes in the heat treated coating samples were also investigated using SEM. Typical SEM-BSE images taken from the middle region of the coating cross-sections which were annealed in air from 1 hour to 16 days at 700°C are shown in Fig 5.12. The mid-grey contrast layers which are the as-sprayed coating matrix phase give a marked reduction in contrast with the precipitation of fine carbide particles after 1 hour air annealing. Extensive carbide precipitation occurred with 8 days heat treatment. Carbide nucleation forming fine precipitates occurred mainly in regions where the greatest dissolution occurred during spraying. However there is no significant change in the large carbide particles after 8 days annealing in air at 700°C. With continued exposure, some carbide particles surrounded with lighter grey contrast are found in the coating after 16 days air annealing. These lighter grey (G) contrast features in Fig 5.12 were analysed by EDX-SEM and results shown in Table 5.2 which did not show any evidence of Cr<sub>7</sub>C<sub>3</sub> and Cr<sub>23</sub>C<sub>6</sub>. In addition, Table 5.2 also gives the composition of the bright phase (M) in coating which corresponds to the Ni(Cr) solid solution matrix with small amount of carbon.

SEM-BSE images of the coating at the interface with the substrate are shown in Fig 5.13. There is no apparent change in the coating interface microstructure before 8 days annealing at 700 °C. With extended exposure, along the coating-substrate interface large carbide particles disappeared but the carbide precipitation was more significant and formed sponge-like agglomerated precipitates with lighter contrast at increased times (Fig 5.13 e). The phase composition of these sponge-like carbides (G) shows relatively low carbon content in Table 5.3 which must be Cr<sub>7</sub>C<sub>3</sub> or Cr<sub>23</sub>C<sub>6</sub> as detected in XRD patterns. After 16 days heat treatment some large dark carbides can still be found within the coating. These carbides (C) are identified as Cr<sub>3</sub>C<sub>2</sub> by EDX analysis from its phase composition. In Table 5.3 the composition of the bright phase (M) corresponding to the Ni(Cr) solid solution matrix in the coating shows a very small amount of carbon dissolution. In addition, some dark layers (O) above the coating interface in Fig 5.13 e show high oxygen content by EDX analysis which

suggests chromium oxide. These fine carbides must be Cr<sub>7</sub>C<sub>3</sub> or Cr<sub>23</sub>C<sub>6</sub> as found by XRD.

### **Microhardness measurements**

The microhardness tests were performed along a line parallel to the mid-plane of cross-sectioned coatings using a 300 g load on a Vickers indenter from three specific areas which were 20 μm away from the coating surface, in the middle of the coating and 20 μm away from the coating-substrate interface. Ten measurements were made through each area as shown in Fig 5.14. The average and standard deviation of these measurements were calculated and compared in Fig 5.15. In each sample, the hardness measured near the coating top surface did not show a significant difference from the hardness measured in the midplane of the coating. However, the measurements near the interface with the substrate showed a lower hardness than that of the mid-line and the difference gradually increased with continued exposure. The same general trend in microhardness occurred at both of the coating mid-plane and the interface after 700°C heat treatment. A rapid reduction in hardness occurred over the initial period of heat treatment. With continued exposure, the hardness quickly increased, reaching a stable value after 8 days of treatment.

### **5.1.3.3 Exposure at 800°C in air**

#### **Optical Microscopy**

Specimens of the as-polished, cross-sectioned NiCr-Cr<sub>3</sub>C<sub>2</sub> coatings which were annealed at 800°C for times ranging from 1 hour up to 16 days were shown in Fig 5.16. Some black holes (P) and layered structures (O) which are probably bands of oxide were presented as arrowed. Comparing these four optical microscopic images taken from the middle of the coating within different heating times, it is difficult to tell an obvious change in these oxide layers. However, the porosity showed a rapid growth with continued exposure which is quite similar to these coatings annealed at 700°C. In addition, the microstructures of the surfaces and interfaces annealed at 800°C for times ranging from 1 hour up to 16 days are shown in Fig 5.17 and Fig

5.18. The microstructure of the as-sprayed coating was used as a reference in Fig 5.17 (a), and it is difficult to find any oxide layer on the coating surface before heat treatment. In Fig 5.17 (b), oxide appears to thicken on the top of the coating within one hour heat treatment. After 2 days a thin oxide layer built up on the coating in Fig 5.17 (c) with continued exposure. In Fig 5.17 (d) and (e) thicker oxide layers (~10 μm) can be found on the surface of the coating after long periods of exposure up to 16 days at 800°C. Meanwhile, oxide and voids also occurred at the coating-substrate interface, and they grew quickly with continued exposure at 800°C. Fig 5.18(e) shows the coating sample exposed for 16 days with a lot of porosity at the coating-substrate interface. Moreover, a thick oxide layer also formed about 10 μm away from interface in the coating. Coatings heat treated at 800°C showed a more obvious increase in the oxide and porosity levels, and it also gave weaker interface integrity than those coatings which were heat treated in 700°C.

### **X-ray Diffraction**

The XRD patterns of the coatings annealed at 800°C for times of 1 hour to 16 days are shown in Fig 5.19. The top layers of these annealed coatings were also ground and removed before XRD examination with approximate 20 μm removed. The spectra of these samples are similar to those of the coatings annealed at 700°C. Cr<sub>3</sub>C<sub>2</sub> is the only carbide phase detected throughout the period of heat treatment. Cr<sub>2</sub>O<sub>3</sub> peaks are also found as the only oxide in coating.

The coatings after 2 days and 16 days annealing at 800°C were removed from the substrate and XRD spectra received from the surface of the coatings that was in contact with the substrate in Fig 5.20. It is apparent that spectrum from the coating bottom layer show a significant difference from the as-sprayed coating. The spectrum reveals a large number of peaks that are related to Cr<sub>23</sub>C<sub>6</sub> or Cr<sub>7</sub>C<sub>3</sub>. Summary of phases present in these annealed NiCr-Cr<sub>3</sub>C<sub>2</sub> coatings compared with the original as-sprayed coating and powder is shown in Table 5.6.

**Scanning Electron Microscopy**

Typical SEM-BSE images taken from the middle area of the coating cross-sections which were annealed in air from 1 hour to 16 days at 800°C are shown in Fig 5.21. Coating samples annealed at 800°C show similar phase changes to coatings annealed at 700°C. Fine carbide precipitates occurred throughout the coating during the initial 2 days exposure and tended to coalesce and form larger carbides of complex morphologies with extended exposure. The originally large carbides did not show significant changes in coating microstructures after 800°C annealing in air. Phase compositions analysed by EDX-SEM are shown in Table 5.4. In Fig 5.21 the dark particles pointed as C can be identified as Cr<sub>3</sub>C<sub>2</sub> and the bright phase (M) corresponds to the Ni(Cr) solid solution matrix. The grey region (G) which contains many fine carbide precipitates shows a Cr-rich phase with significant amounts of carbon. There is still no evidence to show new carbides in this area after heat treatment.

Coating samples annealed at 800°C started to form significant sponge-like agglomerated precipitates along the coating-substrate interface after 2 days exposure shown in Fig 5.22. This sponge-like area expanded towards the coating centre with the increase in exposure time. During heat treatment, the initial carbide grains lost their previous faceted or rounded structure; they grew through coalescence and dissolution, forming a network of carbides where the Ni matrix does not act as the binder for the carbides. The phase composition of these sponge-like carbides (G) in the coating after 16 days 800°C annealing (Fig 5.22d) shows very low carbon content in Table 5.5. New carbides such as Cr<sub>7</sub>C<sub>3</sub> or Cr<sub>23</sub>C<sub>6</sub> detected in XRD patterns might form in this region. While the composition of the bright phase (M) is detected as a region of Ni(Cr) solid solution matrix it contains extremely small amounts of carbon. In addition, some dark areas (O) above and along the coating interface in Fig 5.22d show high oxygen content by EDX analysis which could indicate chromium oxide.

**Microhardness measurements**

Fig 5.23 showed the microhardness measurements from three different areas of cross-sectioned coatings using a 300 g load on a Vickers indenter. The average and standard deviation of these measurements were calculated and compared in Fig 5.24. In each sample the hardness measured near the coating top surface did not show a large difference to the hardness measured in the mid-plane of the coating. However the measurements near the interface showed a lower hardness than that of the mid-plane and the difference gradually increased with continued exposure. On the other hand, coatings after 800°C heat treatment had the same general trend in microhardness as the coatings heat treated after 700°C. A rapid reduction in hardness happened over the initial period of heat treatment. With continued exposure the hardness quickly increased, reaching stable values after 8 days of treatment. In all instances the coating samples with 700°C heat treatment had higher hardness values than the coating samples after 800°C heat treatment at the coating surface, the mid-plane and the interface. The average and standard deviation of these coatings measurements were calculated and compared in Fig 5.25.

#### **5.1.3.4 Summary**

In this section, the microstructure and microhardness response of HVOF sprayed NiCr-Cr<sub>3</sub>C<sub>2</sub> coatings were assessed following exposure in air at 700 and 800°C for periods of up to 16 days. Transformation from amorphous phase to crystalline phase within the Ni(Cr) binder is found to occur within 1 hour at both temperatures. With long term exposure new carbide phases, Cr<sub>7</sub>C<sub>3</sub> and Cr<sub>23</sub>C<sub>6</sub>, started to form near the coating/ substrate interface. However, the bulk of the coatings did not appear to form new carbides. All samples showed a drop in hardness initially, and it started to increase after 2 days heat treatment. The microhardness from the region near the coating/substrate interface with new carbide phases gave a lower value than that from the middle region of the coating or near the top surface. Coating exposure at 800°C showed more significant microstructural changes than coating exposed at 700°C, especially the structures at the coating-substrate interface.

## **5.1.4 Charactersiation of Ni(Cr)-Cr<sub>3</sub>C<sub>2</sub> coated stainless steel**

### **substrate following high temperature exposure**

#### **5.1.4.1 Introduction**

In this section the changes occurring in the stainless steel substrate as a result of high temperature inter-diffusion between the coating and the substrate will be described. SEM with EDX analysis was used to study the microstructure of the substrate after annealing. XRD was also used to identify the phases which formed close to the coating-substrate interface. Microhardness measurements were also made to investigate its variation with distance from the interface with the coating.

#### **5.1.4.2 Scanning Electron Microscopy**

Microstructures formed in the interface region following the heat treatment are shown in Fig 5.26 and 5.27. Samples were etched in a solution of 12 ml nitric acid and 35 ml hydrochloric acid 53 ml H<sub>2</sub>O.

Fig 5.26 (a), the as-sprayed coated sample, indicate an equiaxed grain structure in the steel substrate. At 700°C after 1 hour, Fig 5.26 (b), significant grain growth in the steel changed the grain size from around 10-20 μm to 20-30 μm. Evidence for precipitates is clear to see at the interface with increasing time at temperature. At higher magnification, very fine scale precipitation appears in a band initially around 10 μm wide but extends to 20-30 μm after 16 days, Fig 5.26 (i). Grain boundaries etch more readily, with fine precipitates becoming visible, which are certainly sub-micron. On the coating side of the interface changes occur to the original Cr<sub>3</sub>C<sub>2</sub> precipitate morphology as described in a previous section. Some elongated precipitates begin to form at the substrate interface after long term exposure.

At 800 °C after 1 hour, in Fig 5.27 (a), significant grain size change occurs within the substrate. Some small equiaxed grains around 2-4 μm appear to be formed along the interface in a band and some large grains grow in the steel from around 10-20 μm to

20-30  $\mu\text{m}$ . At higher magnification (Fig 5.27d), very fine scale precipitates appear to be forming in a band along the interface after 2 days exposure. After 8 days heat treatment, shown in Fig 5.27 (f), two distinct precipitates with needle-like and fine spherical shapes are found in substrate. Grain boundaries etch more readily, with fine precipitates becoming, visible which are certainly sub-micron. After 16 days exposure, it is clear to find three different regions in the stainless steel substrate in Fig 5.27 (g) namely: a precipitate free zone, a precipitate rich zone and a grain boundary precipitate zone. As mentioned above, at both 700°C and 800°C annealing treatment, debonding at the coating/substrate interface is visible after a period of 2 days. However, the degree of the debonding is more severe at the higher temperature. At 800°C the porosity in interface continues to increase over the 16 days of the annealing treatment. But at 700°C the mild porosity at the interface does not worsen significantly.

Further SEM examination of cross-sections at greater distances from the interface was introduced to establish the extent of inter-diffusion and precipitation, Fig 5.28. At 800°C, after 2 days, Fig 5.28 (a) shows that following etching grain boundaries are straight decreased to a depth of around 330  $\mu\text{m}$ . As that the entire section received an identical etching treatment, it seems reasonable to assume that intensity of etching is related to more extensive grain boundary precipitation. It is known, from a previous section, that uncoated heat treated stainless steel 304 will also form grain boundary precipitates but not to such an extent. However at 800°C after 16 days in Fig 5.28, it is evident that precipitates are much coarser at grain boundaries and also grain boundary precipitation has occurred further into the sample due to the longer time available for high temperature diffusion. As the frequency of the carbide precipitates can reveal the extent of carbon diffusion in the substrate, the diffusion distance can be estimated by measuring the distance from the coating/substrate interface to where the precipitates no longer formed on the grain boundaries. Table 5.7 shows the summary of the measured diffusion distance of all the annealed samples.

EDX analysis has been also applied to the sample heat treated at 800°C after 16 days in Fig 5.28. As low carbon content levels cannot be measured with the SEM/EDX analysis, in the present study it is possible to measure interdiffusion only of the elements Fe, Cr and Ni. This has been done in two ways: firstly, a line scan is performed by scanning the area along a line perpendicular to the interface from the coating to substrate and collecting the SE, Cr K $\alpha$ , Fe K $\alpha$  and Ni K $\alpha$  signals. This gives a qualitative identification of the composition variation as plotted in Fig 5.29. Chromium shows a 10  $\mu$ m depleted zone from interface in the steel substrate, iron seems to have been diffused from the steel substrate into the coating around 20  $\mu$ m distance, and nickel shows a relatively high content in the substrate within the distance of 30  $\mu$ m from interface. Secondly, another EDX/SEM analysis has been done by using a series of area scans over the zones indicated at Fig 5.28. The data were collected and compositions calculated using a standard ZAF correction procedure. In each zone, EDX area analysis has been carried out in 5 evenly distributed measuring areas with the size 50x2  $\mu$ m (zone 1), 50x10  $\mu$ m (zone 2) and 50x20  $\mu$ m (zone 3). Each area has been analysed 4 times and results are shown in Table 5.8 and plotted in Fig 5.30. It is clear that Ni is significantly enriched at the interface, Cr is depleted as is Fe. The estimated diffusion distance for the elements are around 25  $\mu$ m for Fe and Ni and 10  $\mu$ m for Cr in the 304 stainless steel.

#### **5.1.4.3 X-ray Diffraction**

XRD was performed on the substrate side of interfaces after the coating was removed by a mechanical method. As before, the examination was done on 700 and 800°C annealed samples which had been exposed for 2 days and 16 days respectively and shown in Fig 5.31. With the XRD, method the X-rays are calculated to penetrate around 4-5  $\mu$ m. Therefore in all cases the diffraction data will represent the depleted zone and a distance into the diffusion zone. At 700°C, the phases can be seen as  $\gamma$  (f.c.c), Cr<sub>2</sub>O<sub>3</sub> and carbide phases which include Cr<sub>3</sub>C<sub>2</sub>, Cr<sub>7</sub>C<sub>3</sub> and Cr<sub>23</sub>C<sub>6</sub>. Cr<sub>3</sub>C<sub>2</sub> is probably a residual particle since less porosity forms at the interface at 700°C. However, at 800°C the phases identified are  $\gamma$  (f.c.c), Cr<sub>23</sub>C<sub>6</sub>, Cr<sub>7</sub>C<sub>3</sub> and Cr<sub>2</sub>O<sub>3</sub>. With

increasing annealing time less Cr<sub>7</sub>C<sub>3</sub> and more Cr<sub>23</sub>C<sub>6</sub> phases were found. Oxide formed due to air reaching the interface layer during annealing.

#### **5.1.4.4 Microhardness measurements**

Microhardness measurements on coating and coated substrate samples after 700°C and 800°C air annealing are shown in Fig 5.32 and 5.33. NiCr-CrC coating shows a much higher hardness than the stainless steel. The microhardness of each coated substrate was measured from the coating/substrate interface penetrating into the substrate with 50 μm between each indent. The average microhardness values of each substrate sample measured far from interface are also shown in Fig 5.32 and 5.33. In these figures, it is immediately visible that the microhardness variation occurred on every annealed 25Ni(Cr)-75Cr<sub>3</sub>C<sub>2</sub> thermal spray coatings and substrate. The values of these microhardness indents measured on the coated substrates from the interface to the middle, are gradually decreasing and getting steady towards to the end. The hardness decreased with distance into the substrate until a constant value is reached. The microhardness measurements taken from the coating across the interface into the substrate for these annealed samples are plotted in Fig 5.34. It can be seen that a gradual decrease occurs in the coating-substrate interface. From the SEM images it is evident that carbide precipitates occurs due to carbon diffusion from the coating and the diffused C encourages the formation of carbide precipitates on grain boundaries it is these precipitates which are the reason for the increased hardness. According to this, a summary of diffusion distance in substrate can be given in Table 5.9 which is based on the microhardness variation versus distance away from bonded interface.

#### **5.1.4.5 Summary**

Inter-diffusion between the coating and the substrate (the stainless steel 304) has been described above. A distribution of precipitates can be clearly found from the SEM images of these etched substrate samples. A precipitate free zone, a precipitate rich zone and grain boundary precipitate zone can be observed in each sample. XRD results detected from the substrate interface show Cr<sub>23</sub>C<sub>6</sub> as the main precipitate in the

diffusion zone. Moreover, the variation in the microhardness measured away from the interface also revealed that diffusion occurred between coating and substrate during the annealing period. By measuring the appearance of the precipitates and variation in microhardness away from the interface, the diffusion distance was estimated which is useful as a reference for diffusion modelling.

## 5.2 Discussion

### 5.2.1 Influence of heat treatment on the structure of Ni(Cr)-Cr<sub>3</sub>C<sub>2</sub> coatings

#### 5.2.1.1 Microstructures of Ni(Cr)-Cr<sub>3</sub>C<sub>2</sub> coatings after heat treatment

Annealing of NiCr-Cr<sub>3</sub>C<sub>2</sub> coated samples for 1 hour to 16 days at 700 and 800°C then slow cooling caused a disappearance of the diffuse diffraction halo from the coating spectrum as shown by XRD trace in Figs 5.10 and 5.19. The fcc Ni peaks have clearly increased in intensity and Cr<sub>3</sub>C<sub>2</sub> has been detected as the only carbide phase. According to the ternary phase diagram for Cr, Ni and C at 800°C shown in Fig 2.7 (d) and the average composition of the coating (70 wt% Cr, 20 wt% Ni, 10 wt% C), the equilibrium phases for that composition are fcc Ni-based alloy and Cr<sub>3</sub>C<sub>2</sub>. That means there is a thermodynamic driving force for the formation of the phases present in the annealed coatings. The formation of carbides following annealing has been reported in the case of chromium carbide coatings with 25 wt% Ni20Cr binder by many investigators (Matthews, 2003) (Guilemany, 2002) (Edris, 1997) etc. In Matthews' XRD spectrum of the HVOF NiCr-Cr<sub>3</sub>C<sub>2</sub> coating after 2 days annealing at 900°C, Cr<sub>3</sub>C<sub>2</sub> was detected as the only carbide phase throughout the period of heat treatment. The same results have been documented by Guilemany (2002) from his short term annealing of coatings at 723K, 1033K and 1153K. Conversely, Edris indicated in his thesis that the XRD trace of heat treated 25Ni(Cr)-75Cr<sub>3</sub>C<sub>2</sub> coating at 900°C after the top 50 µm had been removed showed clear evidence for the presence of Cr<sub>7</sub>C<sub>3</sub>.

According to the SEM images Fig 5.12 and 5.21, it is evident that with continued exposure carbide nucleation forming fine precipitates occurs mainly in Ni(Cr) alloy matrix which contains a high retained carbon concentration. Due to the low annealing temperature diffusion of dissolved Cr and C is limited to those regions forming precipitation in close proximity to the retained carbides. EDX results provided in previous section did not show any evidence of new carbides such as Cr<sub>7</sub>C<sub>3</sub> and Cr<sub>23</sub>C<sub>6</sub>.

The XRD spectrum detected from the bottom layer of the coatings, Fig 5.11 and 5.20, shows the decrease of Cr<sub>3</sub>C<sub>2</sub> peaks and the formation of new carbides such as Cr<sub>23</sub>C<sub>6</sub> and Cr<sub>7</sub>C<sub>3</sub> specifically after 800°C annealing. The lattice shows an entire disappearance of Cr<sub>3</sub>C<sub>2</sub> peaks at 2θ from 46 to 49°. The initial Cr<sub>3</sub>C<sub>2</sub> carbide decomposes into Cr<sub>23</sub>C<sub>6</sub> and Cr<sub>7</sub>C<sub>3</sub> during the heat treatment due to carbon loss by oxidation. This has been proved by EDX analysis in Table 5.3 and 5.5 which all show high content of oxygen in some areas. It is also due to carbon loss by diffusion into the substrate.

With continued exposure diffusive processes become important and morphological modifications take place at the coating interface. As shown in Figs 5.13 and 5.22, the coating after 16 days at 800°C shows an important modification in its structure. The initial faceted or rounded carbides are lost and the growth of the individual carbide grains led to coarsening of the ‘sponge-like’ agglomerates, generating a more porous appearance to these features. Since a network of carbides is produced, Ni(Cr) alloy matrix does not act as the binder anymore. Similar microstructures were found by Matthews (2003) in his coating samples after 20 and 60 days of heat treatment in air at 900°C and Guilemany (2002) in his sample treated at 880°C for 24 hours. The difference between their work and the present are (i): Annealing temperatures and exposure time are different, in this work, relatively lower temperature were used. (ii): In their results the network of carbides was formed in whole coating, in this work it only forms at the coating interface. This is because their heat treatment experiments were carried out using the coating removed from substrate, whilst in this work the sample and substrate were heat treated together. From the above, it can be predicted that temperature is very important to the change of coating microstructure, and a temperature of around 800°C seems to be border line. On the other hand, in our work the coalescent carbide structure only formed near coating interface which is due to the carbon diffusion from coating into substrate. So far there is no report about the investigation of the characteristics of the NiCr-Cr<sub>3</sub>C<sub>2</sub> coating which is heat treated at

higher temperatures with coated substrate. The diffusion between this coating and stainless steel substrate has not been reported in the previous research either.

### **5.2.1.2 Microhardness of Ni(Cr)-Cr<sub>3</sub>C<sub>2</sub> coatings after heat treatment**

The microhardness value of a material is based on the hardness and volume fraction of the hard phase and the hardness of the matrix phase. A rapid reduction in hardness occurred to the coating after heat treatment at 700 or 800°C, Fig 5.25. The as-sprayed coating had a supersaturated Ni(Cr) solid solution as its matrix due to the carbide dissolution during spraying which gives significantly higher hardness. During the heat treatment, the dissolved Cr and C precipitated in the form of fine carbides and recrystallized the matrix which is evident in the BSE images by reducing matrix contrast, also there is a change in the d-spacing of the Ni peaks due to a reduction in the amount of dissolved Cr and C. Crystallization of the amorphous phase usually causes a decrease in hardness (Inoue, 2000), therefore the change in microstructure of amorphous phase has a negative influence on hardness of the coatings. Additionally, in the initial heat treatment the formation of secondary carbide precipitates in the binder will also lead to softening of the Ni(Cr) matrix and a decrease in the coating hardness. This has been observed in case of chromium carbide coating with 20 wt% Ni20Cr binder by Murthy (2007). With continued exposure, the microhardness starts to recover after 8 days at both 700 and 800°C. Hardness recovery occurred with carbide nucleation and growth forming an expansive carbide skeletal network in the matrix. The transition from the growth of individual carbide precipitates to the development of a widespread carbide network in the matrix can be seen in the SEM images provided in the previous section. The larger carbides, formed through agglomeration and coalescence, increase the hardness value of the coating. The same general trend in microhardness changes was reported by Matthews (2003). In his work, the microhardness response of HVOF 25Ni(Cr)-75Cr<sub>3</sub>C<sub>2</sub> coatings was assessed following treatment at 900°C for periods of up to 60 days in air. He indicated the initial decrease of hardness was attributed to the reduction in strengthening mechanisms of the matrix phase. And the hardness recovery after 5 days resulted

from the precipitation and development of a carbide phase. However, Guilmany (2002) suggested that 25Ni(Cr)-75Cr<sub>3</sub>C<sub>2</sub> coatings show a rapid increase in hardness after heat treatment in air in his work. He indicated that higher microhardness values are achieved in the samples heat treated in an oxidising atmosphere due to the formation of the hard Cr<sub>2</sub>O<sub>3</sub> phase. In our work, the samples were all annealed in air as well, but from XRD and SEM images, there is no evidence of a significant increase of Cr<sub>2</sub>O<sub>3</sub> phase. This suggests the present coating had less porosity.

Microhardness measured at the coating interface is relatively lower than that of the coating bulk which is due to the different microstructures in both regions. As shown in the previous SEM-BSE images, significant sponge-like agglomerate precipitates were found at the coating interface which causes a decrease in hardness. With continued exposure, the initial carbide grains grow through coalescence and dissolution forming a network of carbides where the Ni matrix does not act as the binder for the carbides. EDX results show that the region of Ni(Cr) solid solution matrix contains extremely small amount of dissolved carbon and gives a softer matrix. On the other hand, in the carbide series (Cr<sub>3</sub>C<sub>2</sub>, Cr<sub>7</sub>C<sub>3</sub> and Cr<sub>23</sub>C<sub>6</sub>), Cr<sub>3</sub>C<sub>2</sub> has the best mechanical properties with higher hardness (Hays, 1994). XRD patterns show Cr<sub>7</sub>C<sub>3</sub> and Cr<sub>23</sub>C<sub>6</sub> peaks only occurred in the coating interface after heat treatment which is the other reason why coating interface gives a lower hardness.

## **5.2.2 Diffusion between the coating and the substrate at elevated temperature**

### **5.2.2.1 Activity calculations for elements diffusion between coating and substrate**

The direction of element diffusion is driven by chemical potential which can be given as  $\mu = RT \ln a$  according to Henry's law (Porter, 1992). In this equation  $a$  is the activity which is very important for the diffusion process. In this work, the activities of the elements in Ni(Cr,C) coating matrix and 304 substrate at 800°C were calculated by Thermo-Calc<sup>®</sup>4 for windows with SSOL4 and TCFE5 steel databases respectively. The element composition of Ni(Cr, C) coating matrix can be estimated from the Cr-Ni-C phase diagram in Fig 2.7 (d). The matrix with the maximum dissolved carbon at 800°C was pointed as G on this phase diagram which gives the composition of 89 wt% Ni, 9 wt% Cr and 2 wt% C. According to the results in Table 5.10 carried out by Thermo-Calc<sup>®</sup>4, Fig 5.35 shows a much higher carbon activity value in the coating than in the substrate which means carbon might diffuse from coating to substrate during heat treatment. For element Ni, the diffusion direction could be from coating to substrate. However, the diffusion of element Fe and Cr might happen from the substrate to the coating during the heat treatment process according to this chart Fig 5.35.

The diffusion directions of alloy elements predicted by activity can be also revealed by experimental results. Fig 5.30 shows the diffusion occurring at the interface between the coating and the substrate during the heat treatment. In Fig 5.30, the loss of Cr and Fe from the substrate interface is caused by elements diffusing into the coating while the increase of Ni is caused by the element diffusing from the coating. Moreover, the line scan result shown in Fig 5.30 also gives the same diffusion direction of Cr, Fe and Ni. On the other hand, because it is difficult to measure the weight percentage of carbon in the sample by SEM-EDX due to its low energy on the EDX spectrum, the carbon change between coating and substrate cannot be obtained

like other alloy elements. But the precipitate distribution (Fig 5.26~5.28) and microhardness variation (Fig 5.34) can be used as a reference to prove the carbon diffusion has happened in the stainless steel substrate during exposure. Additionally, the coating interface shows sponge-like carbide structures forming Cr<sub>7</sub>C<sub>3</sub> and Cr<sub>23</sub>C<sub>6</sub> after heat treatment. It is evident that carbon loss occurs in this region by carbon diffusion from the coating to substrate.

#### **5.2.2.2 Modelling of carbon diffusion in as-coated stainless steel 304**

According to the results mentioned in the previous sections, a schematic diagram of the carbon diffusion progress between the coating and the 304 substrate at high temperature is shown in Fig 5.36. In the as-sprayed condition ( $t=t_0$ ), the coating matrix is Ni(Cr,C) due to the rapid solidification during thermal spraying. In some cases, the surface region of Cr<sub>3</sub>C<sub>2</sub> has become dissolved forming a surrounding Cr(Ni)<sub>3</sub>C<sub>2</sub> phase. At this time, the main constituents in the substrate are Fe(Ni,Cr), with low carbon concentration (<0.1 wt%).

As heat treatment begins ( $t=0$ ), more of the surface region of Cr<sub>3</sub>C<sub>2</sub> becomes dissolved. Due to the higher ratio of diffusion, carbon is able to diffuse into the matrix from the Cr(Ni)<sub>3</sub>C<sub>2</sub> phase. Diffusion also occurs across the coating/substrate interface, C and Ni diffuse into the substrate matrix and Fe diffuse into the coating. Little diffusion of Cr across the coating/substrate interface occurs, due to its higher atomic mass and thus lowers the diffusion ratio.

As heat treatment continues ( $t=1$ ), the surrounding carbide phase continues to grow forming a network. Due to the carbon diffusion into the coating matrix, the carbide phases surrounding the original carbide particles contain lower carbon content. This results in lower carbon Cr(Ni)<sub>7</sub>C<sub>3</sub> phase forming in addition to the Cr(Ni)<sub>3</sub>C<sub>2</sub> phase. At the coating/substrate interface, pores which were formed due to the rough grit blasted substrate surface start to grow during the heat treatment and hinder the

diffusion flux across the interface. In the substrate matrix, precipitates of  $M_{23}C_6$  start to form nearby the interface due to the carbon diffusion from coating.

As heat treatment continues further ( $t=2$ ), the surrounding carbide phase continues to grow, completely dissolving the original  $Cr_3C_2$  particles near the interface. The continued carbon diffusion from the surrounding carbide phase into the matrix results in lower carbon concentration in carbide phases forming  $Cr(Ni)_7C_3$  and  $Cr(Ni)_{23}C_6$ . At the interface, pores continue to grow; chromium oxide starts to form around the pore surfaces. Oxygen at the interface may react with carbon diffusing from the coating matrix and carbide precipitates in substrate near interface, resulting in loss of carbon as  $CO_2$  or  $CO$  gas. The carbide precipitation continues to occur, progressing deeper into the substrate matrix.

As heat treatment continues further ( $t=3$ ), the carbide phase in the coating continues to grow forming a linked sponge-like carbide network of  $Cr(Ni)_7C_3$  and  $Cr(Ni)_{23}C_6$  phases. At the interface, porosity increases and extends at which only a low diffusion flux passes. Carbide precipitation continues to occur progressing deeper still into the substrate matrix.

The above, describes the effect of high temperature heat treatment on the coating substrate microstructures near interface, by diffusion. Since carbon diffusion is the key issue for the formation of precipitates in as-coated stainless steel substrate during annealing, the modelling of carbon diffusion is then an effective way to understand this process. In this modelling work, two conditions have to be considered in order to simplify the process of carbon diffusion from coating to steel. First, the diffusion of Ni and Cr from the coating to the steel during the carbon diffusion will be ignored, due to the speed of interstitial diffusion of carbon at low temperature being much quicker than that of the substitutional diffusion of these Ni and Cr alloy elements in steel. Second, as the original coating contains much higher carbon concentration than

that of stainless steel substrate, during the diffusion process the high concentration of carbon maintains at a stable constant value at the interface with the stainless steel substrate. According to these two conditions, the equation of carbon diffusion distance in substrate stainless steel 304 was given as

$$x = \sqrt{D_c t}$$

The equations of carbon diffusivity  $D_c$  were mentioned in the previous literature chapter.

$$D_c = D_{c(0)} \exp(\beta_C^{Cr} N_{Cr})$$

Sample heat treated at 700°C and 800°C:

$$D_{c(0)700^\circ\text{C}} = 1.91 \exp\left(-\frac{143.6}{RT}\right) = 3.69 \times 10^{-8} (\text{cm}^2 / \text{s})$$

$$D_{c(0)800^\circ\text{C}} = 2.25 \times 10^{-3} \exp\left(-\frac{92.7}{RT}\right) = 6.87 \times 10^{-8} (\text{cm}^2 / \text{s})$$

$$\beta_C^{Cr}{}_{700^\circ\text{C}} = 99.7 - \left(\frac{121000}{T}\right) = -24.66 (\text{at.fr.}^{-1})$$

$$\beta_C^{Cr}{}_{800^\circ\text{C}} = 94 - \left(\frac{133000}{T}\right) = -29.95 (\text{at.fr.}^{-1})$$

According to Table 2.8, 2.9 and 2.10  $N_{Cr}$  of stainless steel can be expressed as

$$N_{Cr} = \sum K_{Cr(C)}^j N_j = 18\% \times 1_{(Cr)} + 8\% \times (-0.442)_{(Ni)} + 2\% \times 0.386_{(Mn)} + 1\% \times (-0.673)_{(Si)} = 0.146$$

$$\Rightarrow D_{c(700^\circ\text{C})} = 1.05 (\mu\text{m}^2 / \text{s})$$

$$\Rightarrow D_{c(800^\circ\text{C})} = 2.86 (\mu\text{m}^2 / \text{s})$$

So the equation of carbon diffusion in substrate stainless steel 304 is expressed as:

(1) at 700°C

$$x_{700^\circ\text{C}} = \sqrt{1.05 \cdot t} \quad (5.1)$$

(1) at 800°C

$$x_{800^\circ\text{C}} = \sqrt{2.86 \cdot t} \quad (5.2)$$

According to equation 5.1 and 5.2 the distance of carbon diffusion in samples heat treated at 700 and 800°C after 1 hour, 2 days, 8 days and 16 days can be calculated and summarised in Table 5.11.

Compared with Table 5.7 and 5.9, after a period of 1 hour, the carbon diffusion model indicates slightly shorter diffusion distances at both 700 and 800°C than is measured in the sample. It is likely that, this increased diffusion distance in the sample is due to further diffusion during the cooling period in the furnace, whereas, the period of the diffusion in the model is exactly 1 hour. After extended exposure, the diffusion distance predicted by the model is significantly greater than the measured diffusion distances in the sample in Table 5.7 and 5.9. It is proposed that the low diffusion distance measured in the sample is due to the porosity at the interface, blocking the carbon flux into the substrate. The higher porosity at 800°C thereby leads to a greater difference in predicted diffusion distance relative to measured than the 700°C samples. In addition, the oxidation within the coating near the interface might react with carbon forming CO or CO<sub>2</sub> gas which escapes. This may also cause reduced carbon flux across the interface.

The precipitate free zone forms due to the depletion of chromium which is because of Cr<sub>2</sub>O<sub>3</sub> at the interface. Additionally, carbon loss in this area might be the second reason of forming a precipitate free zone. This absence arises from the combination of carbon diffusing into the substrate and loss as CO or CO<sub>2</sub> by oxidation and the extent porosity at the interface preventing carbon diffusing into this region from the coating resulting in net carbon loss. After formation at 2 days the precipitate free zone continued to grow suggesting very little carbon diffusion occurred from the coating the substrate after this point and the concentration gradient will resemble that in Fig 5.37. The maximum carbon concentration in the substrate is below the precipitate free zone and continues to move away from the interface as time goes on. In conclusion after the formation of precipitate free zone diffusion occurs from this maximum point and not the interface.

### **5.2.3 Summary**

During heat treatment of the coated samples, strong chemical potential gradients across the interface line can induce significant long range diffusion of rapidly diffusion elements, such as carbon. This transfer of carbon across the sample is responsible for significant changes in microstructure, such as dissolution of carbides on the coating side and precipitation on the substrate side.

**Table 5.1** EDX area analysis results for average compositions of stainless steel 304

(Average of 4 area analyses)

Elements	Atomic %	Weight %
Cr	20.9 ± 0.8	19.5 ± 0.8
Mn	1.4 ± 0.1	1.3 ± 0.1
Fe	69.8 ± 1.2	70.5 ± 1.2
Ni	7.8 ± 0.6	8.6 ± 0.6

**Table 5.2** EDX (Cobalt standard) analysis results for average compositions of different phases from coating middle area after 16 days air annealing at 700°C

(Average of 4 area analyses)

Phase	Phase composition			
	Average	Cr	Ni	C
M (bright area)	Atomic%	16±2.2	82±3.2	2±0.6
C (dark area)	Atomic%	58±2.0	0	42±2.7
G (grey area)	Atomic%	57±2.7	8± 1.1	35±2.1

**Table 5.3** EDX (Cobalt standard) analysis results for average compositions of different phases from the coating interface after 16 days air annealing at 700°C

(Average of 4 area analyses)

Phase	Phase composition				
	Average	Cr	Ni	C	O
M (bright area)	Atomic%	17±2.1	82±2.8	1±0.6	0
C (dark area)	Atomic%	63±3.1	0	37±2.6	0
G (grey area)	Atomic%	81±2.9	5±0.9	14±1.9	0
O (dark layer)	Atomic%	29±2.2	4±0.6	0	67±2.1

**Table 5.4** EDX (Cobalt standard) analysis results for average compositions of different phases from coating middle area after 16 days air annealing at 800°C

(Average of 4 area analyses)

Phase	Phase composition			
	Average	Cr	Ni	C
<b>M</b> (bright area)	<b>Atomic%</b>	17±1.8	82±2.9	1±0.3
<b>C</b> (dark area)	<b>Atomic%</b>	63±2.7	0	37±2.1
<b>G</b> (grey area)	<b>Atomic%</b>	60±2.2	6±1.1	34±2.1

**Table 5.5** EDX (Cobalt standard) analysis results for average compositions of different phases from the coating interface after 16 days air annealing at 800°C

(Average of 4 area analyses)

Phase	Phase composition				
	Average	Cr	Ni	C	O
<b>M</b> (bright area)	<b>Atomic%</b>	13±1.3	86±2.3	1±0.8	0
<b>G</b> (grey area)	<b>Atomic%</b>	86±3.2	2±0.8	12±1.2	0
<b>O</b> (dark layer)	<b>Atomic%</b>	30±1.9	1±0.2	0	69±2.5

**Table 5.6** Summary of phases present in the Praxair NiCr-Cr<sub>3</sub>C<sub>2</sub> powders, as-sprayed and heat treated coatings

	Coating middle	Coating interface
<b>Powder</b>	Cr <sub>3</sub> C <sub>2</sub> , Ni(Cr)	
<b>As-sprayed coating</b>	Cr <sub>3</sub> C <sub>2</sub> , Ni(Cr), Cr <sub>2</sub> O <sub>3</sub>	
<b>700°C air annealing for 2 days</b>	Cr <sub>3</sub> C <sub>2</sub> , Ni(Cr), Cr <sub>2</sub> O <sub>3</sub>	Cr <sub>3</sub> C <sub>2</sub> , Cr <sub>7</sub> C <sub>3</sub> , Cr <sub>23</sub> C <sub>6</sub> , Ni(Cr), Cr <sub>2</sub> O <sub>3</sub>
<b>700°C air annealing for 16 days</b>	Cr <sub>3</sub> C <sub>2</sub> , Ni(Cr), Cr <sub>2</sub> O <sub>3</sub>	Cr <sub>7</sub> C <sub>3</sub> , Cr <sub>23</sub> C <sub>6</sub> , Cr <sub>3</sub> C <sub>2</sub> , Ni(Cr), Cr <sub>2</sub> O <sub>3</sub>
<b>800°C air annealing for 2 days</b>	Cr <sub>3</sub> C <sub>2</sub> , Ni(Cr), Cr <sub>2</sub> O <sub>3</sub>	Cr <sub>23</sub> C <sub>6</sub> , Cr <sub>7</sub> C <sub>3</sub> , Cr <sub>3</sub> C <sub>2</sub> , Ni(Cr), Cr <sub>2</sub> O <sub>3</sub>
<b>800°C air annealing for 16 days</b>	Cr <sub>3</sub> C <sub>2</sub> , Ni(Cr), Cr <sub>2</sub> O <sub>3</sub>	Cr <sub>23</sub> C <sub>6</sub> , Cr <sub>7</sub> C <sub>3</sub> , Cr <sub>3</sub> C <sub>2</sub> , Ni(Cr), Cr <sub>2</sub> O <sub>3</sub>

**Table 5.7** Summary of the diffusion distance of the annealed coated substrate samples by SEM-BSE images

	Diffusion distance estimated by SEM-BSE images	
	700°C	800°C
1 hour	100 μm	180 μm
2 days	140 μm	300 μm
8 days	230 μm	400 μm
16 days	370 μm	590 μm

**Table 5.8** EDX analysis results for average compositions of different diffusion areas on the stainless steel substrate after 16 days air annealing at 800°C. (Average of 4 area analyses) See Fig 5.28 and 5.30

Substrate region		Element (Wt. %)		
		Cr	Fe	Ni
Zone 1	1	14.6±0.2	64.3±0.3	21.1±0.4
	2	15.7±1.0	65.1±0.5	19.2±0.5
	3	16.8±1.2	64.9±1.2	18.3±0.4
	4	17.7±0.8	65.6±0.5	16.7±0.5
	5	20.2±0.9	65.4±1.0	14.4±0.5
Zone 2	1	19.4±0.4	67.5±0.1	13.1±0.4
	2	19.9±0.7	70.8±1.5	9.3±0.8
	3	19.6±0.3	71.6±0.9	8.8±1.1
	4	20.2±0.2	71.4±0.4	8.4±0.3
	5	20.2±0.5	71.4±0.8	8.4±0.8
Zone 3	1	20.4±0.1	71.5±0.2	8.1±0.1
	2	20.3±0.6	71.5±0.4	8.2±0.5
	3	19.6±0.1	71.8±0.2	8.6±0.2
	4	19.6±0.9	72.0±0.9	8.4±0.1
	5	19.5±0.2	71.9±0.2	8.6±0.1

**Table 5.9** Summary of the diffusion distance of the annealed coated substrate samples by microhardness variation

	Diffusion distance estimated by microhardness variation	
	700°C	800°C
1 hour	100 µm	200 µm
2 days	150 µm	350 µm
8 days	250 µm	450 µm
16 days	400 µm	750 µm

**Table 5.10** Activities of the elements in NiCr-Cr<sub>3</sub>C<sub>2</sub> coating and stainless steel 304 substrate at 800°C calculated by Thermo-Calc<sup>®</sup>4

Element	Activity in NiCr-Cr <sub>3</sub> C <sub>2</sub> coating	Activity in Stainless steel 304
C	1.9x10 <sup>-1</sup>	5.8x10 <sup>-4</sup>
Cr	4.1x10 <sup>-4</sup>	5.3x10 <sup>-3</sup>
Ni	3.3x10 <sup>-3</sup>	1.7x10 <sup>-4</sup>
Fe	0	3.5x10 <sup>-3</sup>

**Table 5.11** Summary of the diffusion distance of the annealed coated substrate samples by carbon diffusion modelling

	Diffusion distance estimated carbon diffusion modelling	
	700°C	800°C
<b>1 hour</b>	62 µm	101 µm
<b>2 days</b>	426 µm	703 µm
<b>8 days</b>	852 µm	1405 µm
<b>16 days</b>	1204 µm	1987 µm

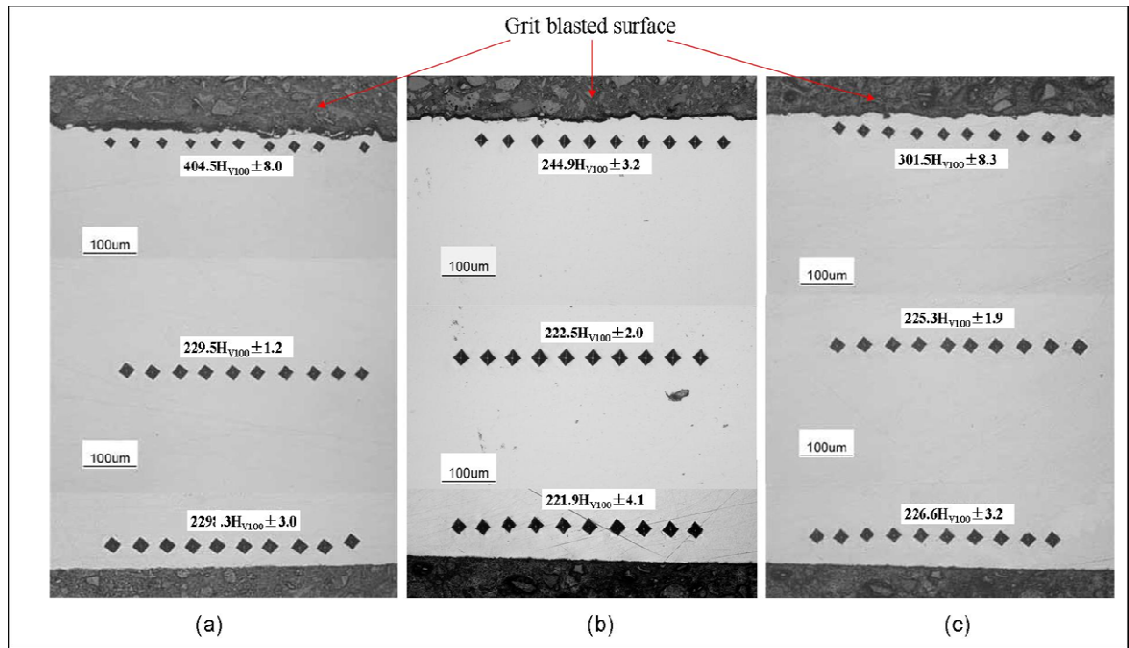


Fig 5.1 Microhardness (100 g load) of (a) grit blasted stainless steel 304 and grit blasted stainless steel 304 after 20 minutes 750°C annealing followed by (b) air cooling (c) oil quenching

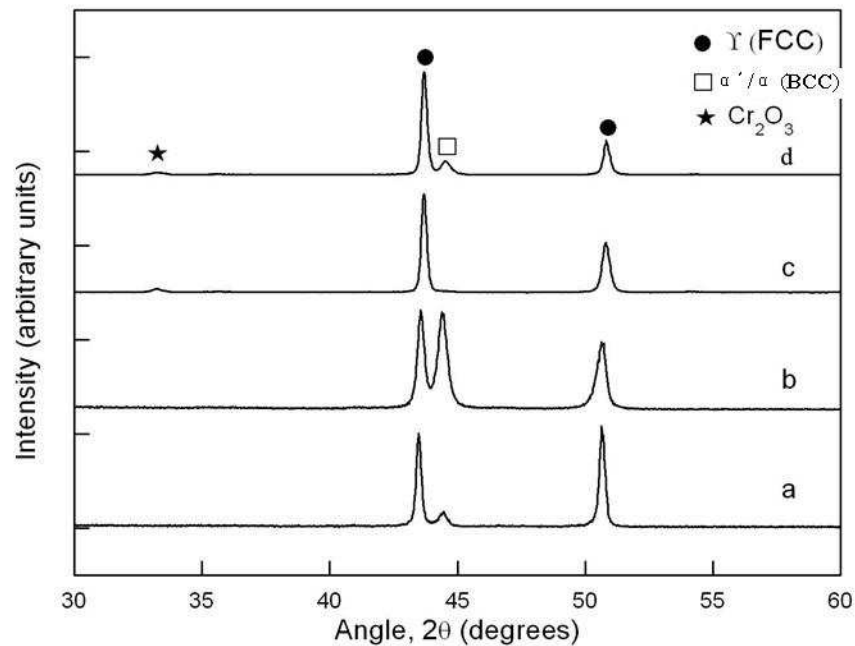


Fig 5.2 X-ray diffraction patterns from 304 stainless steel surface with Cu K $\alpha$  radiation. (a), Original as-received surface. (b), Surface after grit blasting. (c), Grit blasted surface after a thermal annealing procedure at 750°C for 20 min with oil quenching. (d) Annealing at 750°C for 20 min with air cooling. (XRD patterns of these samples are provided in appendix)

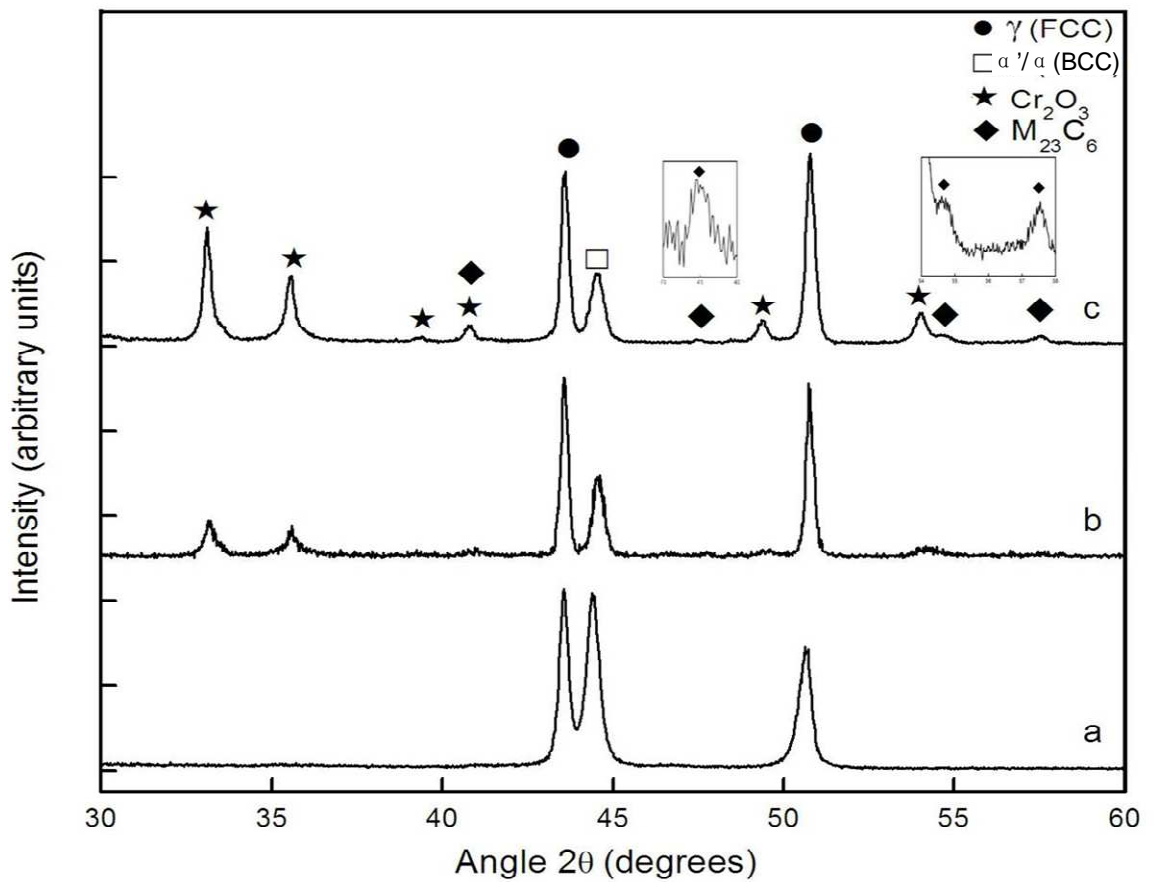


Fig 5.3 XRD patterns of following heat treatment of stainless steel 304 (a)as-received grit blasted surface, (b)700°C 2 days air cooled, (c)800°C 2 days air cooled.

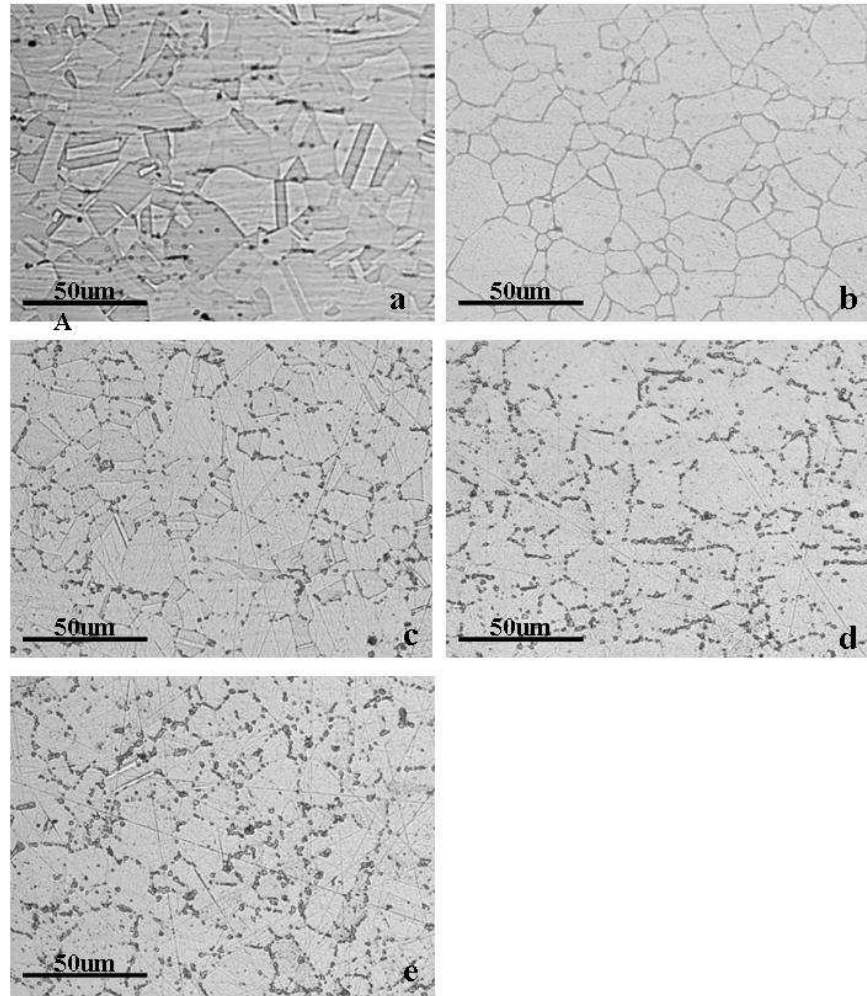


Fig 5.4 Optical morphology of 304 stainless steel (a) as-received, b,c,d,e following heat treated at 800°C for 1 hour, 2 days, 8 days, and 16 days and air cooling

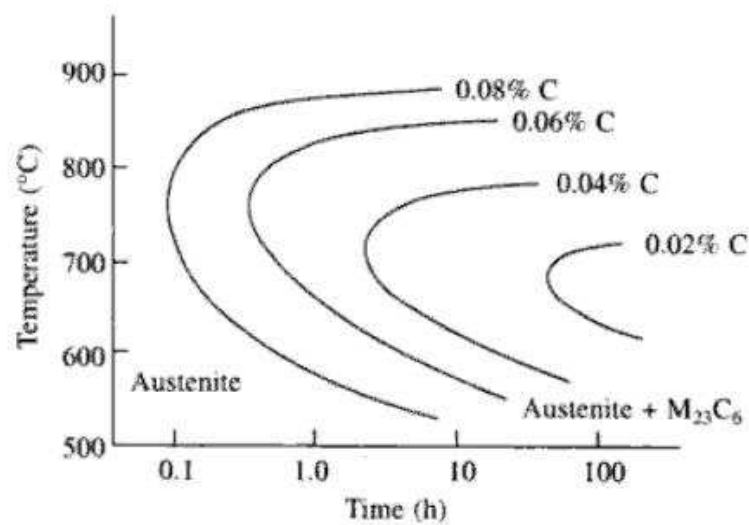
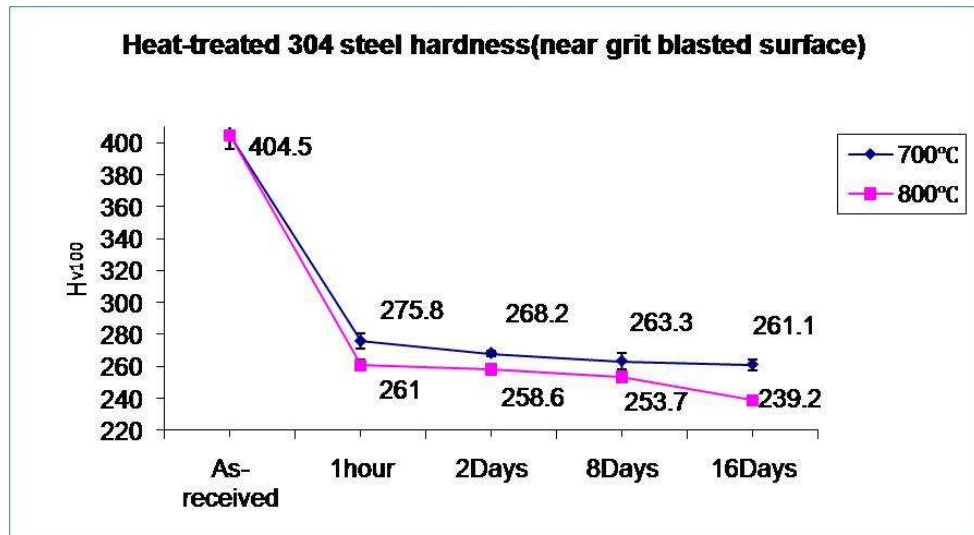
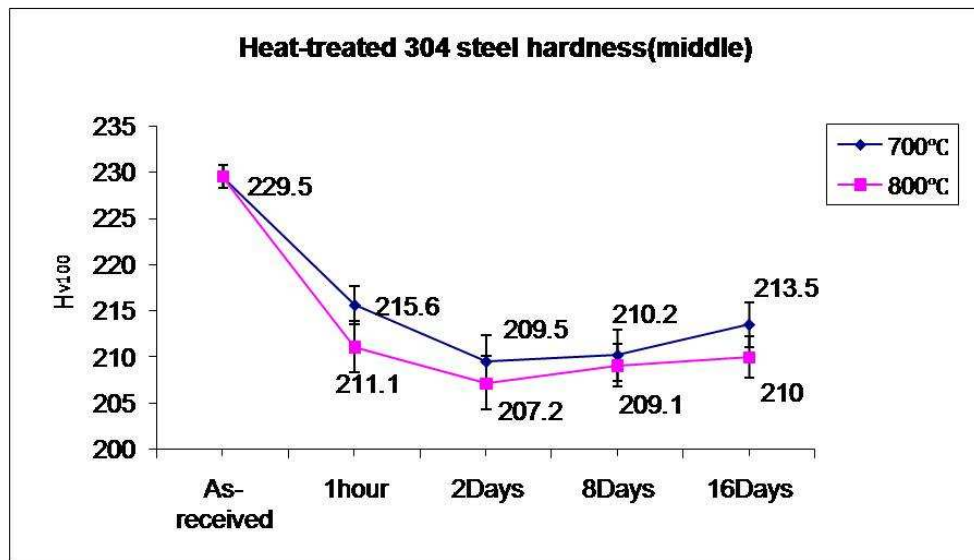


Fig 5.5 Influence of C content on the kinetics of M<sub>23</sub>C<sub>6</sub> precipitation austenitic stainless steel (Philip, 2003)



(a)



(b)

Fig 5.6 Bar chart showing (a) Microhardness of as-received and heat-treated 304 measured approximately 5  $\mu$ m from the grit blasted surface. (b) Microhardness of heat-treated stainless steel 304 measured in the mid-plane of the sheet. In both cases values are the average of 10 indents.

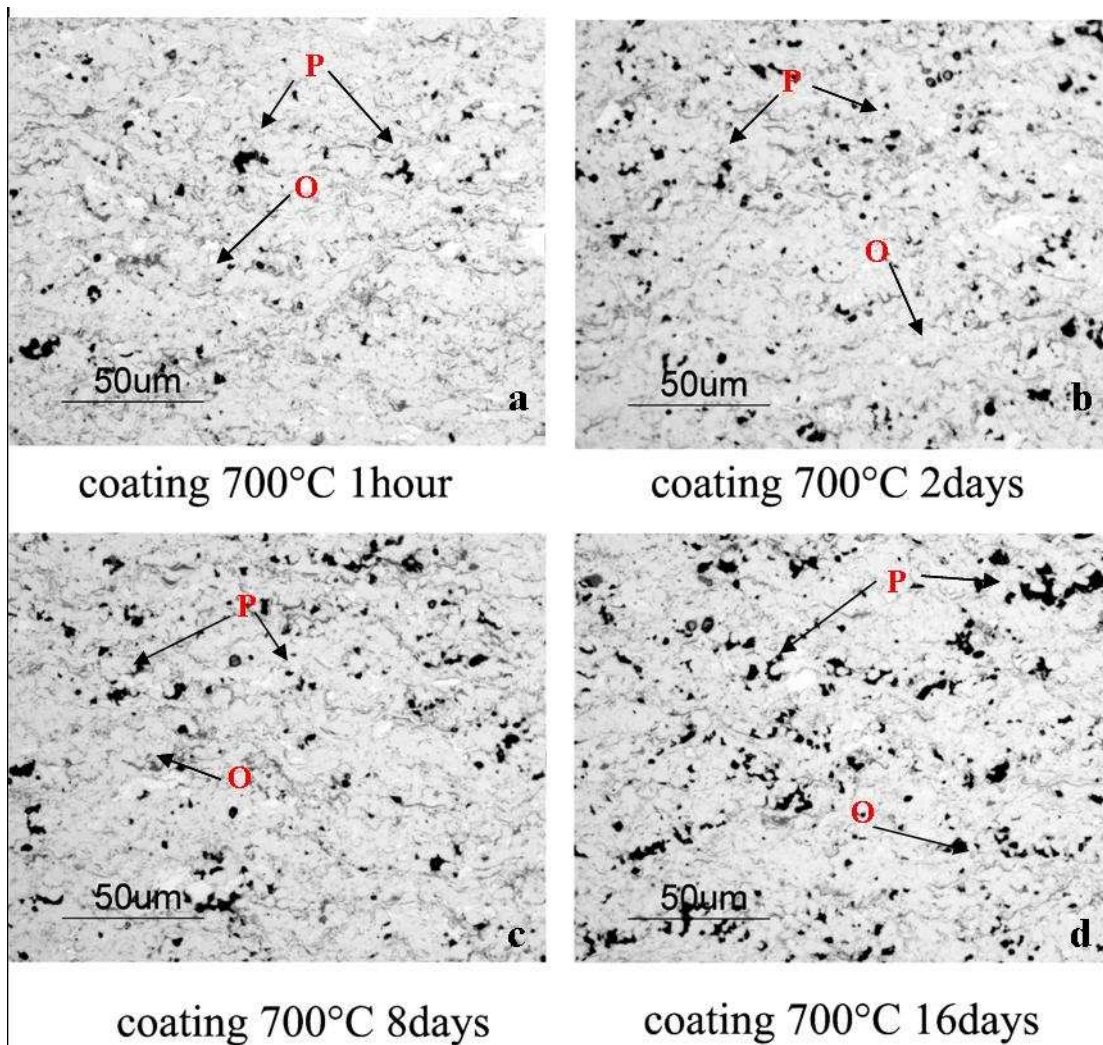


Fig 5.7 Optical micrograph of the polished cross-section of the 700°C annealed NiCr-Cr<sub>3</sub>C<sub>2</sub> coatings for times of 1 hour, 2 days, 8 days and 16 days in air (P: pores; O: oxide )

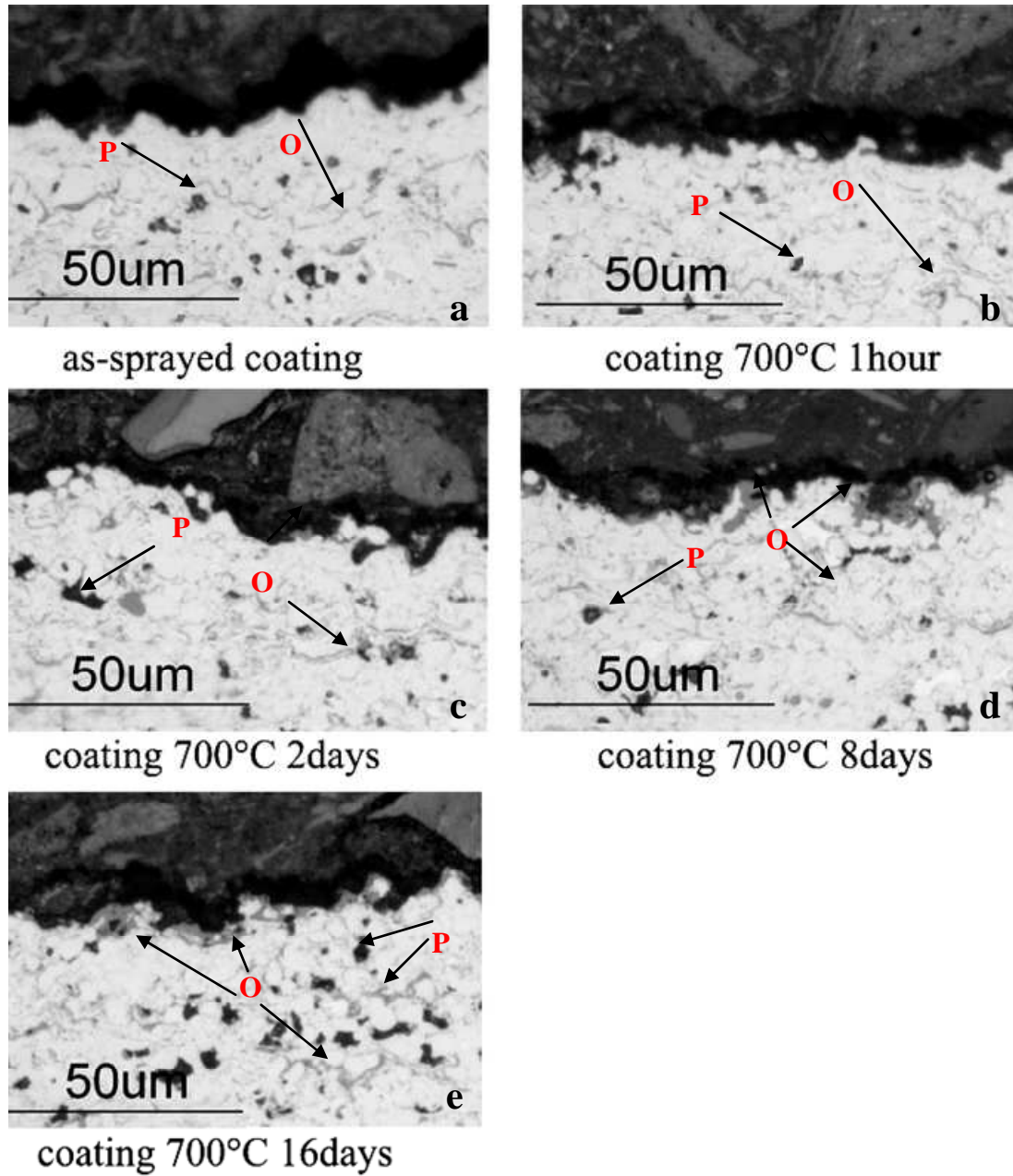


Fig 5.8 Optical micrograph of the polished, cross-sectioned top surface region of as-sprayed and 700°C air annealed NiCr-Cr<sub>3</sub>C<sub>2</sub> coatings for times of 1 hour, 2, 8 and 16 days (P stands for pores; O stands for oxide )

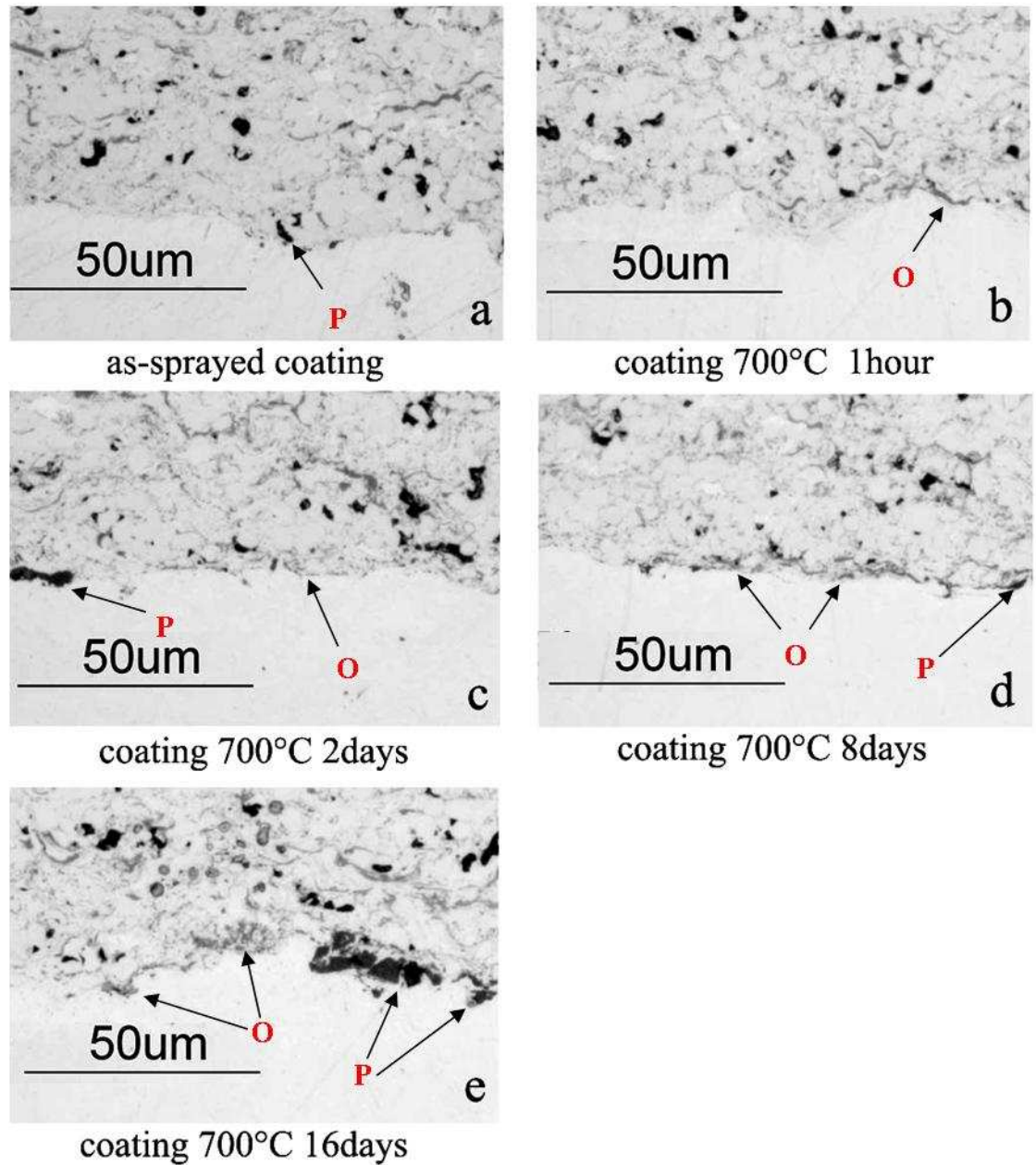


Fig 5.9 Optical micrograph of the polished, cross-sectioned interface of as-sprayed and 700°C air annealed NiCr-Cr<sub>3</sub>C<sub>2</sub> coatings for time of 1 hour, 2, 8 and 16 days (P stands for pores; O stands for oxide )

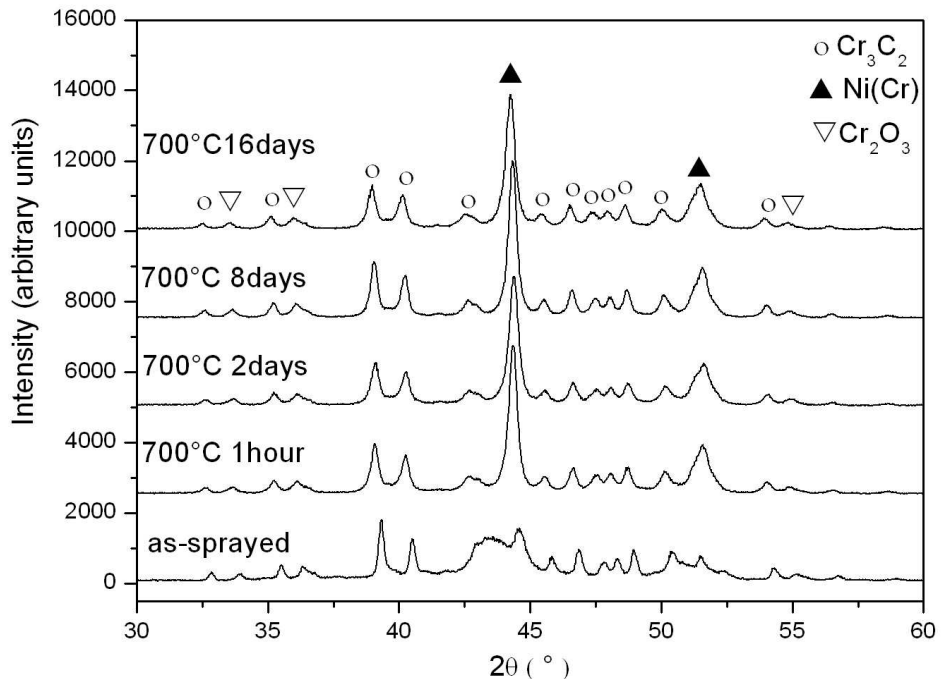


Fig 5.10 X-ray diffractograms from ground top surface of coatings annealed at 700°C from 1 hour to 16 days. The XRD spectrum of the as-sprayed coating is used as a reference. (XRD pattern of 700°C 16 days annealing sample is provided in appendix)

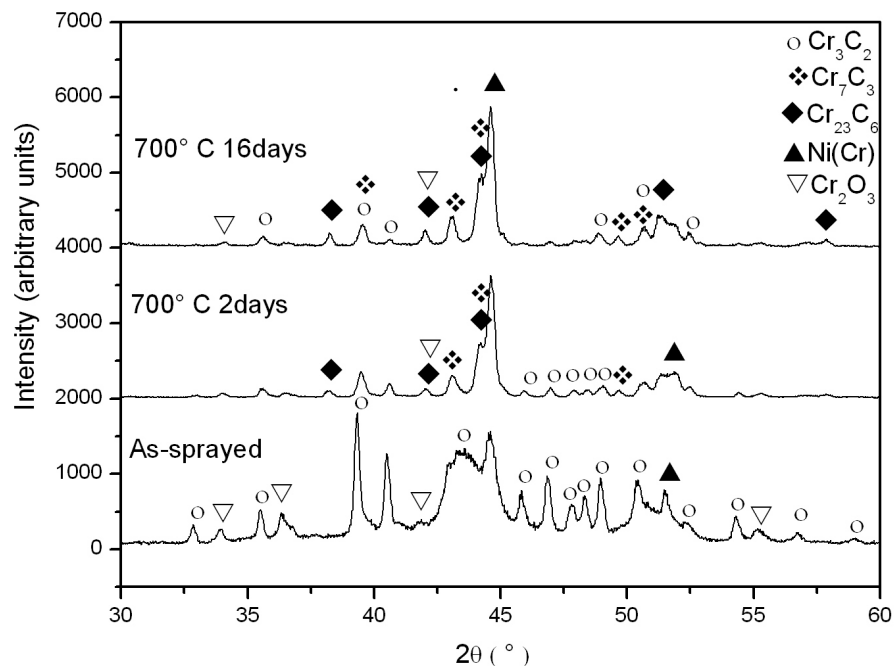


Fig 5.11 X-ray diffractograms from the coating-substrate interface followed by annealing at 700°C for 2 days and 16 days. The XRD spectrum of as-sprayed coating is used as reference. (XRD pattern of 700°C 16 days annealing sample is provided in appendix)

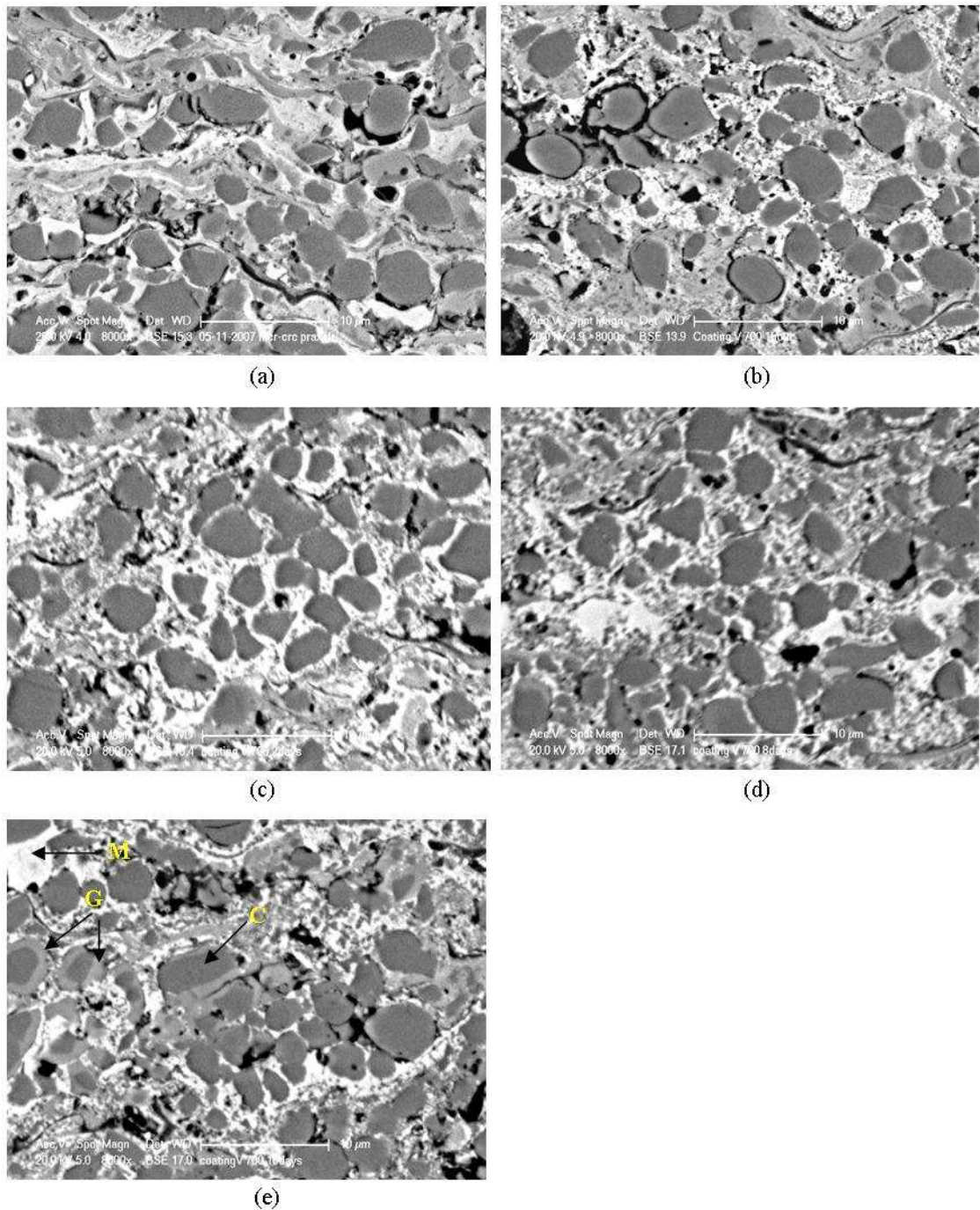


Fig 5.12 SEM-BSE cross-section images of coating middle area in the (a) as- sprayed condition and following heat treatment at 700°C for (b)1 hour, (c)2 days, (d)8 days and (e)16 days

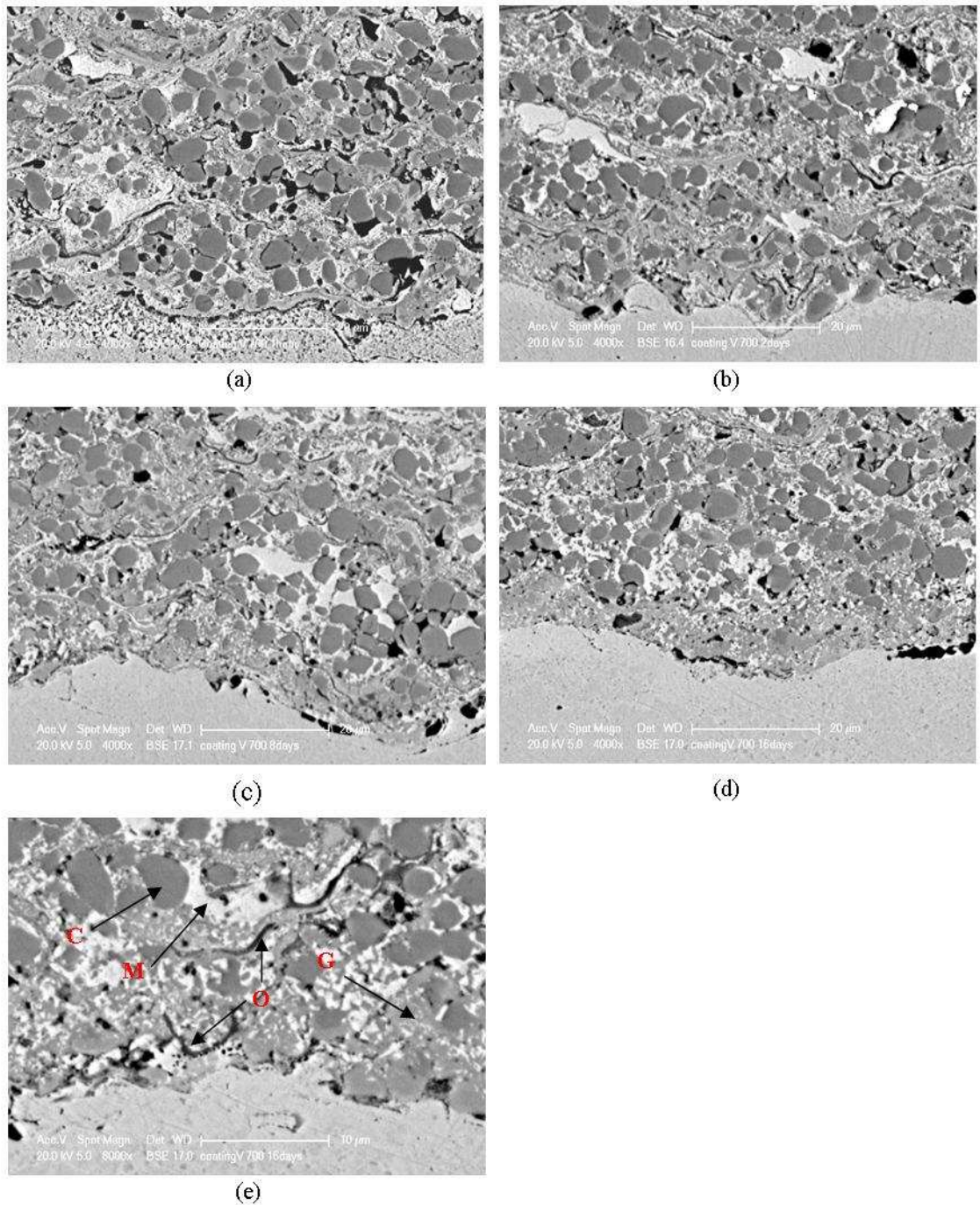


Fig 5.13 SEM-BSE cross-section images of the coating interface area after heat treatment at 700°C for (a) 1 hour, (b) 2 days, (c) 8 days and (d) & (e) 16 days

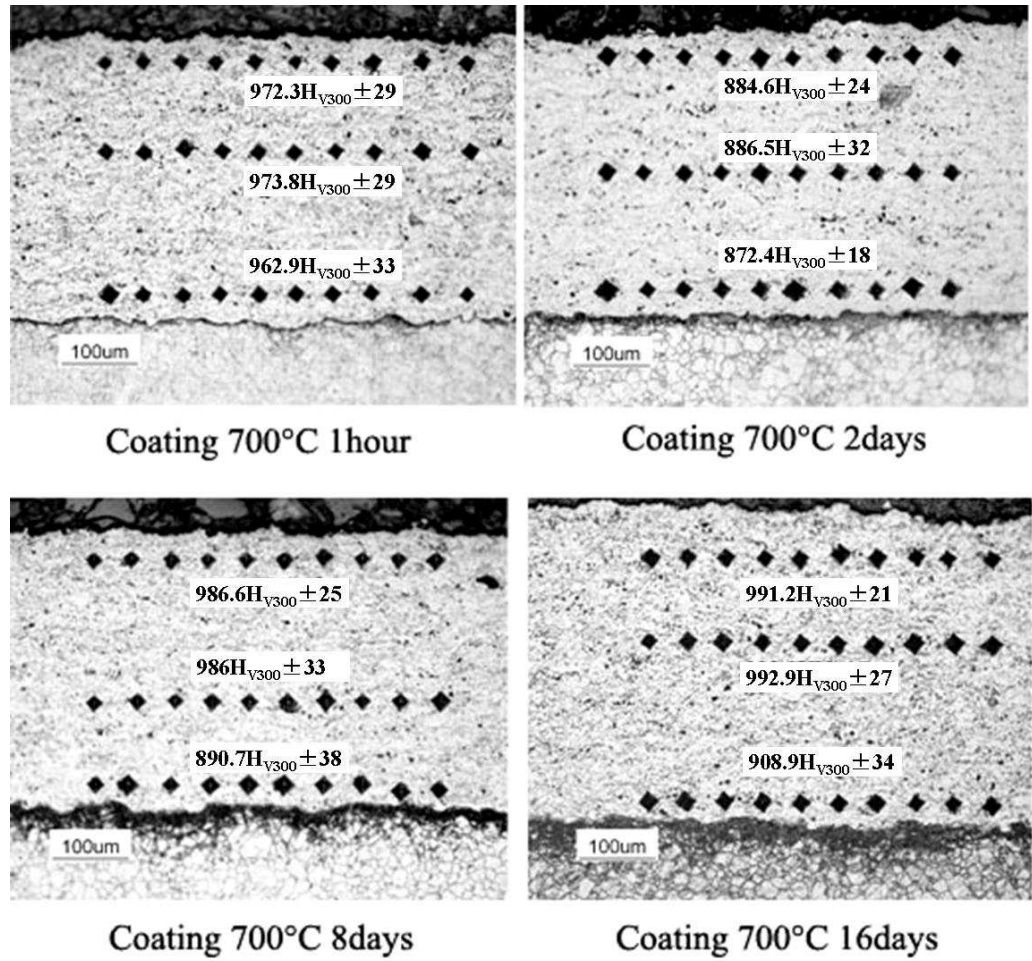


Fig 5.14 Microhardness measurements (300 gm load) on coating samples after 700°C heat treatment with 1 hour, 2 days, 8 days and 16 days

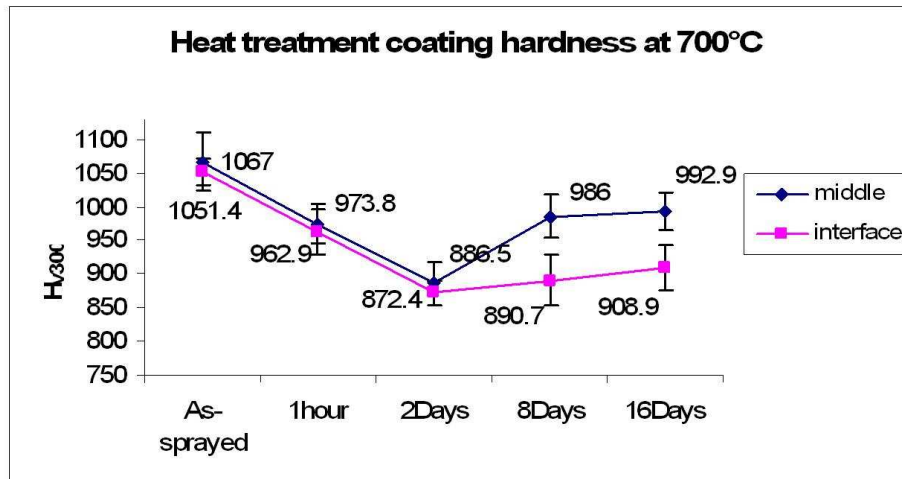


Fig 5.15 Microhardness measurements from middle and interface on coating samples after 700°C heat treatment

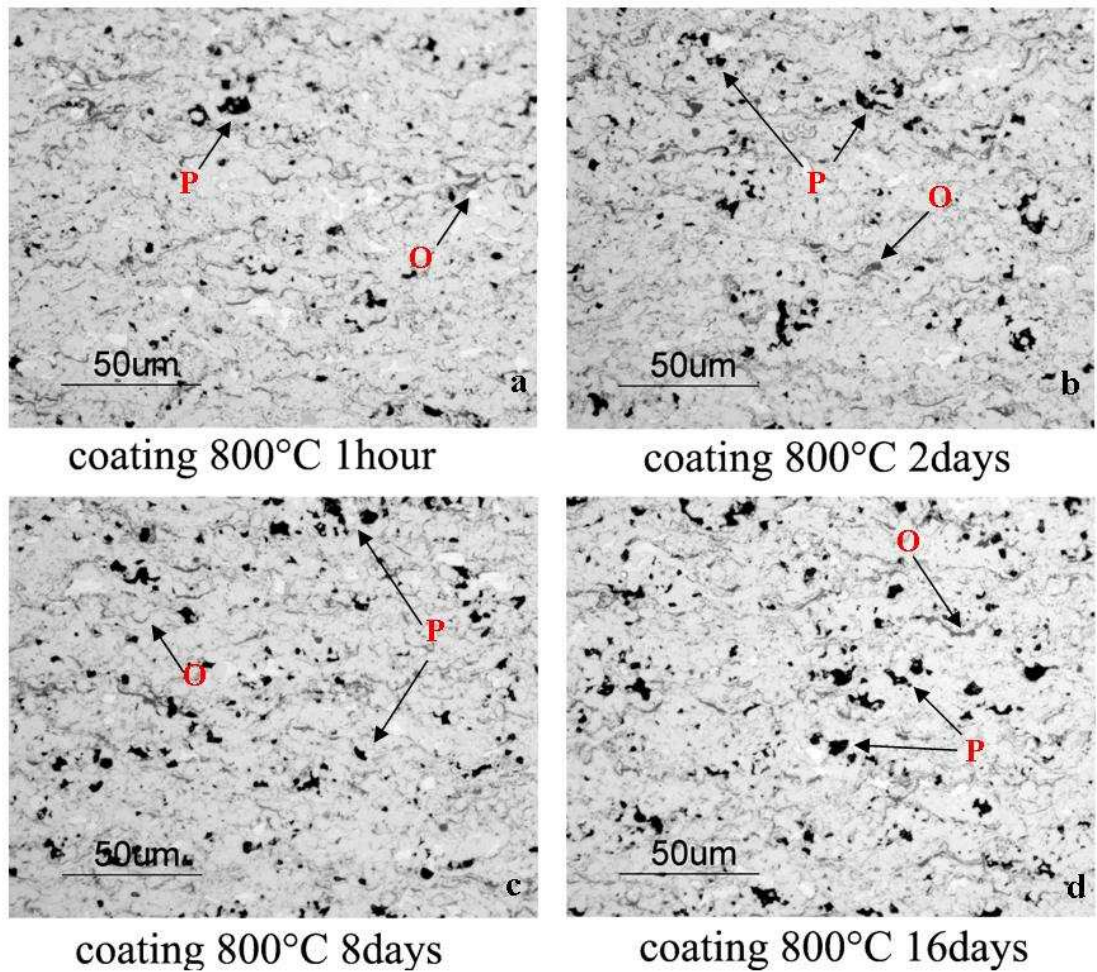


Fig 5.16 Optical micrograph of the polished cross-section of the 800°C air annealed NiCr-Cr<sub>3</sub>C<sub>2</sub> coatings for times of 1 hour, 2 days, 8 days and 16 days (P stands for pores; O stands for oxide )

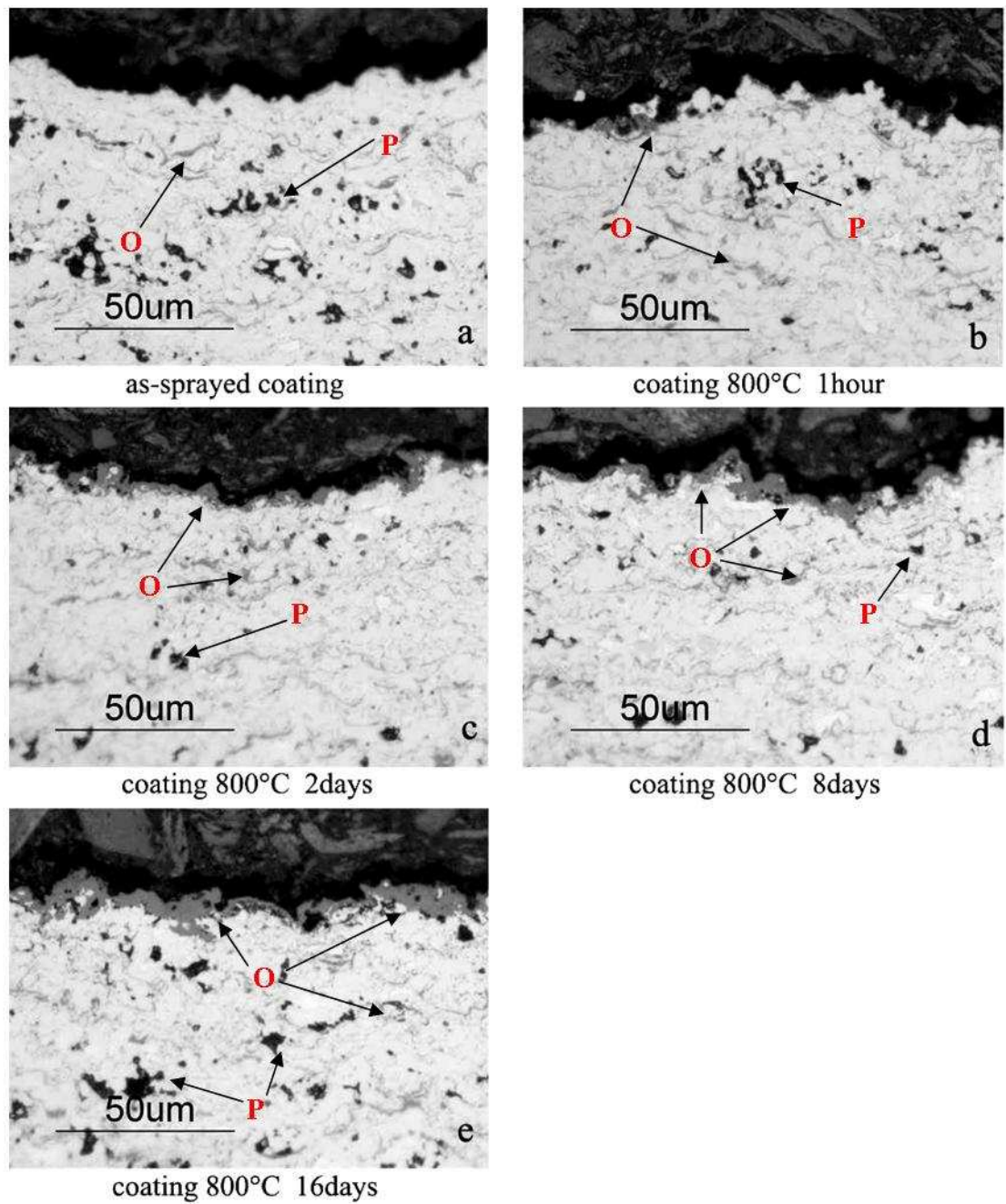


Fig 5.17 Optical micrograph of the polished, cross-sectioned top surface region of as-sprayed and 800°C air annealed NiCr-Cr<sub>3</sub>C<sub>2</sub> coatings for times of 1 hour, 2, 8 and 16 days (P stands for pores; O stands for oxide )

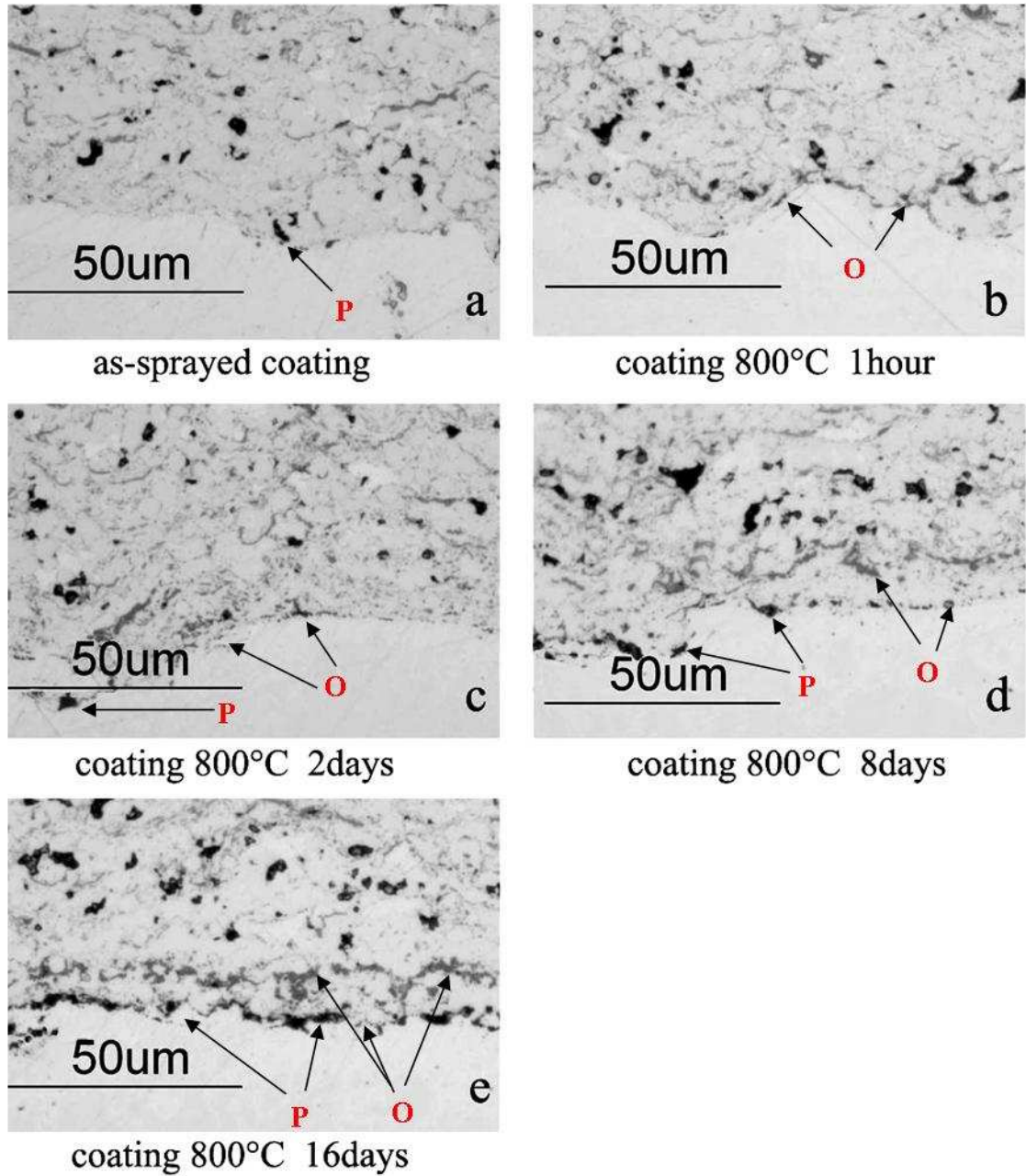


Fig 5.18 Optical micrograph of the polished, cross-sectioned interface region of as-sprayed and 800°C air annealed NiCr-Cr<sub>3</sub>C<sub>2</sub> coatings for times of 1 hour, 2, 8 and 16 days (P stands for pores; O stands for oxide )

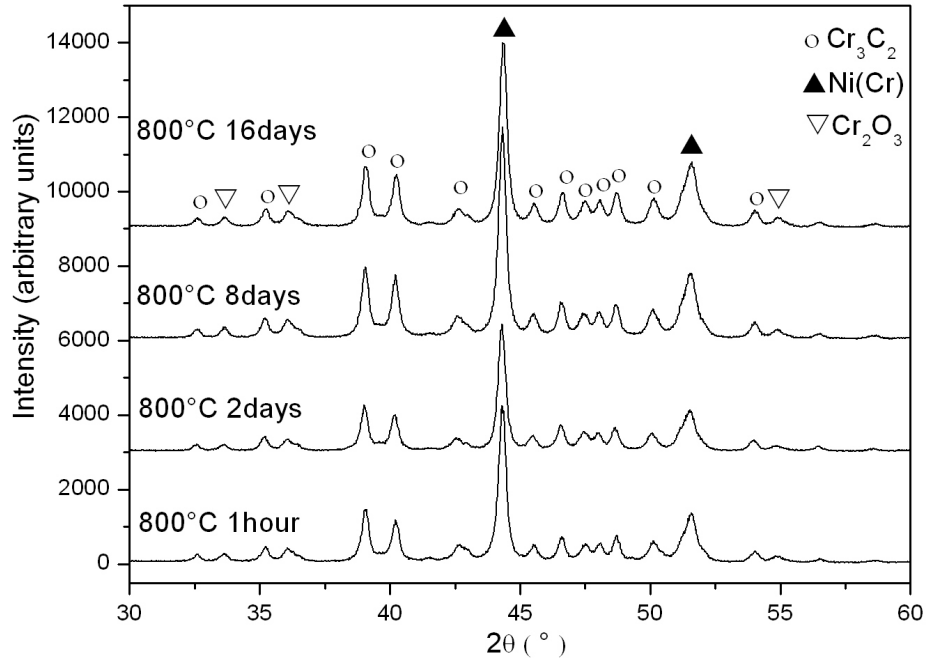


Fig 5.19 X-ray diffractograms from ground top surface of coatings annealed at 800°C from 1 hour to 16 days

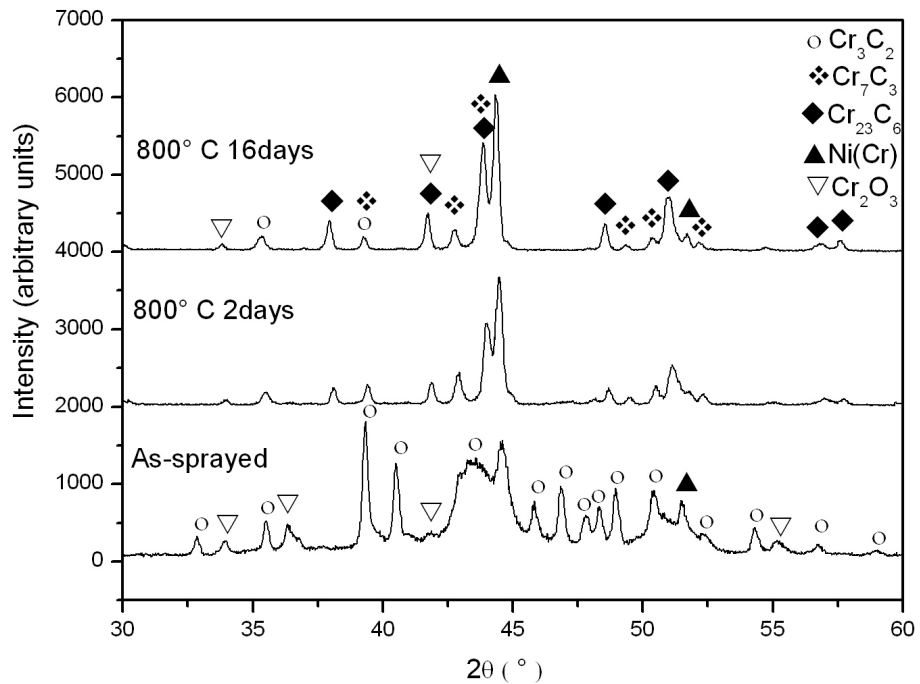


Fig 5.20 X-ray diffractograms from the coating-substrate interface followed by annealing at 800°C for 2 days and 16 days. The XRD spectrum of the as-sprayed coating is used as a reference.

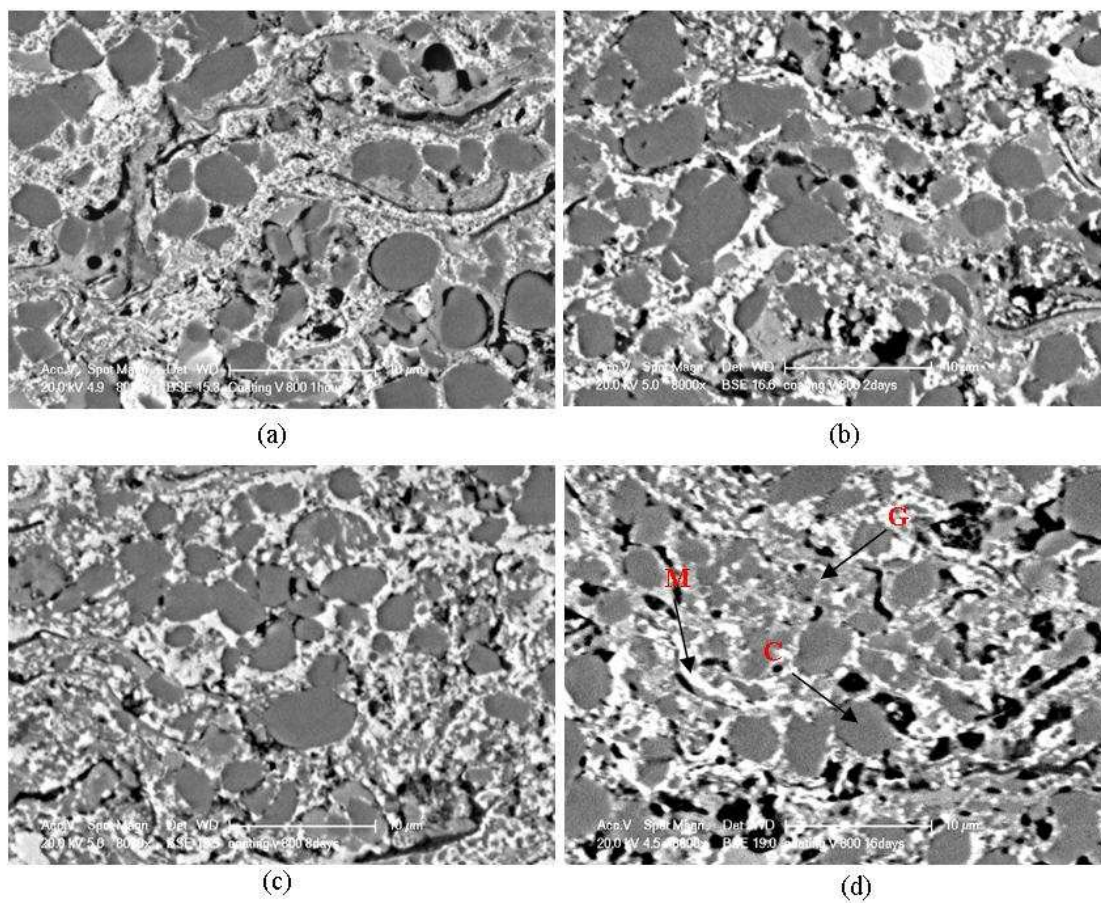


Fig 5.21 SEM-BSE cross-section images of coating middle area after heat treatment at 800°C for (a) 1 hour, (b) 2 days, (c) 8 days and (d) 16 days

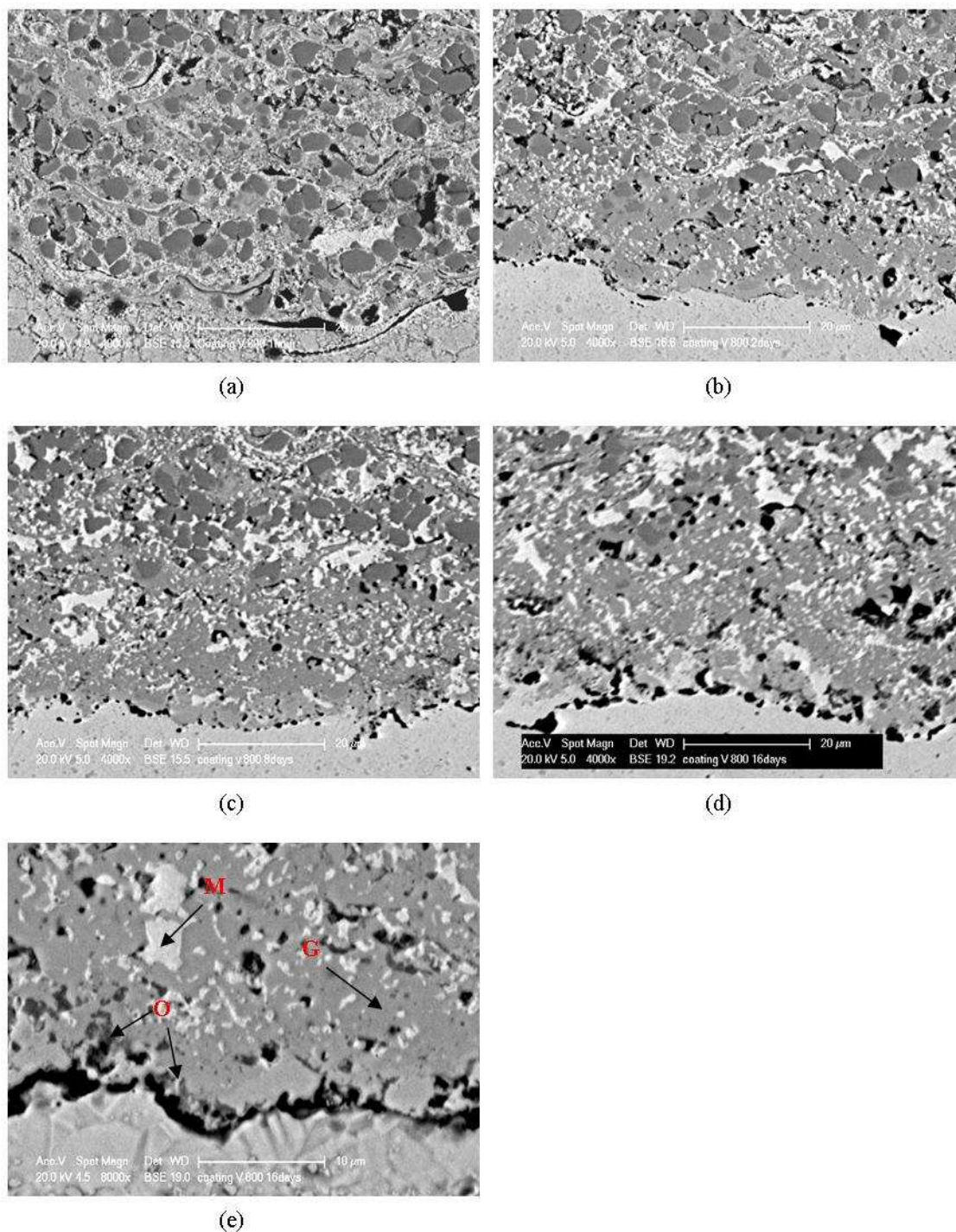


Fig 5.22 SEM-BSE cross-section images of the coating interface area after heat treatment at 800°C for (a) 1 hour, (b) 2 days, (c) 8 days and (d) & (e) 16 days

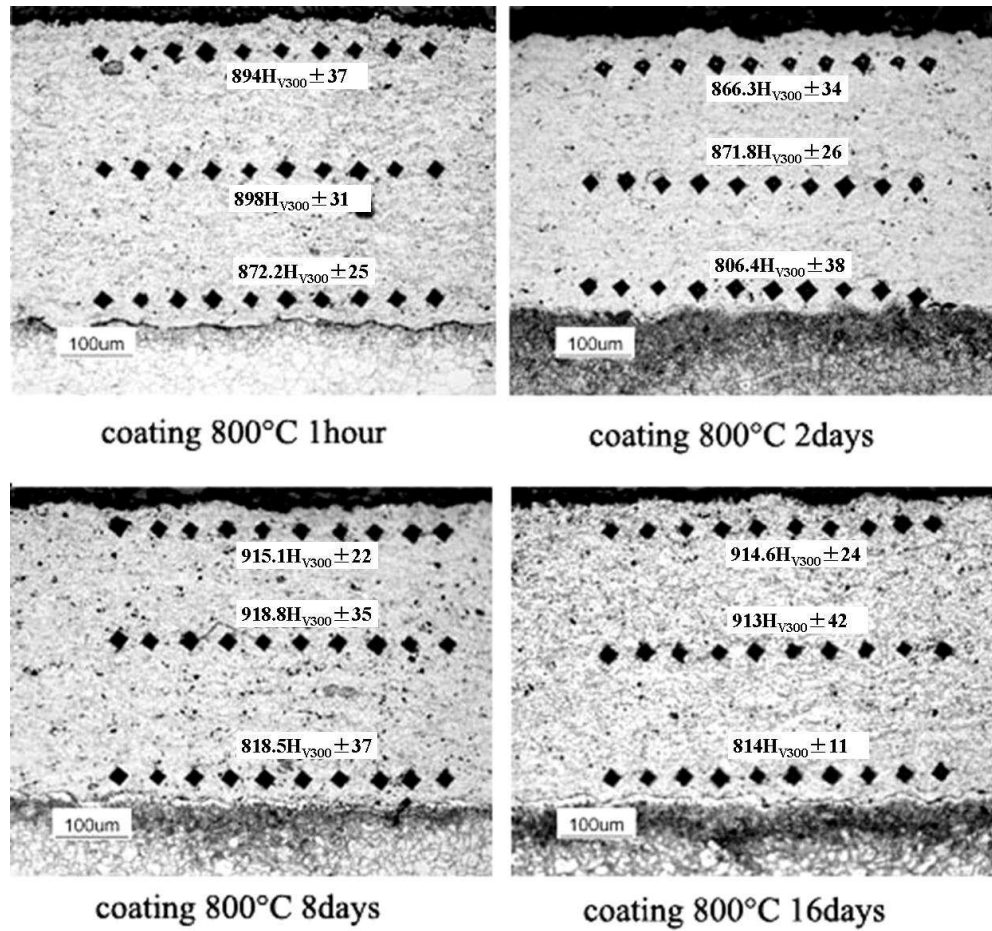


Fig 5.23 Microhardness measurements (300 mg load) on coating samples after 800°C heat treatment with 1 hour, 2 days, 8 days and 16 days

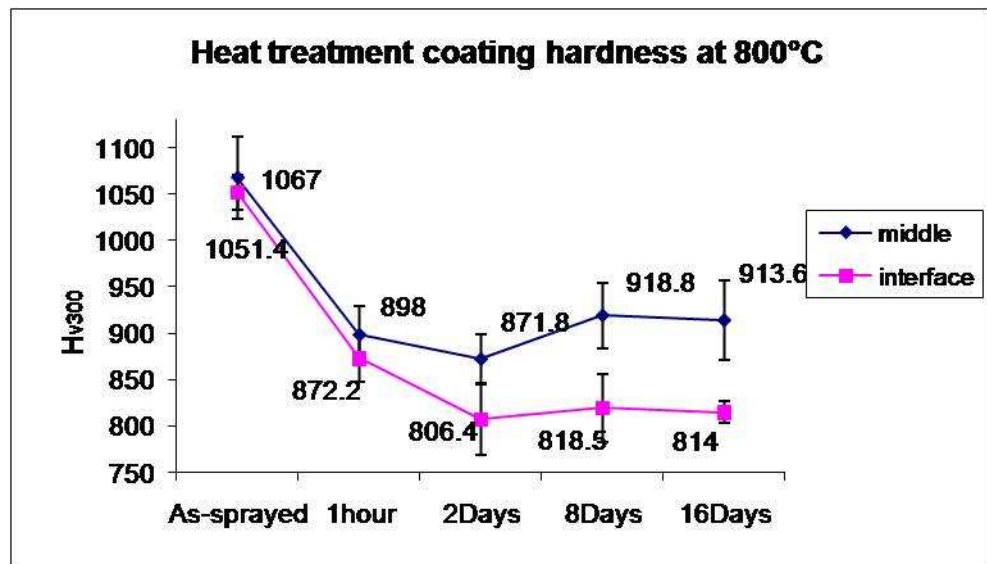


Fig 5.24 Microhardness measurements from middle and interface on coating samples after 800°C heat treatment

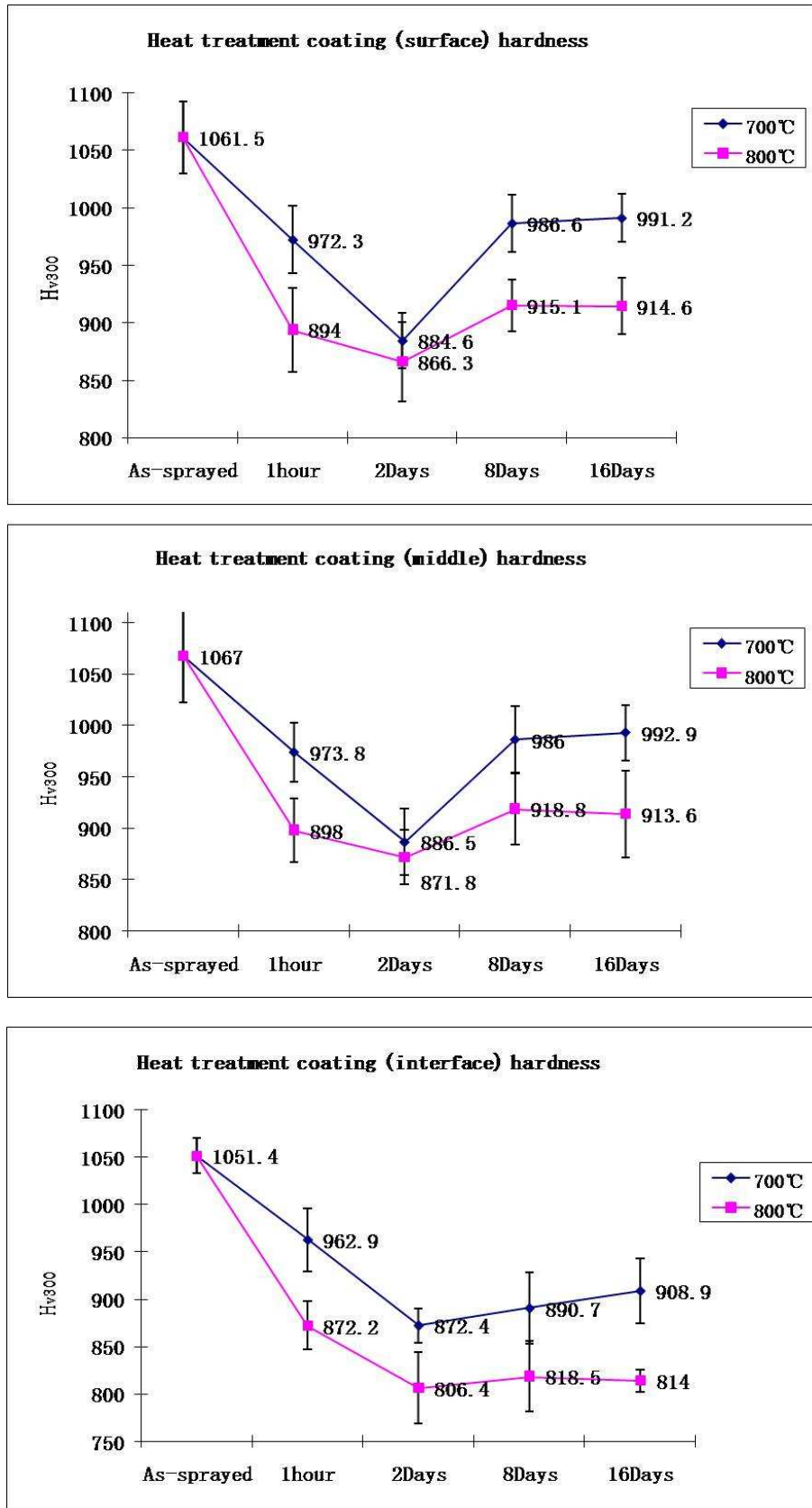


Fig 5.25 Microhardness comparisons on coatings after 700°C and 800°C heat treatment

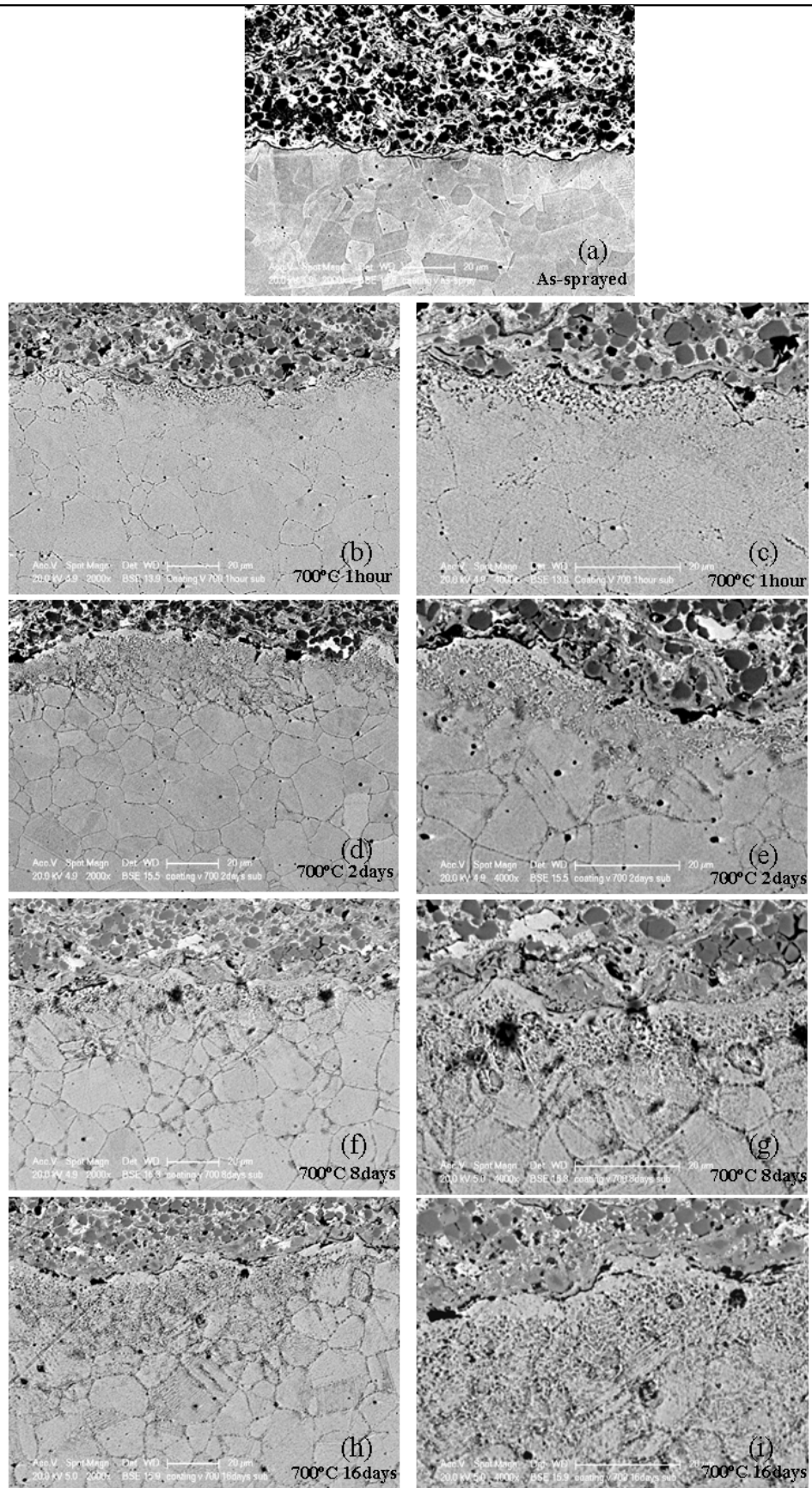


Fig 5.26 SEM/BSE lower and higher magnification images of etched cross-sections of coating-substrate interface following annealing for increasing times at 700°C

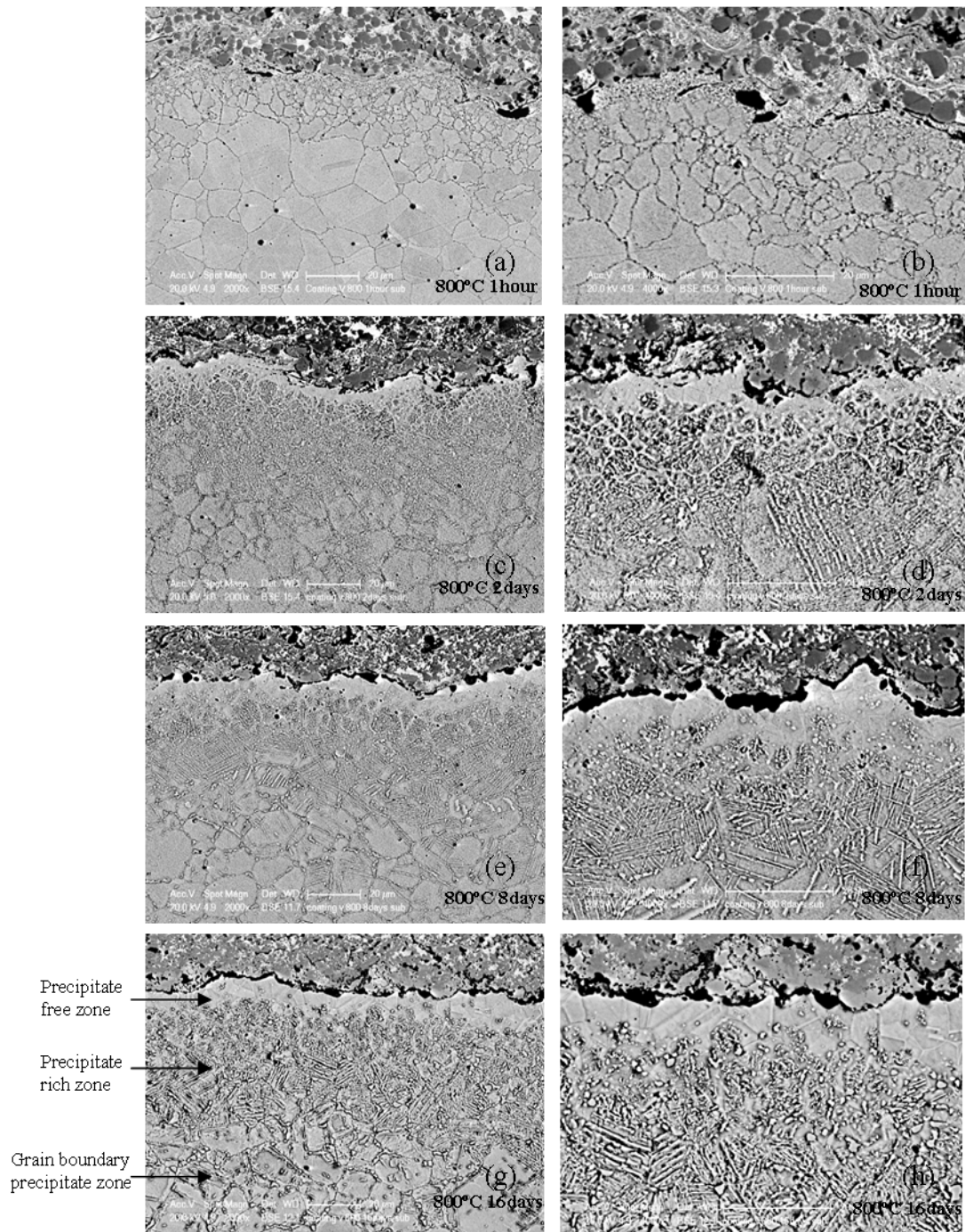


Fig 5.27 SEM/BSE lower and higher magnification images of etched cross-sections of coating-substrate interface following annealing for increasing times at 800°C

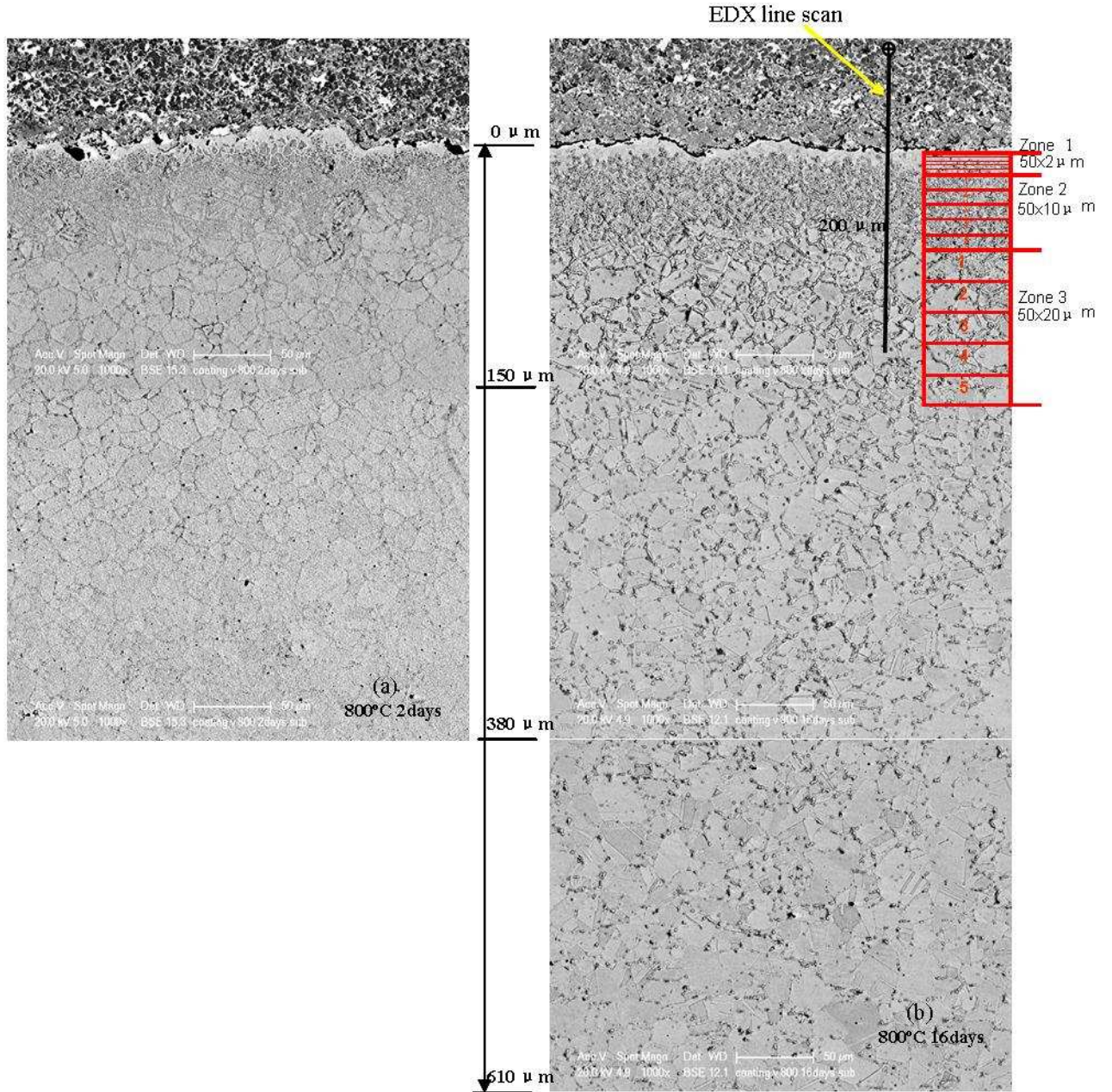


Fig 5.28 SEM-BSE images of etched NiCr-Cr<sub>3</sub>C<sub>2</sub> coated substrate samples which have been annealed at 800°C for 2 days and 16 days

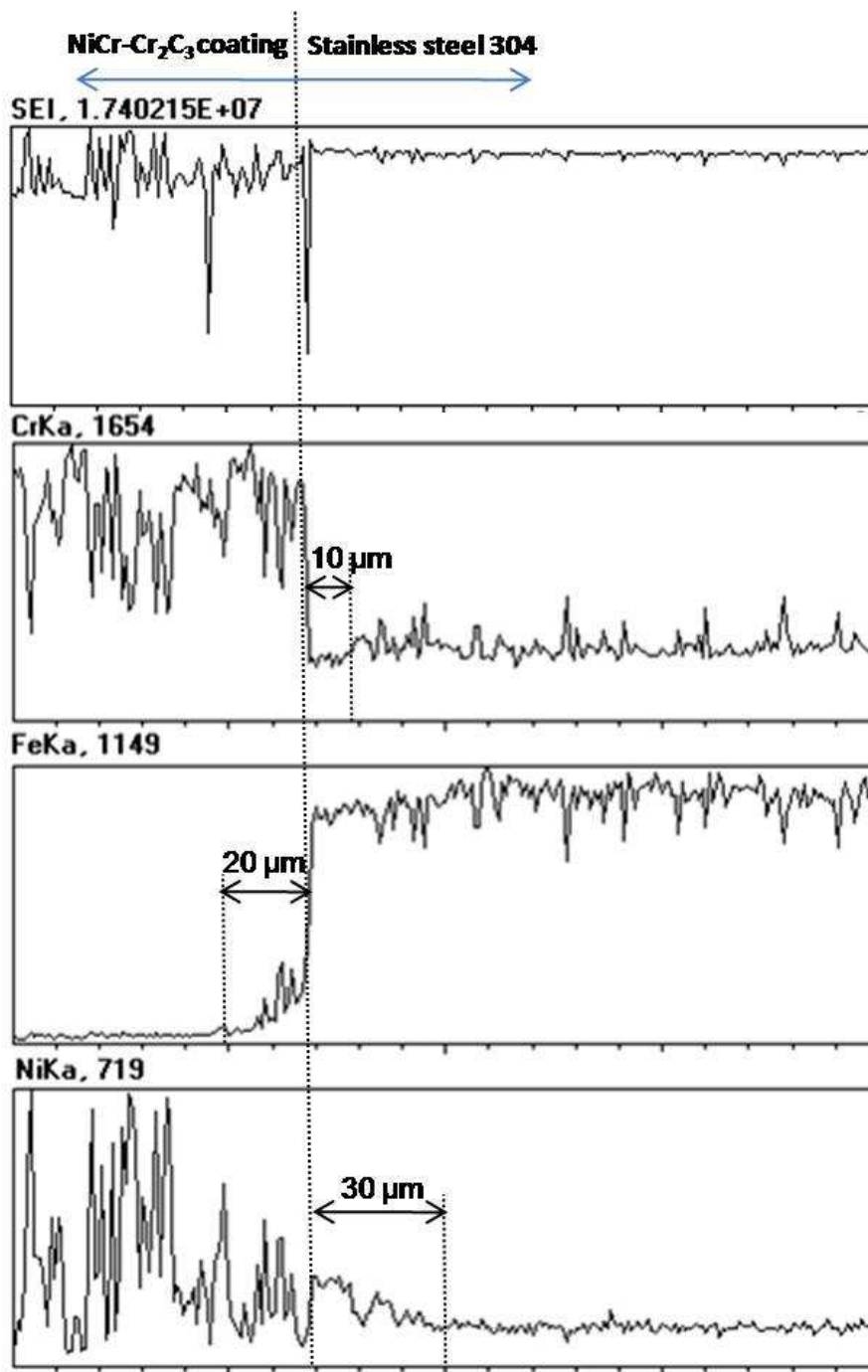


Fig 5.29 EDX line scan across the coating/substrate interface of the sample after 16 days 800°C air annealing shown in Fig 5.28 (b). The total scan length was 200 μm.

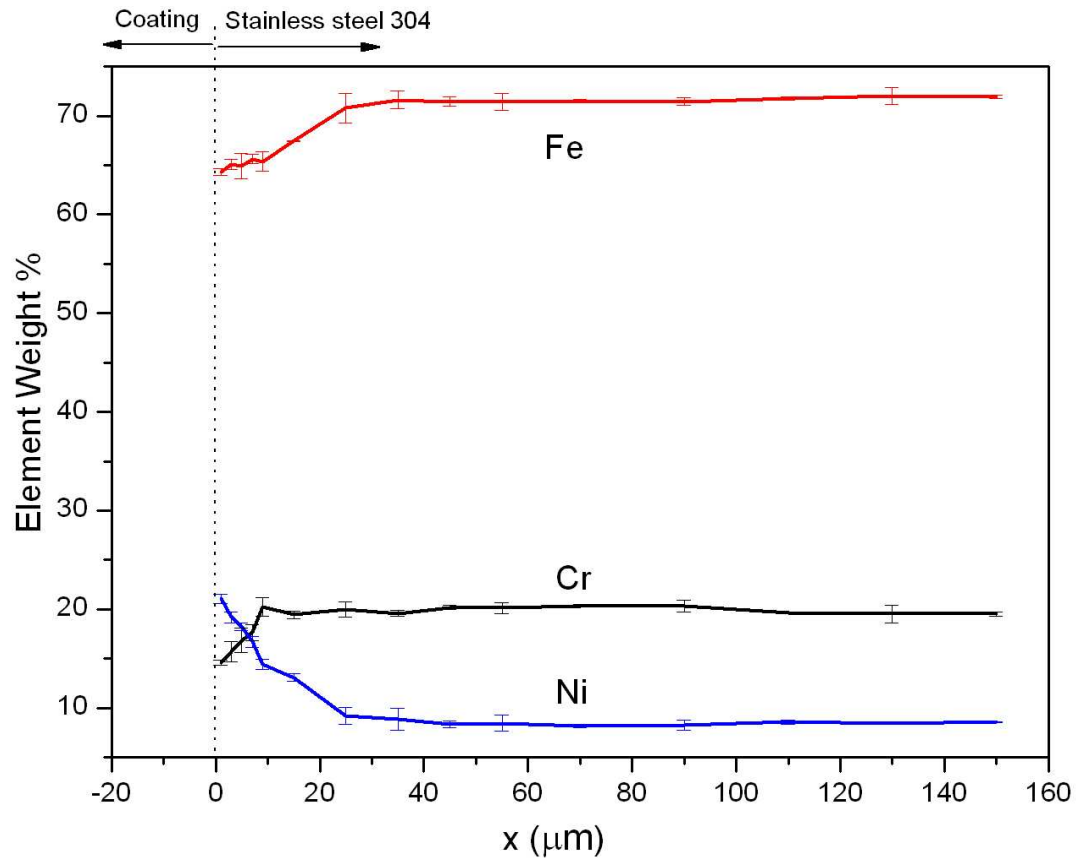


Fig 5.30 EDX composition analysis of coated stainless steel substrate after 16 days at 800°C using the area analysis shown in 5.28 (b)

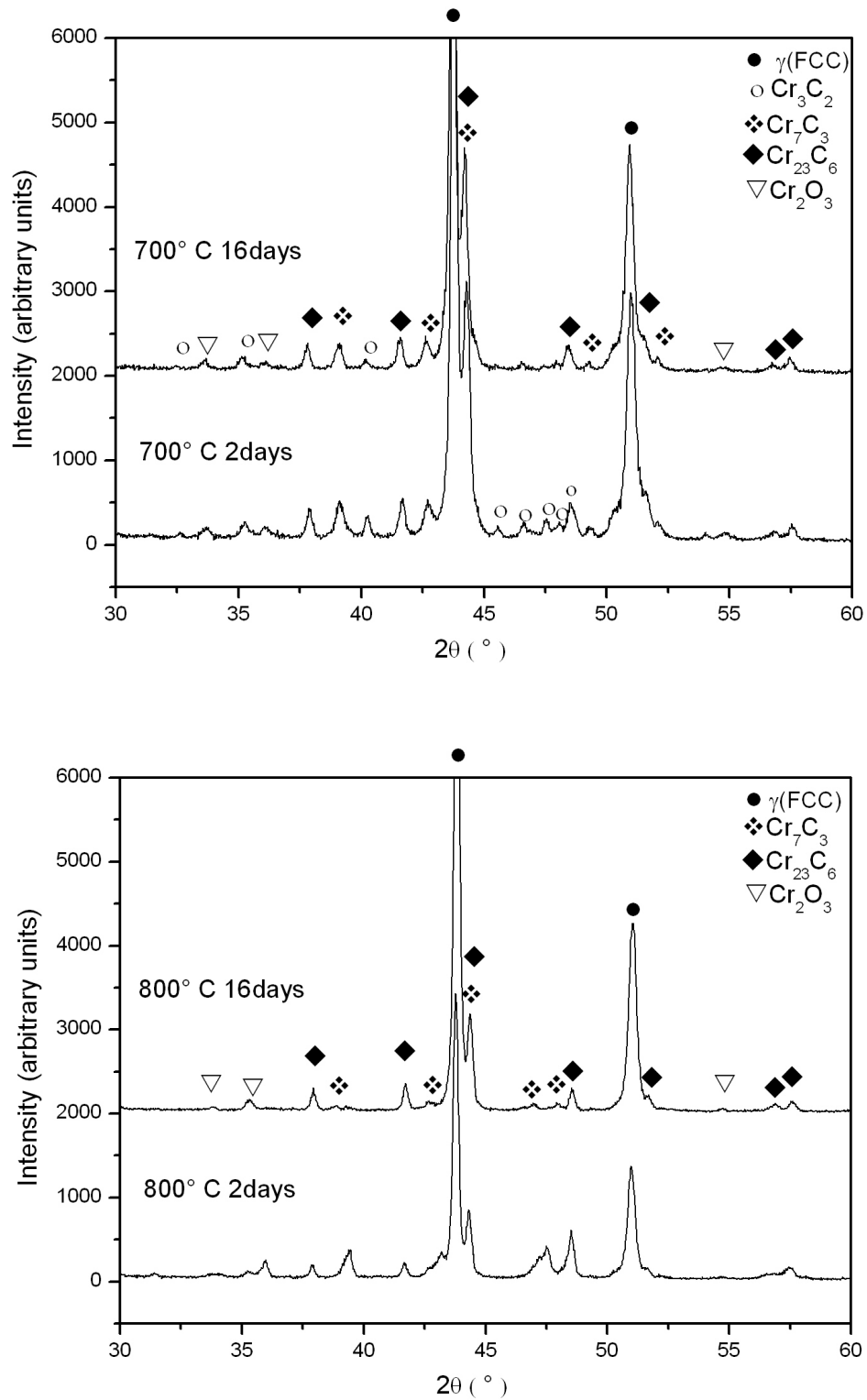


Fig 5.31 X-ray diffractograms from the substrate side of the interface following annealing at 700 and 800°C for 2 days and 16 days. (XRD pattern of 800°C 16 days annealing sample is provided in appendix)

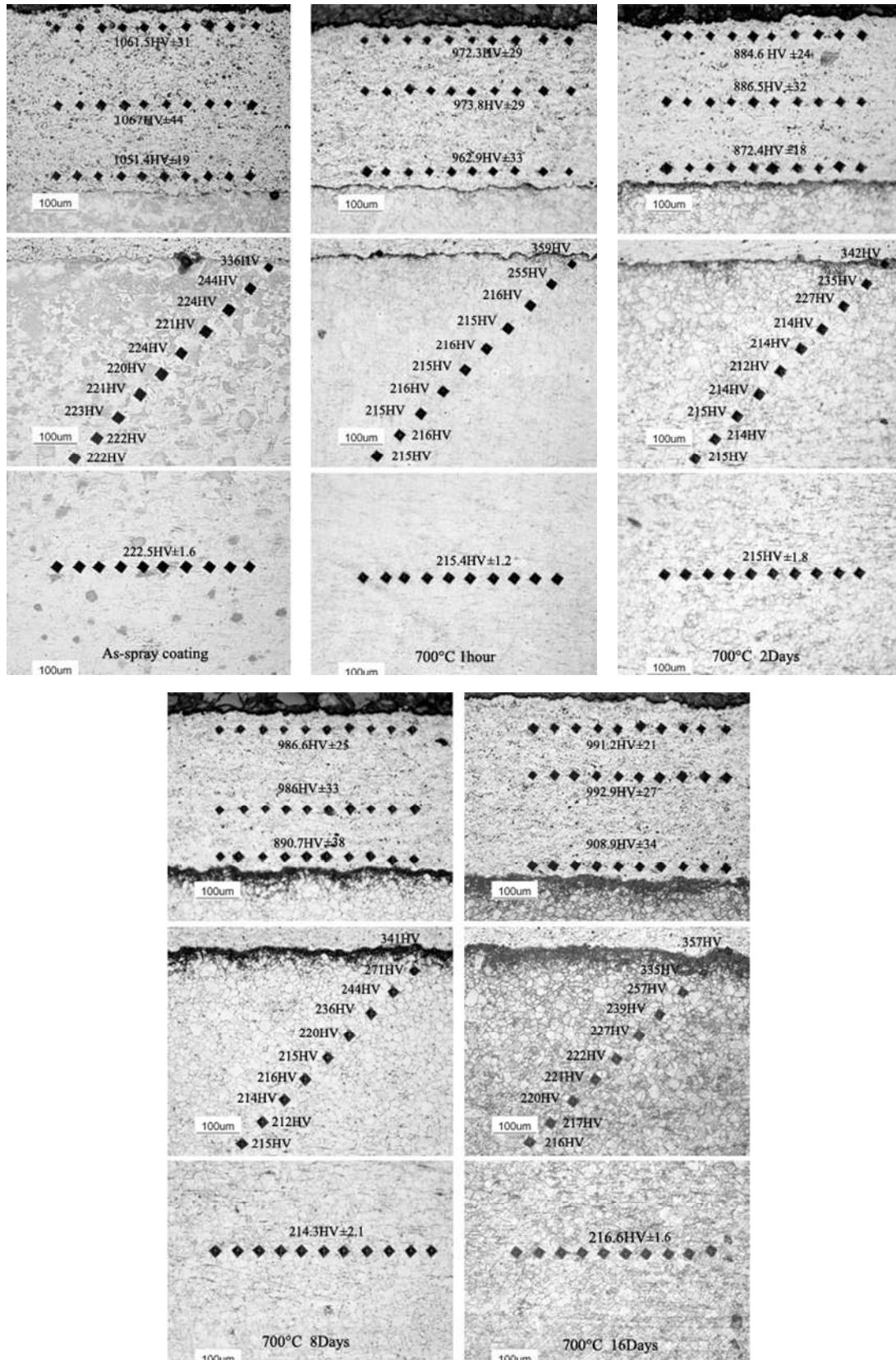


Fig 5.32 Microhardness measurements on coating (300 g load applied) and coated substrate (100 g load applied) samples following 700°C heat treatment for 1 hour, 2, 8 and 16 days

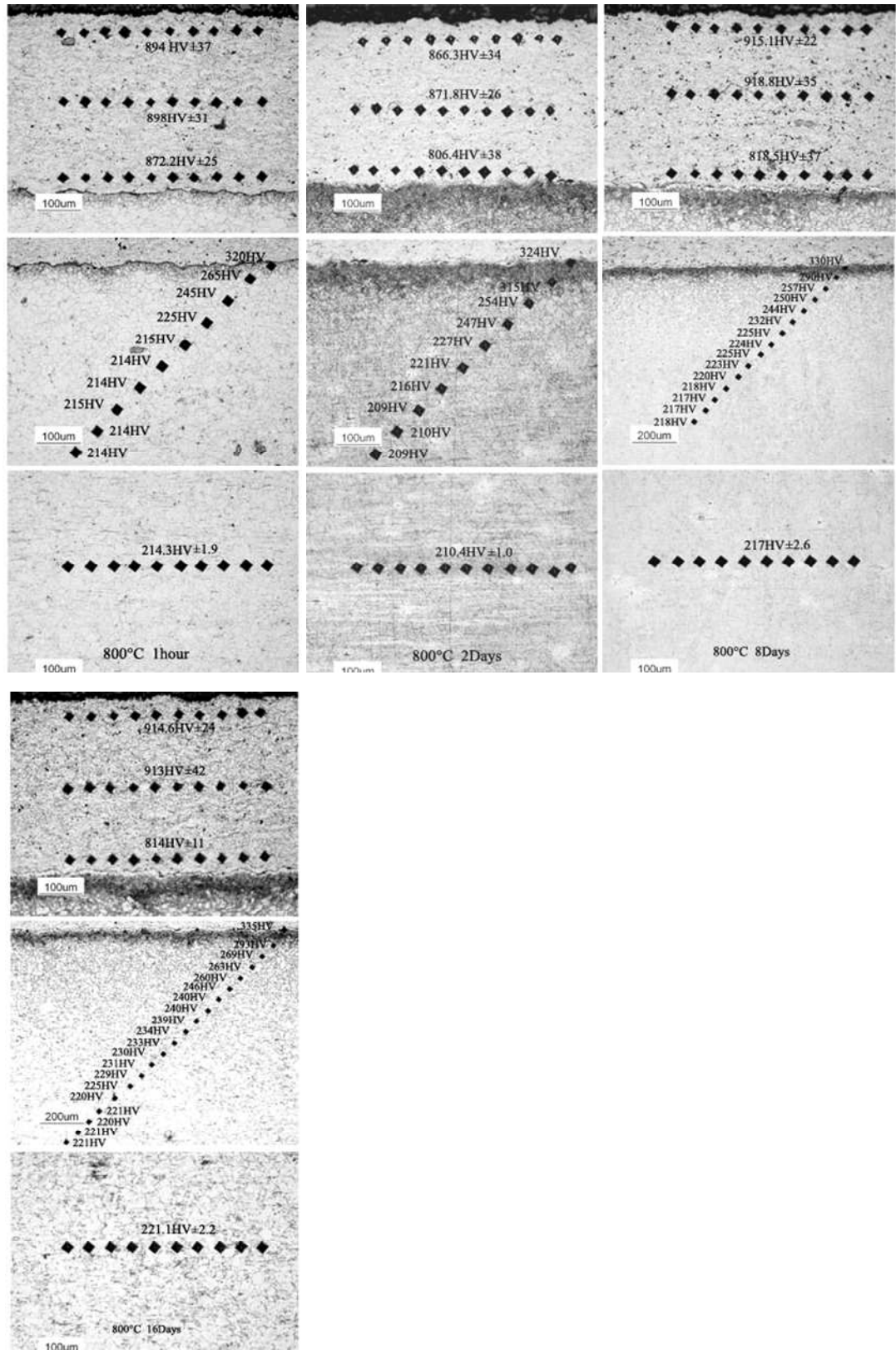


Fig 5.33 Microhardness measurements on coating (300 g load applied) and coated substrate (100 g load applied) samples following 800°C heat treatment for 1 hour, 2, 8 and 16 days

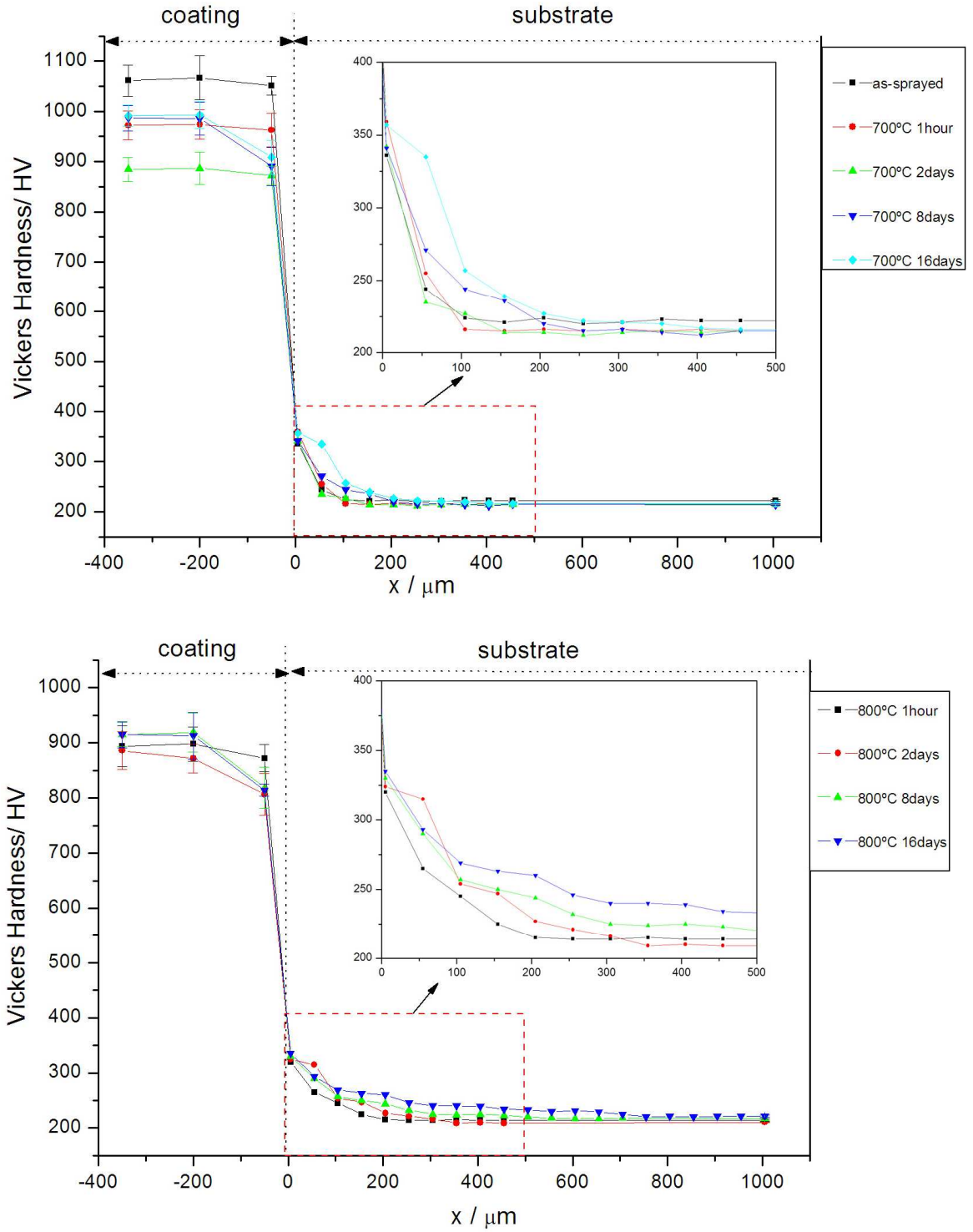


Fig 5.34 Microhardness profiles of the coating and coated substrate samples before and after annealing

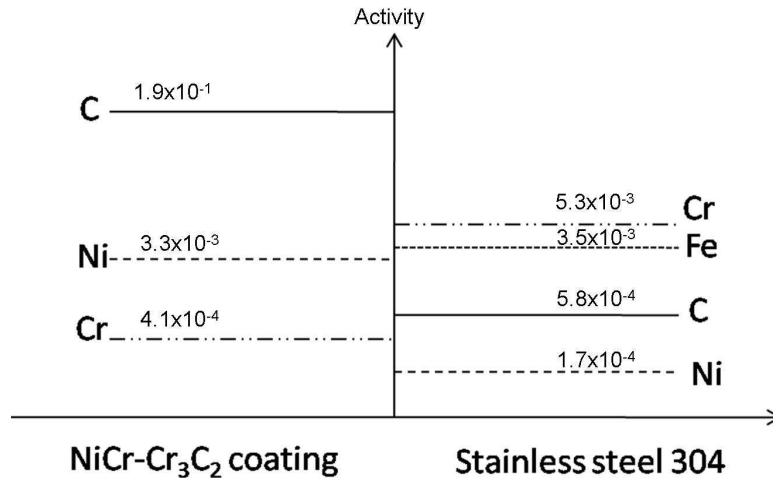


Fig 5.35 Chart of the elements activities in NiCr-Cr<sub>3</sub>C<sub>2</sub> coating and stainless steel 304 substrate at 800°C t=0 (values based on Table 5.10)

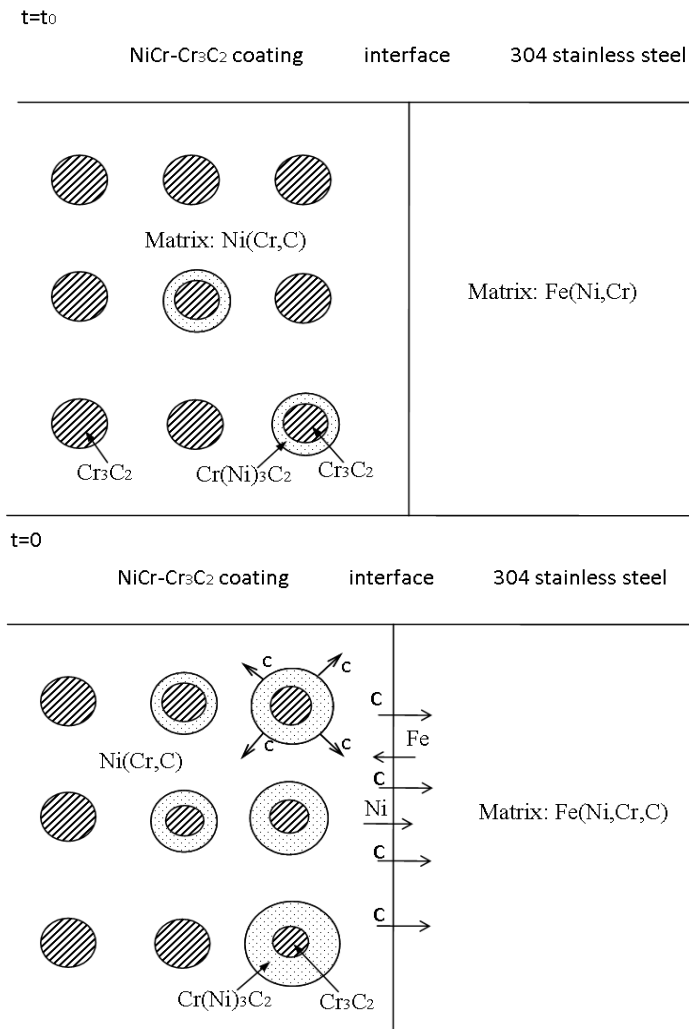


Fig 5.36 (continued) Schematic diagram of the element diffusion progress between coating and 304 substrate at high temperature

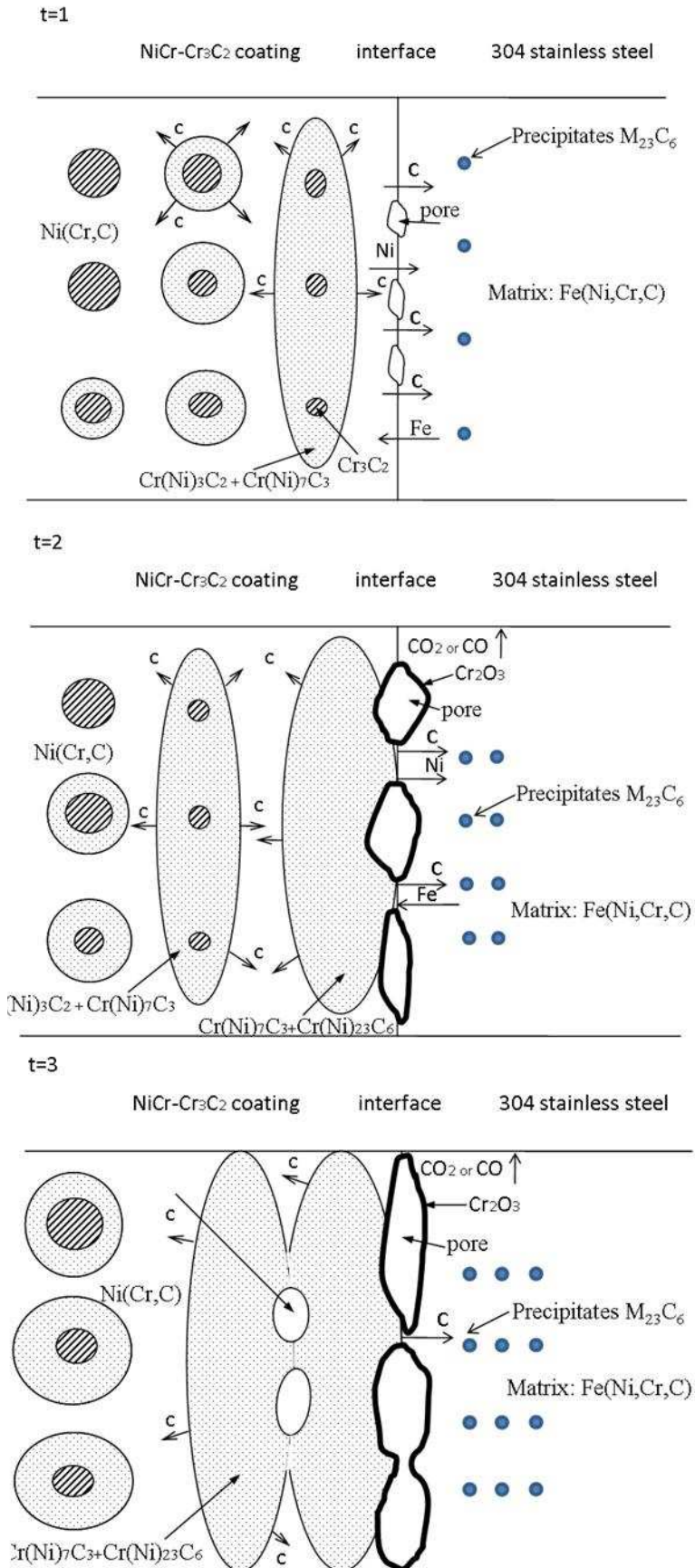


Fig 5.36 Schematic diagram of the element diffusion progress between coating and 304 substrate at high temperature

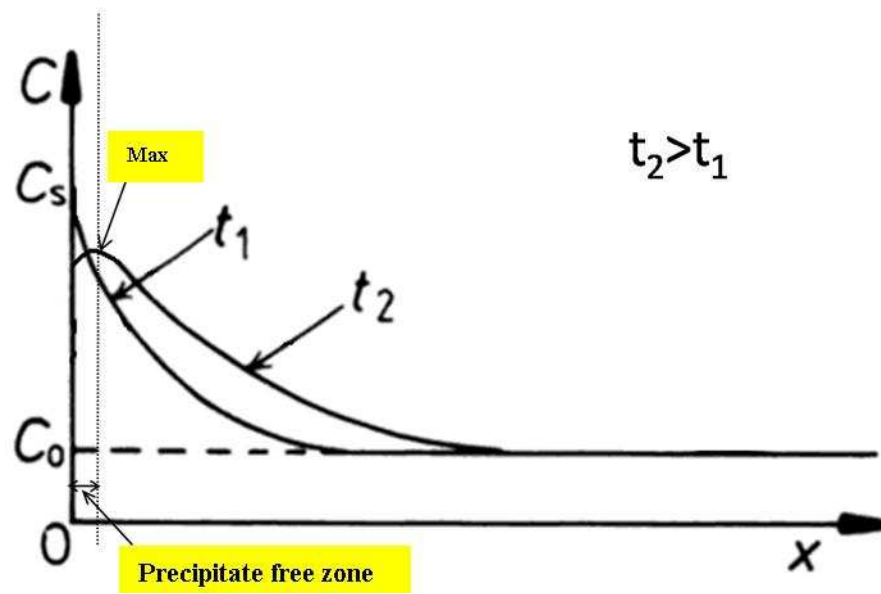


Fig 5.37 The schematic concentration profiles for carbon diffusion in stainless steel substrate at initial heat treatment time ( $t_1$ ) and the time after the formation of precipitate free zone at interface ( $t_2$ ). ( $C_s$  is the carbon concentration in coating;  $C_0$  is the original carbon concentration of the 304 stainless steel)

## **Chapter 6 Effect of elevated temperature oxidation on Ni(Cr)-Cr<sub>3</sub>C<sub>2</sub> coating: Results and Discussion**

### **6.1 Results**

#### **6.1.1 Introduction**

Thermally sprayed 25Ni(Cr)-75Cr<sub>3</sub>C<sub>2</sub> coatings have better oxidation resistance than WC-Co coatings and are thus employed as protective coatings at temperatures above 500°C (Matthews, 2008). In high-temperature oxidation, 25Ni(Cr)-75Cr<sub>3</sub>C<sub>2</sub> can react with oxygen in air environment to form a stable and dense chromium oxide Cr<sub>2</sub>O<sub>3</sub> on top of the coating (Kamal, 2009).

The characterisation of the oxidation of powder and coatings during heating in air using the thermogravimetric analysis (TGA) technique will be introduced first in this chapter. The aim of this work was to quantify the relationship between the oxidation rate and temperature. Powder was heated in air at 700°C and 800°C and coatings were heated at 650°C, 700°C, 800°C, 850°C, 900°C and 1000°C in air.

The coating cross-sectional and top surface oxide morphology will be described in a following section. Exposure of 25Ni(Cr)-75Cr<sub>3</sub>C<sub>2</sub> coatings at 700°C and 800°C for 1 hour, 2 days, 8 days and 16 days showed an oxide scale growth in cross-section. Oxide morphology on the top surface was examined using scanning electron microscopy (SEM). Furthermore, in a subsequent section the x-ray diffraction patterns from oxidised coating top surfaces are provided and show complex phases which vary with temperature and time. It can be used to identify the oxide phases and help to better understand the phase transformations.

## 6.1.2 Thermogravimetric analysis and oxidation kinetics

### 6.1.2.1 Oxidation of Praxair Ni(Cr)-Cr<sub>3</sub>C<sub>2</sub> powder

Oxidation experiments on 25Ni(Cr)-75Cr<sub>3</sub>C<sub>2</sub> Praxair powder were carried out at 700°C and 800°C and a sample was held at the test temperature for approximately 200 minutes after the set temperature was attained. A continuous plot of mass gain (percentage) as a function of time was recorded for each of the test temperatures and these are shown in Fig 6.1.

For powder oxidized in air at 700°C in Fig 6.1(a), pronounced oxidation starts during the initial 30 minutes. During this period the sample was heating to the set temperature and shows a rapid increase in mass gain. After that the weight gradually increased with increasing time. The total weight gain of the 25Ni(Cr)-75Cr<sub>3</sub>C<sub>2</sub> powder heat treated at 700°C for 200 minutes was about 6.3wt%.

Powder oxidized in air at 800°C shows a similar trend in mass gain as that of the powder oxidized at 700°C, Fig 6.1(b). In the initial 30 minutes the curve of weight gain shows a rapid increase and then it increases slowly with time. Compared with the curve of 700°C after 30 minutes, the sample heated at 800°C shows a greater weight gain rate with a total weight gain of 10.9 wt%.

### 6.1.2.2 Oxidation of Praxair Ni(Cr)-Cr<sub>3</sub>C<sub>2</sub> powder coatings

TGA experiments on 25Ni(Cr)-75Cr<sub>3</sub>C<sub>2</sub> coatings removed from the substrate were carried out at 650°C, 700°C, 800°C, 850°C, 900°C and 1000°C in air and they were held at the test temperature for approximately 200 minutes after the set temperature was attained. A continuous plot of mass gain (%) as a function of time was recorded for each of the test temperatures and they are shown in Fig 6.2. In the 650°C, 700°C and 800°C samples the mass gain (%) at the end of the 200 minute period increased with increasing temperature suggesting that oxidation rate increased with temperature in this range. However, the 850°C, 900°C and 1000°C, samples show little change in

a gain after 50 minute. The 1000°C sample showed an increased mass gain but there was also a small mass loss at around 100 minute. For the total mass gain of 25Ni(Cr)-75Cr<sub>3</sub>C<sub>2</sub> coating, the coating heated at 1000°C has the highest mass gain which is 0.52 wt%. The mass gain (%) of other samples oxidized at 650°C, 700°C, 800°C, 850°C and 900°C after 200mins were 0.137wt%, 0.293wt%, 0.418wt%, 0.401wt% and 0.391 wt%.

Comparing these TGA results of coatings with those of powder, the curves of these powder samples show a much higher mass gain (%) than those of the coatings within same oxidation condition. This occurs because the powder has a porous structure giving it a significant greater area to volume ratio per unit weight.

### **6.1.2.3 Calculation of Ni(Cr)-Cr<sub>3</sub>C<sub>2</sub> Praxair powder coating oxidation kinetics**

Oxidation kinetics of 25Ni(Cr)-75Cr<sub>3</sub>C<sub>2</sub> coatings were quantified through measurement of their mass gain per unit area ( $\Delta m/a$ ) as a function of time at temperatures of 650°C, 700°C, 800°C, 850°C, 900°C and 1000°C in air by using thermogravimetric analysis (TGA). For coatings, pronounced oxidation starts at approximately 650°C. Typical plots of mass gain per unit area vs. time for the oxidation of 25Ni(Cr)-75Cr<sub>3</sub>C<sub>2</sub> coatings at temperatures from 650°C to 1000°C are illustrated in Fig 6.3. Up to 850°C the oxidation of 25Ni(Cr)-75Cr<sub>3</sub>C<sub>2</sub> coating samples appear to follow parabolic kinetics. Above 900°C the coating follows a complex kinetics in 200 minutes exposure time.

Parabolic oxidation rates can be represented by the following equation, where  $t$  is oxidation time and  $K$  and  $C$  represent oxidation kinetic constants (Birks, 1983):

$$(\Delta m / a)^2 = Kt + C \quad [6.1]$$

To establish whether the oxidation follows parabolic kinetic behaviour the data were plotted as  $(\Delta m / a)^2$  vs  $t$ . Fig 6.4(a) shows a plot of  $(\Delta m/a)^2$  vs time at 650°C. The

data appear to show a linear relationship and a best fitting line passes through the origin gives a k value of  $2.02 \times 10^{-10} (\text{kg}^2 \text{m}^{-4} \text{min}^{-1})$ . Fig 6.4(b) and (c) shows a similar plot at temperatures of 700°C and 800°C k value of  $3.55 \times 10^{-9} (\text{kg}^2 \text{m}^{-4} \text{min}^{-1})$  and  $1.40 \times 10^{-8} (\text{kg}^2 \text{m}^{-4} \text{min}^{-1})$ . Fig 6.4(d) shows a different plot with two stages of oxidation at temperature 850°C, in the first step there are some indications of initial transient behaviour up to approximately 50 minutes which shows a linear relationship and gives the k value of  $5.34 \times 10^{-8} (\text{kg}^2 \text{m}^{-4} \text{min}^{-1})$  are obtained. Thereafter in the second step the relationship also appears linear and the best fitting line gives the k<sub>2</sub> value of  $1.21408 \times 10^{-8} (\text{kg}^2 \text{m}^{-4} \text{min}^{-1})$ . Fig 6.4(e) and (f) shows a more complex parabolic kinetic behaviour with three stages of oxidation at temperature of 900°C and 1000°C. In the initial 30 minutes the data from each temperature show a rapid increase in  $\Delta m$  with a best fitting line passing through the origin gives a k value of  $6.49 \times 10^{-8} (\text{kg}^2 \text{m}^{-4} \text{min}^{-1})$  heated at 900°C, and  $1.63 \times 10^{-7} (\text{kg}^2 \text{m}^{-4} \text{min}^{-1})$  heated at 1000°C. From 30 minutes up to 110 minutes, the coating sample oxidized at 900°C shows a smaller rate of oxidation with a k<sub>2</sub> value of  $9.42 \times 10^{-10} (\text{kg}^2 \text{m}^{-4} \text{min}^{-1})$ . Whereas the data of coating sample oxidized at 1000°C shows a weight loss during this time period and gives a k<sub>2</sub> value of  $-6.10 \times 10^{-9} (\text{kg}^2 \text{m}^{-4} \text{min}^{-1})$ . The reason of this is CrO<sub>3</sub> volatilisation which will be discussed in a subsequent section. In step III, after 110 minutes the oxidation rate of both coating samples started to grow again with a stable increase rate. k<sub>3</sub> value of each best fitting line is  $6.82 \times 10^{-9} (\text{kg}^2 \text{m}^{-4} \text{min}^{-1})$  at 900°C and  $3.19 \times 10^{-8} (\text{kg}^2 \text{m}^{-4} \text{min}^{-1})$  at 1000°C.

The experiments at 650°C, 700°C, 800°C, 850°C, 900°C and 1000°C were repeated 3 times and the k value of the individual experiments are summarized in Table 6.1. The average oxidation kinetic constant k will be used for the calculation of 25Ni(Cr)-75Cr<sub>3</sub>C<sub>2</sub> coating activation energy of the oxidation reaction Q. Values of k<sub>2</sub> and k<sub>3</sub> after 850°C are also listed in Table 6.2.

In Table 6.1 the oxidation rate at 650°C shows the lowest k value and the rate at 1000°C is significantly higher than others. The rate constant k is normally found to depend upon temperature according to the Arrhenius equation

$$k = A \exp(-Q / RT) \quad [6.2]$$

Where the pre-exponential constant A is called the frequency factor and Q is the activation energy of the reaction. Taking logarithms

$$\ln k = \ln A - (Q / RT) \quad [6.3]$$

so that a graph in which ln k is plotted against 1/RT will have a slope of -Q in Fig 6.5, R is the gas constant (8.21J/mol K). The activation energy of coating oxidation reaction Q for a parabolic rate of oxidation of 25Ni(Cr)-75Cr<sub>3</sub>C<sub>2</sub> coating is 164.5kJ/mol.

### **6.1.3 X-ray Diffraction and phase identification**

The original top surfaces of coatings oxidised at 700°C and 800°C in air with different exposure times were examined using XRD and results obtained are described below.

#### **6.1.3.1 Ni(Cr)-Cr<sub>3</sub>C<sub>2</sub> coating heated at 700°C in air**

The XRD patterns of the coating top surfaces heated to a temperature of 700°C from times from 1 hour to 16 days are shown in Fig 6.6. The XRD pattern of as-sprayed coating is also used as a reference. In the as-sprayed coating, the principal phases were identified as Cr<sub>3</sub>C<sub>2</sub> and a fcc phase with a lattice parameter close to that of Ni. Nevertheless, after 1 hour heat treatment significant Cr<sub>2</sub>O<sub>3</sub> peaks were found at 2θ values of 24.7°, 33.8°, 36.3° and 54.9°. With longer exposure time at 700°C, the intensity of the Cr<sub>2</sub>O<sub>3</sub> peaks present increased. A coating with 16 days heat treatment had the highest oxide peaks from coating surface. A small peak which could have come from Cr<sub>3</sub>O<sub>4</sub>, was also found at 2θ values of 31.2° in the XRD spectrum from the coating with 16 days heat treatment (provided in Appendix).

#### **6.1.3.2 Ni(Cr)-Cr<sub>3</sub>C<sub>2</sub> coating heated at 800°C in air**

XRD analyses indicate that heat treatments carried out at a temperature of 800°C from 1 hour to 16 days gave the same phases as the coating heated at 700°C. In Fig 6.7 some intense Cr<sub>2</sub>O<sub>3</sub> peaks were found at 2θ values of 24.7°, 33.8°, 36.3° and 54.9° from the coating after 1 hour heat treatment. The intensity of the Cr<sub>2</sub>O<sub>3</sub> peaks present show a tremendous increase in the samples oxidised at 800°C following 2 days heat treatment. With longer exposure time, the intensity of the Cr<sub>2</sub>O<sub>3</sub> peaks shows increased. The coating following 16 days heat treatment had the greatest oxide thickness on the coating surface as indicated by the high ratio of Cr<sub>2</sub>O<sub>3</sub> to Ni peaks. At 8 days and 16 days exposure time, a small peak of Cr<sub>3</sub>O<sub>4</sub> is identified at 2θ values of 31.2° in the XRD spectrum. Coatings heated at 800°C shows a significant increase of Cr<sub>2</sub>O<sub>3</sub> peaks as compared with coatings heated at 700°C.

#### **6.1.4 Scanning electron microscopy and EDX analysis of the microstructure**

Oxide scale formed on the coated surface at 700°C and 800°C from 1 hour to 16 days exposure time was characterized by cross-sectional examination using a backscattered electron imaging coupled with EDX analysis to determine the phase compositions.

##### **6.1.4.1 Cross-sectional morphology of Ni(Cr)-Cr<sub>3</sub>C<sub>2</sub> coating heated at 700°C in air**

Microstructures of polished, cross-sectioned 25Ni(Cr)-75Cr<sub>3</sub>C<sub>2</sub> coatings were revealed by BSE imaging. Fig. 6.8 shows the microstructures taken from near the surface of the coatings which were heated in air at 700°C from 1 hour up to 16 days. In Fig 6.8 (a), there is a very thin and discontinuous oxide layer which is less than 1 μm thick formed on the top of the coating following 1 hour in air. However, the oxide layer started to increase in thickness and continuously with longer periods of exposure. The thickness of a continuous oxide layer increased into (~1 μm) for the coating sample that was exposed for a longer period of 2 days (Fig 6.8b). After 8 days (Fig 6.8c) exposure the thickness of the oxide scale reached ~2 μm. For the coating sample which was exposed for 16 days at 700°C (Fig 6.8d), a thick oxide layer can be found on the top of the coating cross-section with the average thickness of ~3 μm.

As shown in Table 6.3 which corresponds to Fig. 6.8(d), phase compositions of different regions were determined using the EDX spot analysis. Region O shows high oxygen content which can be identified as oxide phase including Cr, O and a small quantity of Ni. Surely, region M has a fine scale microstructure possibly matrix and carbides whilst region C shows grey irregular particle corresponds to the carbide phase.

##### **6.1.4.2 Cross-sectional morphology of Ni(Cr)-Cr<sub>3</sub>C<sub>2</sub> coating heated at 800°C in air**

BSE imaging of the polished, cross-sectioned 25Ni(Cr)-75Cr<sub>3</sub>C<sub>2</sub> coatings which were heated in air at 800°C from 1hour up to 16 days are shown in Fig. 6.9. Oxide scale

started to form with the thickness of ~1  $\mu\text{m}$  on the top of the coating within 1 hour heat treatment at 800°C in Fig 6.9(a). Thickness of the oxide layer increased into (~2.5  $\mu\text{m}$ ) for the coating sample that was exposed for a longer period of 2 days (Fig 6.9b). After 8 days (Fig 6.9c) exposure the thickness of the oxide scale reached ~4  $\mu\text{m}$ . For the coating sample which was exposed for 16 days at 800°C (Fig 6.9d), a very thick oxide layer was formed on the top of the coating cross-section with the average thickness of ~5  $\mu\text{m}$ . Coatings heat treated at 800°C gave a higher oxide thickness on the coating surface than those heated at 700°C.

EDX analyses of phase compositions from different regions of coating heat treated at 800°C after 16 days (Fig. 6.9d) are shown in Table 6.4. Region O gives high oxygen content which can be identified as oxide phase. Region M is probably a Ni solid solution since C level is so low, whilst region C grey irregular particle corresponds to the carbide phase.

### **6.1.5 Top surface oxide morphology of Ni(Cr)-Cr<sub>3</sub>C<sub>2</sub> coating**

Topographic features of the oxide scale formed on 25Ni(Cr)-75Cr<sub>3</sub>C<sub>2</sub> coatings oxidised at 700°C and 800°C in air from 1 hour to 16 days exposure time are compared in this section.

#### **6.1.5.1 Top surface oxide morphology of as-sprayed Ni(Cr)-Cr<sub>3</sub>C<sub>2</sub> coating**

The typical surface topography of the as-sprayed coating is shown in the SEM micrograph of Fig. 6.10. The coating shows a rough surface and the spherical particles of the prior agglomerated powder do not form a uniform distribution with a number of spherical particles which are typically 5 µm in diameter. Large splats ~10 µm along with much finer spherical pattern (B) which is possibly a result of droplet disintegration at impact into small size particles during the spraying process are observed as shown in Fig. 6.10(b). Phase compositions were analysed by EDX-SEM. Due to the oxygen K peak overlapping the chromium L peak in spectrum, pure chromium EDX spectrum was obtained in Fig. 6.11 as a reference (the Cr K $\alpha$  to Cr L $\alpha$  peak length). Fig. 6.12 shows the EDX spectrum of the region on the top surface of the as-sprayed coating corresponding to Fig 6.10(a) and (b). The EDX analysis from the smooth spherical particle (A) in Fig 6.10(a) does not show a significant quantity of oxygen. Those small particles (B) with a diameter less than 2 µm show a small oxygen peak in Fig 6.10(b). The evidence from this is a change in the ratio of Cr L-line to Cr K-line compared with the pure chromium reference. These oxides were probably produced during the spray process.

#### **6.1.5.2 Top surface oxide morphology of Ni(Cr)-Cr<sub>3</sub>C<sub>2</sub> coating heated at 700°C and 800°C in air**

##### **Ni(Cr)-Cr<sub>3</sub>C<sub>2</sub> coating air heated at 700°C after 1 hour**

The surface topography of the coating after heating from 1 hour in air at 700°C is shown in the SEM micrograph of Fig 6.13 which shows multiple surface morphologies. At high magnification a number of cubic-shape (A) particles ~0.5 µm

and plate-like crystals (B) produced on the original as-sprayed spherical phases (C) in Fig. 6.13. EDX spectra of these phases in Fig. 6.14 show a change in ratio of Cr L-line to Cr K-line indicates the presence of oxygen in both the cubic-shape and the plate-like crystal phases. However, the EDX spectra from spherical surfaces do not indicate any oxygen. These cubic-shape particles have been fully oxidised and the small plate-like crystals are the projection of the oxide phase with the preferred direction of growth in the early stage of their development.

#### **Ni(Cr)-Cr<sub>3</sub>C<sub>2</sub> coating air heated at 700°C after 2 days**

The surface topography of the coating after 2 days air heat treatment at 700°C is shown in the SEM micrograph of Fig. 6.15 which shows the entire surface of the coating has been covered with oxide. The small plate-like crystals have changed into fine cubic crystals and the larger spherical crystals have become more angular. The size of the oxide precipitates grows (approximately 1 µm) and there are no plate-like crystals or spherical phases in this stage. The preference direction of growth of the plate-like crystals disappeared and all of the oxide become into cubic shape. The EDX spectra (Fig 6.16) show region A and B marked in Fig. 6.15(a) and (b) have very high content of oxygen.

#### **Ni(Cr)-Cr<sub>3</sub>C<sub>2</sub> coating air heated at 700°C after 8 days**

After 8 days air heat treatment at 700°C, the surface topography of Ni(Cr)-Cr<sub>3</sub>C<sub>2</sub> coating is shown in the SEM micrograph of Fig 6.17. In this stage nothing has significantly changed, apart from the growth of the oxide phase (up to ~3 µm) shown in Fig 6.17(b). However, there are still some small oxide particles (A) which are due to the different growth rates of the different particles. The EDX results (Fig 6.18) of region A and B marked in Fig 6.17 show very high content of oxygen. On the other hand, the Ni peak in the EDX spectra has decreased rapidly and nearly disappeared. This is a result of the Cr oxide that was formed very dense and thick scale to stop the penetration of the X-ray beam. Hence the Ni rich phase underneath can not be readily detected.

**Ni(Cr)-Cr<sub>3</sub>C<sub>2</sub> coating air heated at 700°C after 16 days**

The surface topography of the coating after 16 days air heat treatment at 700°C is shown in the SEM micrograph Fig. 6.19. The majority of the oxide phases (Fig. 6.19a) have grown up to ~4 µm and some larger crystals of ~ 5 µm can also be found along the coating surface in Fig. 6.19b. The EDX results (Fig 6.20) of region A and B marked in Fig 6.19 show high content of oxygen and the Ni peak is now barely visible.

**Ni(Cr)-Cr<sub>3</sub>C<sub>2</sub> coating air heated at 800°C from 1hour to 16 days**

Fig. 6.21 shows the surface of the oxidised coating after 1hour air heat treatment at 800°C. The entire surface has been oxidised and covered by cubic-like crystals of ~ 2 µm. Some nano-sized plate-like crystals can also be found in places. EDX results (Fig. 6.22) of region A, B and C marked in Fig. 6.21 show a high content of oxygen. Compared with those samples heated at 700°C in 1hour, the coating treated at 800°C indicates greater oxide growth. Temperature has more significant effect on oxidation process than time. When exposed for over 2 days, no obvious changes are observed from the plan view except for the increase in grain size. Fig. 6.23, 6.25, 6.27 are images of the samples treated in 800°C from 2 days to 16 days. They show similar oxidation progress as the samples treated at 700°C. After 2 days heat treatment at 800°C, two kinds of surface morphology are seen to co-exist which are cube-shaped and elongated grains. The size of these grains increases with increasing exposure time. EDX results of these analysed regions (Fig. 6.24, 6.26, 6.28) all show very high oxygen content and the Ni peak in EDX spectra disappeared after 2days heat treatment at 800°C. The characterisation of the as-sprayed coating and the coatings oxidised at 700°C and 800°C are summarised in Table 6.5.

### **6.1.6 Summary**

As mentioned above, the oxidation kinetics of the powder and coatings during elevated temperature oxidation in air at 650°C to 1000°C have been studied using TGA experiments. The activation energy of coating oxidation reaction  $Q$  for the Ni(Cr)-Cr<sub>3</sub>C<sub>2</sub> coating was found to be 164.5 kJ/mol. SEM examination and XRD analysis show a significant increase in the oxide scale formed on coating surfaces during the heat treatment. The oxide morphological changes in coating show that in the initial exposure cubic-shaped and plate-like crystal phases were found on coating surface, with continued exposure these crystals grow quickly and form large cubic-shaped and long crystals.

## 6.2 Discussion

### 6.2.1 Kinetics of the elevated temperature oxidation for Praxair Ni(Cr)-Cr<sub>3</sub>C<sub>2</sub> powder coating

TGA results of 25Ni(Cr)-75Cr<sub>3</sub>C<sub>2</sub> Praxair powder carried out at 700°C and 800°C show significant mass increase after 200 minutes. The total mass gain of the samples heat treated at 700°C and 800°C is 6.3 wt% and 10.9 wt%, respectively. While the Praxair 25Ni(Cr)-75Cr<sub>3</sub>C<sub>2</sub> powder coating heat treated at 700°C and 800°C giving much lower mass gain which is only 0.293wt% and 0.418wt%. This occurs because the powder has a more porous structure giving it a significant greater area to volume ratio per unit weight than the coating.

Oxidation of 25Ni(Cr)-75Cr<sub>3</sub>C<sub>2</sub> coating could start with nucleation and growth of both NiO and Cr<sub>2</sub>O<sub>3</sub>, and this transient stage finishes when the Cr<sub>2</sub>O<sub>3</sub> scale becomes continuous. It was indicated in last section that the oxide formed during the transient oxidation stage is mainly of Cr<sub>2</sub>O<sub>3</sub> since no NiO was detected in the parts of external oxide that remained on surface after test. Then it is considered here that the total mass gain that results from the transient oxidation stage is essentially due to Cr<sub>2</sub>O<sub>3</sub>. However the weight loss due to the formation of CO will not be considered in this section.

The thermogravimetric study of the oxidation of 25Ni(Cr)-75Cr<sub>3</sub>C<sub>2</sub> coating in the temperature range 650 to 1000°C indicates that the kinetic curves deviate from the parabolic rate law above 800°C. Temperatures between 650-800°C, the specific weight gain curves follow a parabolic kinetic (Fig 6.2) law. According to Wagner's theory (Birks, 1983), to get a parabolic law implies that the oxidation process is dominated by the diffusion of species through the growing Cr<sub>2</sub>O<sub>3</sub> scale. The lower values of the rate constant K, for 650°C and 700°C are indicative of very slow oxidation. The oxidation rate increases at 800°C. At lower temperatures, Cr<sub>2</sub>O<sub>3</sub> has a low oxygen diffusivity value and hence acts as a protective layer against oxidation to

control the outwards Cr cation diffusion or inwards oxygen anion diffusion through this existing chromia scale. This fact is corroborated by Table 6.1, which shows a slower oxidation rate for 600°C than 700°C. Fig 6.8 (a)&(b) show a thin layer on coating than in Fig 6.9 (a)&(b), which further validates the slow oxidation rate at lower temperature.

With further temperature rise up to 1000°C oxidation rate increases sharply and oxidation follows complex parabolic kinetics. In the initial stage of the coatings from 850-1000°C the oxidation rate increases rapidly. Whereas the curve of the sample oxidized at 1000°C shows a weight loss during second oxidation stage due to the chromia volatilization, because chromia is not stable when the exposure temperature is too high. The external part of the Cr<sub>2</sub>O<sub>3</sub> scale is continuously oxidised into CrO<sub>3</sub>, a new oxide that is volatile and leaves the scale in a gaseous form. The formation of CrO<sub>3</sub> by the reaction is



In these conditions Cr<sup>3+</sup> ions and oxide species form at the metal-oxide interface and transport through the oxide lattice and mechanically formed cracks in the oxide layer. With continuing exposure, the volatile oxide CrO<sub>3</sub> forms directly at the oxide-gas interface and oxygen diffuses through a barrier layer of the volatilized oxides Cr<sub>2</sub>O<sub>3</sub>. The evaporation of CrO<sub>3</sub> is explained schematically in Fig 6.31, results in the continuous thinning of the protective Cr<sub>2</sub>O<sub>3</sub> scale so the diffusive transport through it is rapid. During the TGA we do have a mass spectrum to detect some gases such as CrO<sub>3</sub>.

In the previous researches, none of the investigators have studied the high temperature oxidation of bare Ni-Cr-C cermet coatings. Ye (2008) gave the TGA results with the squares of the mass gain as a function of oxidation time for the Cr39Ni7C coated SS400 sample at 1073K which followed by parabolic rate law  $y^2=kt$ . Kamal (2009)

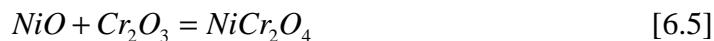
have studied the high temperature oxidation studies of 25Ni(Cr)-75Cr<sub>3</sub>C<sub>2</sub> coating on Fe- and Ni-based superalloys at 900°C. His results showed (weight gain/area)<sup>2</sup> versus number of cycles plot for 25Ni(Cr)-75Cr<sub>3</sub>C<sub>2</sub> coated superalloys for 100 cycles at 900°C followed the parabolic rate law. On the other hand, Castello (1998) has studied the oxidation of Ni-Al-Cr<sub>3</sub>C<sub>2</sub> alloy at 1100 and 1200°C; he indicated that the formation of volatile chromium oxide CrO<sub>3</sub>, at high temperature could have enhanced disruption of the scales. Berthod (2005) reported the vaporization of chromia into volatile CrO<sub>3</sub> happens at temperature higher than 1000°C by studying the oxidation of a Ni-30Cr alloy. Same studies also have been done by Bethod (2007) on Ni-30Cr-0.2C alloy which shows a significant rate of chromium volatilization at 1200°C. In Bethod's report, the activation energy Q value for a parabolic rate of oxidation of 70Ni30Cr alloy is 167 kJ·mol<sup>-1</sup> which is very close to the Q value of the 25Ni(Cr)-75Cr<sub>3</sub>C<sub>2</sub> coating (164.5 kJ/mol). This shows that the oxidation of Ni(Cr) alloy phase has dominated the process of the 25Ni(Cr)-75Cr<sub>3</sub>C<sub>2</sub> coating oxidation.

## 6.2.2 Mechanism of the elevated temperature oxidation for Ni(Cr)-Cr<sub>3</sub>C<sub>2</sub> coating

### 6.2.1.1 Mechanism of the high temperature oxidation of Ni(Cr)

The agglomerated and sintered 25Ni(Cr)-75Cr<sub>3</sub>C<sub>2</sub> powder coatings consist of large amount of Ni(Cr) in matrix. Cr<sub>2</sub>O<sub>3</sub>, NiO and NiCr<sub>2</sub>O<sub>4</sub> are expected to be formed as the main oxides on Ni(Cr) matrix during the high temperature oxidation. The oxidation of matrix before steady state can be explained by transient oxidation which often affects the ultimate selective oxidation process in which only the most stable oxide is formed.

In the initial stage both Cr and Ni form oxide scales, Cr<sub>2</sub>O<sub>3</sub> and NiO, on coating top surface (Allam, 1978). Since the Ni-containing oxides grow much quicker than Cr<sub>2</sub>O<sub>3</sub> a significant amount of oxide mixed with NiO and NiCr<sub>2</sub>O<sub>4</sub> form on the top of Cr<sub>2</sub>O<sub>3</sub> layer. NiCr<sub>2</sub>O<sub>4</sub> spinel here is formed via solid phase reaction between NiO and Cr<sub>2</sub>O<sub>3</sub> with the reaction indicated as below.



In the further stage, there is no more NiO on the top which might be fully reacted with Cr<sub>2</sub>O<sub>3</sub> as Ni(Cr)<sub>2</sub>O<sub>4</sub>, thus a continued NiCr<sub>2</sub>O<sub>4</sub> spinel external oxide layer forms with Cr<sub>2</sub>O<sub>3</sub> as internal oxide scale. With continued exposure, Since Ni ions diffusion is much slower through the NiCr<sub>2</sub>O<sub>4</sub> spinel than it is through NiO, NiCr<sub>2</sub>O<sub>4</sub> in the scale act as diffusion blocks for migrating Ni ions. Thus as the Cr content of the alloy increases, the volume of fraction of spinel increases which reduces the total Ni flux through the scale and the oxidation rate starts to fall then Cr<sub>2</sub>O<sub>3</sub> starts to form on the NiCr<sub>2</sub>O<sub>4</sub>. Finally a complete external scale of Cr<sub>2</sub>O<sub>3</sub> forms at steady state. The model used to explain this behaviour is summarized in Figure 6.29.

To compare, Matthews (2008) has studied the oxide scales formed on blended NiCr-Cr<sub>2</sub>C<sub>3</sub> coatings after 850°C heat treatment. He indicated carbide elements are diffused into the NiCr matrix during the heat treatment and increase the Cr content of the phase. Then Cr<sub>2</sub>O<sub>3</sub> is therefore able to dominate the matrix phase scale from an

early time and prevented bulbous NiO formation. With extended oxidation, lateral Cr<sub>2</sub>O<sub>3</sub> growth from the matrix phase begins to encroach over the carbide splats and dominate the coating scale with Cr<sub>2</sub>O<sub>3</sub> crystals on coating top surface. On the other hand, other several investigators reported the presence of NiCr<sub>2</sub>O<sub>4</sub> in either Ni-Cr or 25Ni(Cr)-75Cr<sub>3</sub>C<sub>2</sub> coatings. The formation of NiCr<sub>2</sub>O<sub>4</sub> via solid phase reaction between NiO and Cr<sub>2</sub>O<sub>3</sub> in the oxide scales has been reported by Kamal (2008), he also found NiCr<sub>2</sub>O<sub>4</sub> spinel presented in the top surface scale of 25Ni(Cr)-75Cr<sub>3</sub>C<sub>2</sub> coatings after 900 °C oxidation.

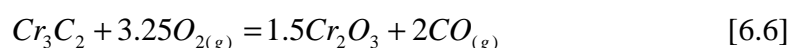
### **6.2.1.2 Mechanism of the high temperature oxidation of Cr<sub>3</sub>C<sub>2</sub> particles in coating**

The agglomerated and sintered 25Ni(Cr)-75Cr<sub>3</sub>C<sub>2</sub> powder coatings consist of 75wt% chromium carbides which are used to mitigate high temperature wear and erosion. Cr<sub>2</sub>O<sub>3</sub> scales are frequently formed on the surface of the chromium carbides at high temperatures to protect the alloys. In other cases carbon in Cr<sub>3</sub>C<sub>2</sub> particles can be lost by the formation of CO.

Studies on the oxidation of chromium carbides are quite limited, but the research on other carbides such as titanium carbides can be helpful. According to Bellucci's (2003) studies on the oxidation mechanism on TiC, a scheme diagram of proposed oxidation of chromium carbides is presume in Figure 6.30. The scheme shows in the initial oxidation outside of chromium carbide particles forms a continued external Cr<sub>2</sub>O<sub>3</sub> layer within which the solid-state transport of chromium and oxygen occurs. From previous studies on oxidation of chromium (Kofstad, 1980) (Lillerud, 1980), it was shown that chromium diffusion is quicker than oxygen diffusion in Cr<sub>2</sub>O<sub>3</sub> under 1100 °C. Tsai (1995) calculated the oxygen and chromium bulk diffusion coefficient ( $D_B$ ) and grain boundary diffusion coefficient ( $D_{gb}$ ) in Cr<sub>2</sub>O<sub>3</sub> scales. The oxygen  $D_B$  and  $D_{gb}$  at 800°C are equal to  $2.6 \times 10^{-18} \text{ cm}^2 \text{ s}^{-1}$  and  $5.9 \times 10^{-13} \text{ cm}^2 \text{ s}^{-1}$ . The chromium  $D_B$  and  $D_{gb}$  values are equal to  $5.9 \times 10^{-18} \text{ cm}^2 \text{ s}^{-1}$  and  $1.1 \times 10^{-12} \text{ cm}^2 \text{ s}^{-1}$  respectively.

The scale growth is dominated by counter-current diffusion of oxygen and chromium by both the bulk and the grain boundary, the main phenomenon being grain boundary diffusion. On the other hand the chemical potential gradient of carbon decreases from the carbide/chromia to chromia/gas interface where the rapid consumption of carbon sustained by the combustion reaction. The growth mechanism of Cr<sub>2</sub>O<sub>3</sub> scales on chromium carbides can be explained as chromium diffuses through the initial chromia scale and form new external chromium oxide, simultaneously carbon from chromium carbides also diffuse through the chromia scale to the top surface and burnt as CO.

XRD results in (Fig 6.6&6.7) show clearly Cr<sub>3</sub>C<sub>2</sub> is the only carbide in coating surface after oxidation. The depth of x-ray penetration in Cr<sub>2</sub>O<sub>3</sub> oxide scale is also concerned which is from 1.34~5.93 μm calculated in the previous chapter of experimental procedures. Comparing with the SEM cross-section images in Fig 6.8 and Fig 6.9 show that the average thickness of oxide is about from 1~5 μm which is still in the range of the depth of x-ray penetration. These results can be used to presume the reaction between chromium carbide and oxygen are fully reacted without forming new carbides such as Cr<sub>7</sub>C<sub>3</sub> or Cr<sub>23</sub>C<sub>6</sub>. The equation between Cr<sub>3</sub>C<sub>2</sub> and O<sub>2</sub> can be written as:



In the previous studies by Kamal (2009), who indicated the oxidation of the Cr<sub>3</sub>C<sub>2</sub> phase would lead to decarburisation and formation of Cr<sub>7</sub>C<sub>3</sub> and Cr<sub>23</sub>C<sub>6</sub> as observes from his XRD analysis of 25Ni(Cr)-75Cr<sub>3</sub>C<sub>2</sub> coated superalloys after air oxidation at 900°C. He also gives the equation  $Cr_3C_2 \xrightarrow{+O_2} Cr_7C_3 \xrightarrow{+O_2} Cr_{23}C_6 \xrightarrow{+O_2} [Cr_{MET}] \xrightarrow{+O_2} Cr_2O_3$ , which describes how the carbides follow the stepwise reaction of Cr<sub>3</sub>C<sub>2</sub> with air and form Cr<sub>2</sub>O<sub>3</sub>.

### 6.2.1.3 Mechanism of the high temperature oxidation of Ni(Cr)-Cr<sub>3</sub>C<sub>2</sub> coating

The life of Cr<sub>3</sub>C<sub>2</sub>-NiCr coating in oxygen containing atmosphere at high temperature is dependent upon the formation of a protective oxide scale. The schematical diagram

in Fig 6.29 gives a whole picture of the mechanism of the high temperature oxidation of 25Ni(Cr)-75Cr<sub>3</sub>C<sub>2</sub> coatings. Essentially, in the early stage of oxidation a significant amount of oxide mixed with NiO, NiCr<sub>2</sub>O<sub>4</sub> and Cr<sub>2</sub>O<sub>3</sub> are first formed on Ni(Cr) matrix. Equally Cr<sub>2</sub>O<sub>3</sub> are also formed outside of the chromium carbide particles which are exposed on the top of the coatings. In the further stage, a continued NiCr<sub>2</sub>O<sub>4</sub> external oxide layer with Cr<sub>2</sub>O<sub>3</sub> as internal oxide scale are formed on Ni(Cr) matrix, and a continued Cr<sub>2</sub>O<sub>3</sub> oxide layer are formed surround Cr<sub>3</sub>C<sub>2</sub>. With continued exposure, a complete external scale of Cr<sub>2</sub>O<sub>3</sub> is formed in both matrix and chromium carbide with a small amount of NiCr<sub>2</sub>O<sub>4</sub> spinel remaining in the Ni(Cr) matrix. The Cr<sub>2</sub>O<sub>3</sub> phase is thermodynamically stable up to very high temperatures due to its high melting points as well as it forms a dense, continuous and adherent layers that grow relatively slow. The Cr<sub>2</sub>O<sub>3</sub> forms a solid diffusion barrier on top of the coating which inhibits interaction of oxygen with the underlying coating. The reaction rate is high initially as oxygen and the reacting elements in the coating are in direct contact. Once the Cr<sub>2</sub>O<sub>3</sub> oxide form a complete external complete scale, diffusion of either species becomes increasingly difficult due to the growing diffusion barrier. As a result, the rate of mass gain due to oxygen uptake reduces with time. The growth of oxide scale typically displays a parabolic dependence with time and its longevity is dependent upon the concentration of the scale-forming element in the coating material, temperature, oxidising conditions and alloy microstructure (Birks, 1983).

### **6.2.3 Summary**

As discussed above, the 25Ni(Cr)-75Cr<sub>3</sub>C<sub>2</sub> coating indicated a less mass gain compared to its feedstock 25Ni(Cr)-75Cr<sub>3</sub>C<sub>2</sub> powder in the same oxidation condition. The oxidation behaviour of all the 25Ni(Cr)-75Cr<sub>3</sub>C<sub>2</sub> coatings at different temperatures followed a parabolic rate law. The Ni(Cr)-Cr<sub>3</sub>C<sub>2</sub> coatings after high temperature oxidation show the presence of mainly oxide of Cr in the upper region of the scale. In the subscale region, the phases revealed were oxides of Cr and Ni spinels.

**Table 6.1** Oxidation kinetics constants for 25Ni(Cr)-75Cr<sub>3</sub>C<sub>2</sub> coating for various constant temperatures of exposure

Temperature	k			Average k±ε ( kg <sup>2</sup> m <sup>-4</sup> min <sup>-1</sup> )
	Expt 1	Expt 2	Expt 3	
650°C	2.02x10 <sup>-10</sup>	2.41x10 <sup>-10</sup>	1.66x10 <sup>-10</sup>	2.03x10 <sup>-10</sup> ±9.69x10 <sup>-12</sup>
700°C	3.55x10 <sup>-9</sup>	4.35x10 <sup>-9</sup>	2.63x10 <sup>-9</sup>	3.51x10 <sup>-9</sup> ±2.22x10 <sup>-10</sup>
800°C	1.40x10 <sup>-8</sup>	8.98x10 <sup>-9</sup>	2.31x10 <sup>-8</sup>	1.54x10 <sup>-8</sup> ±1.85x10 <sup>-9</sup>
850°C	5.34x10 <sup>-8</sup>	4.88x10 <sup>-8</sup>	5.87x10 <sup>-8</sup>	5.36x10 <sup>-8</sup> ±1.27x10 <sup>-9</sup>
900°C	6.49x10 <sup>-8</sup>	7.98x10 <sup>-8</sup>	4.44x10 <sup>-8</sup>	6.30x10 <sup>-8</sup> ±4.59x10 <sup>-9</sup>
1000°C	1.63x10 <sup>-7</sup>	1.70x10 <sup>-8</sup>	9.98x10 <sup>-8</sup>	9.32x10 <sup>-8</sup> ±1.89x10 <sup>-8</sup>

**Table 6.2** Oxidation kinetics constants of k<sub>2</sub> and k<sub>3</sub> for 25Ni(Cr)-75Cr<sub>3</sub>C<sub>2</sub> coating from 850 900 and 1000°C

Temperature	Average k <sub>2</sub> ±ε ( kg <sup>2</sup> m <sup>-4</sup> min <sup>-1</sup> )	Average k <sub>3</sub> ±ε ( kg <sup>2</sup> m <sup>-4</sup> min <sup>-1</sup> )
850°C	1.56x10 <sup>-8</sup> ±1.09x10 <sup>-8</sup>	
900°C	9.61x10 <sup>-10</sup> ±5.36x10 <sup>-12</sup>	6.62x10 <sup>-9</sup> ±3.71x10 <sup>-10</sup>
1000°C	-5.76x10 <sup>-9</sup> ±4.70x10 <sup>-10</sup>	3.35x10 <sup>-8</sup> ±1.23x10 <sup>-9</sup>

**Table 6.3** EDX analysis results for average composition of the phases present in 25Ni(Cr)-75Cr<sub>3</sub>C<sub>2</sub> coating heat treated at 700°C with 16days

Phase	Phase composition				
	Average	Cr	Ni	C	O
<b>O</b> <b>(oxide)</b>	at%	27.8±1.4	8.5±1.6	0	63.7±1.3
	wt%	48.8±1.2	16.7±1.4	0	34.5±1.1
<b>C</b> <b>(angular carbide)</b>	at%	57.5±2.4	1.6±0.5	40.9±2.9	0
	wt%	80.5±1.8	5.1±0.2	14.4±2.0	0
<b>M</b> <b>(metal alloy)</b>	at%	19.9±1.3	75.9±1.6	4.2±1.2	0
	wt%	18.6±1.0	80.3±1.4	1.1±0.9	0

**Table 6.4** EDX analytical results for average composition of different phases of the 25Ni(Cr)-75Cr<sub>3</sub>C<sub>2</sub> coating heat treated at 800°C with 16days

Phase	Phase composition				
	Average	Cr	Ni	C	O
<b>O</b> <b>(oxide)</b>	at%	28.9±1.2	6.6±1.3	0	64.5±1.0
	wt%	51.5±1.0	13.2±1.1	0	35.3±0.9
<b>C</b> <b>(angular carbide)</b>	at%	61.2±1.8	1.1±0.4	37.7±2.0	0
	wt%	84.2±1.5	3.1±0.4	12.7±1.6	0
<b>M</b> <b>(metal alloy)</b>	at%	17.5±1.4	81.7±1.5	0.8±0.4	0
	wt%	15.9±1.2	83.7±1.3	0.4±0.1	0

**Table 6.5** Summary of the surface topography characterisation of the as-sprayed coating and coatings oxidised at 700°C and 800°C

	<b>As-sprayed</b>	<b>700°C 1hour</b>	<b>700°C 2days</b>	<b>700°C 8days</b>	<b>700°C 16days</b>
<b>Types of morphology</b>	1. spherical 2. splats	1. cubic-shape 2. plate-like 3. spherical	1. cubic-shape only	1. cubic-shape only	1. cubic-shape only
<b>Oxygen content</b>	None Very low	Very High High Low	Very high	Very high	Very high
<b>Average grain size</b>	5 µm in diameter	~0.5µm x 0.5µm	~1µm x 1µm	~3µm x 3µm	~4µm x 4µm
<b>Ni peak in EDX spectra</b>	Strong	Weak	Very weak	None	None

	<b>800°C 1hour</b>	<b>800°C 2days</b>	<b>800°C 8days</b>	<b>800°C 16days</b>
<b>Types of morphology</b>	1. plate-like 2. cubic-shape	1. cubic-shape 2. long grains	1. cubic-shape 2. long grains	1. cubic-shape 2. long grains
<b>Oxygen content</b>	High Very high	Very high Very high	Very high Very high	Very high Very high
<b>Average grain size</b>	~2µm x 2µm	~3µm x 3µm ~1µm x 3µm	~5µm x 5µm ~2µm x 3µm	~5µm x 5µm ~2µm x 4µm
<b>Ni peak in EDX spectra</b>	Very weak	None	None	None

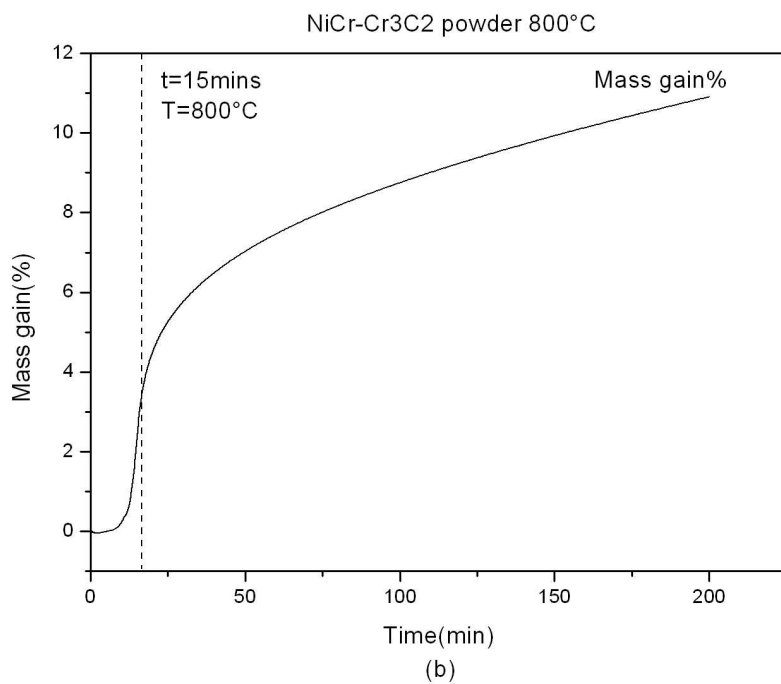
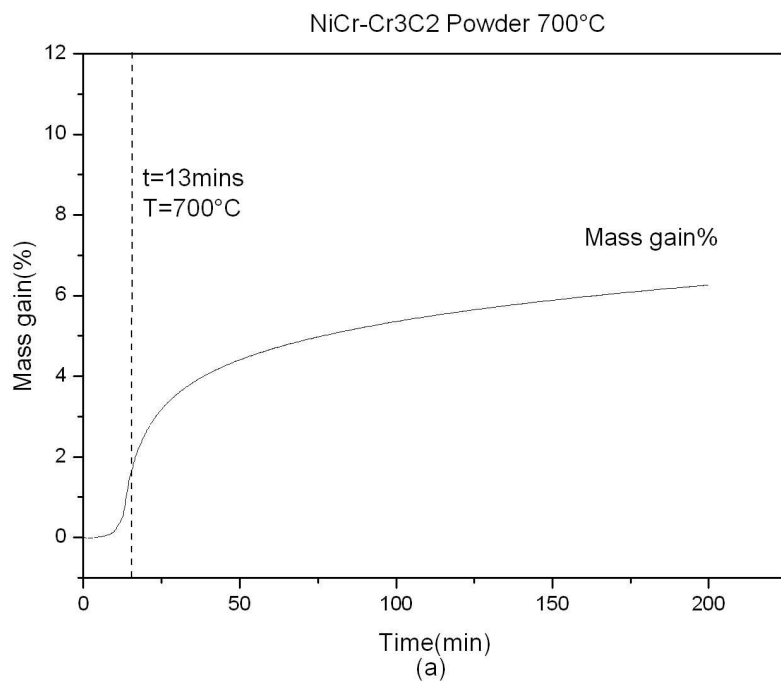
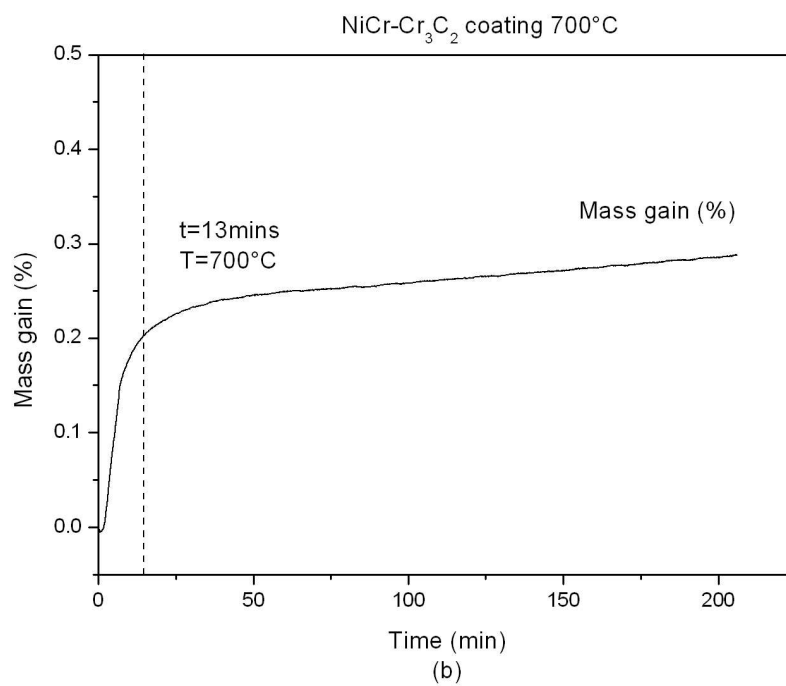
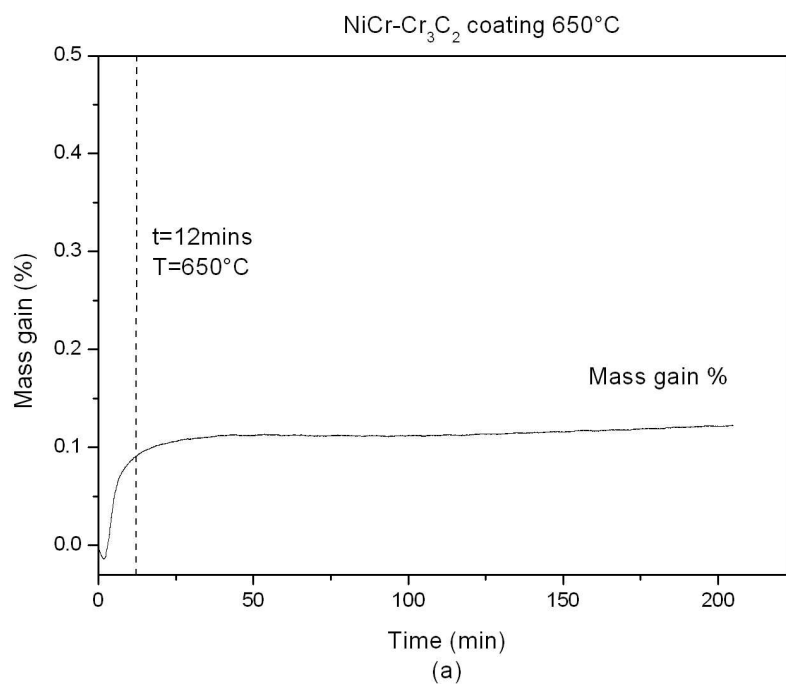
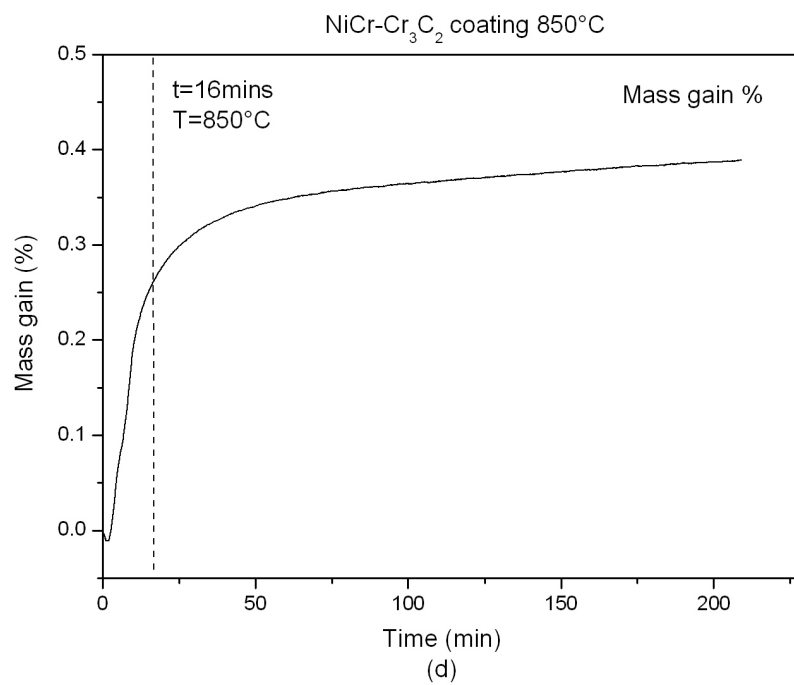
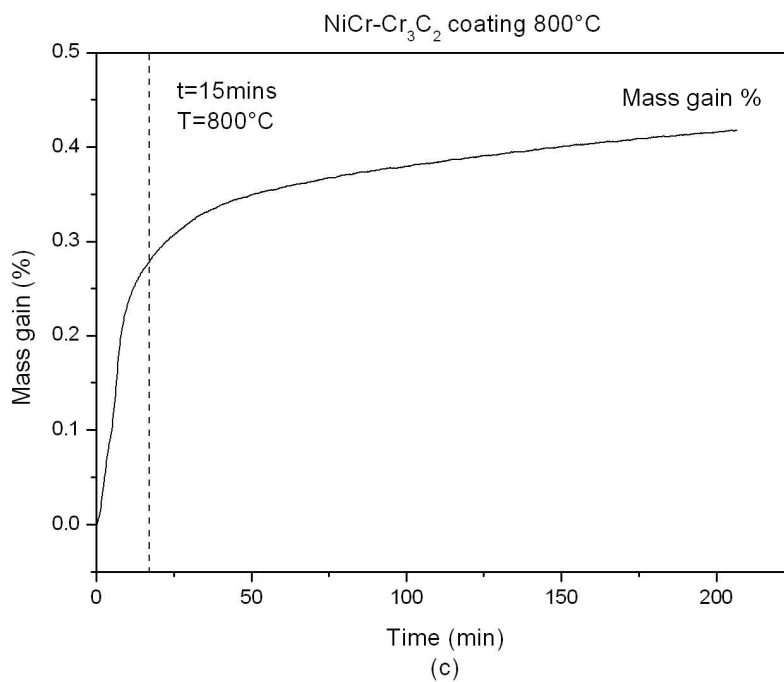


Fig 6.1 Plot of change in mass gain percentage as a function of time for 25Ni(Cr)-75Cr<sub>3</sub>C<sub>2</sub> powder at (a) 700°C and (b) 800°C in air, the dotted line shows the time when the holding temperature was reached





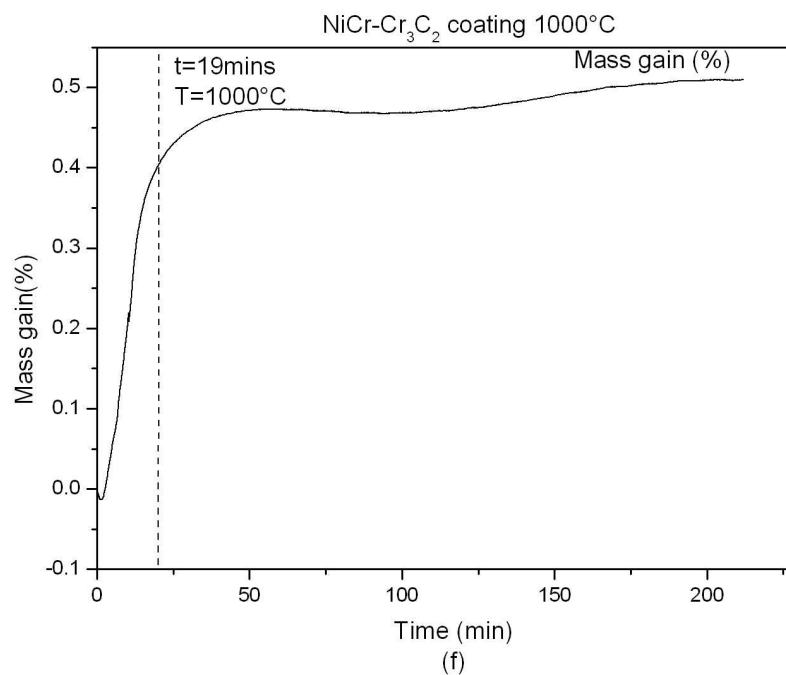
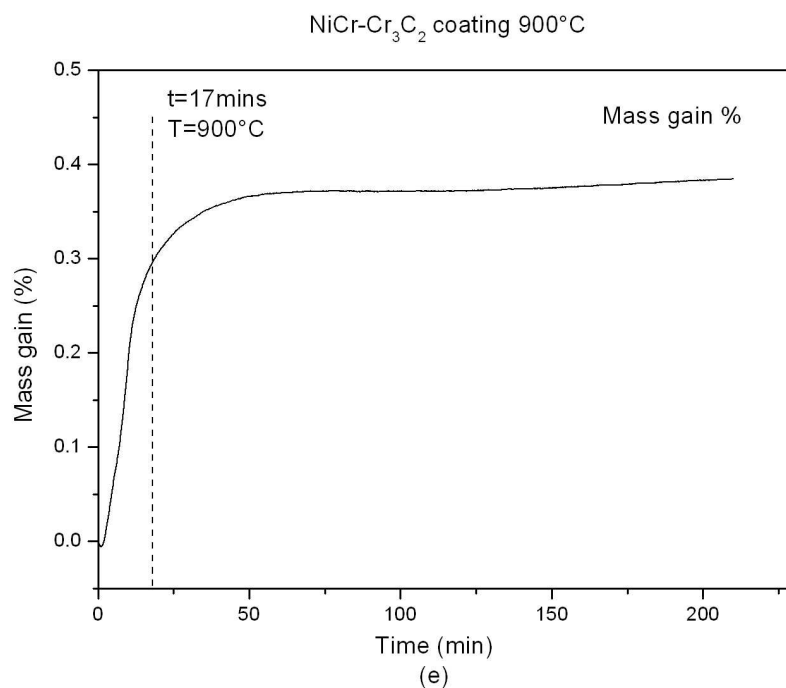


Fig 6.2 Plot of in mass gain (percentage) as a function of time for 25Ni(Cr)-75Cr<sub>3</sub>C<sub>2</sub> coatings at (a) 650°C (b) 700°C (c) 800°C (d) 850°C (e) 900°C and (f)1000°C in air. Dotted line shows the temperature at which the set temperature was reached in each case.

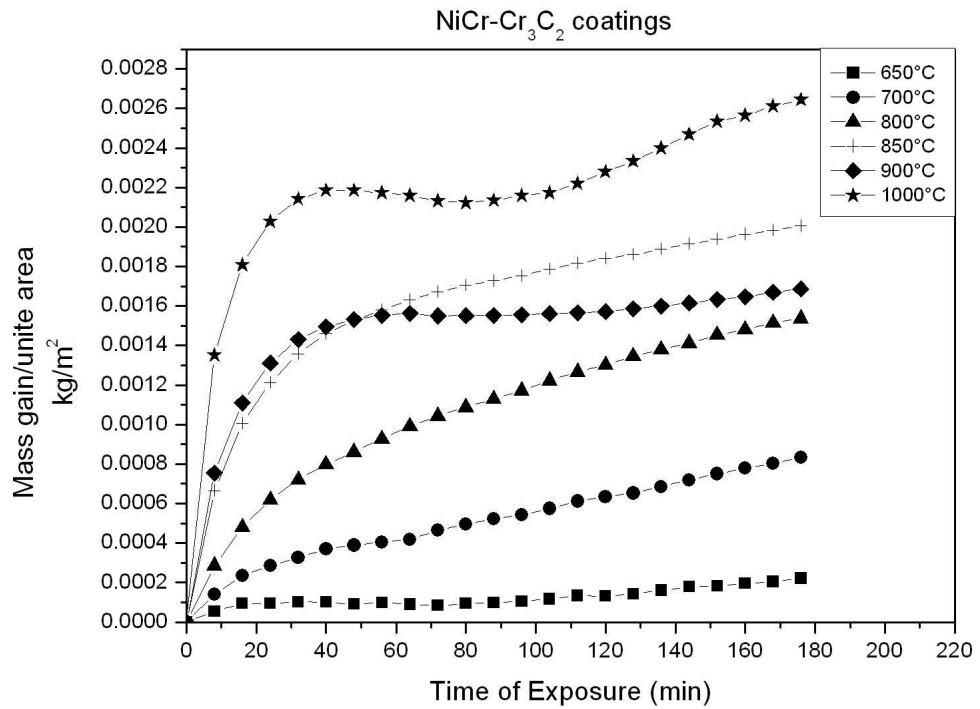
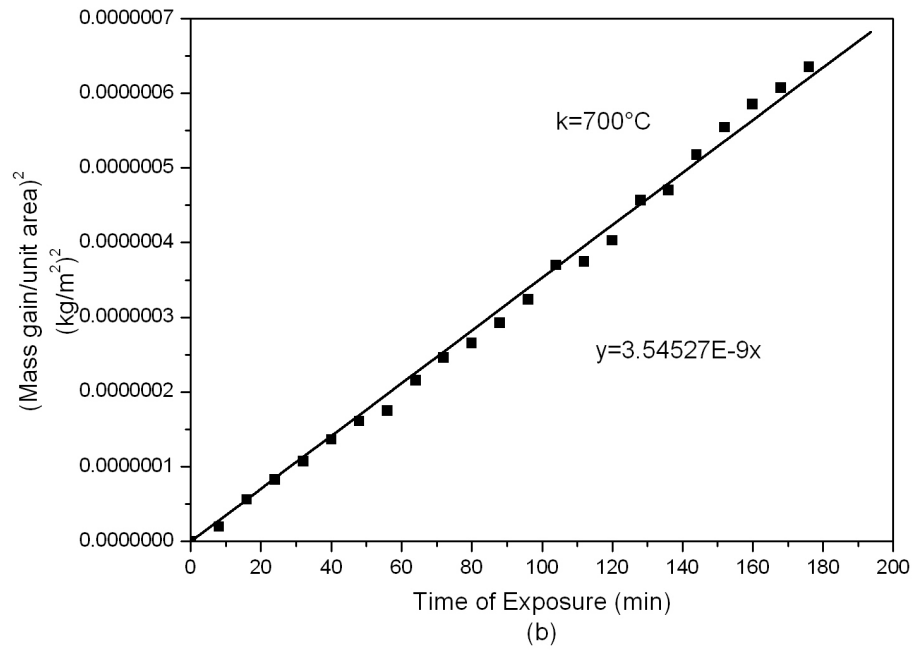
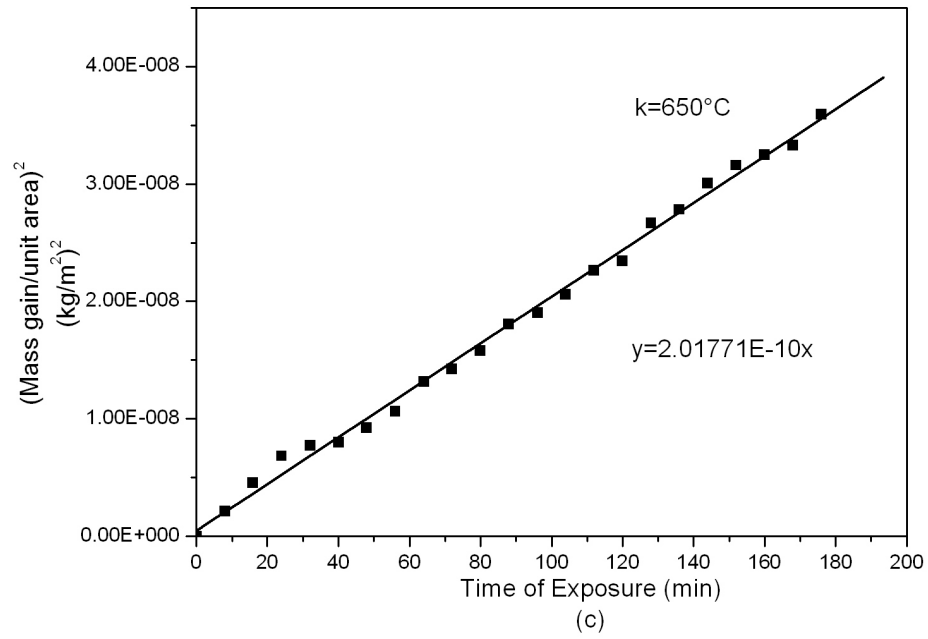
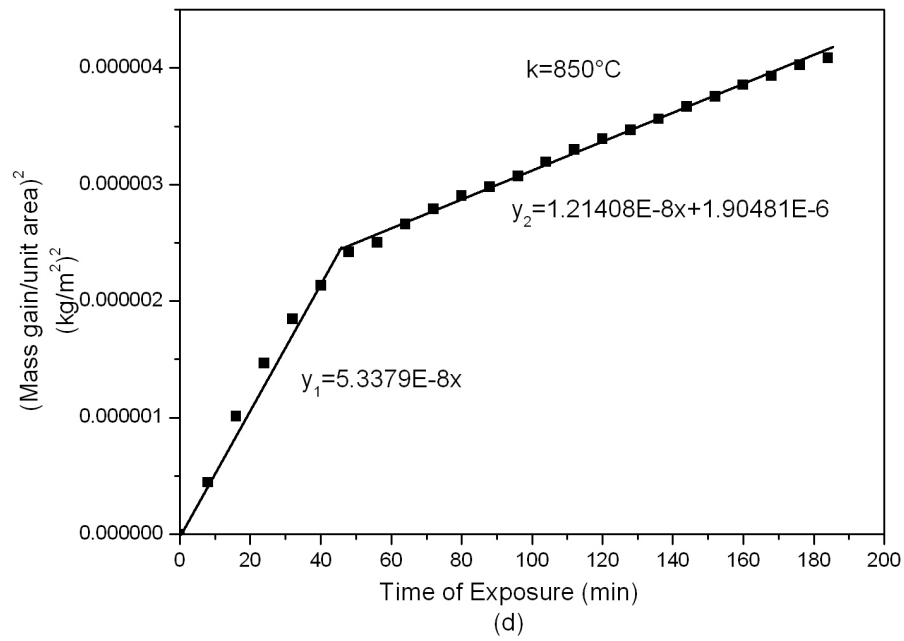
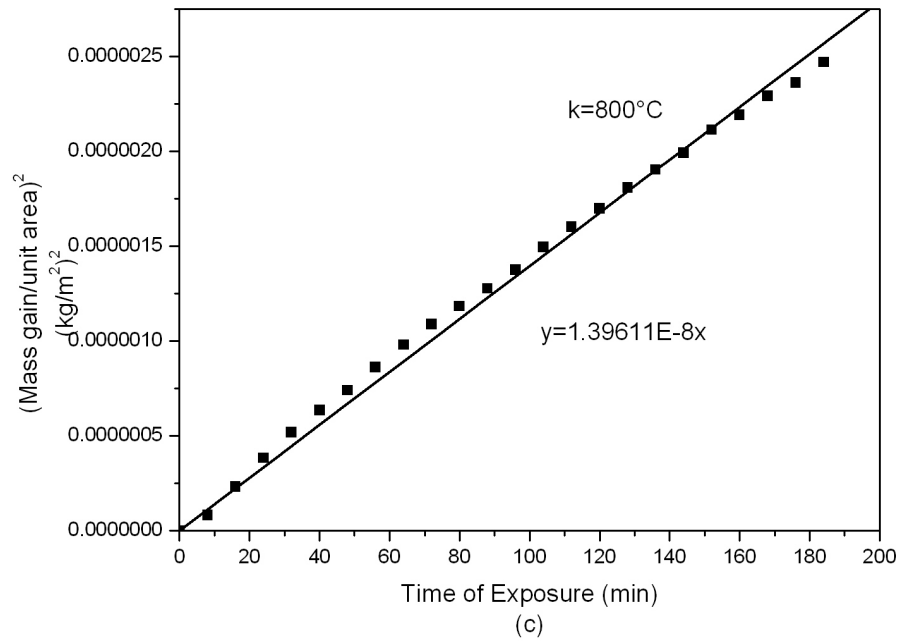


Fig 6.3 Oxidation kinetics for 25Ni(Cr)-75Cr<sub>3</sub>C<sub>2</sub> plot of mass gain per unit area versus exposure time for temperatures in the range 650°C ~1000°C. (t=0 concerted to the time when the sample reached set temperature)





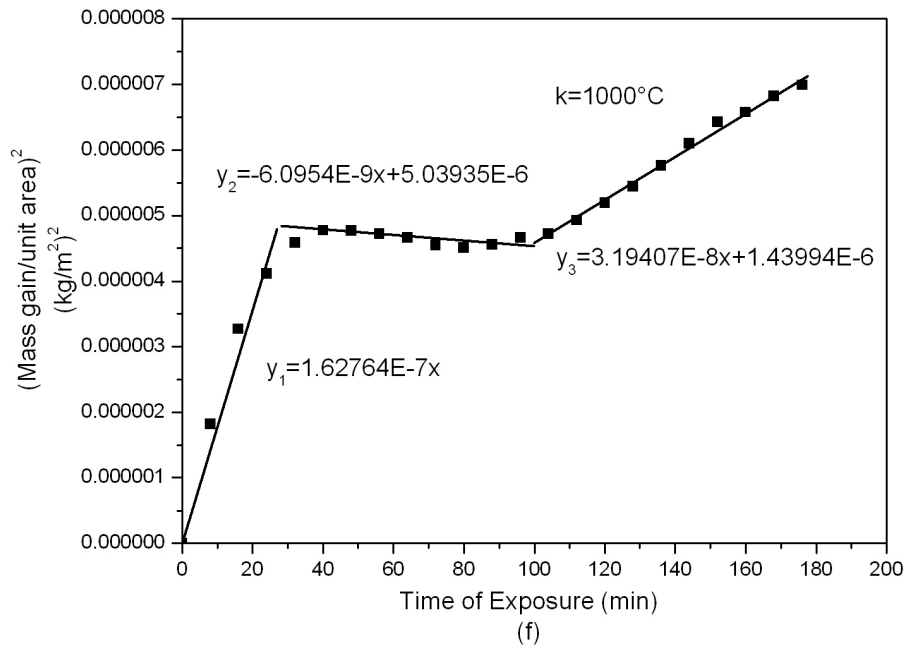
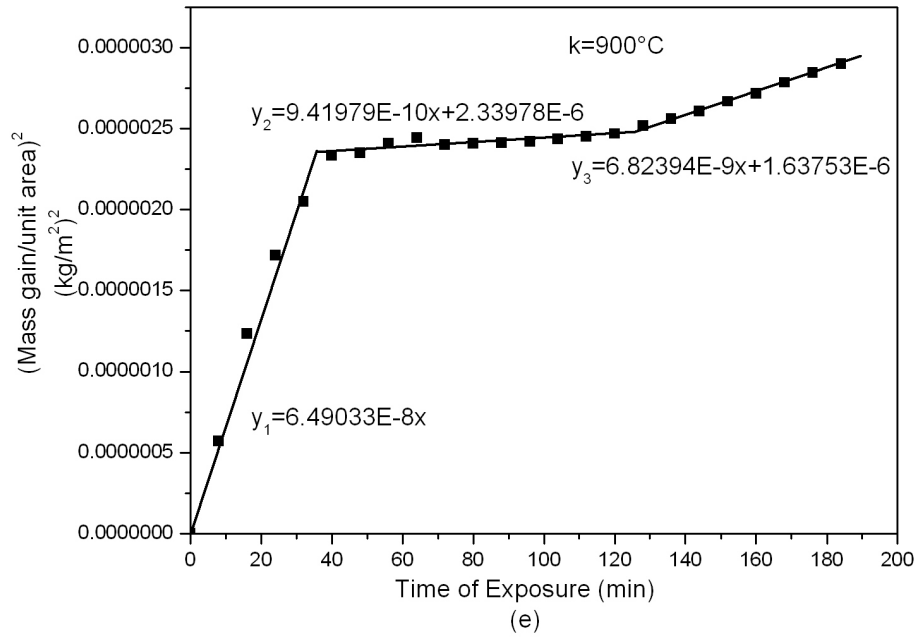


Fig 6.4 Plots of  $(\Delta m/a)^2$  versus time of exposure for 25Ni(Cr)-75Cr<sub>3</sub>C<sub>2</sub> coatings at (a) 650°C (b) 700°C (c) 800°C (d) 850°C (e)900°C and (f)1000°C

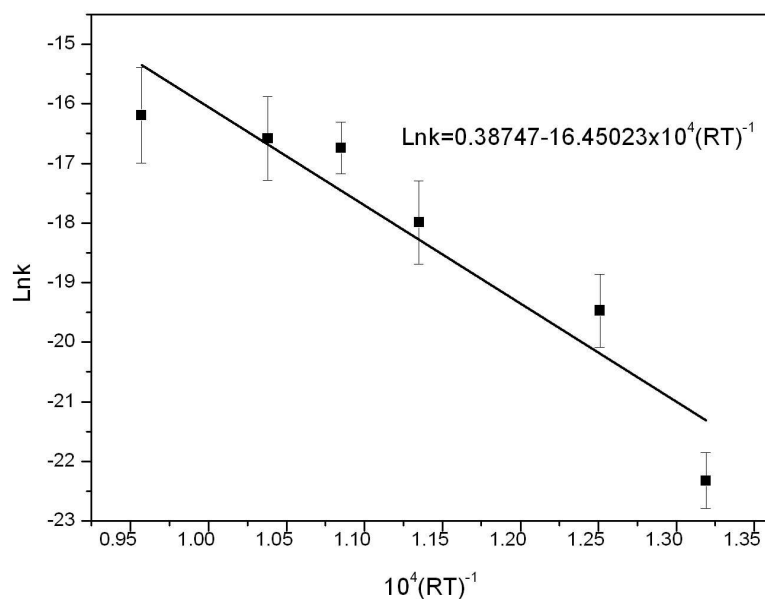
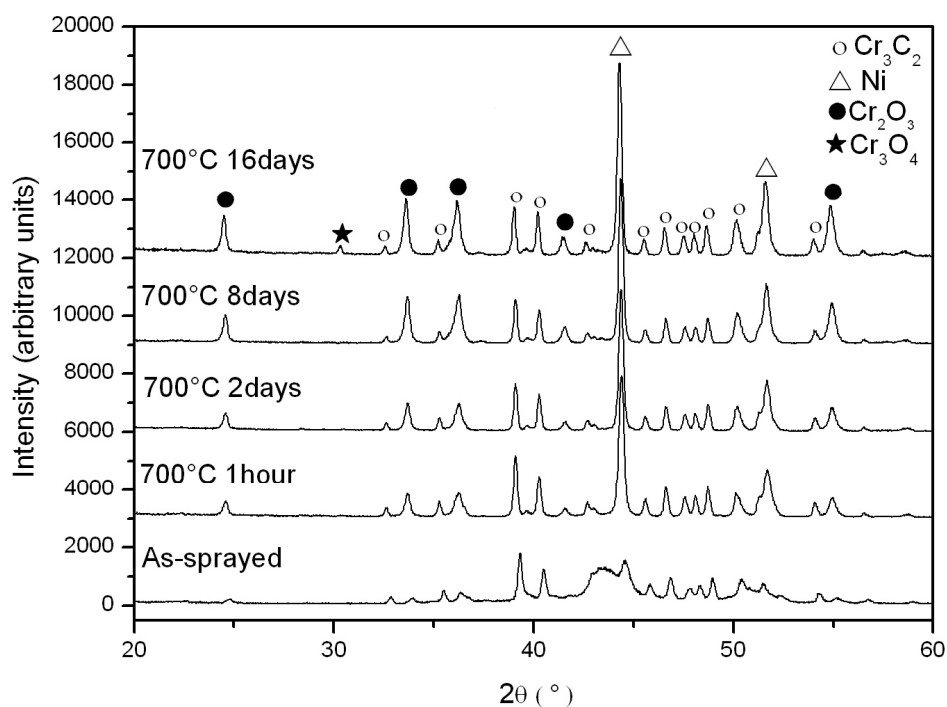
Fig 6.5 Arrhenius plot for oxidation of 25Ni(Cr)-75Cr<sub>3</sub>C<sub>2</sub> coating

Fig 6.6 XRD spectra obtained from top surface of coatings oxidised at 700°C with different exposure times from 1 hour to 16 days and the XRD spectra of the as-sprayed coating given as a reference (Provided in appendix)

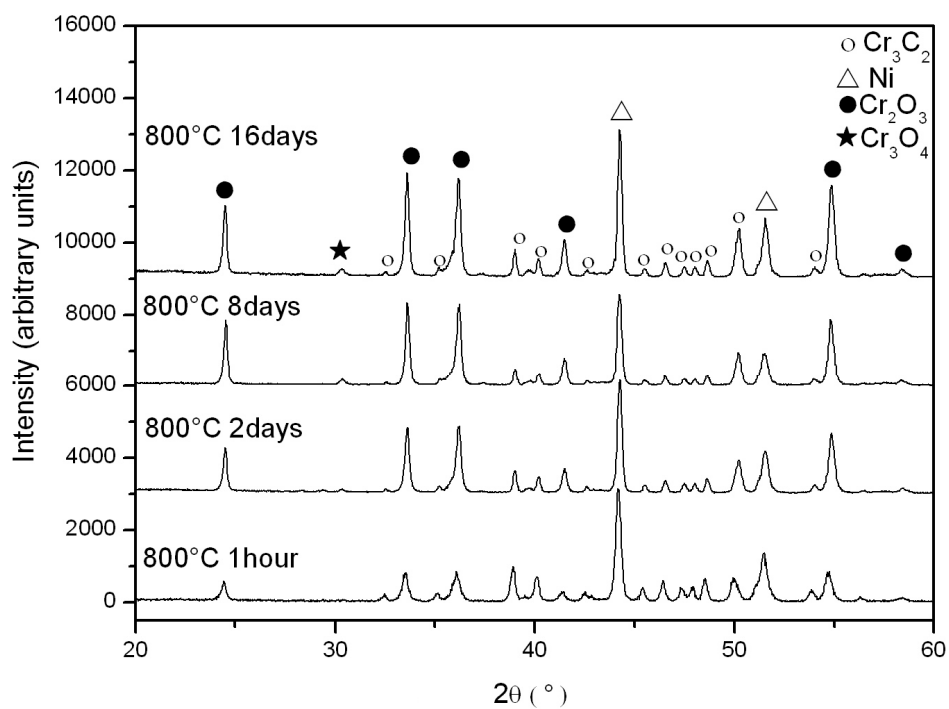
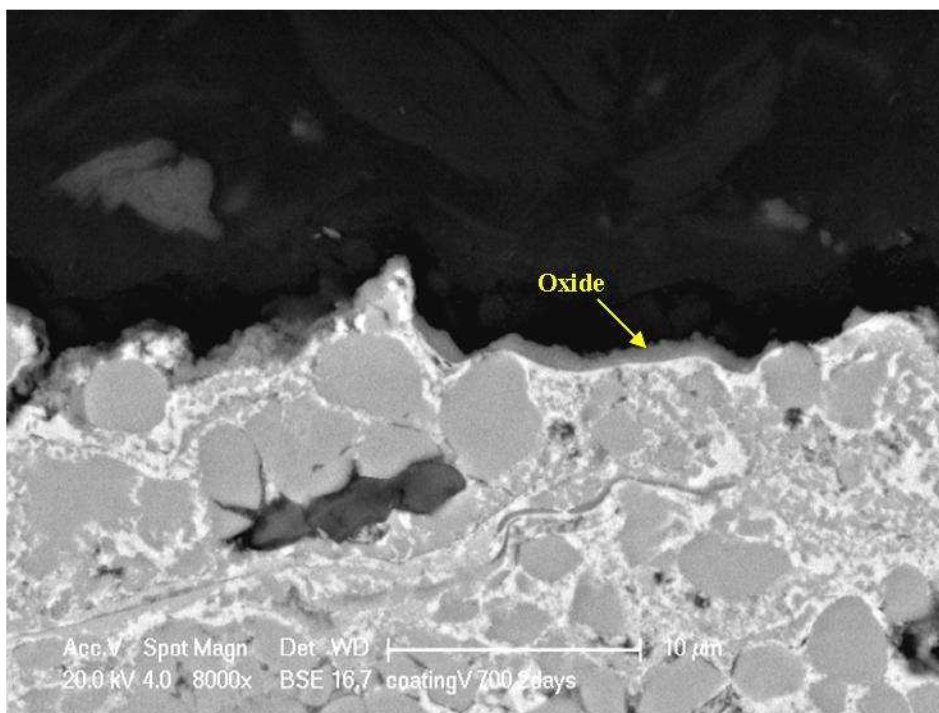


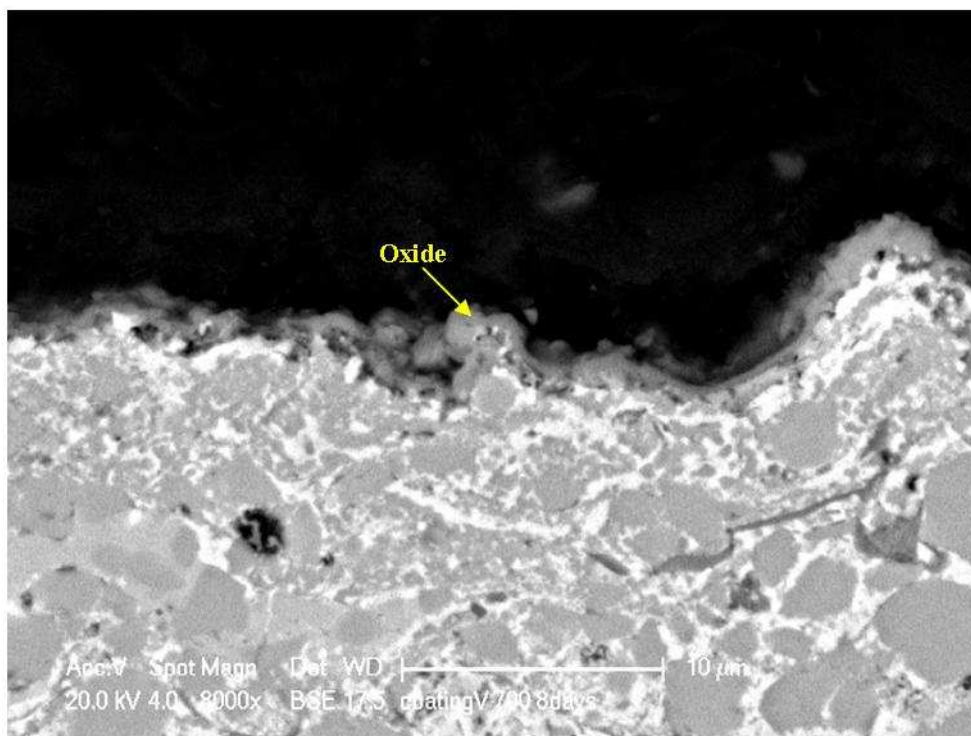
Fig 6.7 XRD spectra detected from top surface of coatings oxidised at 800°C with different exposure times from 1 hour to 16 days (Provided in appendix)



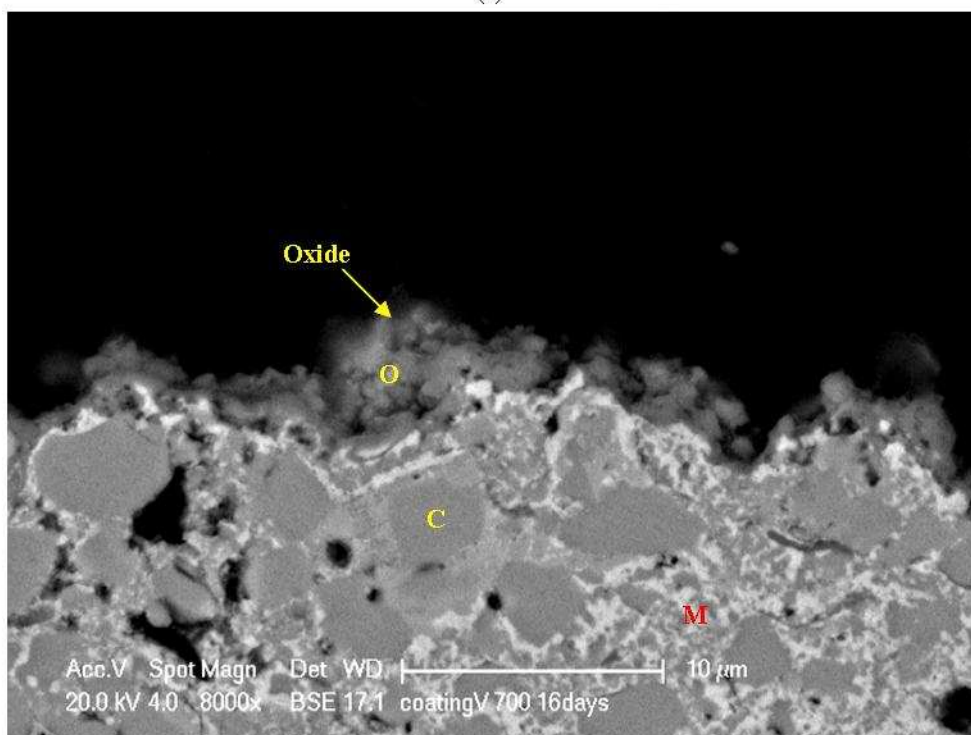
(a)



(b)

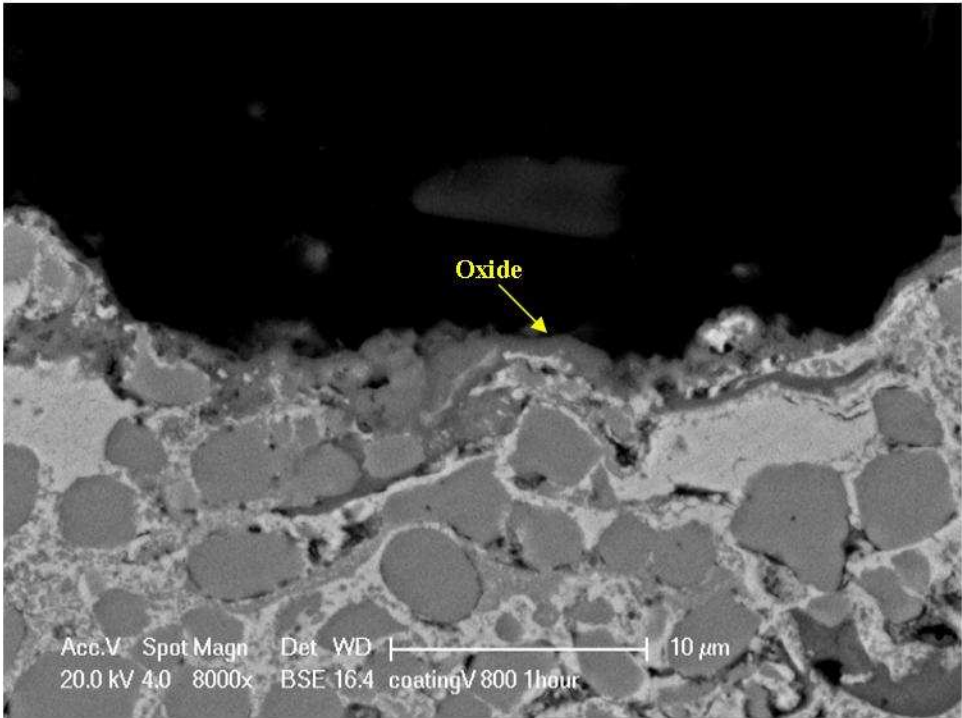


(c)

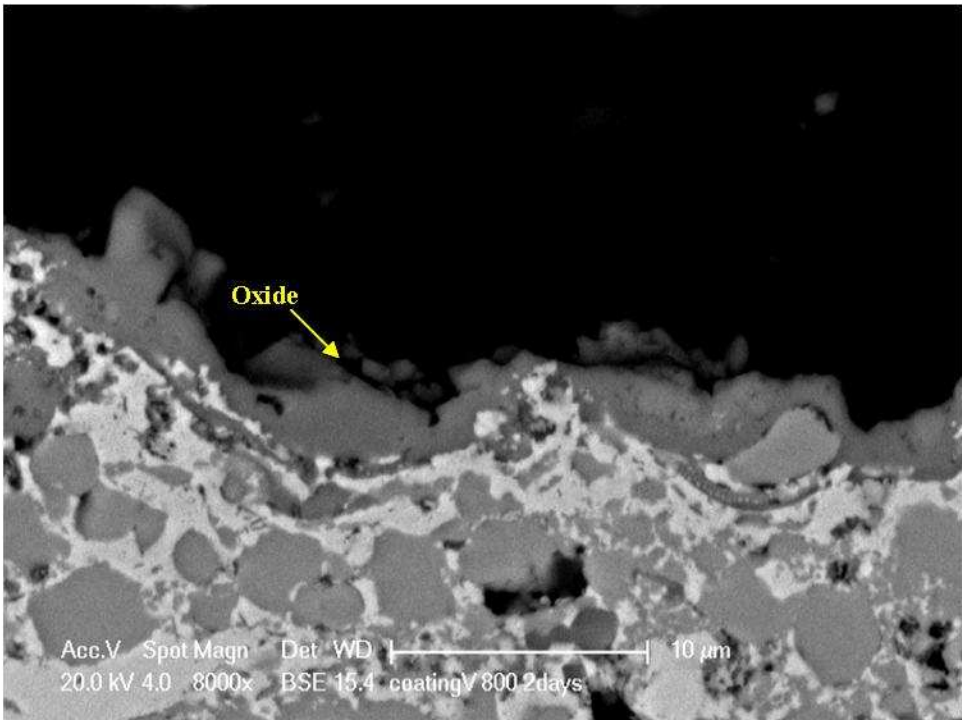


(d)

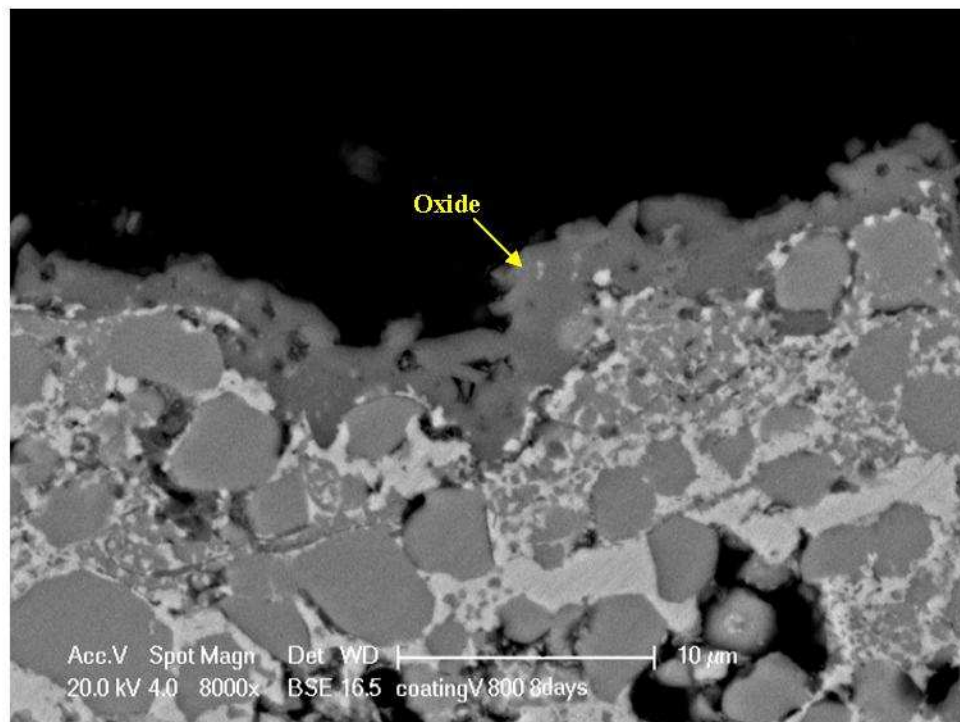
Fig 6.8 High magnification BSE images showing a cross-sectional view of the 25Ni(Cr)-75Cr<sub>3</sub>C<sub>2</sub> coatings heat treated at 700°C with different exposure times (a) 1 hour, (b) 2 days, (c) 8 days and (d) 16 days



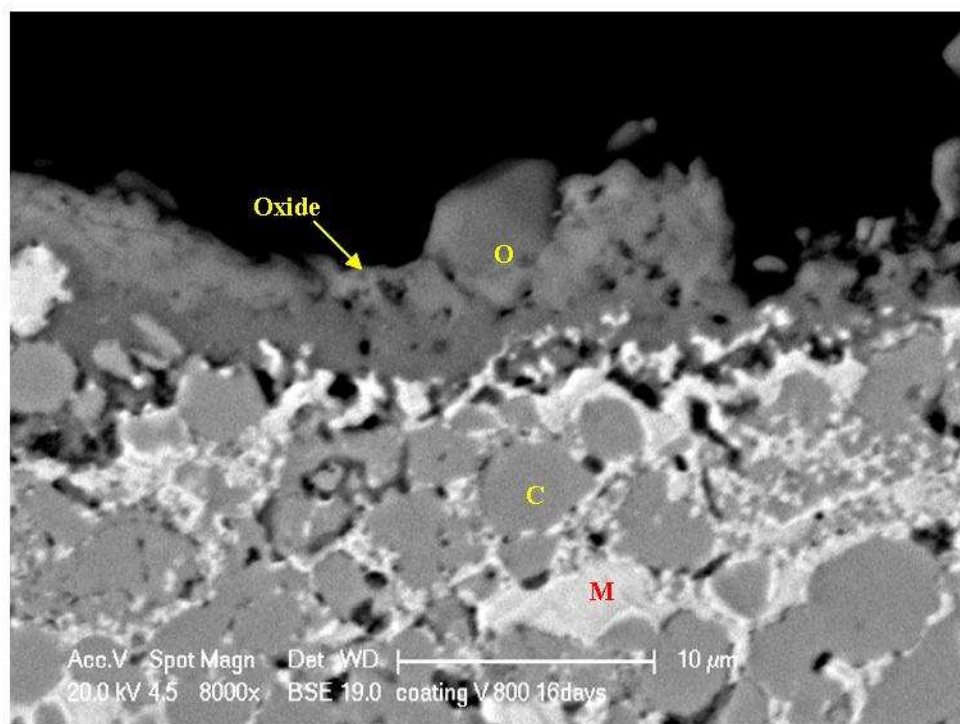
(a)



(b)



(c)



(d)

Fig. 6.9 High magnification BSE images showing a cross-sectional view of the 25Ni(Cr)-75Cr<sub>3</sub>C<sub>2</sub> coatings heat treated at 800°C with different exposure times (a) 1 hour, (b) 2 days, (c) 8 days and (d) 16 days

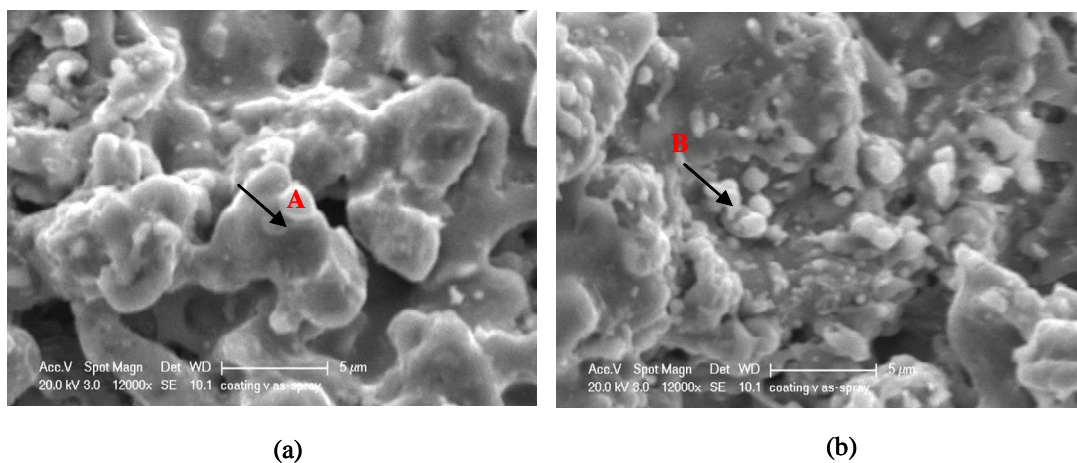


Fig. 6.10 SEM images of top surface morphology of as-sprayed 25Ni(Cr)-75Cr<sub>3</sub>C<sub>2</sub> coating with high magnifications

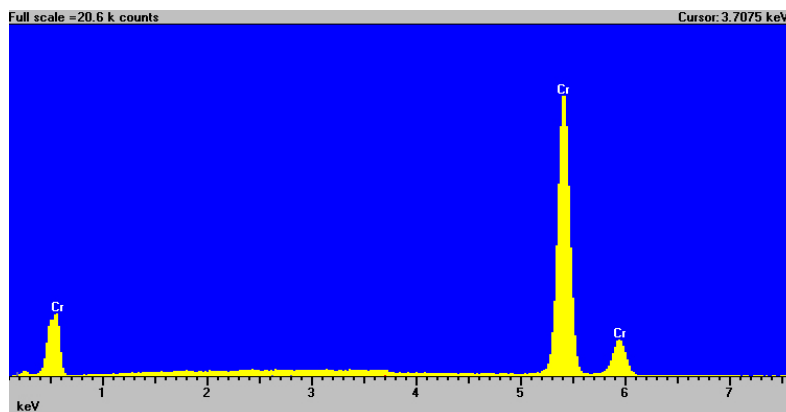


Fig. 6.11 EDX spectrum of pure chromium

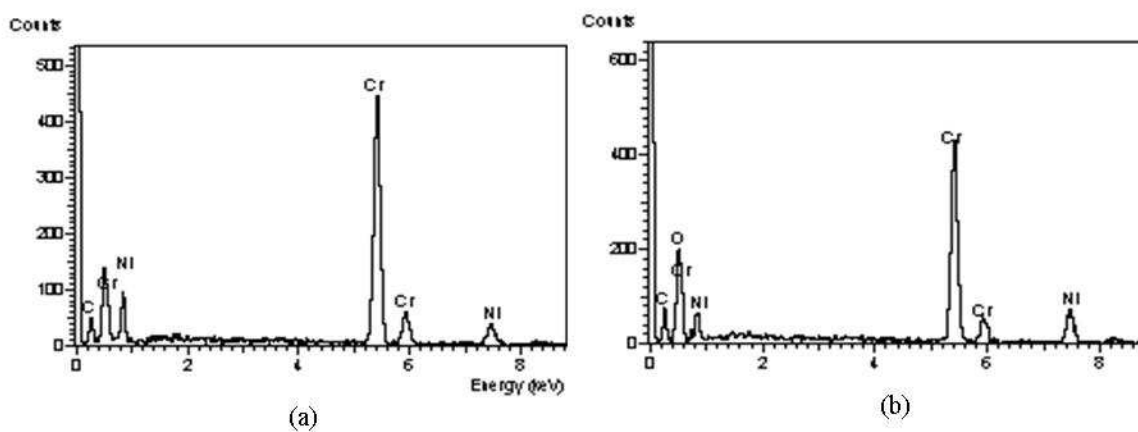


Fig. 6.12 EDX spectra of the phases detected on top surface of the as-sprayed coating, (a) and (b) corresponding to Fig 6.10 A and B

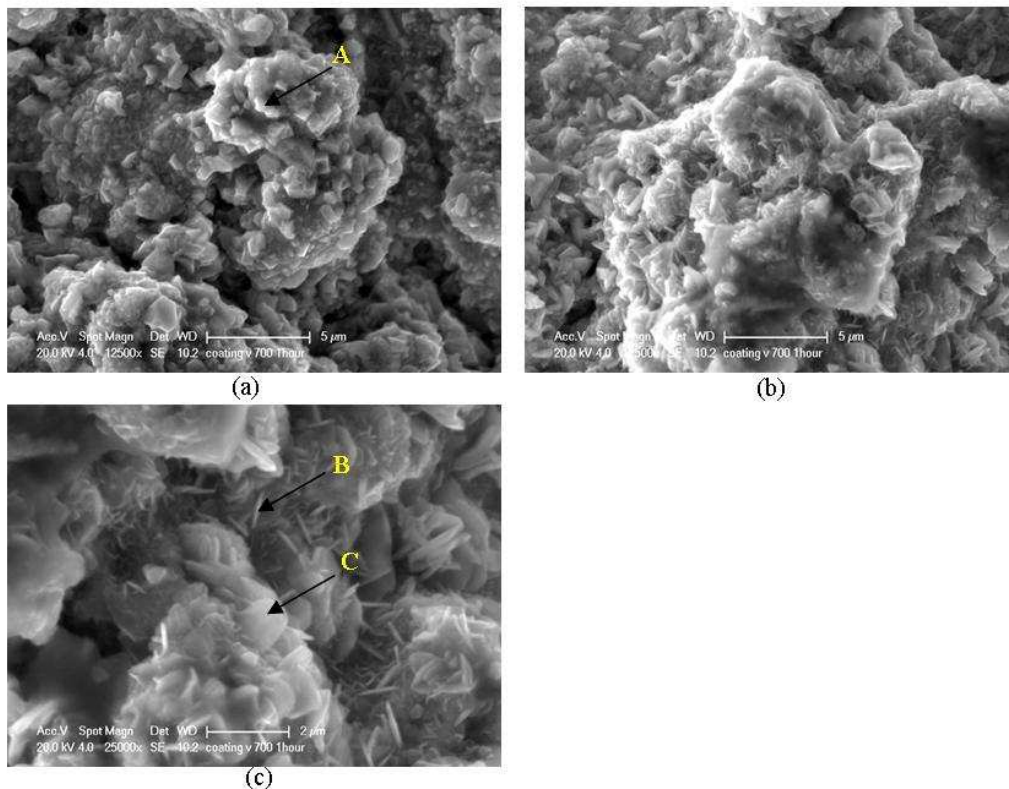


Fig. 6.13 SEM images of top surface morphology of 25Ni(Cr)-75Cr<sub>3</sub>C<sub>2</sub> coating oxidised at 700°C for 1 hour in air

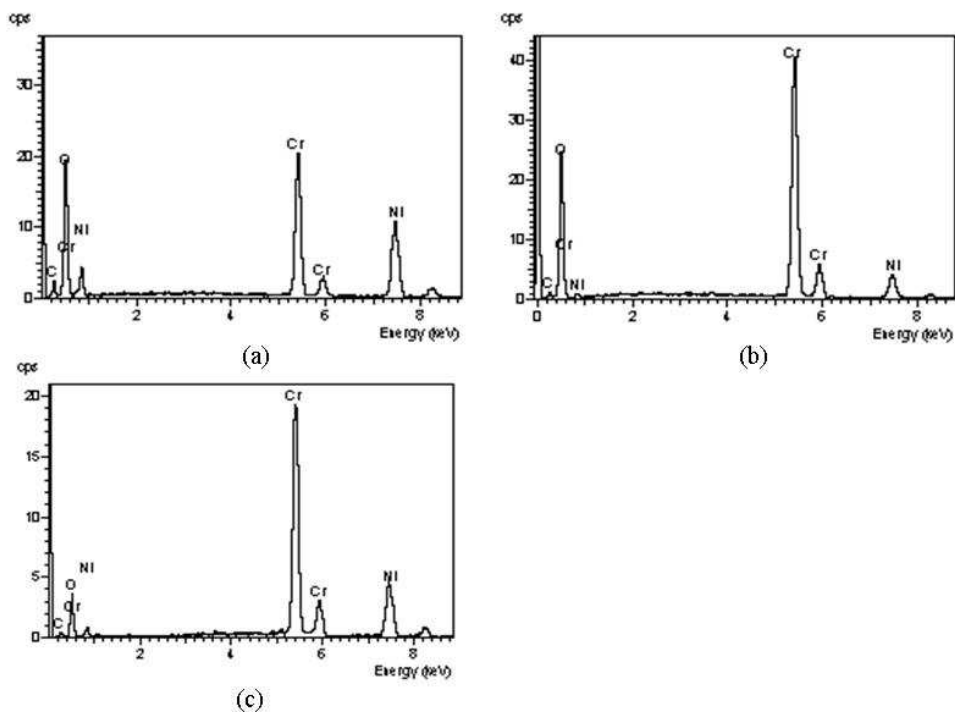


Fig. 6.14 EDX spectra of the phases detected on top surface of the Ni(Cr)-Cr<sub>3</sub>C<sub>2</sub> coating oxidised at 700°C for 1 hour in air, (a) (b) and (c) corresponding to Fig 6.13 A,B and C

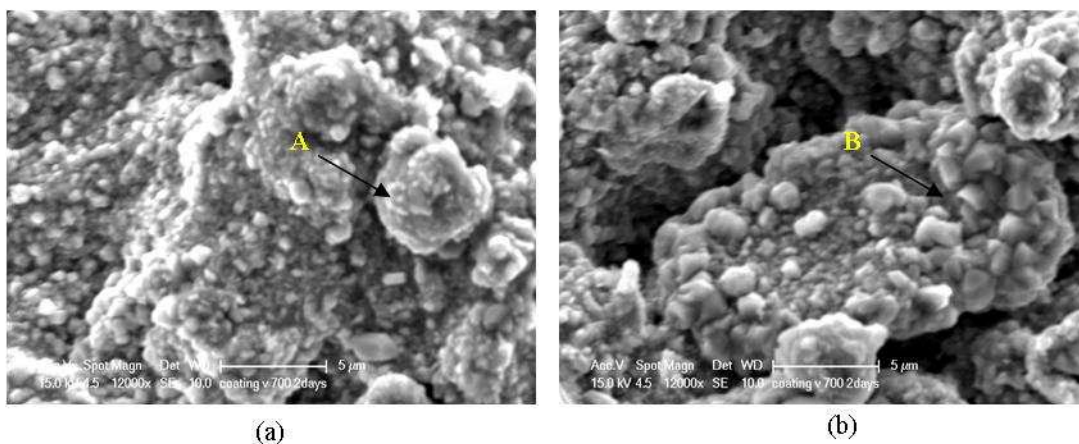


Fig. 6.15 SEM images of top surface morphology of the 25Ni(Cr)-75Cr<sub>3</sub>C<sub>2</sub> coating oxidised at 700°C for 2 days in air with the magnifications

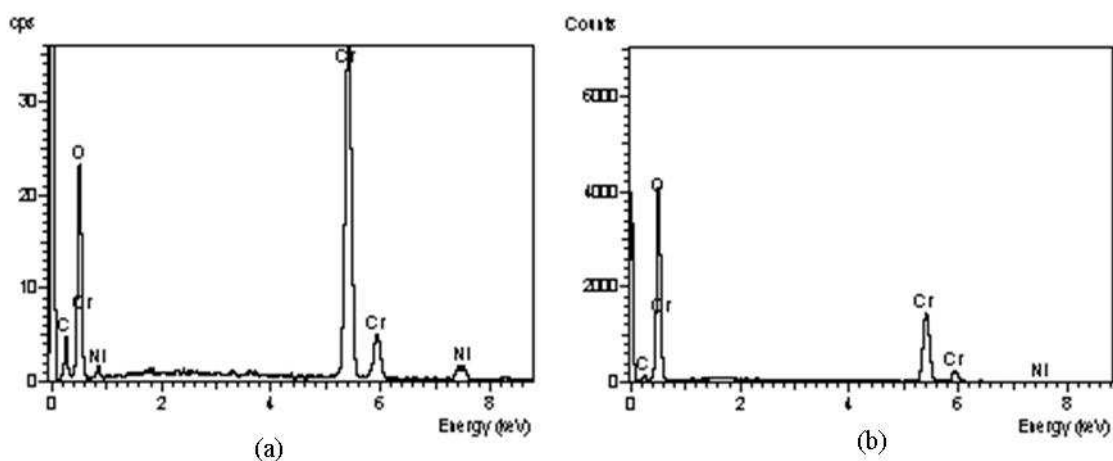


Fig. 6.16 EDX spectra of the phases detected on top surface of the Ni(Cr)-Cr<sub>3</sub>C<sub>2</sub> coating oxidised at 700°C for 2 days in air, (a) and (b) corresponding to Fig 6.15 A and B

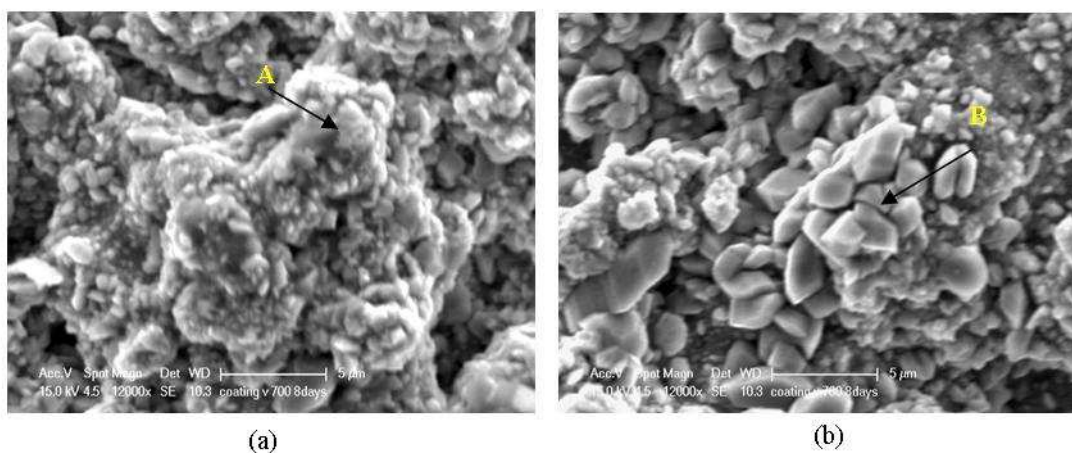


Fig. 6.17 SEM images of top surface morphology of 25Ni(Cr)-75Cr<sub>3</sub>C<sub>2</sub> coating oxidised at 700°C for 8 days in air

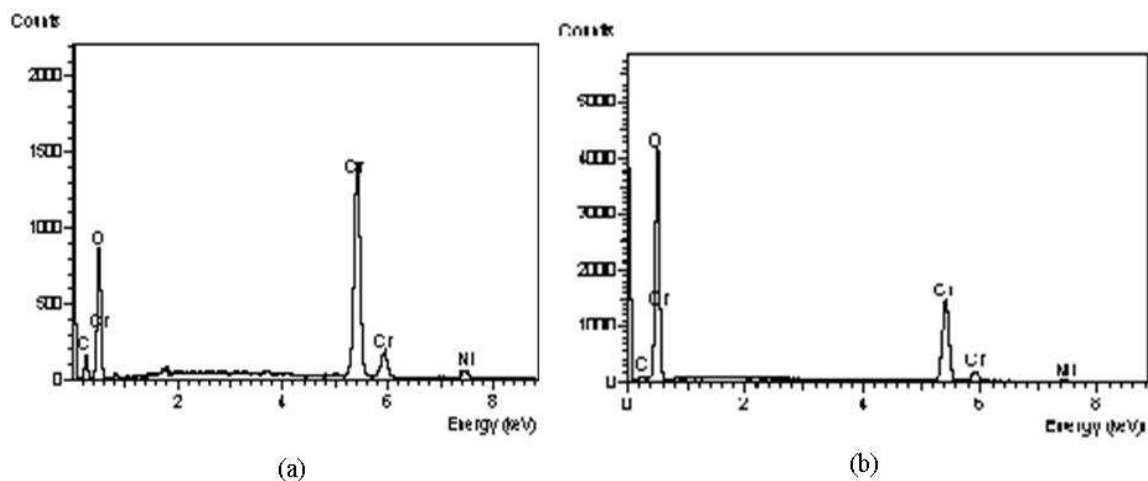


Fig. 6.18 EDX spectra of the phases detected on top surface of the Ni(Cr)-Cr<sub>3</sub>C<sub>2</sub> coating oxidised at 700°C for 8 days in air, (a) and (b) corresponding to Fig 6.17 A and B

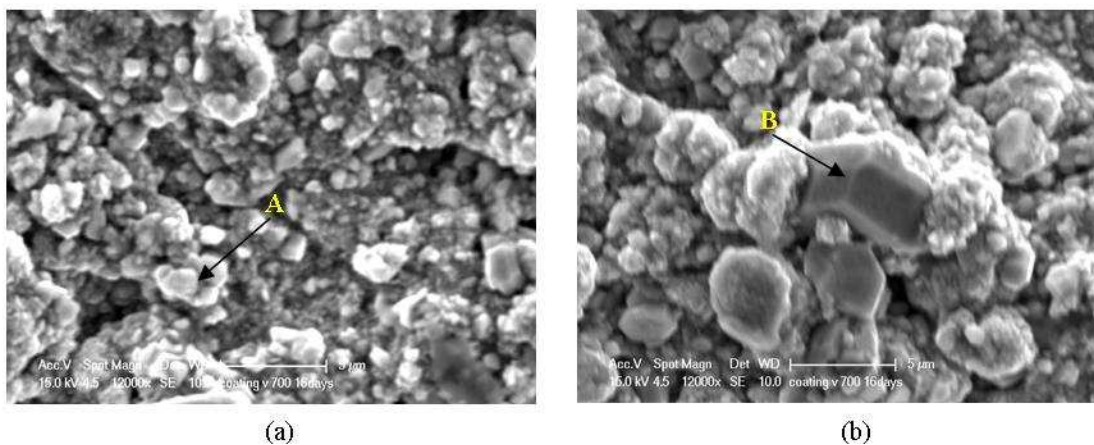


Fig. 6.19 SEM images of top surface morphology of 25Ni(Cr)-75Cr<sub>3</sub>C<sub>2</sub> coating oxidised at 700°C for 16 days in air

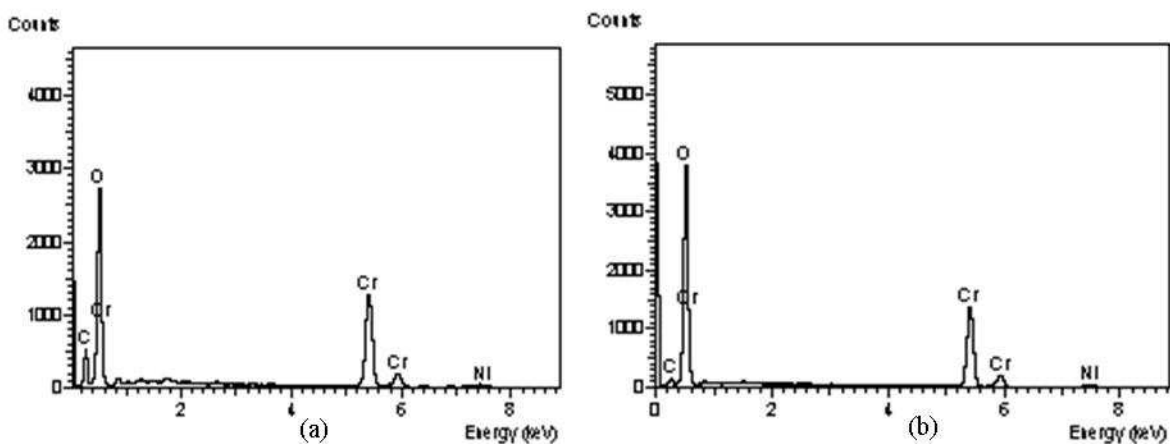


Fig. 6.20 EDX spectra of the phases detected on top surface of the Ni(Cr)-Cr<sub>3</sub>C<sub>2</sub> coating oxidised at 700°C for 16 days in air, (a) and (b) corresponding to Fig 6.19 A and B

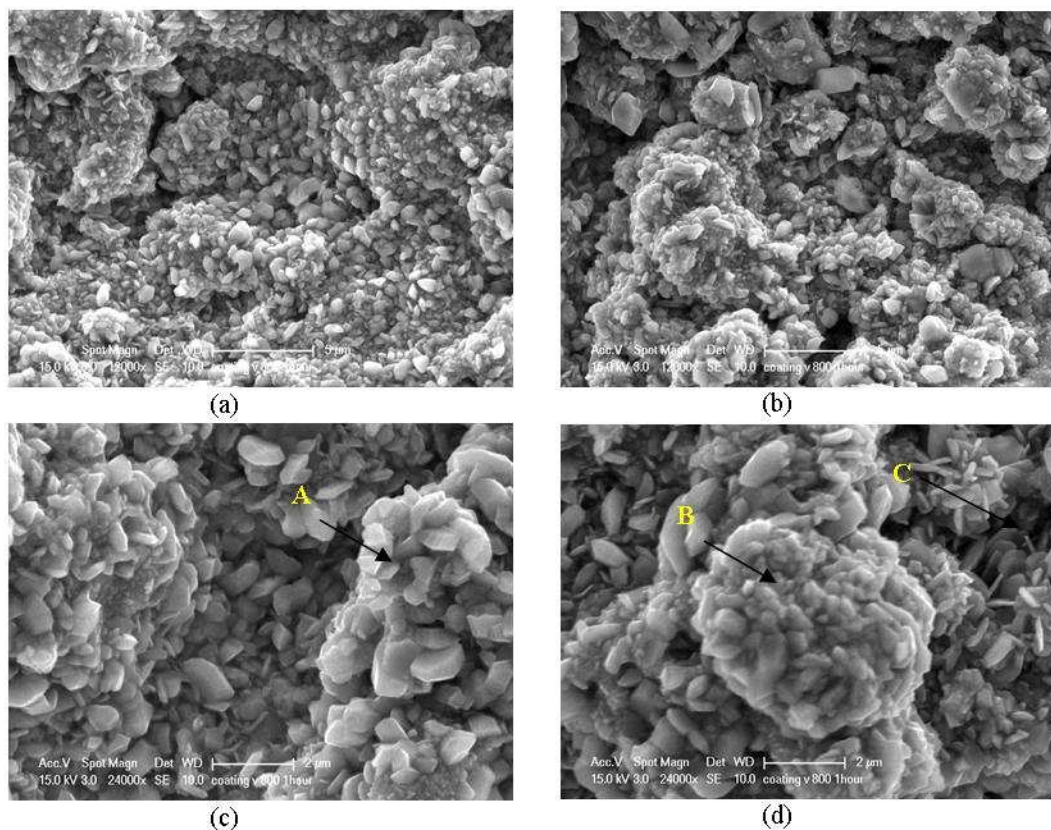


Fig. 6.21 SEM images of top surface morphology of 25Ni(Cr)-75Cr<sub>3</sub>C<sub>2</sub> coating oxidised at 800°C for 1hour in air

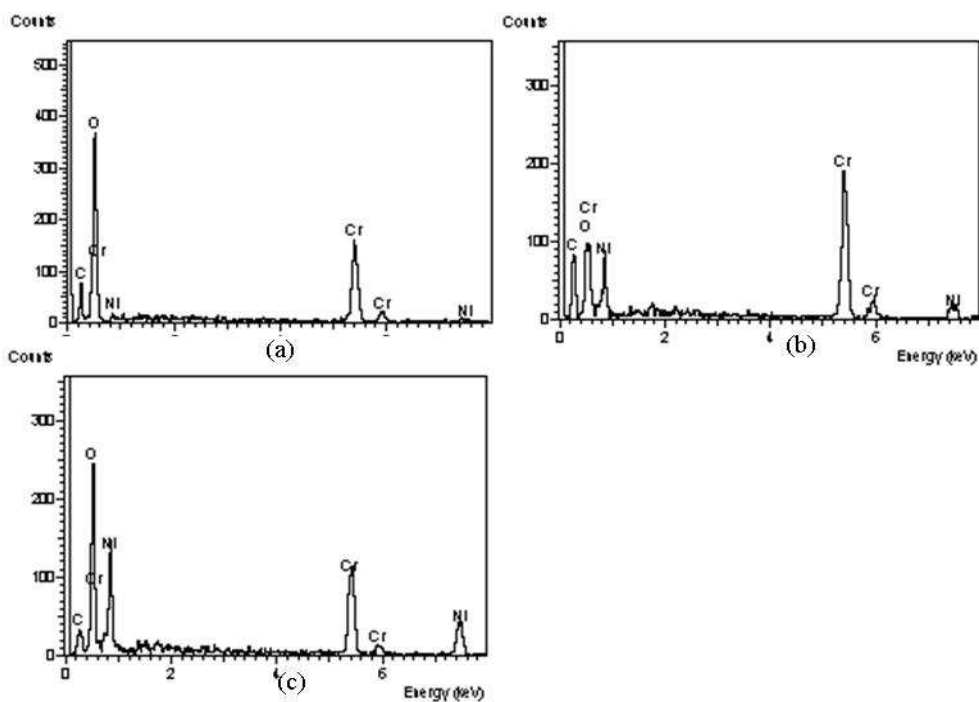


Fig 6.22 EDX spectra of the phases detected on top surface of the Ni(Cr)-Cr<sub>3</sub>C<sub>2</sub> coating oxidised at 800°C for 1hour in air, (a) (b) and (c) corresponding to Fig 6.21 A, B and C

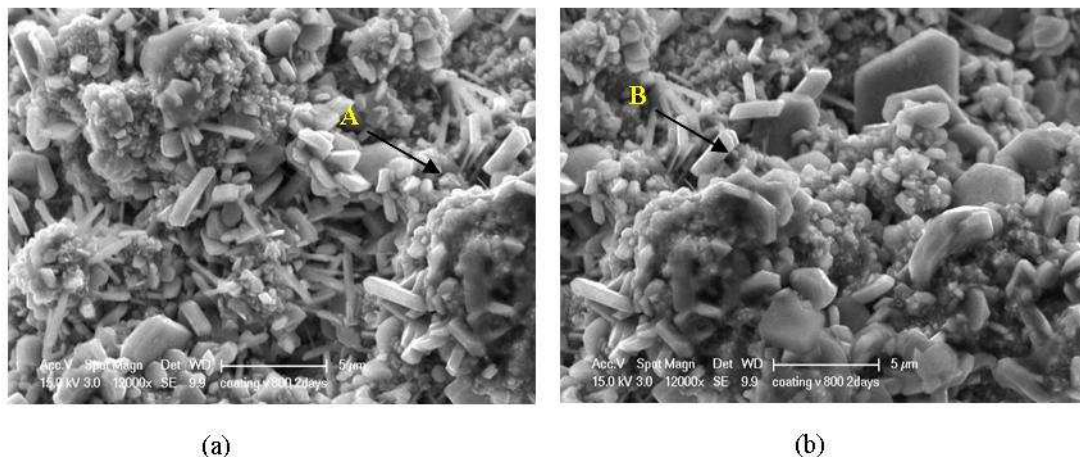


Fig. 6.23 SEM images of top surface morphology of 25Ni(Cr)-75Cr<sub>3</sub>C<sub>2</sub> coating oxidised at 800°C for 2 days in air

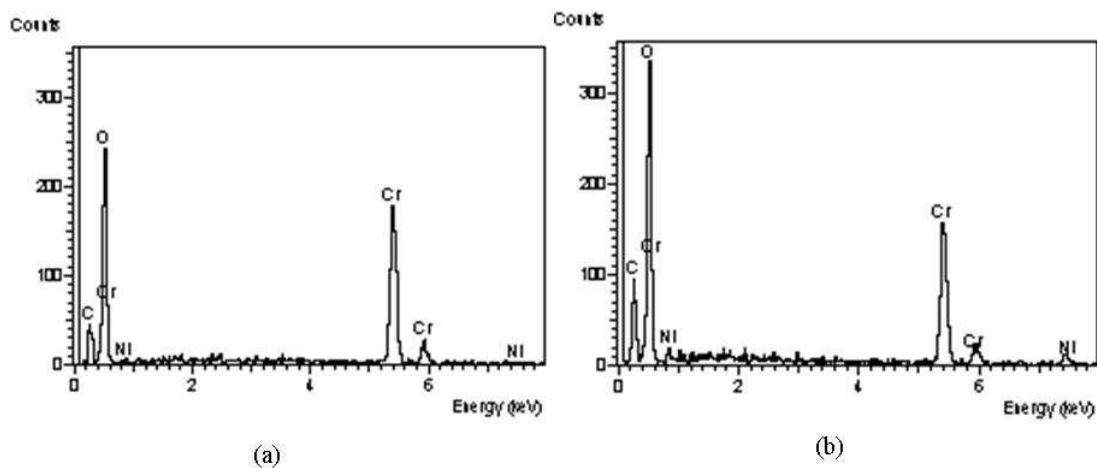


Fig. 6.24 EDX spectra of the phases detected on top surface of the Ni(Cr)-Cr<sub>3</sub>C<sub>2</sub> coating oxidised at 800°C for 2 days in air, (a) and (b) corresponding to Fig 6.23 A and B

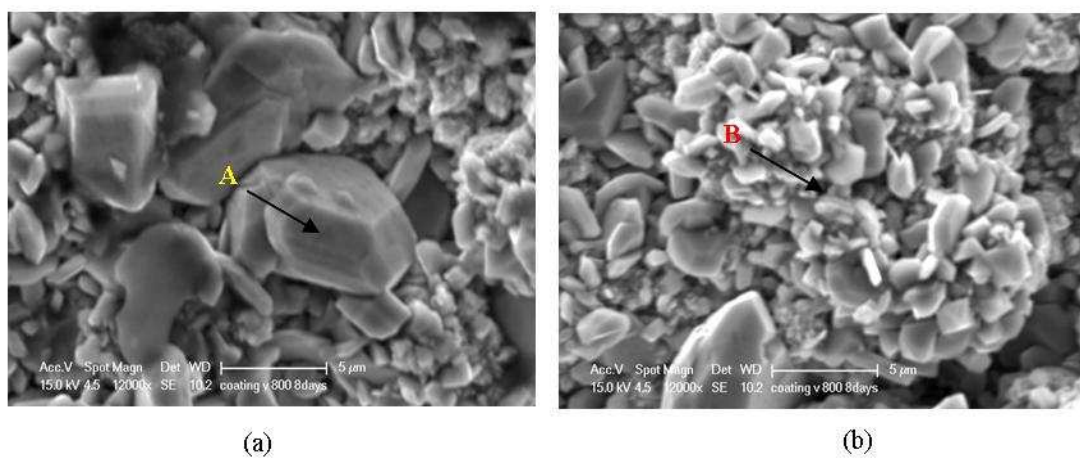


Fig. 6.25 SEM images of top surface morphology of 25Ni(Cr)-75Cr<sub>3</sub>C<sub>2</sub> coating oxidised at 800°C for 8 days in air

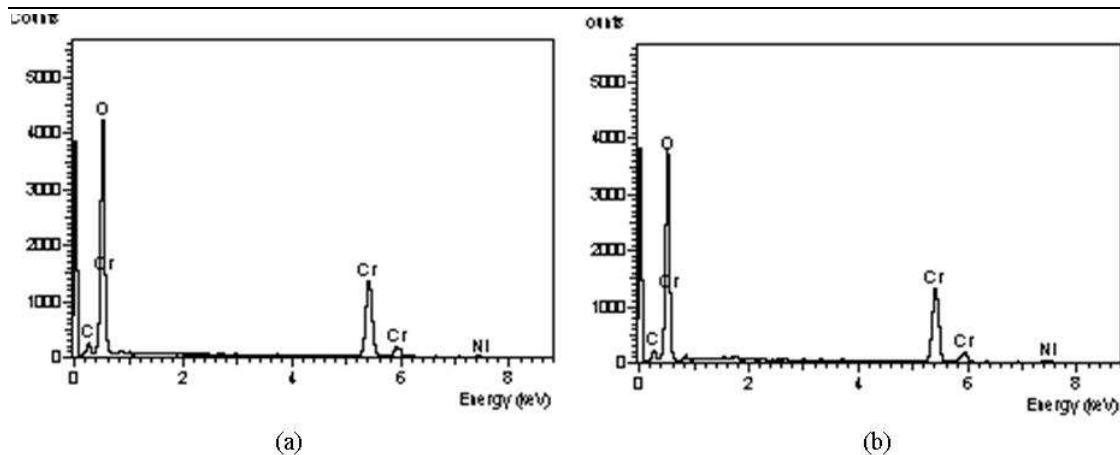


Fig. 6.26 EDX spectra of the phases detected on top surface of the Ni(Cr)-Cr<sub>3</sub>C<sub>2</sub> coating oxidised at 800°C for 8 days in air, (a) and (b) corresponding to Fig 6.25 A and B

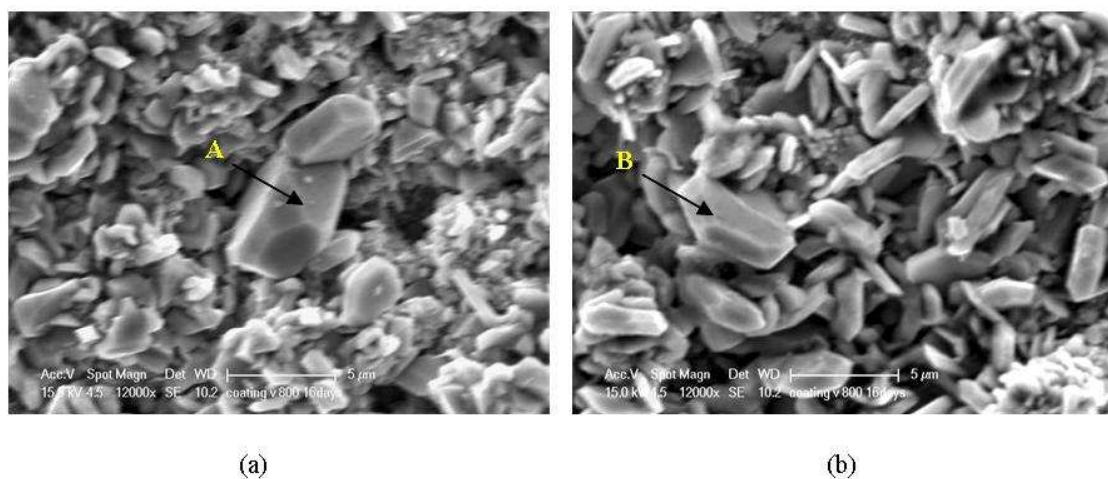


Fig. 6.27 SEM images of top surface morphology of 25Ni(Cr)-75Cr<sub>3</sub>C<sub>2</sub> coating oxidised at 800°C for 16 days in air

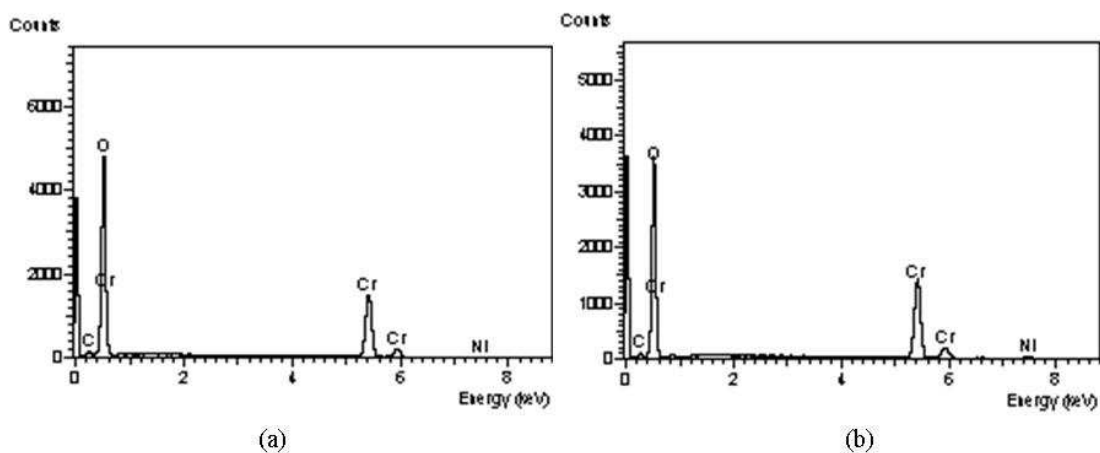


Fig. 6.28 EDX spectra of the phases detected on top surface of the Ni(Cr)-Cr<sub>3</sub>C<sub>2</sub> coating oxidised at 800°C for 16 days in air, (a) and (b) corresponding to Fig 6.27 A and B

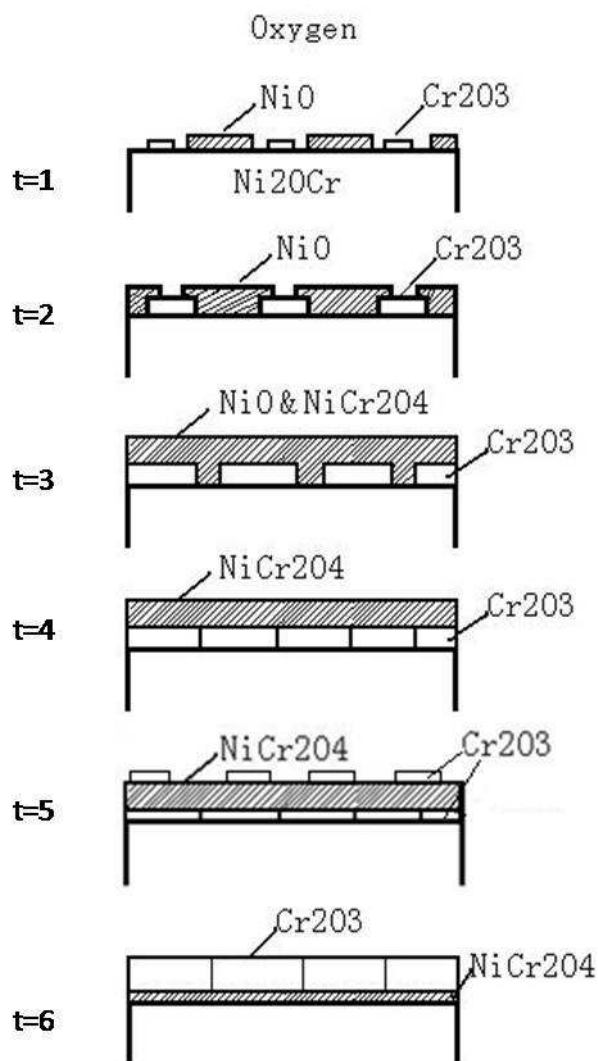


Figure 6.29 Schematic diagrams illustrating the oxidation of Ni-20Cr alloy

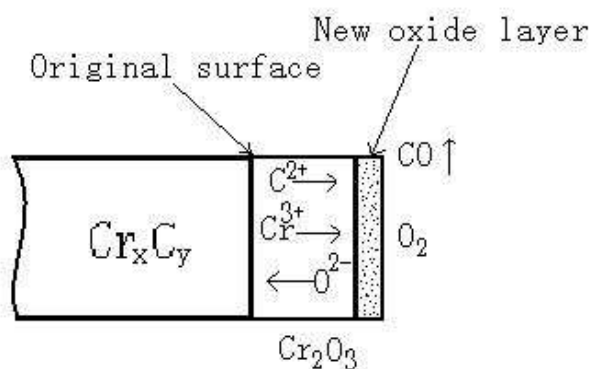


Figure 6.30 Schematic diagrams illustrating the oxidation of chromium carbide

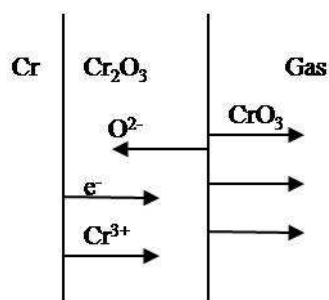


Fig 6.31 Schematic diagram of combined scale growth and oxide volatilization from Cr at temperature over 1000°C

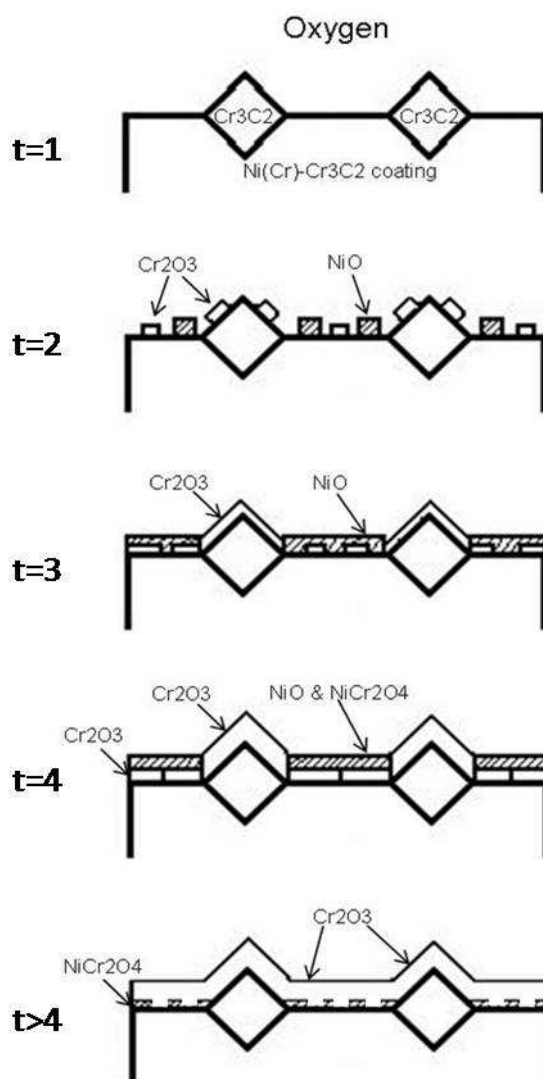


Fig 6.32 Schematic diagrams illustrating the oxidation on Ni(Cr)-Cr<sub>3</sub>C<sub>2</sub> coating surface

## Chapter 7: Conclusions

This research work has concentrated on the investigation of microstructure evolution of NiCr-Cr<sub>3</sub>C<sub>2</sub> coated 304 stainless steel during elevated temperature air exposure in the aspects of microstructure, microhardness, and coating-substrate inter-diffusion and coating oxidation. The findings lead to the following conclusions:

(i) Two kinds of agglomerated and sintered 25Ni(Cr)-75Cr<sub>3</sub>C<sub>2</sub> powder from different suppliers Metallisation and Praxair were used in HVOF thermal spraying. Praxair powder coating exhibited a higher deposition efficiency than the Metallisation powder coating. It also gave higher microhardness than that of the Metallisation powder coating. Praxair powder coatings were thus chosen for all the experiments in this work.

(ii) The study on the as-sprayed Praxair powder coating show that a complex microstructure comprising both unmelted angular particles. XRD analysis confirmed the presence of crystalline phases in the coating including f.c.c Ni(Cr), Cr<sub>3</sub>C<sub>2</sub> and Cr<sub>2</sub>O<sub>3</sub> together with a significant fraction of amorphous phase as indicated by a broad halo at the XRD pattern around 2θ range 40° to 50°. Cr<sub>3</sub>C<sub>2</sub> was confirmed as the only carbide present in the as-sprayed coating. The amorphous phase formation appeared to be due to the dissolution of carbide into the molten Ni-rich phase and the consequent super-saturation of the matrix with Cr and C, leading to amorphous phase formation on rapid cooling during deposition.

(iii) The microstructure and microhardness response of HVOF sprayed NiCr-Cr<sub>3</sub>C<sub>2</sub> coatings were assessed following exposure in air at 700 and 800°C for periods of up to 16 days. Transformation from amorphous phase to crystalline phase within the Ni(Cr) binder is found to occur within 1 hour at both temperatures. With long term exposure new carbide phases, Cr<sub>7</sub>C<sub>3</sub> and Cr<sub>23</sub>C<sub>6</sub>, started to form near the coating/

substrate interface. However, the bulk of the coating did not appear to form any new carbide. With heat treatment, matrix phase super-saturation was reduced, while widespread carbide nucleation and growth generated a carbide skeletal network near the coating/substrate interface. All samples showed a drop in hardness initially, but the hardness subsequently increased again after 2 days. The microhardness of the coating from the region near the coating/substrate interface showed a lower value than that from the middle region of the coating, it was as a result of losing carbon by carbon diffusion from the coating to the substrate during heat treatment.

(iv) During heat treatment, as the strong chemical potential gradients occur across the interface, carbon started to have a significant long range diffusion from the coating to substrate. Microhardness values measured on the substrate showed a significant increase near the coating/substrate interface and gradually decreased further away from the interface. Precipitates of  $(Cr_{23}C_6)$  found by BSE-SEM from the etched substrate samples started to grow further away from the interface in the substrate with continued exposure to high temperature. EDX analysis by line scans showed that during the heat treatment Ni also diffused from the coating in to substrate and Fe diffused from the substrate into the coating. At the interface between coating and substrate there was an increased pore size and this reduced the flux of elements by diffusion. A physical model of the element diffusion between coating and 304 substrate at high temperature has been proposed based on these phenomena.

(v) The oxidation of 25Ni(Cr)-75Cr<sub>3</sub>C<sub>2</sub> coatings during elevated temperature oxidation in air at temperatures ranging from 650°C to 1000°C were also investigated. The thermogravimetric study of the oxidation of 25Ni(Cr)-75Cr<sub>3</sub>C<sub>2</sub> coating indicated that the specific weight gain curves followed a parabolic kinetic law between temperature 650-800°C. With further temperature rise up to 1000°C oxidation rate increased sharply and oxidation follows complex parabolic kinetics. Weight loss occurred in the sample oxidised at 1000°C due to the volatilization of chromia. The

analysis of the rate constant as a function of temperature revealed that the activation energy of the coating oxidation reaction,  $Q$ , was 164.5 kJ/mol.

The principal topics for future work on HVOF thermally sprayed 25Ni(Cr)-75Cr<sub>3</sub>C<sub>2</sub> coatings are recommended as follows:

- The mathematical modelling of inter-diffusion in this work needs considerable developments. In future work, the diffusion of Ni, Cr and C from coating to the steel and diffusion of Fe from substrate to coating should be considered. The carbon concentration near the coating interface should not be considered as a constant value, as the value could decrease with continuous carbon diffusion from coating to substrate. For this complex modeling, the computer based software such as DICTRA, Thermol-Calc or MatCalc could be used to simulate and model the element distribution in the coating system.
- TEM is required to investigate precipitates in the substrate during elevated exposure temperature. Electron probe microanalysis (EPMA) to obtain more accurate quantitative composition analysis of interdiffusion is also required.

## References

- Allam IM, Whittle DP, Stringer J (1978) Oxidation behavior of CoCrAl systems containing active element additions, Oxidation of Metals, 12, 35-66
- Ardell AJ, (1985) Precipitation hardening, Metallurgical transactions A-physical metallurgy and materials science, 16, 2131-2165
- ASM (1987) Metals Handbook, 5 Ed 9, Surface Engineering, p. 367
- Atkinson A (1982) Conditions for the formation of new oxide within oxide-films growing on metals, Corrosion science, 22, 347-357
- Bellucci A, Gozzi D (2003) The TiC/TiO<sub>2</sub> interface, High temperature corrosion and materials chemistry IV, 2003, 298-309
- Berger LM, Vuoristo P, Mantyla T, Gruner W, (1998) A study of oxidation behaviour of WC-Co, Cr<sub>3</sub>C<sub>2</sub>-NiCr and TiC-Ni-based materials in thermal spray processes, THERMAL SPRAY, 1 & 2, 75-82
- Berger Z, Livshitz M, (1996) The structure and properties of hypervelocity oxy-fuel (HVOF) sprayed coatings, High temperature materials and processes, 15, 179-186
- Berthod P (2005) Kinetics of high temperature oxidation and chromia volatilization for a binary Ni-Cr alloy, Oxidation of Metals, 64, 235-252
- Berthod P (2007) Influence of chromium carbides on the high temperature oxidation behavior and on chromium diffusion in nickel-base alloys, Oxidation of Metals, 68, 77-96
- Bhadeshia H.K.D.H, (2006) Steel microstructure and properties, Elsevier Ltd, (Third edition), p259
- Birks N, Meier G.H (1983) Introduction to High Temperature Oxidation of Metals, Edward Arnold, London, p. 31, 61, 91
- Burstein G.T, Hutchings I.M, Sasaki K, (2000) Electrochemically induced annealing of stainless-steel surfaces, Nature, 407, 885-887
- Castello P, Stott F.H, Gesmundo F, (1998) The oxidation of a directionally solidified Ni-Al-Cr<sub>3</sub>C<sub>2</sub> alloy at 1100 and 1200°C in oxygen, Oxidation of metals, 49,583-610
- Chawla S.L. and Gupta, R.K. (1993) Materials selection for corrosion control. Ohio: ASM International.

Chevalier S, Desserrey F, Larpin J (2005) Oxygen transport during the high temperature oxidation of pure nickel, Oxidation of Metals, 64, 219-234

Colombier, Louis (1967) *Stainless and heat resisting steels*, Edward Arnold, London UK

Cottrell.A.H (1995) Crystal structures of transition metal carbides, Materials Science and Technology, 11, 329-333

Crawmer D.C, Krebsbach J.D, Riggs W.L (1992) Coating development for HVOF process using design of experiments Proceeding of The National Thermal Spray Conference, USA, pp 127-136

Cullity B.D, Stock S.R (2001) *Elements of X-ray diffraction*, Prentice Hall, (Third edition), P397, p630

Donald R. Askeland (2006) *The science and Engineering of Materials*, Fifth Edition, Thomson Canada Limited, Page 829

Dulin B, Kushner B, Rotolico A, (1990) High velocity oxy-fuel (HVOF) sprayed Inconel 718 coatings internal diameter, SAE technical paper, series No 900954, 1-13

Edris H, (1997) *Studies on High Velocity Oxy-Fuel Sprayed Coatings of Inconel 625 and Ni-Cr<sub>3</sub>C<sub>2</sub>*, PhD Thesis

Esteve.J, Romero.J, Go´mez.M, Lousa.A (2005) Cathodic chromium carbide coatings for molding die applications, Surface & Coatings Technology, 188–189, 506– 510

Foret R, Million B, Svoboda M, Stransky K (2001) Structural stability of dissimilar weld joints of steel P91, Science and technology of welding and joining, 6, 405-411

Gauzzi F, Montanari R, Principi G, Perin A, Tata ME (1999) Martensite formation during heat treatments of AISI 304 steel with biphasic structure, Materials Science and Engineering A, 273, 443-447

Guilemany JM, Nutting J, Llorca-Lsern N (1994) Characterisation of the Cr<sub>3</sub>C<sub>2</sub>-NiCr cermet powder for high velocity oxyfuel spraying, Powder Metallurgy, 37, 289-292

Guilemany JM, Nutting J, Llorca-Lsern N (1996) Microstructural Examination of HVOF Chromium Carbide Coatings for High-Temperature Applications, Thermal Spray Technology, 5(4), 483-489

- Guilemany JM, Miguel JM, Vizcaino S, et al. (2002) Role of heat treatments in the improvement of the sliding wear properties of Cr<sub>3</sub>C<sub>2</sub>-NiCr coatings Surface & coating technology, 157, 207-213
- Guy K.B, Butler E.P, West D.R.F (1983) Reversion of bcc alpha' martensite in Fe-Cr-Ni austenitic stainless-steels, Metal Science, 17, 167-176
- Haasen P (1996) Physical Metallurgy, third ed., Cambridge University Press, p 370.
- Han YF, Deb P, Chaturvedi MC (1982) Coarsening behavior of gamma'-particles and gamma'' particles in nickel alloy-718, Metal science, 16, 555-561
- Hays C, Douglas R, Sokal LS (1994) Thermal Spray Industrial Applications, ASM International, Material Park, Boston, pp 99-104
- He JH, Tamg XY, Fukuyama S, Yokogawa K (1995) Boundary in gamma''-precipitates in inconel-718 nickel-base super alloy, ACTA Metallurgica et Materialia, 43, 4403-4409
- He Jianhong, Ice M, Lavernia EJ (2000) Synthesis of nanostructured Cr<sub>3</sub>C<sub>2</sub>-25(Ni20Cr) coatings Metallurgical and materials transactions a-physical metallurgy and materials science, 31, 555-564.
- He Jianhong, Enrique J. Lavernia EJ (2001) Precipitation phenomenon in nanostructured Cr<sub>3</sub>C<sub>2</sub>-NiCr coatings, Materials Science and Engineering A, 301, 69-79
- He Jianhong, et al (2001) Thermal stability of nanostructureed Cr<sub>3</sub>C<sub>2</sub>-NiCr coatings, Thermal Spray Technol, 10, 293-300
- Herman H, (1988) Plasma Sprayed coatings, Scientific American, 259, No. 3, 78-83
- Herman H, Sampath S (1996) Thermal spray coatings, In: Stren K.H(ed), Metallurgical and ceramic protective coatings, London, Chapman&Hall, pp274-289
- Hong HU, Rho BS, Nam SW, (2001) Correlation of the M<sub>23</sub>C<sub>6</sub> precipitation morphology with grain boundary characteristics in austenitic stainless steel, Materials Science & Engineering A, 318, 285-292
- Hwang S.Y, Seong B.G (1993) Degradation behaviour of plasma sprayed Cr<sub>3</sub>C<sub>2</sub>-NiCr coating at high temperature (700-1000°C) Proceeding of The National Thermal Spray Conference, 7-11 June, California, pp 587-592
- Ignatov DV, Zhukov LL (1965) Rate of oxidation and scale structure of Nickel-Chromium alloys, Russian Metallurgy, 110

- Inoue A, (2000) Stabilization of metallic super cooled liquid and bulk amorphous alloys, Acta Materialia, 48, 279-306
- Javad M, Mohammad PF, Sanjeev C, (2002) Dynamics of splat formation in Plasma Spray Coating Process, Plasma Chemistry and Plasma Processing, 22, 59-84
- Ji Gang-Chang, Li Chang-Jiu, Wang Yu-Yue, Li Wen-Ya, (2006) Microstructural characterization and abrasive wear performance of HVOF sprayed  $\text{Cr}_3\text{C}_2$ -NiCr coating, Surface & Coatings Technology, 200, 6749-6757
- Kamal S, Jayaganthan R, Prakash S (2009) High temperature oxidation studies of detonation-gun-sprayed  $\text{Cr}_3\text{C}_2$ -NiCr coating on Fe- and Ni-based superalloys in air under cyclic condition at 900°C, Journal of alloys and compounds, 472, 378-389
- Karimi N, Riffard F, (2008) Characterization of the oxides formed at 1000 8C on the AISI 304 stainless steel by X-ray diffraction and infrared spectroscopy, Applied Surface Science, 254, 2292–2299
- Kajihara.M, Hillert.M (1990) Thermodynamic evaluation of the Cr-Ni-C system, Metallurgical transactions A, 21a, 2777-2787
- Kamnis S, Gu S, Zeoli N (2008) Mathematical modelling of Inconel 718 particles in HVOF thermal spraying, Surface & coating technology, 202, 2715-2724
- Kim BH, Suhr DS (2001) Characteristics of HVOF-sprayed  $\text{Cr}_3\text{C}_2$  (20 mass % NiCr) coatings part 2: Effect of heat treatment of the coatings, Materials Transactions, 42, 870-875
- Kofstad P, Lillerud K.P, (1980) On high-temperature oxidation of chromium II. Properties of  $\text{Cr}_2\text{O}_3$  and the oxidation mechanism of chromium, Journal of the electrochemical society, 127, 2410-2419
- Kozeschnik E, Polt P, Brett S, Buchmayr B (2002) Dissimilar 2 center dot 25Cr/9Cr and 2Cr/0 center dot 5CrMoV steel welds - Part 1: Characterisation of weld zone and numerical simulation, Science and Technology of Welding and Joining, 7, 65-68.
- Kunioishi CT (2006) High temperature oxidation and erosion-oxidation behaviour of HVOF sprayed Ni-20Cr, WC-20Cr-7Ni and  $\text{Cr}_3\text{C}_2$ -Ni-20Cr coatings, surface engineering, 22, 121-127
- Lee HM (1974) Carbon activity in austenite, Metallurgical Transactions, 5, 787-789
- Llewellyn D.T, Hudd R.C, (1998) Steel metallurgy and applications, Elsevier Ltd, (Third edition), p315

- Li Chang-Jiu, Ji Gang-Chang, Wang Yu-Yue, (2002) Dominant effect of carbide rebounding on the carbon loss during high velocity oxy-fuel spraying of Cr<sub>3</sub>C<sub>2</sub>-NiCr, Thin solid films, 419, 137-143
- Li CJ, Yang H, Li H (1999) Effect of gas conditions on HVOF flame and properties of WC-Co coatings, Materials and Manufacturing process, 14, 383-395
- Llewellyn D.T, Hudd R.C, (1998) Steel metallurgy and applications, Elsevier Ltd, (Third edition), p295
- Lillerud K.P, Kofstad P, (1980) On high-temperature oxidation of chromium I. Oxidation of annealed, thermally etched chromium at 800-1100°C, Journal of the electrochemical society, 127, 2397-2410
- Louis E. Toth (1971) Transition Metal Carbides and Nitrides, Refractory materials, vol 7
- Manish Roy, Andreas Pauschitz, Reinhard Polak, Friedrich Franek (2006) Comparative evaluation of ambient temperature friction behaviour of thermal sprayed Cr<sub>3</sub>C<sub>2</sub>-25(Ni20Cr) coatings with conventional and nano-crystalline grains, Tribology International, 39, 29-38
- Mangonon P.L, Thomas G (1970) Martensite phases in 304 stainless steel, Metallurgical transactions, 1, p. 1577
- Matthews SJ, James BJ, Hyland M (2009) The role of microstructure in the mechanism of high velocity erosion of Cr<sub>3</sub>C<sub>2</sub>-NiCr thermal spray coatings: Part 1-As-sprayed coatings, Surface & Coatings Technology, 203, 1086-1093
- Matthews. SJ, James. BJ, Hyland. MM (2009) The role of microstructure in the mechanism of high velocity erosion of Cr<sub>3</sub>C<sub>2</sub>-NiCr thermal spray coatings: Part 2-Heat treated coatings, Surface & Coatings Technology, 203, 1094-1100
- Matthews. S, Hyland. M, James. B (2003) Microhardness variation in relation to carbide development in heat treated Cr<sub>3</sub>C<sub>2</sub>-NiCr thermal spray coatings ACTA Materialia, 51, 4267-4277
- Mangonon P.L, Thomas Martensite G (1970) phases in 304 stainless steel, Metallurgical transactions, 1, 1577
- Michal GM, Ernst F, Heuer AH, (2006) Carbon paraequilibrium in austenitic stainless steel, Metallurgical and Materials Transactions A: Physical Metallurgy and Materials Science, 37A, 1819-1824
- Million B, Bacilek K, Kucera J, Michalicka P, Rek A, Stransky A, (1995) Carbon diffusion and thermodynamic characteristics in chromium steels, Zeitschrift Fur Metallkunde, 86,

706-712

Mohanty M, Smith R.W, Bonte M.De, Celis J.P, Lugscheider E (1996) Sliding wear behavior of thermally sprayed 75/25 Cr<sub>3</sub>C<sub>2</sub>/NiCr wear resistant coatings, Wear, 198, 251-266

Moreau C, Cielo P, Lamontagne M (1992) Flattening and solidification of thermal sprayed particles, Proceedings of the Institution of Mechanical Engineers, 181, 215-221

Mott NF, Nabarro FRN (1940) An attempt to estimate the degree of precipitation hardening, with a simple model, Proceedings of the Physical Society, 52, 86-89

Music.D, Kreissig.U, Mertens.R, Scheider.J.M (2004) Electronic structure and mechanical properties of Cr<sub>7</sub>C<sub>3</sub>, Physics Letters A, 326, 473-476

Murthy JKN, Bysakh S, Gopinath K, Venkataraman B (2007) Microstructure dependent erosion in Cr<sub>3</sub>C<sub>2</sub>-20(NiCr) coating deposited by a detonation gun, Surface and Coating Technology, 202, 1-12

Nishizawa T (1977) Experimental study of Fe-Mn-C and Fe-Cr-C systems at 1000 degrees-C, Scandinavian Journal of Metallurgy, 6, 74-78

Ohliger A, Szelagowski P, Schafstall H-G, (1990) Thermal spraying-recent development for underwater application, The 3<sup>rd</sup> National Thermal Spray Conference, USA, 193-200

Oneill H, Rottherham L, Humerothery W, (1948) Miro-hardness testing of metals-discussion, Journal of the institute of metals, 74, 725-736

Pawlowski, L (1995) The science and engineering of thermal spray coatings, England, P6

Pecker d, Bernstein M.I (1977) Handbook of Stainless steels, McGraw-Hill Book Company, p 4.

Peraldi R, Monceau D, Pieraggi B (2002) Correlations between growth kinetics and microstructure for scales formed by high-temperature oxidation of pure nickel. I. Morphologies and microstructures, Oxidation of Metals, 58, 249-273

Peterson SF, Mataya MC, Matlock DK (1997) The formability of austenitic stainless steels, Jom-Journal of the Minerals Metals & Materials Society, 49, 54-58

Philip A. Schweitzer, P.E. (2003) Metallic materials physical, mechanical, and corrosion properties, Marcel Dekker, Inc, p110

Pilous V, Stransky K. (1998) Structural stability of deposits and welded joints in power engineering, Cambridge international science publishing

- Porter D.A, Easterling K.E (1992) Phase Transformations in Metals and Alloys, second edition, Chapman & Hall, London, UK, p73
- Reed RP, (1962) Spontaneous martensitic transformations in 18 percent Cr, 8 percent Ni steel, Acta metallurgica, 10, p. 865
- Rozenak P, Bergman R (2006) X-ray phase analysis of martensitic transformations in austenitic stainless steels electrochemically charged with hydrogen, Materials Science & Engineering A, 437, 366-378
- Sasaki. M, Kawakami.F, Komaki.C and Ishida.M (1992) Characterization of HVOF Sprayed Cr<sub>3</sub>C<sub>2</sub> Coating Proceedings of International Thermal Spray Conference & Exposition, Florida, USA
- Sanbongi K, Ohtani M, Toita K (1957) On the effect of alloying elements on the solubility of carbon in molten iron, The Research Institution of Mineral Dressing and Metallurgy, 147-158
- Sedriks A. John (1996) Corrosion of stainless steel, John Wiley & Sons Inc, New York, (Second edition), p13
- Shaw K.G, Gruninger M.F, Jarosinski W.J (1994) High temperature intermetallic binders for HVOF carbides, Proceeding of The 7<sup>th</sup> National Thermal Spray Conference, USA, pp 185-190
- Smith E B, Power GD, Barber TJ, Chiappetta LM (1991) United technology research centre report 91-8, East Hartford, CT
- Sobolev VV, Guilemany JM(1999), Effect of oxidation on droplet flattening and splat–substrate interaction in thermal spraying, J Therm Spray Technol, 8(4), 523–530.
- Sobolev.V.V, Guilemany J.M, Calero J.A (1995) Dynamic Processes during In-Flight Motion of Cr<sub>3</sub>C<sub>2</sub>-NiCr Powder Particles in High Velocity Oxy-Fuel (HVOF) Spraying, Materials Processing & Manufacturing Science, 4, 25-39
- Sourmail, T; Too, CH; Bhadeshia, HKDH (2003) Sensitisation and evolution of chromium-depleted zones in Fe-Cr-Ni-C systems, ISIJ International, 43, 1814-1820
- Sopousek J, Foret R (2008) More sophisticated thermodynamic designs of welds between dissimilar steels. Science and Technology of Welding and Joining, 13, 17-24
- Sopousek J, Foret R, Jan V (2004) Simulation of dissimilar weld joints of steel P91. Science and Technology of Welding and Joining, 9, 59-64.

- Stasiek M, Oechsner A (2006) Numerical simulation of carburization and decarburization profiles in steels, Diffusion in Solids and Liquids - MASS DIFFUSION, 258-260, 366-371
- Storms E.K. (1967) The refractory carbides, Refractory materials, vol 2,108-112
- Sturgeon A.J (1992) High velocity oxyfuel spraying promises better coatings, Powder Technology, pp 547-548
- Suegama PH, Espallargas N, Guilemany JM (2006) Electrochemical and structural characterization of heat-treated Cr<sub>3</sub>C<sub>2</sub>-NiCr coatings, Journal of the Electrochemical Society, 153, B434-B445
- Sundararaman M, Mukhopadhyay P, Banerjee S (1988) Deformation-behavior of gamma' strengthened inconel-718, ACTA Metallurgica, 36, 847-864
- Tao Kai, Zhou Xianglin, Cui Hua, Zhang Jishan (2009) Microhardness variation in heat-treated conventional and nanostructured NiCrC coatings prepared by HVOF spraying, Surface & Coatings Technology, 203, 1406-1414
- Tavares S.S.M, Silva da M.R etc, (2006) Microstructural changes produced by plastic deformation in the UNS S31803 duplex stainless steel, Journal of materials processing technology, 180, 318-322
- Thorpe M.L (1993) Thermal spray industry in transition, Advance materials and processes, 5, pp 50-61
- Tsai S.C, Huntz A.M, Dolin C, (1995) Growth mechanism of Cr<sub>2</sub>O<sub>3</sub> scales: oxygen and chromium diffusion, oxidation kinetics and effect of yttrium, Materials science and engineering, 212, 6-13
- Xie Jia-ying, Lidong Teng, Chen Nan-xian Seshadri Seetharaman, (2006) Atomistic study on the structural properties and phase stability for Cr<sub>23</sub>C<sub>6</sub>, Mn<sub>23</sub>C<sub>6</sub>, Alloys and compounds, 420, 269-272
- Xie Jia-ying, Chen Nan-xian, Jiang Shen, Lidong Teng, Seshadri Seetharaman, (2005) Atomistic study on the structure and thermodynamic properties of Cr<sub>7</sub>C<sub>3</sub>, Mn<sub>7</sub>C<sub>3</sub>, Fe<sub>7</sub>C<sub>3</sub>, Acta Materialia, 53, 2727-2732
- Velikanova T.Ya, Bondar A.A, Grytsiv A.V, (1998) The Chromium-Nickel-Carbon (Cr-Ni-C) Phase Diagram, Journal of Phase Equilibria, 20, 125-147
- Venkatraman.M and Neumann.J.P, (1990) ASM, Metal Handbook,3 Ed. 10, Alloy phase diagram. P.2. 109,155,112

Venkataraman R, Das G, Singh S.R, Pathak L.C, Ghosh R.N, (2007) Study on influence of porosity, pore size, spatial and topological distribution of pores on microhardness of as plasma sprayed ceramic coatings, Materials Science and Engineering A, 445-446, 269-274

Voitovich VB (1997) Mechanism of the high temperature oxidation of titanium carbide, High temperature materials and processes, 16, 243-253

William D. Callister, Jr. (1997) Materials Science and Engineering An Introduction, 4<sup>th</sup> edition, Department of Metallurgical Engineering, The University of Utah, P578

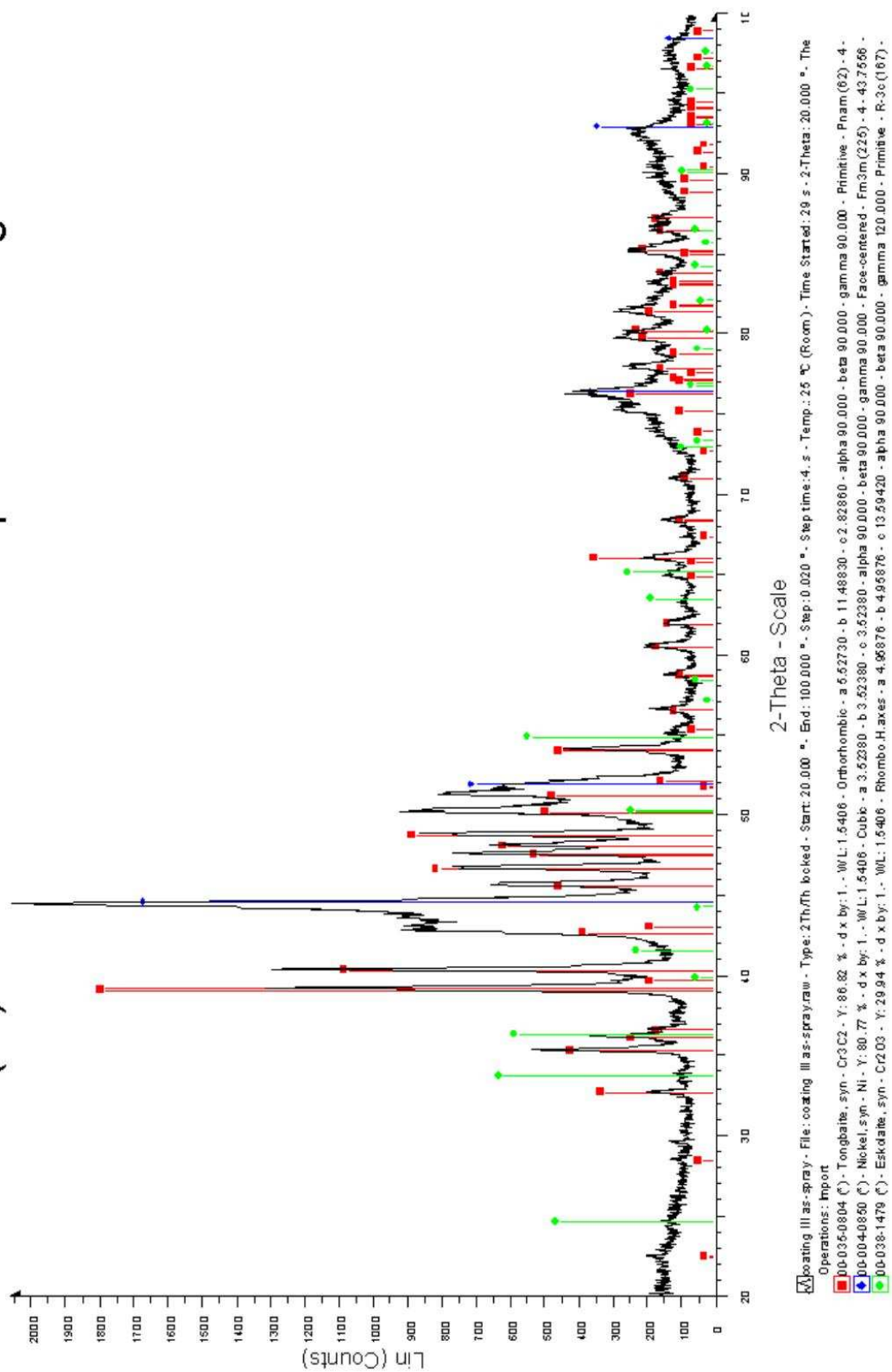
Wirojanupatump S, P.H. Shipway, D.G. McCartney (2001) The influence of HVOF powder feedstock characteristics on the abrasive wear behaviour of Cr<sub>x</sub>C<sub>y</sub>-NiCr coatings Wear, 249, 829-837

Ye FX, Wu SH, Ohmori A (2008) Microstructure and Oxidation Behavior of Cr<sub>39</sub>Ni<sub>7</sub>C Cermet Coatings Deposited by Diamond Jet Spray Process, Thermal Spray Technology, 17, 942-947

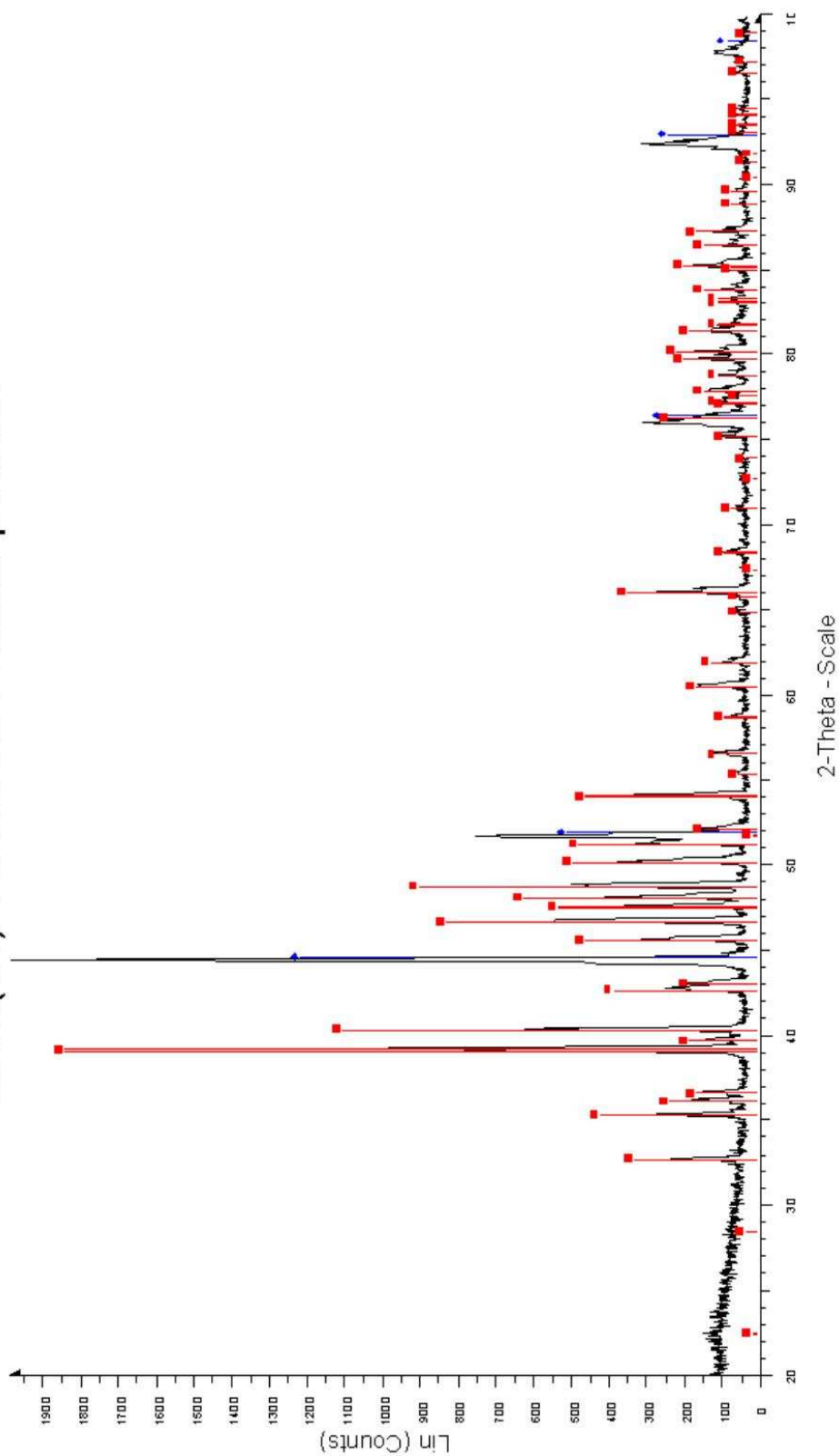
Zimmermann S, Kreye H. (1996) Chromium carbide coatings produced with various HVOF spray systems, Thermal spray: practical solutions for engineering problems, p147-52



# 25Ni(Cr)-75Cr3C2 Metallisation powder coating

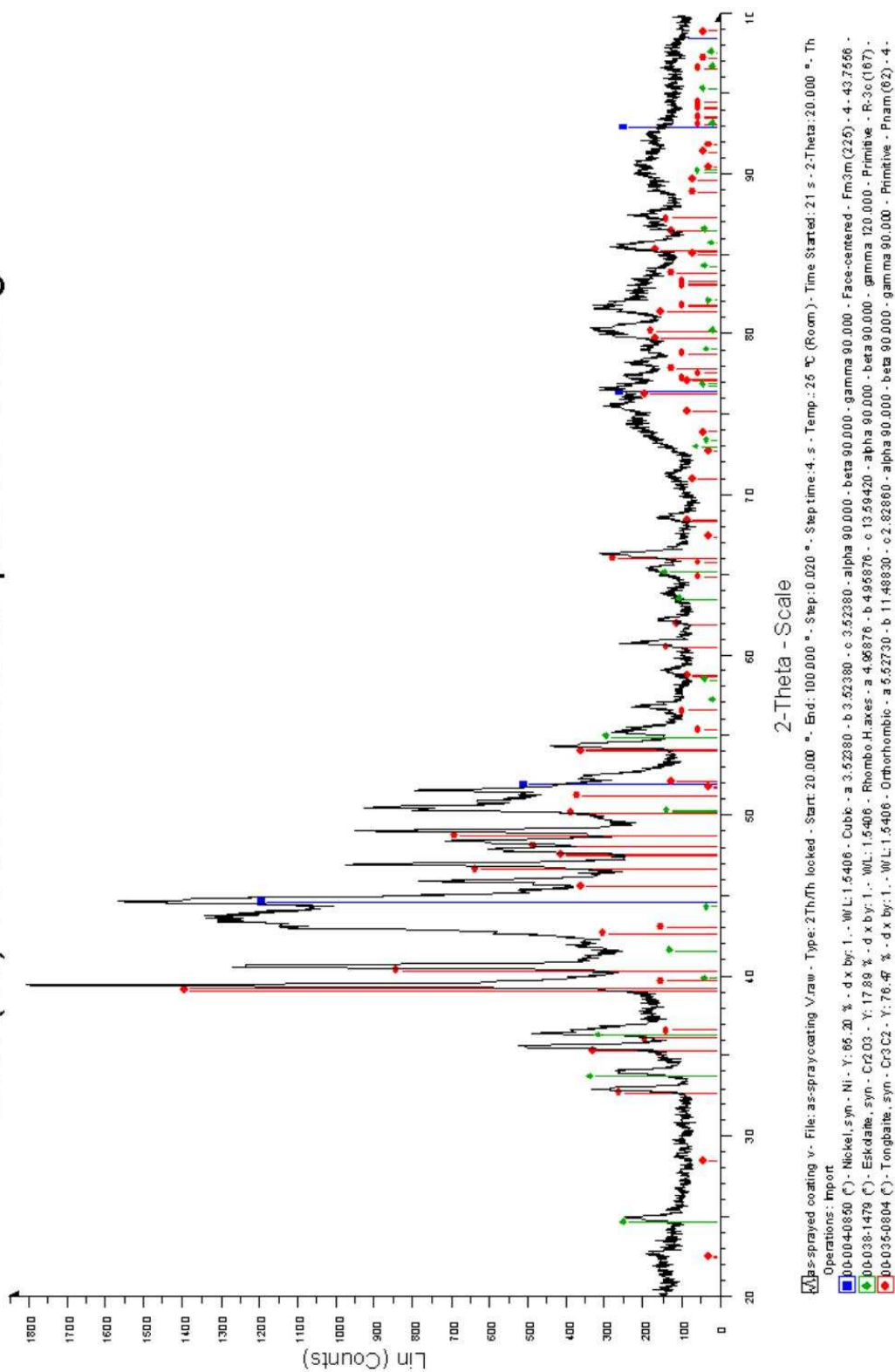


# 25Ni(Cr)-75Cr3C2 Praxair powder

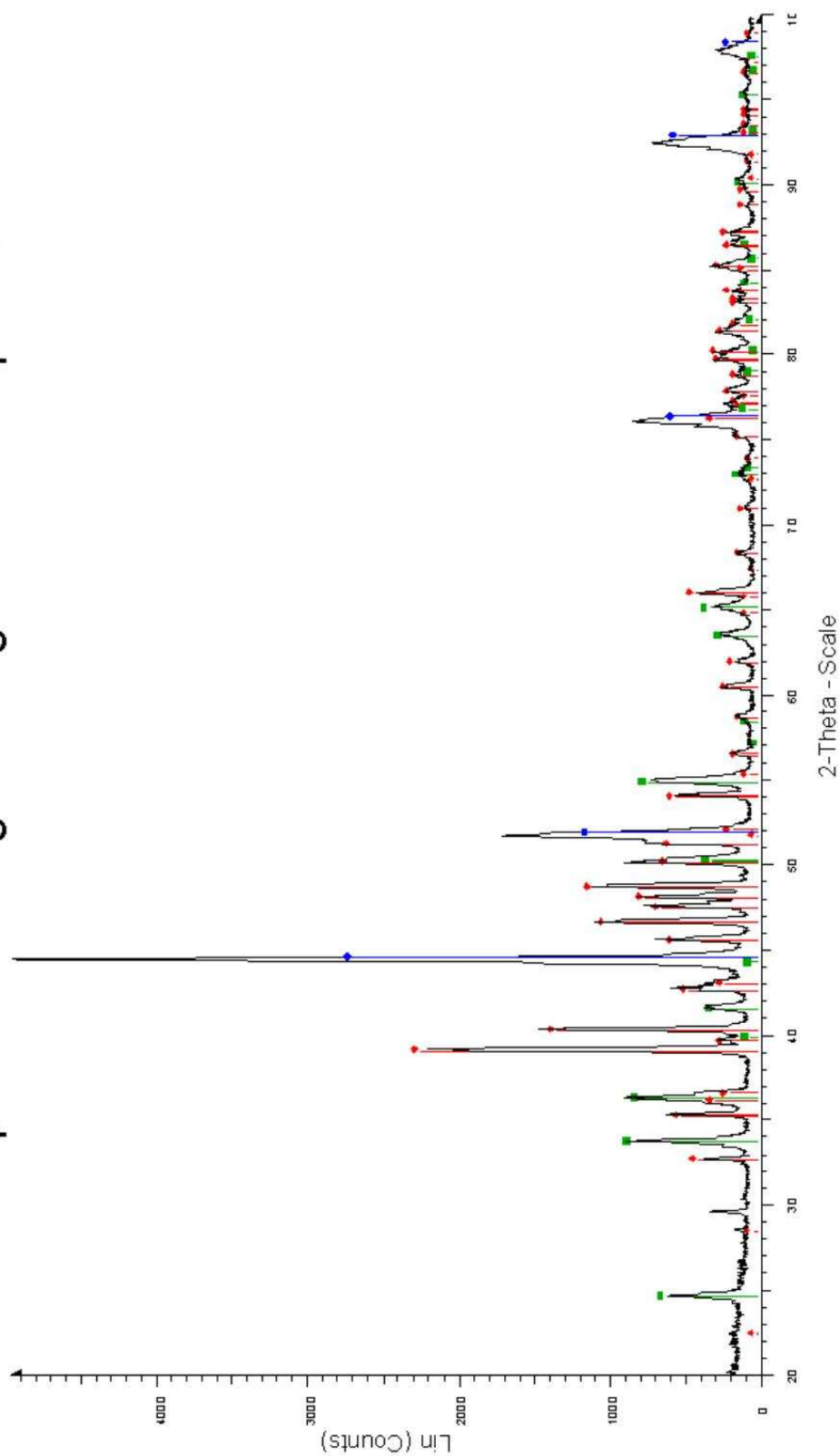


new powder - File: new powder.raw - Type: 2Th/Th locked - Start: 20.000 ° - End: 100.000 ° - Step: 0.020 ° - Step time: 4. s - Temp.: 25 °C (Room) - Time Started: 29 s - 2-Theta: 20.000 ° - Theta: 10.000 ° -  
 Operations: Import  
 00-035-0804 (°) - Tongbate, syn - Cr3C2 - Y: 93.02 % - d x by: 1. - W/L: 1.5406 - Orthorhombic - a 5.5730 - b 11.48830 - c 2.82860 - alpha 90.000 - beta 90.000 - gamma 90.000 - Primitive - Pnam(62) - 4 -  
 00-004-0880 (°) - Nickel, syn - Ni - Y: 81.46 % - d x by: 1. - W/L: 1.5406 - Cubic - a 3.52380 - b 3.52380 - c 3.52380 - alpha 90.000 - beta 90.000 - gamma 90.000 - Face-centered - Fm3m(225) - 4 - 43.7586 -

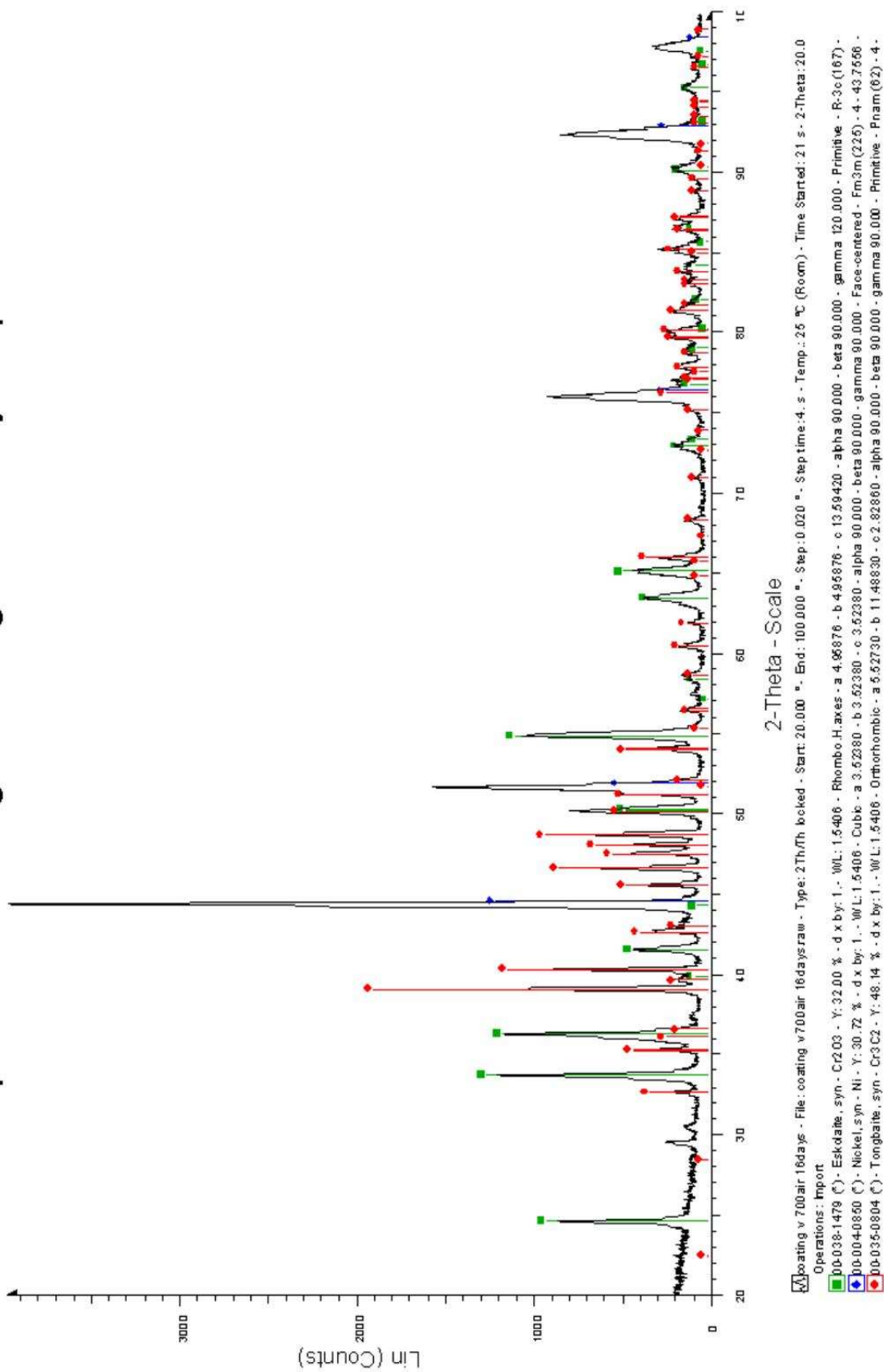
## 25Ni(Cr)-75Cr3C2 Praxair powder coating



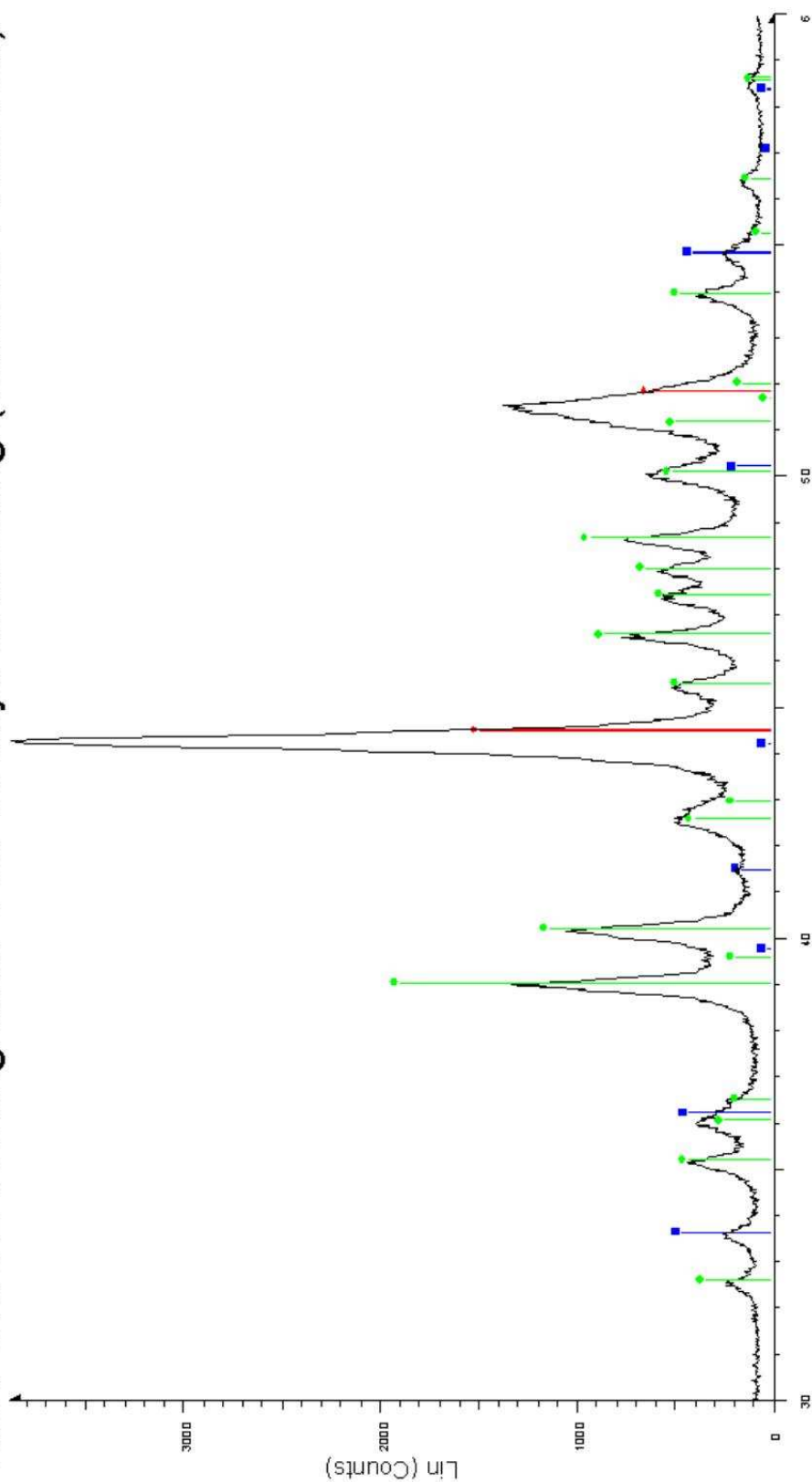
# Praxair powder coating 700 degree 1 hour top surface



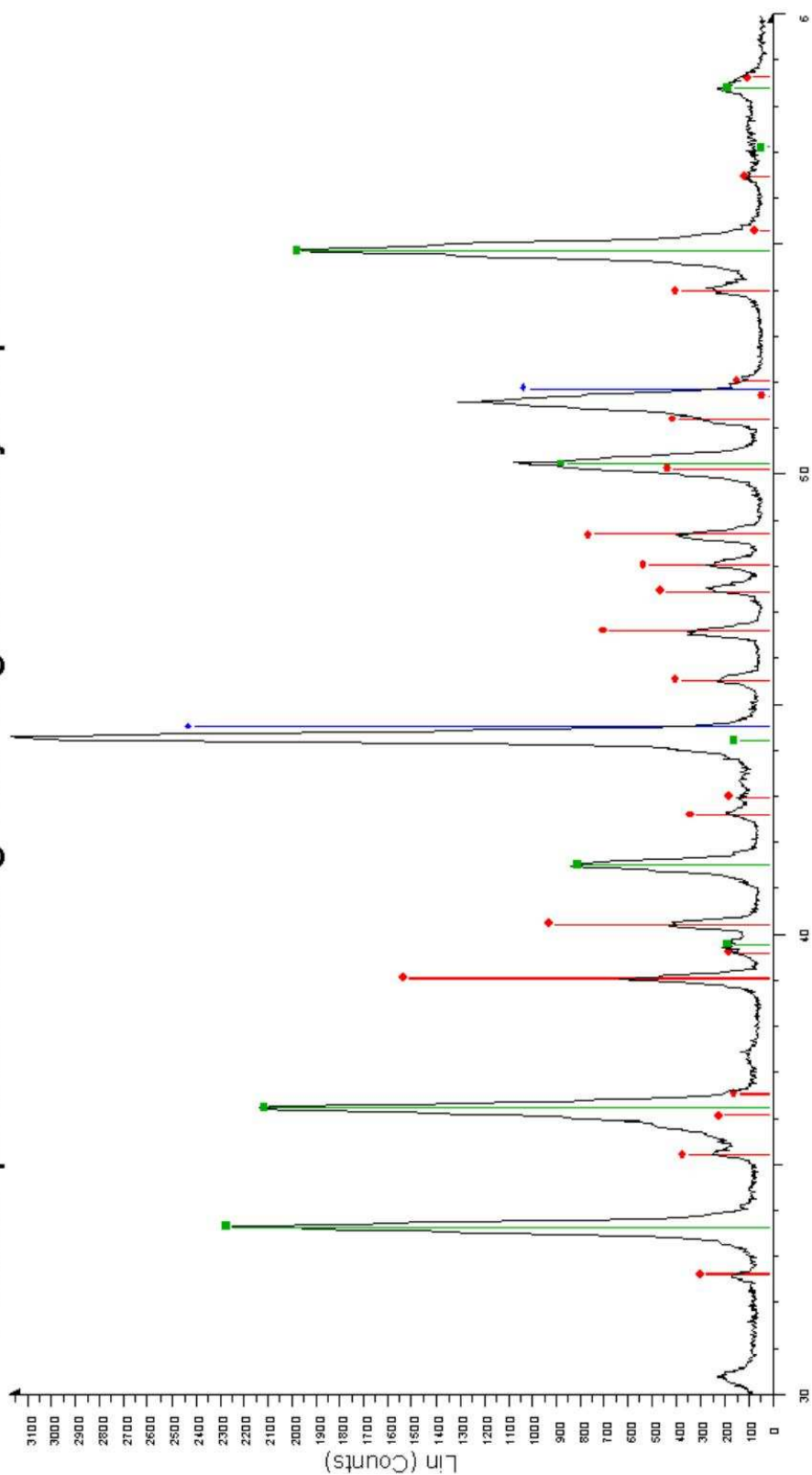
# Praxair powder coating 700 degree 16days top surface



# NiCr-Cr3C2 coating after 700 16days annealing (surface removed)

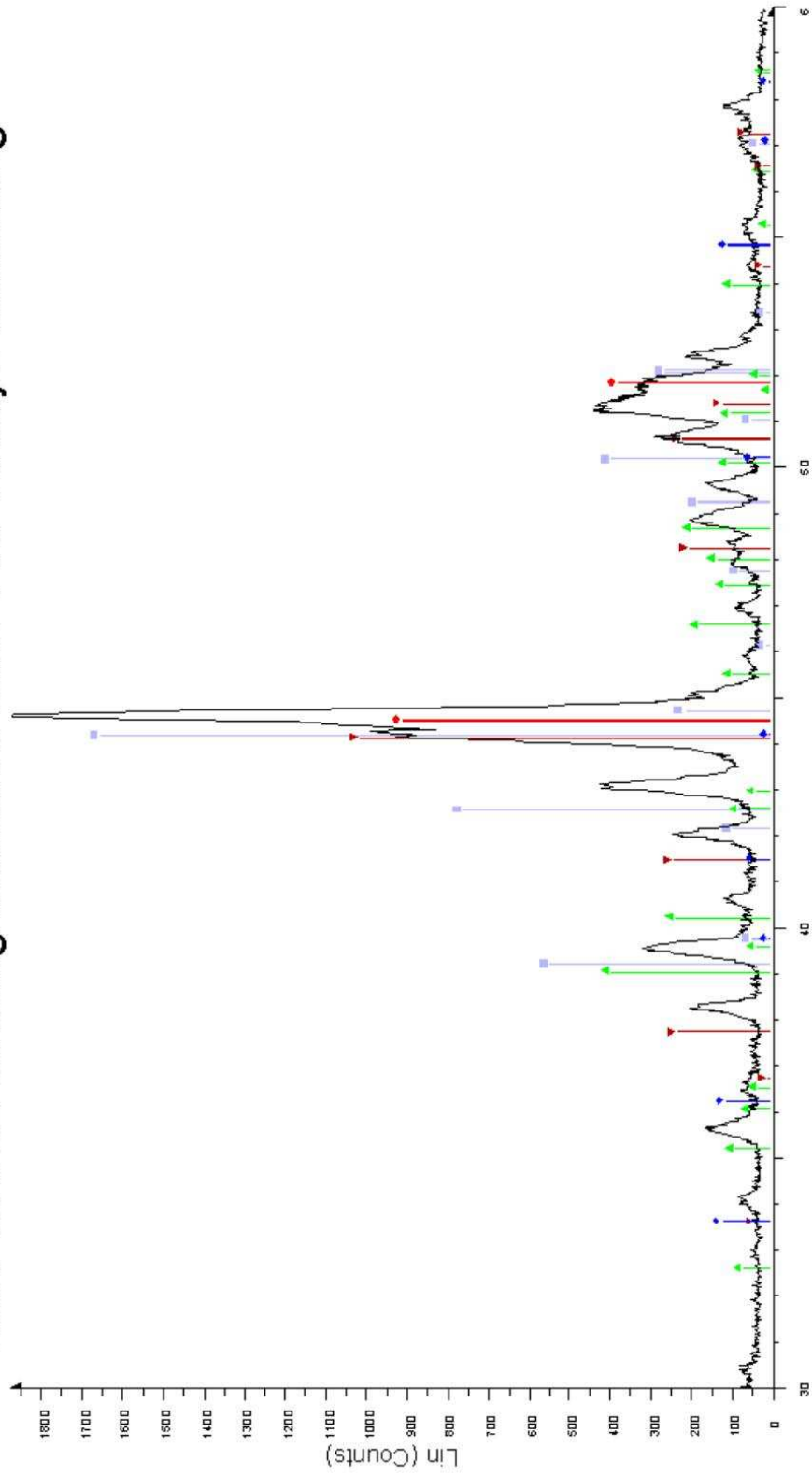


# Praxair powder coating 800 degree 16days top surface



coating v 800air 16days - File: coating v800air 16daysraw - Type: 2Th/Th locked - Start: 20.000 ° - End: 100.000 ° - Step: 0.020 ° - Step time: 4. s - Temp.: 25 °C (Room) - Time Started: 29 s - 2-Theta: 20.0  
 Operations: Import  
 00-038-1479 (°) - Eskolaite, syn - Cr<sub>2</sub>O<sub>3</sub> - Y: 70.98 % - d x by: 1. - W/L: 1.5406 - Rhombo.H.axes - a 4.96876 - b 4.96876 - c 13.59420 - alpha 90.000 - beta 90.000 - gamma 120.000 - Face-centered - Fm3m (225) - 4 - 43.7566 -  
 00-004-0850 (°) - Nickel, syn - Ni - Y: 75.95 % - d x by: 1. - W/L: 1.5406 - Cubic - a 3.52380 - b 3.52380 - c 3.52380 - alpha 90.000 - beta 90.000 - gamma 90.000 - Face-centered - Fm3m (225) - 4 - 43.7566 -  
 00-035-0804 (°) - Tongbaite, syn - Cr<sub>3</sub>C<sub>2</sub> - Y: 47.89 % - d x by: 1. - W/L: 1.5406 - Orthorhombic - a 5.52730 - b 11.48830 - c 2.82860 - alpha 90.000 - beta 90.000 - gamma 90.000 - Primitive - Pnam (62) - 4 -

# NiCr-Cr3C2 coating interface after 700 16days annealing



Operations: Import

00-036-1482 (C) - Chromium Carbide - Cr7C3 - Y: 88.66 % - d x by: 1. - W/L: 1.5406 - Orthorhombic - a 7.01490 - b 12.15300 - c 4.53200 - alpha 90.000 - beta 90.000 - gamma 90.000 - Primitive - Pnccm (61)

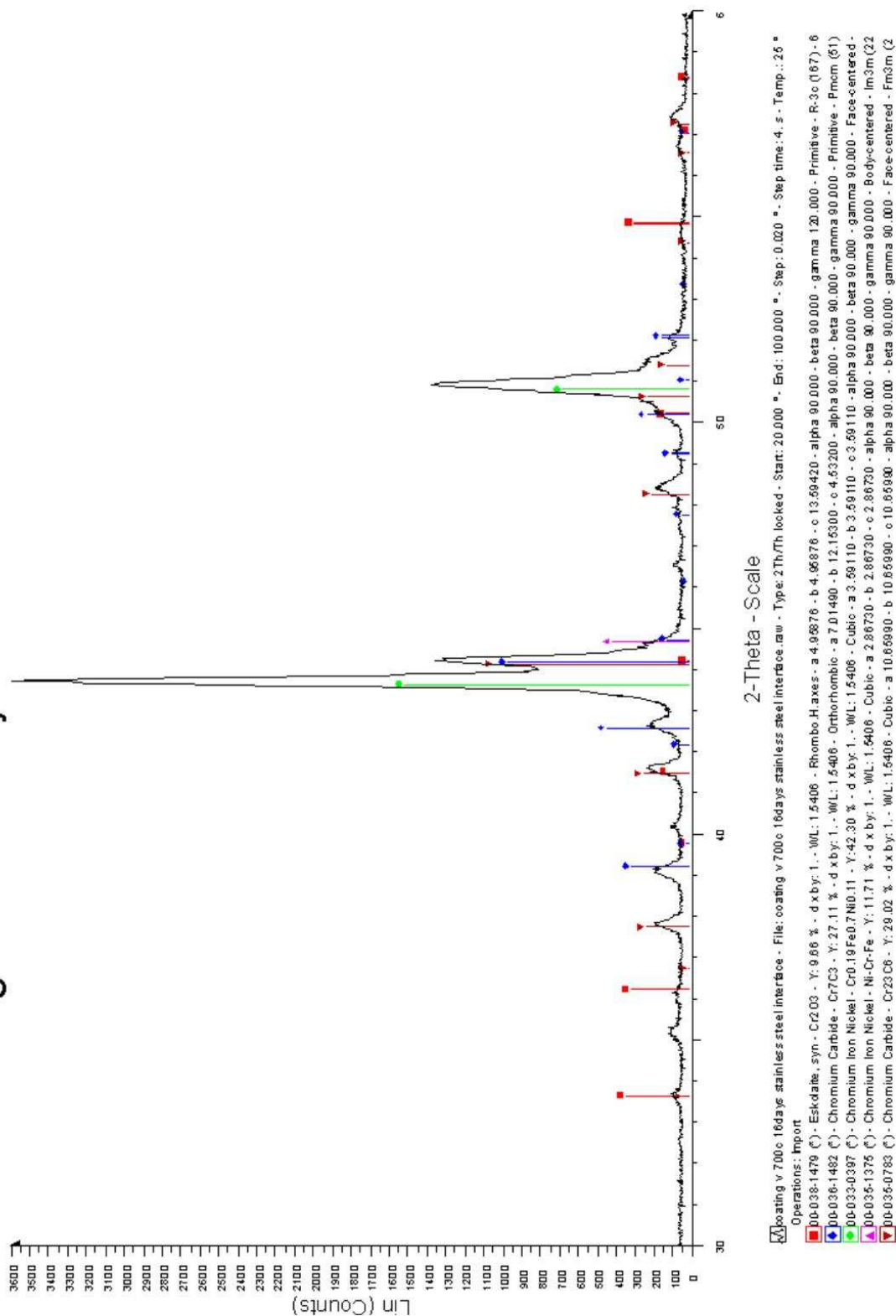
00-038-1479 (C) - Eskolaite, syn - Cr2O3 - Y: 6.62 % - d x by: 1. - W/L: 1.5406 - Rhombo H, axes - a 4.96876 - b 4.96876 - c 13.59420 - alpha 90.000 - beta 90.000 - gamma 120.000 - Primitive - R-3c (167) - 6

00-004-0850 (C) - Nickel, syn - Ni - Y: 48.88 % - d x by: 1. - W/L: 1.5406 - Cubic - a 3.52380 - alpha 90.000 - beta 90.000 - gamma 90.000 - Face-centered - Fm3m (225) - 4 - 43.7566 - 4

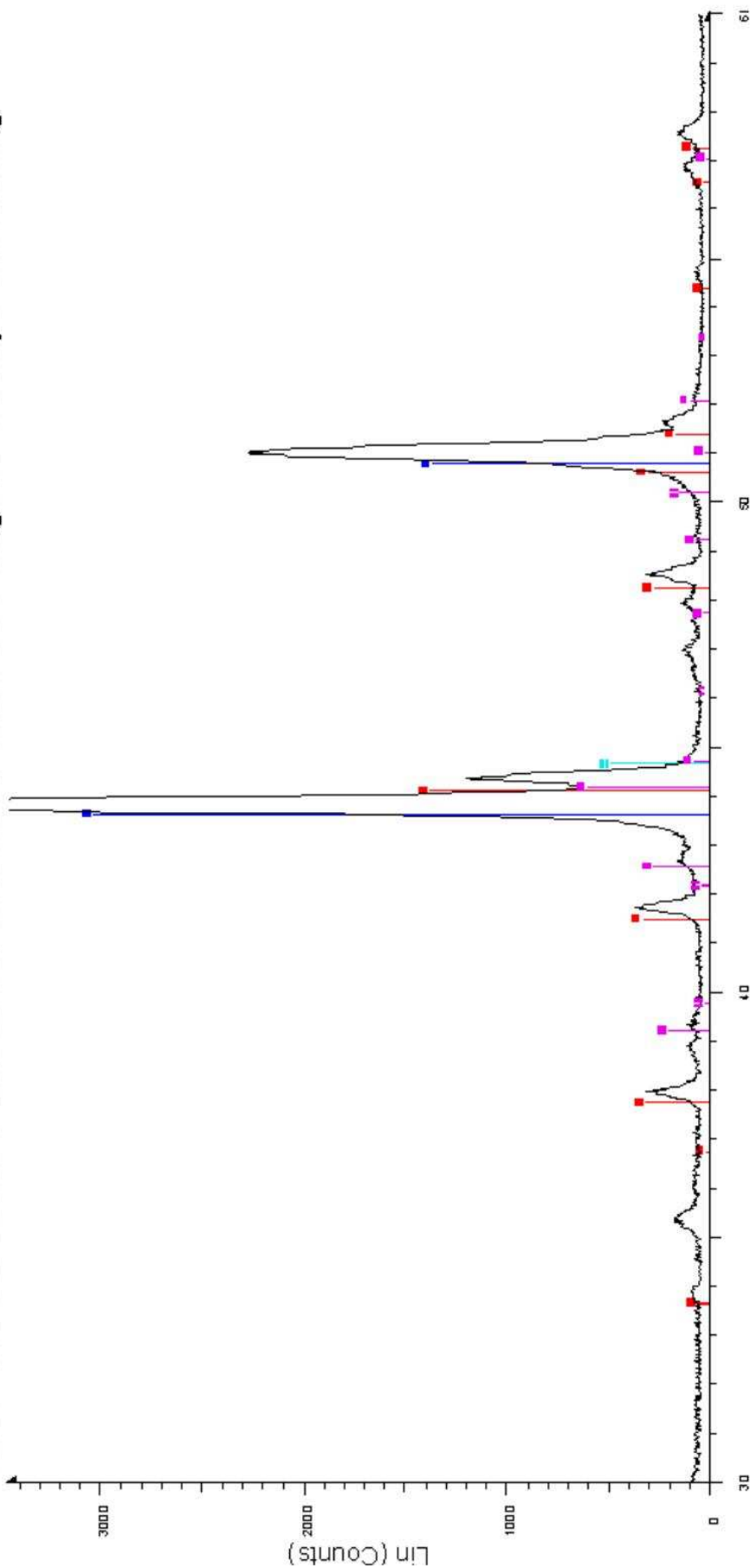
00-035-0804 (C) - Tongbaite, syn - Cr3C2 - Y: 21.26 % - d x by: 1. - W/L: 1.5406 - Orthorhombic - a 6.52730 - b 11.48830 - c 2.82860 - alpha 90.000 - beta 90.000 - gamma 90.000 - Primitive - Pnzm (62) - 4 - 4

00-035-0783 (C) - Chromium Carbide - Cr23C6 - Y: 54.32 % - d x by: 1. - W/L: 1.5406 - Cubic - a 10.65990 - b 10.65990 - c 10.65990 - alpha 90.000 - beta 90.000 - gamma 90.000 - Face-centered - Fm3m (2

# coating v 700c 16days stainless steel interface

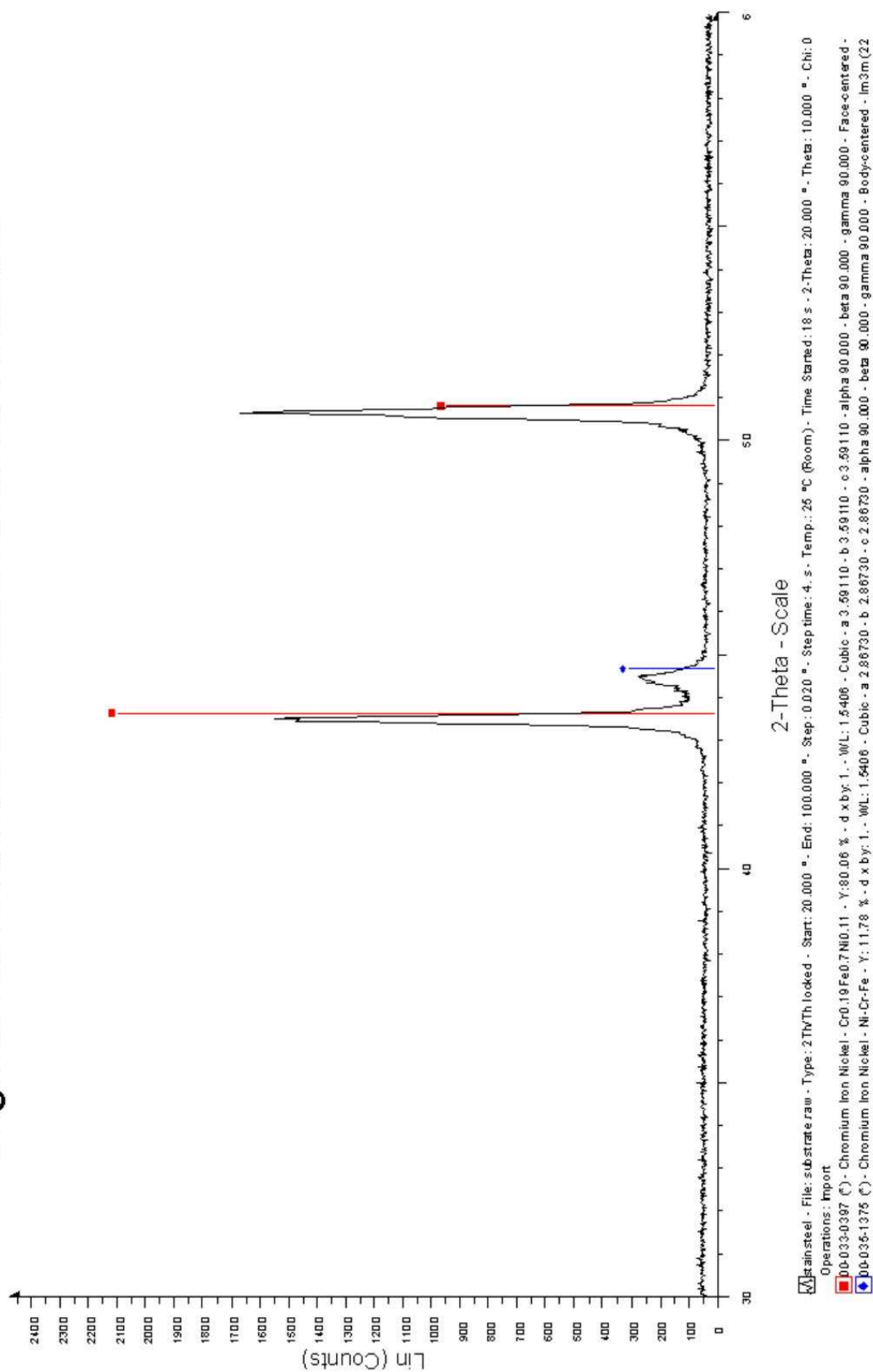


# NiCr-Cr3C2 coated substrate interface after 800 degree 16days annealing

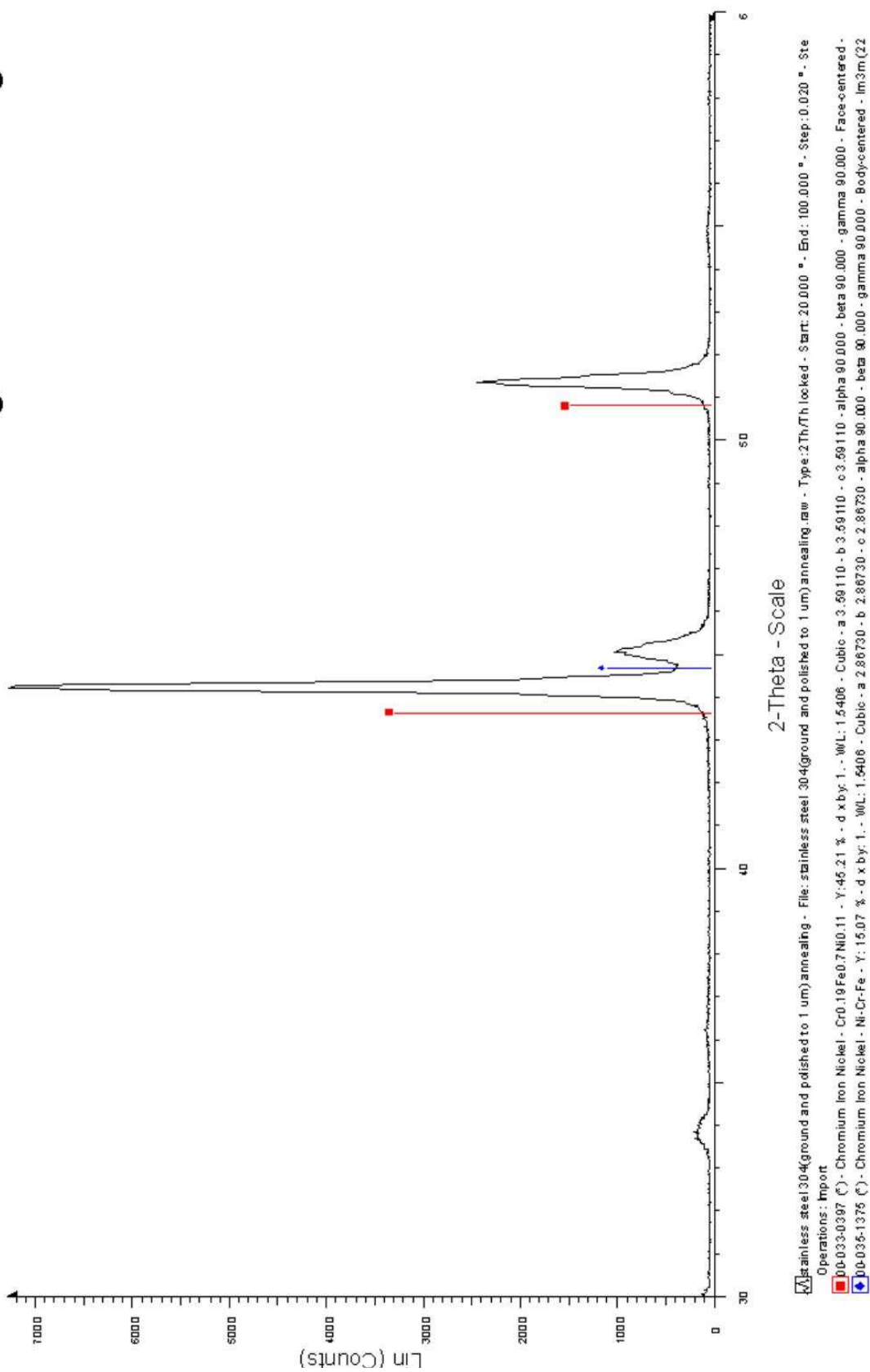


Operating v 800c 8days stainless steel interface2 - File: coating v 800c 8days stainless steel interface2.raw - Type: 2Th/Th locked - Start: 20.000 ° - End: 100.000 ° - Step: 0.020 ° - Step time: 4. s - Temp.: 25 °  
 Operations: Import  
 00-036-0783 (°) - Chromium Carbide - Cr23C6 - Y: 22.60 % - d x by: 1. - W/L: 1.5406 - Cubic - a 10.86990 - b 10.86990 - c 10.86990 - alpha 90.000 - beta 90.000 - gamma 90.000 - Face-centered - Fm3m (2  
 00-036-1375 (°) - Chromium Iron Nickel - Ni-Cr-Fe - Y: 7.96 % - d x by: 1. - W/L: 1.5406 - Cubic - a 2.86730 - b 2.86730 - c 2.86730 - alpha 90.000 - beta 90.000 - gamma 90.000 - Body-centered - Im3m (229  
 00-033-0397 (°) - Chromium Iron Nickel - Cr0.19Fe0.7Ni0.11 - Y: 49.84 % - d x by: 1. - W/L: 1.5406 - Cubic - a 3.59110 - b 3.59110 - c 3.59110 - alpha 90.000 - beta 90.000 - gamma 90.000 - Face-centered -  
 00-036-1482 (°) - Chromium Carbide - Cr7C3 - Y: 9.98 % - d x by: 1. - W/L: 1.5406 - Orthorhombic - a 7.01490 - b 12.15300 - c 4.53200 - alpha 90.000 - beta 90.000 - gamma 90.000 - Primitive - Pnccm (51) -

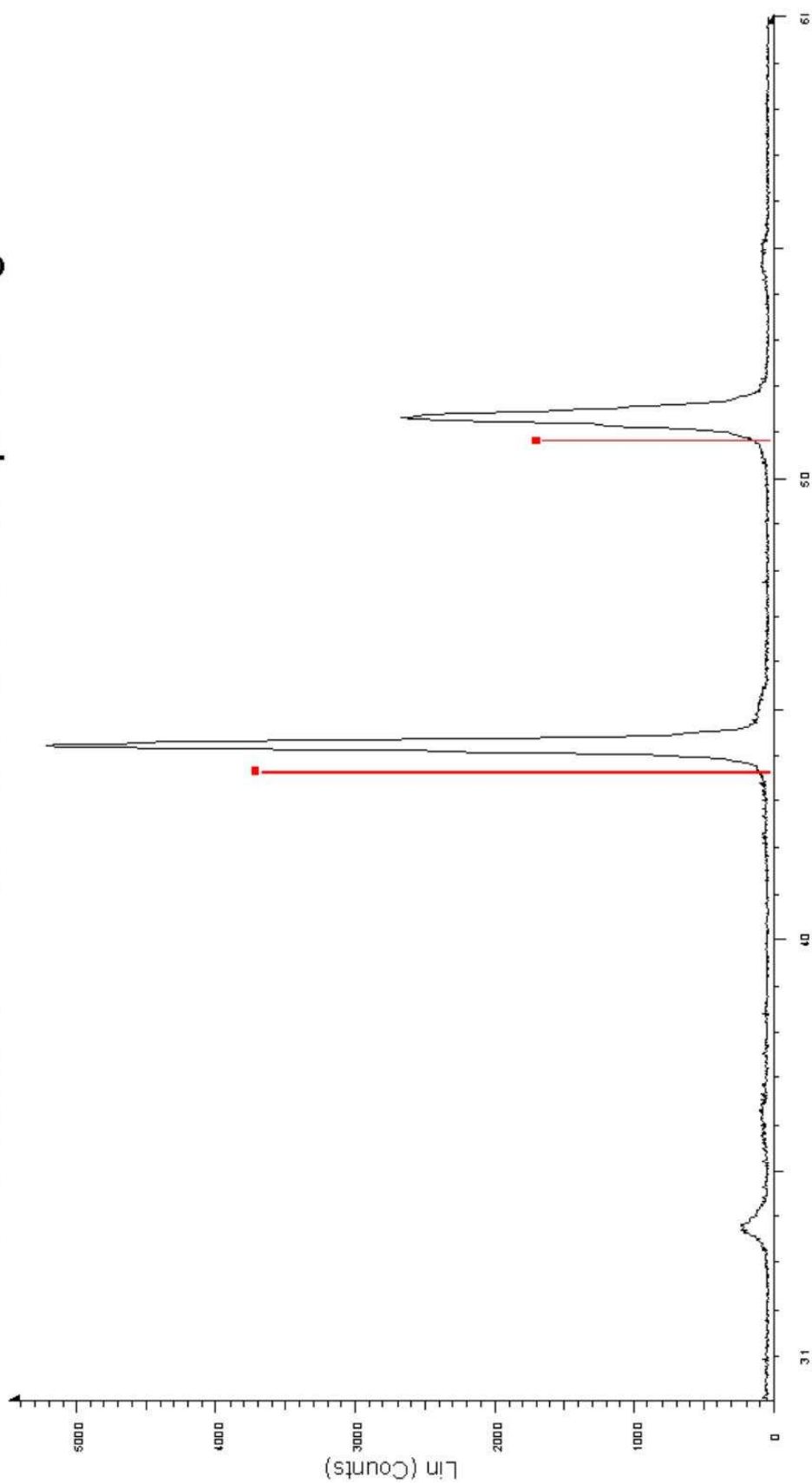
# Original As-revieved stainless steel 304 surface



# Grit blasted ss304 surface after 750 annealing with airl cooling



# Grit blasted ss 304 surface after oil quenching



stainless steel 304(ground and polished to 1 um)quench - File: stainless steel 304(ground and polished to 1 um)quench.raw - Type: 2Th/Th locked - Start: 20.000 ° - End: 100.000 ° - Step: 0.020 ° - Step tm  
 Operations : Import  
 00-033-0397 (C) - Chromium Iron Nickel - Cr0.19Fe0.7Ni0.11 - Y:70.38 % - d x by: 1. - W/L: 1.5406 - Cubic - a 3.59110 - b 3.59110 - c 3.59110 - alpha 90.000 - beta 90.000 - gamma 90.000 - Face-centered -

# grit blasted ss 304 surface after 800 2days

